



# **Electrochemical deposition and dissolution of nickel from electroforming solutions**

**A Thesis submitted by**

**Christine Enowmbi Tambe**

**For the Degree of Doctor of Philosophy**

Department of Chemical and Process Engineering  
University of Strathclyde

May 24, 2023

## **Declaration of Authenticity and Author's Rights**

This thesis is the result of the author's original research. It has been composed by the author and has not been previously submitted for examination, which has led to the award of a degree.

The copyright of this thesis belongs to the author under the terms of the United Kingdom Copyright Acts as qualified by University of Strathclyde Regulation 3.50. Due acknowledgement must always be made of the use of any material contained in, or derived from, this thesis.

Signed: CHRISTINE ENOWMBI TAMBE

Date: May 24, 2023



# Abstract

Nickel sulfamate electrolytes have been traditionally used for electroforming of nickel, which refers to the fabrication of free-standing nickel structures grown by electrodeposition on a mandrel. Despite its early commercialisation in 1939, there remains considerable confusion about the role of boric acid, a constituent added to the sulfamate electrolyte to obtain current efficiencies of 100% and prevent the formation of  $\text{OH}^-$  at the cathode surface resulting from the parasitic hydrogen evolution reaction. The debatable role of boric acid during nickel electroforming is in part due to a lack of adequate systematic data on deposition kinetics and current efficiency under important bath conditions such as boric acid concentration, temperature, and agitation. On the other hand, a variety of nickel materials are routinely employed as anodes in sulfamate electrolytes. Modern nickel anodes come in different shapes and compositions, some of which contain a reasonable amount of sulfur inclusions ( $>0.015$  wt% S) called sulfur-depolarised anodes and others which contain negligible amounts, referred to as low-sulfur nickel anodes. The performance of these modern anodes produced by the Mond process have not been determined in sulfamate-based electrolytes. Therefore, it is unclear if these anodes have a propensity to passivate and breakdown the electrolyte. The purpose of this project is to deliver a critical understanding of the influence of boric acid and anode materials on nickel deposition and dissolution, respectively, during a sulfamate-based electroforming process.

This study uses electrochemical potentiodynamic studies and galvanostatic deposition in a bespoke electrochemical cell alongside Electrochemical Quartz Crystal Microbalance (EQCM) measurements to interrogate and resolve some unanswered questions about the role of boric acid. The current efficiency and kinetics of nickel electrodeposition (and hydrogen evolution) at a stainless-steel electrode at different boric acid concentrations (0 to 0.81 M), solution temperatures (40-55 °C), and electrode rotation speeds (0-1600 rpm) have been determined. The results of EQCM studies were used to verify the current efficiency and rate of nickel deposition at selected boric acid concentrations and temperatures. It was found that addition of boric acid produced deposits with current efficiencies close to 100%, high cathodic Tafel slopes ranging from 120 to 251 mV/decade, and high deposition rates under any condition in unagitated

systems. In contrast to the belief that boric acid provides buffering action, it is proposed that boric acid molecules adsorb on the electrode surface and form complexes with  $\text{NiX}^+$  (where  $\text{X} = \text{OH}$  or  $\text{Cl}$ ) from solution to facilitate nickel ion discharge.

Cathodic potentiodynamic measurements were collected in a blank electrolyte without  $\text{Ni}^{2+}$  to investigate the interaction of boric acid with different substrate materials (Ni, Au, Cu, and 304 SS). In the absence of boric acid, the cathodic Tafel slopes were measured at 243, 213, 189, and 199 mV/decade for 304 SS, Au, Cu, and Ni electrodes, respectively, indicating the presence of surface oxides/hydroxides most probably resulting from  $\text{OH}^-$  generation via water reduction which likely promote the oxidation of the electrode surface. Simultaneous measurements of charge and mass at an EQCM showed that a significant amount of hydroxides/oxides was formed in the early stages of water reduction. The mass change observed in the presence of boric acid showed that the electrode surface got covered by 4-5 monolayers of boric acid molecules at potentials more negative than -0.9 V vs SCE, which later desorbed. Boric acid adsorbed to different extents on the investigated substrates in the following order: 304SS > Ni > Au > Cu. In a second series of experiments, the kinetics of interfacial reactions was studied in the presence of a small amount of  $\text{Ni}^{2+}$  (17.85 mM) in the electrolyte. In this case, the surface hydroxides/oxides grew at a faster rate due to the electroprecipitation of  $\text{Ni}(\text{OH})_2$  or  $\text{NiO}$ . In the presence of boric acid, nickel electrodeposition occurred simultaneously with hydrogen evolution via proton reduction only. Furthermore, the formation of nickel oxides/hydroxides in the presence of boric acid and  $\text{Ni}^{2+}$  was blocked. The high sensitivity of the EQCM ( $\pm 1.3$  ng) made it a useful tool for the investigation of adsorbed species which could not be done using a rotating disc electrode. The findings in this thesis affirm the adsorption of boric acid as a plausible mechanism for suppressing the adsorption of water and facilitating nickel ion discharge. This is attributed to the ability of nickel ions to form Ni-O bonds with adsorbed boric acid molecules which are stronger than hydrogen bonds formed with water. Not only do such nickel borate complexes contribute to an increased stability of nickel ions on the electrode surface, but they also allow for dense packing of nickel ions to form an effective barrier against the diffusion of water from solution to the electrode surface.

In other investigations, it was revealed that low sulfur nickel anodes often re-

quired high anode potentials in the transpassive dissolution region to support current densities employed for electroforming. This led to anode current efficiencies of 50-100%. On the other hand, sulfur-activated nickel could support current densities over  $100 \text{ mA cm}^{-2}$  at low potentials in the active region and dissolved with current efficiencies close to 100%. The generation of sulfamate ion oxidation products, which give rise to a distinct UV band at 245 nm, was investigated using UV-Vis spectroscopy. It was found that these products were not generated at a sulfur-activated anode but were present at low-sulfur and Pt anodes in quantities that were dependent on the anode current density employed; a lower current density led to a lower rate of generation of sulfamate products. Azodisulfonate was determined to be the principal oxidation product. Indication of the presence of sulfite ions could also be gleaned from the UV-Vis spectra of solutions electrolysed with a low-sulfur nickel anode. The sulfamate oxidation products generated at the low-sulfur nickel anode were found to depolarise the cathode but had a minimal influence on the cathode current efficiency. Earlier investigations have indicated that, while the presence of azodisulfonate and sulfite in electroforming solutions led to the generation of nickel deposits with lower internal stress and increased hardness, they also increased the sulfur content in nickel parts making low-sulfur nickel anodes unemployable in applications where sulfur embrittlement is an issue. Therefore, sulfur-activated anodes which do not decompose sulfamate ions are recommended for such applications.

# Acknowledgements

I give thanks to God Almighty for His Grace, love, and mercy to complete this journey, and for the individuals I met along the way.

It would be difficult to overstate the support of my supervisor, Professor Sudipta Roy. I am especially grateful for her intention to teach me and ensure that the research experience is an enriching one by providing opportunities to learn and apply the knowledge. It has been a tremendously valuable experience to work with her, one which will continue to mould me. I would also like to thank my second supervisor, Dr. Todd Green, for his guidance and insightful discussions, especially relating to the anode experiments.

I am grateful to my parents, Mr Christopher Tiku Tambe and Ms. Joan Njanjo Dimitte for their love, prayers, and financial support. Without your encouragement and belief in me, I could not have pursued this Doctoral Research. Special thanks to my siblings, Ayuk and Ada, who are a source of strength in my lowest moments and always provide the medicine of laughter. I love you all.

I would especially like to thank my friend, Dr Priscila Valverde Armas, for the induction in the laboratory, added insight into principles I needed to understand for my work, her encouragement, and kindness. I extend my warmest thanks to all my colleagues in the office and my research group for their cheerful influence, especially Pamela, John, Eleni, Thomas, Shaon, Shahin, and James.

I would like to thank the technical and administrative staff at the Chemical and Process Engineering department for their assistance through out my PhD. I am grateful to Mr James Kelly for preparing my SEM samples and to Dr. Maider Olasolo, and Dr. Tiziana Marrocco for training me on the SEM and EDS. A special thanks to Dr. Yi-Chieh Chen for training me to use the UV-Vis spectrophotometer.

Finally, I would like to thank my uncles, aunties, and friends who have supported and encouraged me along this journey.

# Contents

<b>ABSTRACT</b>	<b>ii</b>
<b>LIST OF FIGURES</b>	<b>xxv</b>
<b>LIST OF TABLES</b>	<b>xxviii</b>
<b>LIST OF SYMBOLS</b>	<b>xxix</b>
<b>LIST OF ABBREVIATIONS</b>	<b>xxx</b>
<b>1 Introduction</b>	<b>1</b>
1.1 Introduction to Electroforming . . . . .	1
1.2 Electroforming versus electroplating . . . . .	3
1.3 Nickel Electroforming . . . . .	4
1.4 Basic concepts of electrodeposition . . . . .	7
1.5 Nickel electrolytes . . . . .	8
1.6 Motivation . . . . .	12
1.7 Aims and objectives of current work . . . . .	14
1.8 Thesis organisation . . . . .	16
<b>2 Literature Review</b>	<b>17</b>
2.1 Proposed mechanisms for the action of boric acid on the kinetics of interfacial processes . . . . .	17
2.1.1 Cathode reactions . . . . .	17
2.1.1.1 Nickel electrodeposition mechanism . . . . .	17
2.1.1.2 Proton and water reduction on nickel electrodes . . . . .	22
2.1.2 Role of boric acid during nickel electrodeposition . . . . .	24
2.1.3 Effect of boric acid on charge transfer kinetics . . . . .	31
2.2 Types of anode materials . . . . .	35
2.2.1 Insoluble anodes . . . . .	37
2.2.2 Soluble anodes . . . . .	38
2.2.2.1 Depolarised nickel . . . . .	41

2.2.2.2	Carbon-containing nickel . . . . .	42
2.2.2.3	Primary nickel . . . . .	42
2.2.2.3.1	Titanium baskets . . . . .	45
2.3	<b>Kinetics and mechanism of nickel dissolution and passivity</b> . . . . .	47
2.3.1	Active dissolution . . . . .	47
2.3.2	Passivation . . . . .	48
2.3.3	Transpassive dissolution . . . . .	51
2.4	<b>Effect of chloride ions on nickel dissolution and passivity</b> . . . . .	54
2.5	<b>Effect of sulfur on nickel dissolution and passivity</b> . . . . .	57
2.6	<b>Review of the anodic behaviour of different materials in nickel plating electrolytes</b> . . . . .	58
2.7	<b>Oxidation of sulfamate ions</b> . . . . .	62
<b>3</b>	<b>Fundamentals</b>	<b>67</b>
3.1	<b>An overview of electroforming</b> . . . . .	67
3.1.1	Laboratory studies of electrodeposition systems . . . . .	68
3.2	<b>Thermodynamics of electrodeposition</b> . . . . .	70
3.2.1	Introduction . . . . .	70
3.2.2	Equilibrium potential . . . . .	71
3.2.3	Thermodynamic considerations in nickel sulfamate electrolytes . . . . .	73
3.2.4	Current efficiency . . . . .	75
3.3	<b>Electrochemical kinetics</b> . . . . .	77
3.3.1	Introduction . . . . .	77
3.3.2	Departure from equilibrium: overpotential . . . . .	77
3.3.3	Charge transfer kinetics . . . . .	79
3.3.4	Charge transfer kinetics of multistep processes . . . . .	81
3.3.5	Charge transfer kinetics: Tafel equation . . . . .	82
3.3.6	Application of kinetics to understanding reaction mechanisms in nickel plating electrolytes . . . . .	83
3.3.7	Overall importance of kinetics in electroforming . . . . .	87
3.4	<b>Mass transport during electrodeposition</b> . . . . .	89
3.5	<b>Electrocrystallisation</b> . . . . .	92

<b>4</b>	<b>Experimental</b>	<b>95</b>
4.1	<b>Nickel Electrodeposition Kinetics</b>	95
4.1.1	Electrolyte preparation	96
4.1.2	Equipment	97
4.1.2.1	Polarisation Experiments	98
4.1.2.2	Deposition Experiments	101
4.1.2.3	Working electrode preparation for polarisation and deposition experiments	102
4.1.2.4	Material characterisation: Scanning Electron Microscopy (SEM) and Energy Dispersive X-ray Spectroscopy (EDS)	103
4.1.2.4.1	SEM instrumentation	103
4.1.2.4.2	Operating principle of the SEM and EDS	104
4.1.2.4.3	Sample preparation for SEM and EDS analysis	106
4.1.3	Procedure	108
4.1.3.1	Polarisation Measurements	108
4.1.3.1.1	Polarisation technique: Linear Sweep Voltammetry (LSV)	108
4.1.3.1.2	Polarisation procedure	109
4.1.3.1.3	Determination and correction of ohmic drop	110
4.1.3.2	Galvanostatic deposition experiments	114
4.1.3.3	Data Interpretation for polarisation and deposition	115
4.1.3.4	SEM and EDS	116
4.2	<b>EQCM studies of interfacial processes during nickel electrodeposition</b>	117
4.2.1	Electrolytes	118
4.2.2	Equipment	119
4.2.2.1	Operating principle of an EQCM	119
4.2.2.2	Substrate materials	121
4.2.2.3	Preparation and re-usability of 304 SS quartz crystals	122
4.2.2.4	EQCM equipment	123
4.2.3	Procedure	125
4.2.3.1	EQCM Calibration procedure	125

4.2.3.1.1	EQCM calibration with Cu electrodeposition . . . . .	126
4.2.3.1.2	EQCM calibration with Ni electrodeposition . . . . .	129
4.2.3.2	EQCM experimental procedure . . . . .	132
4.2.3.2.1	Effect of boric acid on nickel electrodeposition rates and current efficiencies . . . . .	132
4.2.3.2.2	Effect of boric acid on HER kinetics and the initial stages of Ni electrodeposition . . . . .	133
<b>4.3</b>	<b>Characterisation of anode materials for nickel electroforming . . . . .</b>	<b>133</b>
4.3.1	Electrolytes . . . . .	134
4.3.2	Equipment . . . . .	134
4.3.2.1	Anode materials employed . . . . .	135
4.3.2.2	Anode preparation . . . . .	137
4.3.2.3	Polarisation and current efficiency measurements . . . . .	139
4.3.2.4	Sulfamate ion oxidation studies . . . . .	139
4.3.2.4.1	Operating principle of Ultraviolet Visible spec- trophotometer . . . . .	140
4.3.2.4.2	UV-Vis spectroscopy equipment . . . . .	142
4.3.2.5	Influence of anodic processes on electrodeposition and long-term stability of the electrolyte . . . . .	143
4.3.3	Procedure . . . . .	143
4.3.3.1	Polarisation and current efficiency measurements . . . . .	143
4.3.3.2	Sulfamate ion oxidation studies . . . . .	145
4.3.3.2.1	UV-Vis spectroscopy test procedure . . . . .	146
4.3.3.3	Influence of anodic processes on electrodeposition and long-term stability of the electrolyte . . . . .	147
<b>5</b>	<b>Effect of boric acid on nickel electrodeposition under electroforming con-     ditions . . . . .</b>	<b>149</b>
<b>5.1</b>	<b>Nickel electrodeposition from solutions without agitation . . . . .</b>	<b>150</b>
5.1.1	Total vs. partial polarisation curves . . . . .	150
5.1.2	Current-potential data from polarisation and deposition . . . . .	154
5.1.2.1	Effect of boric acid . . . . .	154
5.1.2.2	Inclusion of chloride ions . . . . .	158



5.1.2.3	Influence of temperature . . . . .	161
5.1.2.3.1	In the absence of boric acid . . . . .	162
5.1.2.3.2	In the presence of boric acid . . . . .	163
5.1.3	Kinetics of nickel electrodeposition . . . . .	164
5.1.3.1	Effect of chloride ions . . . . .	164
5.1.3.2	Effect of boric acid . . . . .	167
5.1.3.3	Effect of temperature . . . . .	168
5.1.4	Material analysis: SEM and EDS . . . . .	169
5.1.5	Discussion . . . . .	173
5.2	<b>Nickel electrodeposition from agitated solutions</b> . . . . .	175
5.2.1	Current-potential data from polarisation and deposition . . . . .	176
5.2.2	Kinetics of nickel electrodeposition . . . . .	178
5.2.3	Discussion . . . . .	180
5.3	<b>Summary of main findings</b> . . . . .	181
<b>6</b>	<b>Effect of boric acid on the interfacial processes during nickel electrodeposition: An EQCM study</b>	<b>183</b>
6.1	<b>Response of the quartz crystal to mass changes on the electrode surface</b> . . . . .	184
6.2	<b>Effect of boric acid on nickel electrodeposition</b> . . . . .	187
6.2.1	Ni electrodeposition in the absence of boric acid . . . . .	187
6.2.2	Ni electrodeposition in the presence of boric acid . . . . .	193
6.2.3	Gravimetric analysis . . . . .	196
6.3	<b>Hydrogen evolution reaction (HER) kinetics in the absence of nickel ions</b> . . . . .	198
6.3.1	Study of HER kinetics on different substrates in the absence of boric acid . . . . .	198
6.3.2	Study of HER kinetics in the presence of boric acid . . . . .	206
6.4	<b>Effect of boric acid on the initial stages of nickel deposition</b> . . . . .	213
6.4.1	Nickel electrodeposition in the absence of boric acid . . . . .	214
6.4.2	Nickel electrodeposition in the presence of boric acid . . . . .	218
6.5	<b>Summary of main results</b> . . . . .	223

<b>7</b>	<b>Characterisation of anode materials for nickel electroforming</b>	<b>227</b>
7.1	<b>Polarisation behaviour of different anode materials in nickel sulfamate solution</b> . . . . .	228
7.2	<b>Polarisation behaviour of pure nickel anodes in nickel sulfamate solution</b> . . . . .	232
7.2.1	Effect of electrode rotation speed . . . . .	232
7.2.2	Effect of chloride ions . . . . .	233
7.3	<b>Polarisation behaviour of sulfur-depolarised nickel anodes in nickel sulfamate solution</b> . . . . .	236
7.3.1	Effect of rotation speed . . . . .	236
7.3.2	Effect of chloride ions . . . . .	237
7.4	<b>Concluding remarks on the polarisation behaviour of nickel anodes</b>	238
7.5	<b>Dissolution potential and current efficiency of nickel anodes</b> . . . .	239
7.5.1	Dissolution potential . . . . .	239
7.5.2	Anode current efficiencies . . . . .	242
7.6	<b>Anodic oxidation products in nickel sulfamate solution</b> . . . . .	245
7.6.1	Effect of isolation of the anode . . . . .	246
7.6.2	Effect of anode material and current density . . . . .	251
7.6.3	Nature of the sulfamate decomposition product . . . . .	255
7.7	<b>Impact of the anode process on the electroforming process from sulfamate baths</b> . . . . .	265
7.7.1	Electrodeposition behaviour of nickel . . . . .	266
7.7.2	Current efficiency of nickel electrodeposition . . . . .	268
7.8	<b>Summary of main findings</b> . . . . .	270
<b>8</b>	<b>Conclusions and Future Work</b>	<b>273</b>
8.1	<b>Conclusions</b> . . . . .	273
8.2	<b>Suggestions for Future Work</b> . . . . .	275
	<b>References</b>	<b>277</b>
<b>9</b>	<b>Appendices</b>	<b>305</b>
9.1	<b>Appendix A: Derivation of the ion-transfer kinetic equation</b> . . . . .	305

9.2	<b>Appendix B: Optical micrographs of nickel deposited from sulfamate baths . . . . .</b>	309
9.3	<b>Appendix C: Tafel plot for Ni(II) reduction in pure nickel sulfamate solution . . . . .</b>	310
9.4	<b>Appendix D: EQCM gravimetry curves for Ni(II) reduction on 304 SS in dilute nickel sulfamate electrolytes with and without boric acid .</b>	311
9.5	<b>Appendix E: List of Publications . . . . .</b>	312

# List of Figures

1.1	Lightweight satellite steering rocket nozzle heat shields and a lightweight satellite microwave antenna horn [28]. . . . .	5
1.2	Schematic of a nickel electroforming set-up . . . . .	7
1.3	Variation of mean stress in 20 $\mu\text{m}$ electrodeposits from different nickel electrolytes. Adapted from [49]. . . . .	11
2.1	Idealised anodic polarisation curve obtained potentiodynamically in nickel electroforming solution [137]. Key: $U_{pp}$ : principal or critical passivation potential, $U_b$ : passive film breakdown potential, $j_{pp}$ : critical passivation current density, $j_p$ : the current density in the passive region. AB is the active region for dissolution and BC the active-to-passive transition region for dissolution. Adapted from [138] . . . . .	40
2.2	Historical development of soluble nickel anode materials. . . . .	41
2.3	Industrial setup of nickel electroforming [148]. The red boxes highlight titanium baskets which are filled with nickel pellets . . . . .	46
2.4	The mechanism of voiding and collapse of the oxide layer driven by the potential drop at the metal/oxide interface of an inter-granular boundary in the oxide layer [165]. . . . .	53
2.5	The mechanism of stress induced fracture driven by anion transport through an inter-granular boundary in the oxide layer [165] . . . . .	53
2.6	The effect of chloride ions on the mechanism of local thinning and breakdown of passivity driven by the potential drop at the oxide/electrolyte interface of an inter-granular boundary in the oxide layer [165]. . . . .	55
2.7	Anodic polarisation curves of different nickel anode materials obtained under galvanostatic conditions in Watts and chloride-free nickel sulfate electrolytes [138]. . . . .	59
2.8	Anodic polarisation curves of different nickel anode materials obtained under potentiodynamic conditions in nickel sulfamate-based electrolytes at 60 °C and pH 4.0. The base electrolyte contained 1.86 M $\text{Ni}(\text{SO}_3\text{NH}_2)_2 \cdot 4\text{H}_2\text{O}$ and 0.65 M $\text{H}_3\text{BO}_3$ , plus 0.037-0.1 M $\text{NiCl}_2 \cdot 6\text{H}_2\text{O}$ . Adapted from [50]. . . . .	60

2.9	Anodic polarisation curves, obtained under galvanostatic (black and white markers) and potentiodynamic conditions (red, green, and blue markers), of different anode materials in nickel sulfamate-based electrolytes measured by Nakano et al. [130] and Yang et al. [180], respectively. The base electrolyte of Nakano et al. [130] contained 1 M Ni(SO <sub>3</sub> NH <sub>2</sub> ) <sub>2</sub> ·4H <sub>2</sub> O plus 0.126 M NiCl <sub>2</sub> at 50 °C and pH 4.0. The base electrolyte of Yang et al. [180] contained 1.39 M Ni(SO <sub>3</sub> NH <sub>2</sub> ) <sub>2</sub> ·4H <sub>2</sub> O, 0.65 M H <sub>3</sub> BO <sub>3</sub> , and 1mL/L wetting agent (WT-400), plus 0.021 M NiCl <sub>2</sub> ·6H <sub>2</sub> O at 50 °C and pH 3.6. Adapted from [130] and [180]. . . . .	61
3.1	Schematic of (a) the Helmholtz electrical double layer model and (b) the potential drop across the double layer. Adapted from [183] . . . . .	68
3.2	Schematic of an electrochemical cell with a three-electrode system employing a potentiostat. Current and voltage measurement devices are represented by A and V, respectively. . . . .	69
3.3	Potential-pH diagram for a pure aqueous Ni <sup>2+</sup> system at 25 °C, 1 atm. and a total Ni <sup>2+</sup> concentration of 1.785 M. The numbers in the figure correspond to the reactions given in Table 3.1 . . . . .	74
3.4	Metal/metal ion electrode showing anodic and cathodic currents at equilibrium and during application of an overpotential (subscript a=anodic and c=cathodic). Adapted from [183] . . . . .	79
3.5	Schematic diagram showing (a) ion transfer and (b) electron transfer processes. Adapted from [48] . . . . .	80
3.6	Dependence of exchange current density for hydrogen evolution reaction on the strength of the metal-hydrogen bond formed in the electrode reaction. Adapted from [193] . . . . .	86
3.7	Schematic showing the effect of surface features on the thickness distribution. Thicker deposits are obtained at the edges due to relatively higher currents at these points. . . . .	87

3.8	Schematic showing the reactant ( $\text{Ni}^{2+}$ ) concentration profile which describes the concentration distribution of $\text{Ni}^{2+}$ around the electrode surface where the bulk concentration drops to a lower value at the OHP. The thickness of the depletion layer is approximated using the Nernst diffusion layer thickness ( $\delta$ ). Adapted from [183]. . . . .	91
3.9	Schematic of electrocrystallisation steps: (a) charge transfer to form an ad-atom and its subsequent surface diffusion towards a growth site (steps or kink); and (b) charge transfer directly at a growth site. Adapted from [48]. . . . .	93
4.1	Schematic of the electrochemical glass cell used for polarisation experiments showing a three-electrode configuration. The potential of the 304SS rotating disc electrode (RDE), which acts as the working electrode, is controlled by the potentiostat against a saturated calomel reference electrode while the current flowing between the RDE and Pt counter electrode is measured. . . . .	98
4.2	Components and assembly of the rotating disc electrode (RDE). . . . .	99
4.3	Schematic of the electrochemical glass cell used for galvanostatic deposition experiments showing a two-electrode configuration. A constant current was applied between the RDE working electrode and Pt counter electrode using a potentiostat to electrodeposit Ni for a desired period of time. Pt was placed in a bridge tube to limit diffusion of anode reaction products to the catholyte. . . . .	102
4.4	Schematic of major components of a Scanning Electron Microscope (SEM). Adapted from [204]. . . . .	103
4.5	Illustration of the sample interaction volume of the SEM, the corresponding emissions from various depths, and their respective mechanisms of emission resulting from the interaction of the electron beam with sample atoms. The exact interaction volume will depend on the accelerating voltage of the electron beam and sample composition. Adapted from [204]. . . . .	105
4.6	Image of the epoxy resin containing 5 cross-sectioned Ni deposits held in place by black clippers. . . . .	107

4.7	Equivalent circuit for the working electrode in a three-electrode configuration. Adapted from [47]	111
4.8	Example of a nyquist plot measured in Bath E at 45 °C showing how the uncompensated resistance, $R_U$ can be determined from the real part of the impedance at the highest frequency.	112
4.9	The effect of ohmic drop (IR) correction on the polarisation curve measured from Bath E at 45 °C and 0 rpm; $R_U = 5 \Omega$	114
4.10	A micrograph of Ni electrodeposited from Bath E at 45 °C showing EDS measurements mapped over 6 areas of the deposit cross-section. The arrow in the Figure indicates the direction of growth of the deposit.	117
4.11	Schematic representation of the transverse acoustic wave in a quartz crystal and a composite resonator comprising the quartz crystal and a layer of foreign material. Adapted from [211]	119
4.12	Step-by-step assembly of the quartz crystal into the well cell holder	122
4.13	Measured polarisation and frequency scans performed in 1.78 M $\text{Ni}(\text{SO}_3\text{NH}_2)_2 \cdot 4\text{H}_2\text{O}$ + 0.49 M $\text{H}_3\text{BO}_3$ at $0.005 \text{ V s}^{-1}$ and 45°C on fresh (intercrystal) and used (intracrystal) 304 SS quartz crystal surfaces.	123
4.14	Electrochemical Quartz Crystal Microbalance apparatus.	124
4.15	Variation of the resonant frequency change as a function of charge passed for galvanostatic Cu deposition on (a) 304 SS and (b) Au quartz crystal electrodes from 0.1 M $\text{CuSO}_4$ + 0.5 M $\text{H}_2\text{SO}_4$ at $-10 \text{ mA cm}^{-2}/45 \text{ }^\circ\text{C}$ .	127
4.16	Cyclic voltammograms of 0.1 M $\text{CuSO}_4$ + 0.5 M $\text{H}_2\text{SO}_4$ solution on (a) 304 SS and (b) Au at $10 \text{ mV s}^{-1}/45 \text{ }^\circ\text{C}$ , showing the measured current (black), smoothed calculated currents (green), and frequency change (red). Sensitivity factors ( $C_f$ ) derived from calibrations with copper deposition from the same electrolyte are used to calculate currents.	128
4.17	Variation of the resonant frequency change of the steel quartz crystal electrode as a function of charge passed for galvanostatic Ni deposition from 1.78 M $\text{Ni}(\text{SO}_3\text{NH}_2)_2 \cdot 4\text{H}_2\text{O}$ + 0.49 M $\text{H}_3\text{BO}_3$ at $10 \text{ mA cm}^{-2}/$ (a) 45 °C and (b) 55 °C.	130

4.18	Cyclic voltammograms of 0.1 M CuSO <sub>4</sub> + 0.5 M H <sub>2</sub> SO <sub>4</sub> solution on 304 SS at 10 mV s <sup>-1</sup> /45 °C, showing the measured current (black), smoothed calculated currents (green), and frequency change (red). The sensitivity factor ( $C_f$ ) derived from calibrations with nickel deposition from a solution containing 1.78 M Ni(SO <sub>3</sub> NH <sub>2</sub> ) <sub>2</sub> ·4H <sub>2</sub> O and 0.49 M H <sub>3</sub> BO <sub>3</sub> is used to calculate currents. . . . .	130
4.19	Calibration constants (sensitivity factors) of 304 SS crystals obtained from Ni electrodeposition at different applied cathode current densities and temperatures. . . . .	131
4.20	Forms of Ni anode materials. . . . .	138
4.21	Photograph of a Ni P-pellet assembly. . . . .	138
4.22	Diagram of a single beam spectrophotometric experiment showing the basic instrumentation. Adapted from [224] . . . . .	141
4.23	UV-Vis spectra of fresh Bath E acquired with cuvettes of 1 mm and 10 mm pathlengths. . . . .	142
4.24	(a) Boric acid crystallisation in the cuvette taken at 25 °C and (b) UV-Vis spectra of non-electrolysed Bath E acquired at different temperatures, which were not reproducible due to boric acid crystallisation. . . . .	146
5.1	Polarisation curves: total current densities ( $j$ , solid lines) and partial current densities for Ni deposition ( $j_{Ni}$ , circles) and hydrogen evolution reaction ( $j_{H_2}$ , squares) in quiescent Bath A (black) and Bath B (lightblue) at 40 °C. This data shows the effect of boric acid on the rates of nickel electrodeposition and hydrogen evolution reactions. The Figure inset shows the effect of boric acid on the current breakthrough potential. . .	151
5.2	Polarisation curves: total current densities (solid lines) and Ni current densities (circles) for electrodeposition in quiescent Bath A (●); Bath B (●); Bath C (●); Bath D (●); Bath E (●); and Bath F (●) at different temperatures. . . . .	156
5.3	Effect of boric acid on the appearance of the nickel films plated at 30 mA cm <sup>-2</sup> and 40 °C from: (a) Bath A (without boric acid) and (b) Bath C (containing 0.65 M boric acid). . . . .	157



5.4	Polarisation curves: total current densities (solid lines) and Ni current density (○) for electrodeposition in quiescent Bath D (●) and Bath E (●) at 55 °C. . . . .	159
5.5	Total polarisation (solid lines) and partial Ni polarisation (circles) plots in quiescent (a) Bath A and (b) Bath E at 40 °C, 45 °C, and 55 °C. . . . .	161
5.6	Effect of temperature on the appearance of the nickel films plated at 20 mA cm <sup>-2</sup> from Bath A (no boric acid): (a) 45 °C and (b) 55 °C. . . . .	162
5.7	Tafel plots and reversible potential (thick black line) in quiescent Bath A (●); Bath B (●); Bath C (●); Bath D (●); and Bath E (●) at 40, 45 and 55 °C. . . . .	165
5.8	Tafel plots in quiescent Bath E at 40 °C (●); 45 °C (●); and 55 °C (●). . . . .	169
5.9	W-SEM cross-sectional images of Ni deposited from 1.764 M nickel sulfamate + 0.021 M nickel chloride + xM boric acid at 45 °C as a function of the radial position on the RDE. a) near edge, b) mid-point, c) near centre. . . . .	170
5.10	Schematic representation of the possible interaction of sulfamate anion with the cathode during nickel electrodeposition via [1] chemical interactions or [2] adsorption of a nickel-sulfamate complex. . . . .	172
5.11	Polarisation curves: total current densities (solid lines) and Ni current density (○) for electrodeposition in Bath A (●); Bath B (●); Bath C (●); Bath D (●); Bath E (●); and Bath F (●) at 45 °C and WE rotation speed of 900 rpm. . . . .	176
5.12	Effect of boric acid concentration on current efficiency of pure nickel sulfamate solution for galvanostatic deposition at 45 °C and 10 mA cm <sup>-2</sup> with working electrode rotation speed of 0 rpm (black squares) and 900 rpm (red squares). . . . .	179

6.1	Polarisation scan performed on 304 stainless steel quartz crystal electrode in 1.78 M nickel sulfamate solution at 45 °C with scan rate 5 mV s <sup>-1</sup> , showing the measured current density, calculated current density for Ni deposition, calculated current density for HER, and frequency change. The Figure inset shows the effect of hydrogen evolution on the initial stage of nickel electrodeposition observed from the negative potential shift of frequency and calculated Ni current breakthrough compared to that of the measured current. . . . .	188
6.2	Polarisation scan performed on 304 stainless steel quartz crystal electrode in 1.78 M nickel sulfamate solution at 45 °C and 55 °C with scan rate 5 mV s <sup>-1</sup> . . . . .	190
6.3	Charge vs mass change during Ni electrodeposition on 304SS quartz crystal electrode from 1.78 M nickel sulfamate solution at 45 °C and 55 °C. . . . .	191
6.4	(a) Polarisation and (b) frequency scans for nickel electrodeposition in quiescent Bath A (●); Bath B (●); Bath C (●); and Bath F (●) at 45 °C; scan rate = 5 mV/s . . . . .	194
6.5	LSV of nickel electrodeposition in quiescent Bath A (●); Bath B (●); Bath C (●); and Bath F (●) at 45 °C, showing the measured current densities, <i>j</i> (solid lines) and calculated current densities, <i>j<sub>calc</sub></i> (circles) . . . . .	195
6.6	LSV of nickel electrodeposition in quiescent Bath A (●); Bath B (●); Bath C (●); and Bath F (●) at 55 °C, showing the measured current densities, <i>j</i> (solid lines) and calculated current densities, <i>j<sub>calc</sub></i> (circles) . . . . .	196
6.7	Effect of boric acid concentration: Charge vs mass change during Ni electrodeposition on a steel quartz crystal electrode in quiescent Bath A (●); Bath B (●); Bath C (●); and Bath F (●) at (a) 45 °C and (b) 55 °C. Theoretical plots for H (slope = -10.45 ng/mC), Ni (slope = -304.14 ng/mC), and Ni(OH) <sub>2</sub> (slope = -480.427 ng/mC) are given by the dashed, dotted, and solid red lines, respectively. . . . .	198
6.8	a) Polarisation curves and (b) massograms for HER in 3.57 M potassium sulfamate without boric acid on different quartz crystal electrodes. . . . .	200

6.9	Potential-pH equilibrium diagram for Au, Cu, Ni, and Cr <sub>2</sub> O <sub>3</sub> (passive film on 304 stainless steel) in water (pH = 6-9) at 25 °C. . . . .	204
6.10	Tafel plots for HER in 3.57 M potassium sulfamate without boric acid on 304SS (Red), Au (blue), Cu (black), and Ni (green). . . . .	205
6.11	Polarisation scans measured in 3.57 M potassium sulfamate solution without (black) and with 0.65 M boric acid (blue) with a scan rate of 5 mV/s on 304SS showing the measured current (solid lines) and mass changes (dotted lines). The Figure inset shows the effect of boric acid on the diffusion limited peak associated with H <sup>+</sup> reduction. . . . .	207
6.12	Polarisation scans measured in 3.57 M potassium sulfamate solution without (black) and with 0.65 M boric acid (blue) with a scan rate of 5 mV/s on (a) Au, (b) Cu, and (c) Ni showing the measured current (solid lines) and mass changes (broken lines). The Figure insets show the effect of boric acid on the diffusion limited region associated with H <sup>+</sup> reduction. . . . .	209
6.13	Proposed mechanism for the adsorption of boric acid on the metal substrate. . . . .	211
6.14	Polarisation scans measured in 3.57 M potassium sulfamate solution with 0.65 M boric acid with a scan rate of 5 mV/s on 304 SS (red), Au (blue), Cu (black), and Ni (green) showing the measured current (solid lines) and mass changes (broken lines). . . . .	212
6.15	Mass vs charge plots during HER on different quartz crystal electrode materials in 3.57 M potassium sulfamate solution without (black) and with 0.65 M boric acid (blue) at 45 °C. . . . .	213
6.16	a) Polarisation scans and (b) massograms obtained in x M Ni(II) + 3.57 M potassium sulfamate (pH 4.0) systems at two different Ni(II) concentrations: x = 0 (red line) and x = 17.9 mM (green line) on 304SS quartz crystal electrode; scan rate = 5 mV s <sup>-1</sup> . The inset is an amplification of the region corresponding to Ni deposition . . . . .	215

6.17 Comparison of measured $j$ - $U$ curves from the LSV experiment and $j$ - $U$ curves calculated from $\Delta m$ - $U$ response in 17.9 mM Ni(II) + 3.57 M potassium sulfamate (pH 4.0) system on a 304 SS quartz crystal electrode ; scan rate = 5 mV s <sup>-1</sup> . . . . .	216
6.18 Mass change vs Charge ( $\Delta m$ - $Q$ ) during Ni electrodeposition in 17.9 mM Ni(II) + 3.57 M potassium sulfamate (pH 4.0) system on a 304 SS quartz crystal electrode. The black lines represent best fit lines. Theoretical plots for Ni (slope = -304.14 ng/mC), Ni(OH) <sub>2</sub> (slope = -480.427 ng/mC), and Ni + Ni(OH) <sub>2</sub> (slope = -872.57 ng/mC) are given by the dashed, dotted, and solid red lines, respectively. . . . .	217
6.19 Comparison of measured $j$ - $U$ curves from the LSV experiment and $j$ - $U$ curves calculated from $\Delta m$ - $U$ response in 17.9 mM Ni(II) + 3.57 M potassium sulfamate (pH 4.0) system on a 304 SS quartz crystal electrode with and without 0.65 M H <sub>3</sub> BO <sub>3</sub> ; scan rate = 5 mV s <sup>-1</sup> . . . . .	219
6.20 Polarisation scans measured in 3.57 M potassium sulfamate + 0.65 M boric acid solution without Ni <sup>2+</sup> (black) and with Ni <sup>2+</sup> (blue) with a scan rate of 5 mV/s on 304 SS showing the measured current (solid lines) and mass changes (broken lines). . . . .	220
6.21 Comparison of measured $j$ - $U$ curves from the LSV experiment and $j$ - $U$ curves calculated from $\Delta m$ - $U$ response in 17.9 mM Ni(II) + 3.57 M potassium sulfamate (pH 4.0) system on (a) Au and (b) Cu quartz crystal electrodes with and without 0.65 M H <sub>3</sub> BO <sub>3</sub> ; scan rate = 5 mV s <sup>-1</sup> . . . . .	221
6.22 Polarisation scans measured in 3.57 M potassium sulfamate + 0.65 M boric acid solution without Ni <sup>2+</sup> (black) and with Ni <sup>2+</sup> (blue) at a scan rate of 5 mV/s on (a) Au and (b) Cu showing the measured current (solid lines) and mass changes (broken lines). . . . .	222

6.23	Mass change vs Charge ( $\Delta m$ -Q) during Ni electrodeposition in 17.9 mM Ni(II) + 3.57 M potassium sulfamate (pH 4.0) system without (green) and with (blue) 0.65 M $H_3BO_3$ on a 304 SS quartz crystal electrode. Best fit lines are represented by the black dashed lines. Theoretical plots for Ni (slope = -304.14 ng/mC), $Ni(OH)_2$ (slope = -480.427 ng/mC), and Ni + $Ni(OH)_2$ (slope = -872.57 ng/mC) are given by the dashed, dotted, and solid red lines, respectively. . . . .	224
6.24	Schematic of proposed mechanism for the action of boric acid during nickel electrodeposition as a function increasing cathode potential depicted by the direction of the arrow. . . . .	226
7.1	Polarisation plots for various types of anode materials at a scan rate of 5 $mV s^{-1}$ illustrating active, transpassive, and passive regions. The electrolyte comprised of 1.785 M $Ni(SO_3NH_2)_2 \cdot 4H_2O$ and 0.65 M $H_3BO_3$ . The inset shows the active/passive region in detail. . . . .	229
7.2	Influence of electrode rotation speed on the polarisation plots for a low-sulfur nickel anode material (plating chip) at a scan rate of 5 $mV s^{-1}$ . The base electrolyte comprised of 1.785 M $Ni(SO_3NH_2)_2 \cdot 4H_2O$ and 0.65 M $H_3BO_3$ . The inset shows the active/passive region in detail. . . . .	233
7.3	Influence of chloride ions on the polarisation plots for low-sulfur nickel anode materials at a scan rate of 5 $mV s^{-1}$ . The base electrolyte comprised of 1.785 M $Ni(SO_3NH_2)_2 \cdot 4H_2O$ and 0.65 M $H_3BO_3$ with and without 0.021 M $NiCl_2 \cdot 6H_2O$ . The inset shows the active/passive region in detail. . . . .	234
7.4	Polarisation plots for the nickel P-pellet in sulfamate and sulfate based solutions containing 0.65 M $H_3BO_3$ and 0.021 M $NiCl_2 \cdot 6H_2O$ . The inset shows the active/passive region in detail. . . . .	235
7.5	Influence of electrode rotation speed on the polarisation plots for a sulfur-depolarised nickel anode material (D-crowns) at a scan rate of 5 $mV s^{-1}$ . The base electrolyte comprised of 1.785 M $Ni(SO_3NH_2)_2 \cdot 4H_2O$ and 0.65 M $H_3BO_3$ . . . . .	236

7.6	Influence of chloride ions on the polarisation plots for sulfur-depolarised nickel anode materials at a scan rate of $5 \text{ mV s}^{-1}$ . The base electrolyte comprised of $1.785 \text{ M Ni}(\text{SO}_3\text{NH}_2)_2 \cdot 4\text{H}_2\text{O}$ and $0.65 \text{ M H}_3\text{BO}_3$ with and without $0.021 \text{ M NiCl}_2 \cdot 6\text{H}_2\text{O}$ . . . . .	238
7.7	Time dependence of the anode potential when various current densities are applied to a P-pellet anode. The zoomed inset shows the time it takes for the anode potential to transition from the active to the transpassive region. The base electrolyte comprised of $1.785 \text{ M Ni}(\text{SO}_3\text{NH}_2)_2 \cdot 4\text{H}_2\text{O}$ , $0.021 \text{ M NiCl}_2 \cdot 6\text{H}_2\text{O}$ , and $0.65 \text{ M H}_3\text{BO}_3$ . . . . .	240
7.8	Time dependence of the anode potential when various current densities are applied to an S-pellet. The base electrolyte comprised of $1.785 \text{ M Ni}(\text{SO}_3\text{NH}_2)_2 \cdot 4\text{H}_2\text{O}$ , $0.021 \text{ M NiCl}_2 \cdot 6\text{H}_2\text{O}$ and $0.65 \text{ M H}_3\text{BO}_3$ . Dissolution occurred in the active region. . . . .	241
7.9	UV absorption spectra of the solutions electrolysed at various anode current densities for Pt and Ni electrodes. The base electrolyte comprised of $1 \text{ M Ni}(\text{SO}_3\text{NH}_2)_2 \cdot 4\text{H}_2\text{O}$ only at pH 4 and $50 \text{ }^\circ\text{C}$ . Adapted from [130]	245
7.10	The UV-Vis spectra for catholyte samples electrolysed with a P-pellet anode placed within a fritted tube before and after charges of 250 C and 500 C were passed at an anodic current density of $25 \text{ mA cm}^{-2}$ . . . . .	247
7.11	The UV-Vis spectra for the P-pellet before and after charges of 250, 500, and 1000 C were passed at an anode current density of $25 \text{ mA cm}^{-2}$ . . . . .	249
7.12	UV-spectra of the electrolysis product(s) obtained at a Ni P-pellet after 0.6 Ah/L compared to those obtained by Nakano et al. [130] after 0.5 Ah/L	250
7.13	The UV-Vis spectra for the S-pellet before and after an anodic charge of 500 C was passed at current densities of 5, 10, and $25 \text{ mA cm}^{-2}$ . . . . .	252
7.14	The UV-Vis spectra for a solution employing a P-pellet (a) and a Pt (b) before and after an anodic charge of 500 C was passed at current densities of 5, 10, and $25 \text{ mA cm}^{-2}$ . . . . .	253
7.15	Diagram of electrochemical processes involved in oxidation of sulfamate ions at Pt and low-sulfur Ni anodes. . . . .	255
7.16	UV-vis spectra of a non-electrolysed nickel sulfamate bath with different concentrations of (a) persulfate ions and (b) sulfite ions. . . . .	257

7.17	The UV-Vis spectra for various anode materials before and after a charge of 500 C was passed at an anode current density of 25 mA cm <sup>-2</sup> . . . . .	258
7.18	Anode potential as a function of time at nickel and Pt anodes for an anode current density of 25 mA cm <sup>-2</sup> . The Ni P-pellet shows a transition from active to transpassive dissolution after 10 seconds. . . . .	258
7.19	Comparison of the UV-Vis reference spectrum of azodisulfonate [127] with UV absorption peaks observed in different experiments employing low-sulfur (P-pellets) and Pt anodes. The spectra have been corrected to the non-electrolysed nickel sulfamate electrolyte. . . . .	260
7.20	Spectra changes as a function of heating time at 67 °C for solutions electrolysed employing P-pellet (a) and Pt (b) anodes. During electrolysis, the anodes were maintained at 25 mA cm <sup>-2</sup> while a total charge of 500 C was passed. . . . .	262
7.21	The decay in the absorbance of the UV-Vis peak at 245 nm for solutions electrolysed employing P-pellet (red) and Pt (cyan) anodes during heating at 67 °C. The broken black line shows the absorbance at 245 nm of a non-electrolysed sample. . . . .	262
7.22	Kinetic plots of $\ln(\frac{A_t}{A_0})$ against heating time for ADS hydrolysis in solutions electrolysed with P-pellet and Pt anodes. . . . .	264
7.23	Polarisation plot (scan rate = 5 mV s <sup>-1</sup> ) for the deposition of nickel at a stainless steel cathode from a base sulfamate electrolyte showing the influence of the amount of sulfamate decomposition product (represented as 0, 250 or 500 C of charge passed) on the cathodic process. . . . .	267
7.24	Effect of anode material on the current efficiency of nickel electrodeposition as a function of bath age (charge per unit volume (Ah/L)). A constant cathode current density of 40 mA cm <sup>-2</sup> was applied for electrolysis in an undivided cell . . . . .	268
7.25	The UV-Vis spectra for non-electrolysed and aged (5.12 Ah/L) nickel sulfamate solutions. Electrolysis was performed with different anode materials by applying a constant cathode current density of 40 mA/cm <sup>2</sup> . . . . .	269

9.1	The Gibbs energy profile for the transfer of an ion from across the metal-solution interface in the presence and absence of a Galvani potential difference ( $\Delta\phi$ ). Adapted from [48] . . . . .	306
9.2	Tafel plot in quiescent Bath A at 40 °C. . . . .	310
9.3	Massogram obtained in 17.9 mM Ni(II) + 3.57 M potassium sulfamate (pH 4.0) on 304 SS quartz crystal electrode with (blue) and without (green) boric acid; scan rate = 5 mV s <sup>-1</sup> . . . . .	311



# List of Tables

1.1	Examples of nickel electroforming applications. . . . .	6
1.2	Composition of nickel electroforming solutions [26] . . . . .	8
2.1	Cathode reactions proposed for nickel electrolytes. . . . .	21
2.2	Cathodic Tafel slopes obtained from nickel electrolytes reported in literature. The first six entries provide data on sulfamate-based electrolytes while the last two show a comparison with sulfate- and chloride-based systems. . . . .	33
2.3	Comparison of insoluble and soluble nickel anode materials. Soluble nickel anodes could be categorised into low sulfur and sulfur-activated materials. . . . .	36
2.4	Anode reactions proposed for nickel sulfamate electrolytes. . . . .	39
2.5	Elemental composition of sulfur-activated nickel anode materials produced by the electrolysis and carbonyl processes as seen from the manufacturers' specification sheets. . . . .	45
2.6	Summary of sulfamate decomposition products detected in various studies. . . . .	65
3.1	Relevant electrochemical reactions and their equilibrium potentials in nickel sulfamate electrolytes. The last entry gives the chemical equilibria of nickel hydroxide precipitation and its corresponding pH. Calculations were based on $U^0$ values found in [136] . . . . .	73
3.2	Differences between the underlying principles of the ion transfer equation and the Butler-Volmer equation for electron transfer [48]. . . . .	81
3.3	Calculated cathodic and anodic Tafel slopes, $b_c$ and $b_a$ (mV/dec) for multistep electrode reactions in nickel plating electrolytes (assuming $\beta=0.5$ , $\nu=1$ , $T = 298$ K). . . . .	84
4.1	Composition and initial pH of nickel sulfamate solutions employed to study nickel electrodeposition kinetics. . . . .	96

4.2	Estimated $R_U$ from Equation 4.7 and measured $R_U$ obtained from Nyquist plots of EIS measurements performed in deoxygenated nickel sulfamate electrolytes at 0 rpm and 45 °C . . . . .	113
4.3	Composition of sulfamate solutions used in EQCM studies. . . . .	119
4.4	Sensitivity factors for Au and 304 SS crystals found using copper deposition EQCM experiments. . . . .	127
4.5	Summary of chemical composition (in wt%), forms, and manufacturing process of nickel anode materials employed in electrochemical dissolution characterisation studies (Information taken from the technical datasheet for each material). . . . .	136
5.1	Current efficiencies (%) for 20 $\mu\text{m}$ thick nickel deposits from quiescent sulfamate baths (Table 4.1) as a function of cathode current density and bath temperature. Seven experiments were repeated three times and the standard deviations were found to be within 1.5%. . . . .	155
5.2	Kinetic parameters for nickel deposition obtained in quiescent sulfamate baths at different temperatures. . . . .	166
5.3	EDS results of Ni electrodeposited from 1.764 M nickel sulfamate + 0.021 M nickel chloride + xM boric acid at 45 °C. . . . .	171
5.4	Effect of deposition current densities and temperature on current efficiency for 20 $\mu\text{m}$ thick nickel deposits from stirred sulfamate baths. . . .	177
5.5	Kinetic parameters for nickel deposition obtained from stirred sulfamate baths. . . . .	179
6.1	Theoretical mass and frequency changes calculated for various processes expected to take place during nickel electrodeposition [EQCM surface area = 0.196 $\text{cm}^2$ ]. . . . .	185
6.2	Current efficiencies and mass-charge slopes calculated from EQCM $\Delta f$ signals measured in solutions studied, assuming all of the QCM $\Delta f$ signal arises from the electrochemical deposition of Ni. . . . .	197
6.3	Onset potentials for proton and water reduction and maximum mass changes obtained from the Linear Sweep Voltammograms and massograms measured in the absence of boric acid shown in Figure 6.8. . . .	202

6.4	Metal hydroxide and oxide formation reactions and their equilibrium potentials on the different EQCM substrate materials at 25 °C. Calculations are based on $U^0$ values found in [136]. . . . .	204
6.5	Current efficiencies (%) calculated from EQCM $\Delta f$ signal measured on different substrates in solutions containing 3.57 M potassium sulfamate, 0.65 M boric acid, and 17.85 mM $Ni^{2+}$ at 45 °C, assuming all of the QCM $\Delta f$ signal arises from the electrochemical deposition of Ni. . . . .	223
7.1	Summary of anodic current efficiencies for dissolution of two types of nickel anodes. Total charge passed was 43.77 C. . . . .	243
7.2	Summary of anodic current efficiencies for dissolution of two types of nickel anodes at various anode potentials selected from the active and transpassive regions. Total charge passed was 43.77 C . . . . .	244
7.3	Summary of anodic/cathodic current efficiencies (CE) and anode potentials for the dissolution of two types of nickel anodes and the platinum anode at various anode current densities. Total charge passed was 500 C. For the S-pellet and P-pellet, dissolution occurred in the active and transpassive regions, respectively. . . . .	251
7.4	Kinetic parameters of the hydrolysis reaction involving sulfamate oxidation products generated at different anodes. . . . .	265
9.1	Optical micrographs of nickel deposited at 20 and 40 mA/cm <sup>-2</sup> from sulfamate Baths A-E at 40, 45, and 55 °C, magnification x 1. The table shows that adding boric acid to the bath (Baths B, C, and E) improves deposit appearance. . . . .	309

# LIST OF SYMBOLS

$a$	activity	-
$A$	Area of electrode	$\text{cm}^2$
	Absorbance	-
$b$	Cuvette pathlength	
$-b_c$	Cathodic Tafel slope	$\text{mV decade}^{-1}$
$b_a$	Anodic Tafel slope	$\text{mV decade}^{-1}$
$C$	Concentration	$\text{mol L}^{-1}$
$C_f$	Sensitivity factor	$\text{Hz ng}^{-1}$
$d$	diameter	$\text{m}$
$E$	Activation Energy	$\text{J mol}^{-1}$
$F$	Faraday's constant (96485)	$\text{C mol}^{-1}$
$\Delta f$	Frequency change	$\text{Hz}$
$I$	Applied Current	$\text{mA}$
$j$	Current density	$\text{mA cm}^{-2}$
$j_o$	Exchange current density	$\text{mA cm}^{-2}$
$j_{lim}$	Limiting current density	$\text{mA cm}^{-2}$
$m$	mass of sample	$\text{g}$
$\Delta m$	mass change at an EQCM	$\text{ng}$
$M$	Molecular mass	$\text{g mol}^{-1}$
$N$	Flux of ionic species	$\text{mol m}^2 \text{s}^{-1}$
$N_A$	Avogadro's number ( $6.022 \times 10^{23}$ )	$\text{mol}^{-1}$
$n$	Number of transferred electrons	-
$Q$	Charge passed	$\text{C}$
$r$	radius of the electrode	$\text{cm}$
$R_p$	Polarisation resistance	$\Omega$
$R_u$	Uncompensated resistance	$\Omega$
$t$	Plating or dissolution time	$\text{s}$

T	Temperature	K
	Transmittance	%
U	Electrode potential	V
$U^{\circ}$	Standard electrode potential	V
$U_{eq}$	Equilibrium potential	V
$U_{cell}$	Cell potential	V
<b>Greek letters</b>		
$\alpha$	Charge transfer coefficient	-
$\beta$	Symmetry factor	
$\delta$	Nernst diffusion boundary layer	m
$\Delta G^{\circ}$	Standard Gibbs free energy in a process	$\text{kJ mol}^{-1}$
$\eta$	Overpotential	V
$\kappa$	Conductivity	$\Omega^{-1} \text{ cm}^{-1}$
$\rho$	Density	$\text{g cm}^{-3}$

# LIST OF ABBREVIATIONS

CE	Counter Electrode
DI	Deionised
BSE	Backscattered Electrons
EDS	Energy Dispersive X-ray Spectroscopy
EQCM	Electrochemical Quartz Crystal Microbalance
HER	Hydrogen Evolution Reaction
LSV	Linear Sweep Voltammetry
OCP	Open Circuit Potential
PTFE	Polytetrafluoroethylene
RDE	Rotating Disk Electrode
RE	Reference Electrode
SCE	Saturated Calomel Electrode
SE	Secondary Electrons
SEM	Scanning Electron Microscopy
SHE	Standard Hydrogen Electrode
SiC	Silicon Carbide
UV-Vis	Ultraviolet-Visible
WE	Working Electrode

# Chapter 1

## Introduction

### 1.1 Introduction to Electroforming

Advances in the aerospace and automotive industries will stem from future fabrication of metal parts that provide the same or enhanced mechanical performance, low costs of fabrication, and lightweight, as these industries face challenges of optimising fuel consumption efficiency and stringent regulations to reduce emissions [1]. In 2018, the global aviation industry accounted for 2.4% of anthropogenic CO<sub>2</sub> emissions which are a primary cause of global warming [2]. Therefore, the International Civil Aviation Organization (ICAO) has set a target to reduce aviation emissions by 50% in 2050 [3]. Light-weighting of automotive and aerospace parts create less drag and lift forces which translates to less thrust requirements and fuel consumption [4]. For example, Boeing 787 was able to achieve 10-12% improvement in fuel efficiency from a 20% weight saving [4]. Therefore, lighter parts result in more energy-efficient vehicles and aircrafts with a lower carbon footprint.

One way to achieve lightweight design is through computational-aided structural optimisation of topology, shape, and size. Topological optimised designs which are created from optimal material redistribution tend to result in complex geometries which face manufacturing constraints with conventional methods such as, casting, forging, and drawing [1]. But with cost-effective, high volume production, electroforming has become an important technology to produce metal structures where requirements such as complexity, high precision replication of surface detail, micron tolerances, and lightweight are specified [5–7]. Hence, electroforming provides an opportunity to increase the flexibility of light-weighting design and relax manufacturing constraints.

As defined by ASTM, "Electroforming is the production and reproduction of

articles by electrodeposition upon a mandrel or mould that is subsequently separated from the deposit” [6]. In electrodeposition, metal ions in an electrolytic solution are reduced by electrons, provided by the flow of current, to form atoms on a conductive surface called a mandrel. The surface texture and topography of the mandrel can then be accurately replicated atom-by-atom by the electrodeposited layer to micron tolerances [8, 9]. Electroforming offers high precision reproduction of the mandrel’s dimensions (to  $< 5 \mu\text{m}$ ); and fine detail replication ( $0.01 \mu\text{m}$ ) of the mandrel surface which is unmatched by other production technologies [8].

In addition to high reproduction fidelity of the mandrel shape and surface, electroforming offers several other advantages over other metal forming processes, such as casting, forging, stamping, laser beam machining, and electrical discharge machining (EDM). These advantages include [8, 10]:

- *Mass production.* There is no wear and damage to the mandrel so a master mandrel can be prepared once by other metal forming processes and reused. Electroforming allows for high repetitive forming accuracy from this master mandrel for mass production purposes. The electrolyte which contains the metal ions can also be reused to reduce environmental impact.
- *Production of components with complex shapes and thin walls.* Components with complex-shaped geometries can be produced in a single operation whereas other processes involve multiple operations, such as pressing, drilling, machining, and welding. In addition, thin walled cylinders can be produced without a joint line.
- *Flexible range of thicknesses and sizes.* There is no practical limitation on electroform thickness and size. In fact, the electroform size is only limited by the capacity of the electroforming tank.

There are certain engineering limitations of electroforming that restrict its application as a metal production process. Often, these drawbacks may be reduced or eliminated by careful design of the process. These limitations are [8, 10]:

- *Long deposition time.* This may be reduced by operating multiple production lines



in parallel. Agitation could also be employed to allow the use of a higher current density which is analogous to a higher deposition rate.

- *Material selection.* There are a limited number of materials that can be electroformed practically due to problems associated with brittleness, oxidation, and internal stress. The only materials that have been successfully electroformed are copper, nickel, iron, silver, gold and a few of their alloys. Some studies [11, 12] have reported on the electroforming of aluminium from ionic liquids.
- *Lack of thickness uniformity.* This is a crucial problem particularly in mandrels with recessed areas where current density is lower compared to more exposed areas. This problem may also occur along the edges of a flat cathode [13]. Non-uniform current density distribution results in uneven thicknesses. A variety of methods have been suggested in literature to improve thickness uniformity which include: (1) Application of pulse and pulse reverse current [14]; (2) suitable agitation [15]; (3) the use of conformal anodes (the anode is shaped to conform to the shape of the mandrel) [16] and control of supplementary anode placement [10]; (4) shields [17–19]; and (5) a revolving mandrel [13, 20].
- *Internal stress.* Compressive and tensile stresses in electroforms lead to form distortions, warping, and cracking. Internal stress could be reduced or eliminated through careful selection of bath composition [21], use of pulse power [22], and stress-reducing agents [23].

## 1.2 Electroforming versus electroplating

Electroforming and electroplating both employ the electrodeposition process. However, there are several requirements which differentiate electroforming from the electroplating process. For one, the deposits in electroforming are intended to function as free-standing parts. Deposits for electroplating are intended to act as coatings for decorative or functional (protective) purposes. Since the deposits produced by electroforming are intended to be free-standing, they must possess sufficient mechanical strength to be self-supporting. For this reason, electroforms are made thick, rarely

thinner than 18  $\mu\text{m}$  [8], usually in the range of 250  $\mu\text{m}$  to a few millimetres thick [24]. In electroplating, however, coatings vary in thicknesses from about 7-50  $\mu\text{m}$  [8].

To achieve the intended stand-alone parts, the electroform is subsequently separated from the mandrel, so it is essential that there is as little adhesion as possible between the mandrel and deposit in electroforming. This is dependent on the choice of substrate material and pretreatment method. In electroplating, however, good adhesion between the substrate surface and deposit is a necessity [8].

Additionally, because of the separation requirement in electroforming, the deposit must possess nearly zero internal stress to ensure its shape and dimensions are maintained following separation. As mentioned earlier, stress in electroforms may result in form distortions and loss of mandrel reproduction fidelity. Higher levels of stress could result in the spontaneous premature separation of the deposit from the mandrel, leading to loss of the electroform. Extreme stresses lead to cracks in the deposit [25]. On the other hand, electrodeposited coatings can tolerate a certain level of stress. In summary, high thicknesses ( $> 250 \mu\text{m}$ ), low adhesion, and low internal stress (near zero) are critical requirements for the electroforming process which differentiate it from electroplating.

Since high stress levels are problematic in electroforming, metals with favourable mechanical properties are carefully selected based on the availability of processes that will allow their deposition with zero internal stress. As mentioned earlier, copper, iron, nickel, silver, and gold are the most successfully electroformed metals.

### **1.3 Nickel Electroforming**

The most important material for electroforming is nickel due to its diverse applications, good mechanical properties, and studies of its electrodeposition procedures are further advanced. Electroformed nickel offers extremely low internal stress, relatively high strength, good wear resistance, high temperature resistance, and high-speed deposition [26]. In addition, its mechanical properties could be easily adjusted through changes in process conditions, the use of pulse deposition, addition of additives, alloy-

ing, and addition of particles to the metal matrix [27]. Electroformed nickel is used in a wide variety of industries such as the aerospace, electronics, medicine, and automotive sectors. A compilation of various nickel electroforming applications is given in Table 1.1. The examples given illustrate various features of the electroforming process which show its versatility.

The aerospace industry, with an ambitious target to reduce carbon emissions by 50% in 2050 [3], has taken the lead on using nickel electroforming to redesign final parts with the same functionality and less material. Electroforming is the only practical method to produce these lightweight complex parts such as waveguides, bellows, nozzle heat shields and microwave antenna horns [28]. Figure 1.1 displays images of some complex Ni parts produced by electroforming.

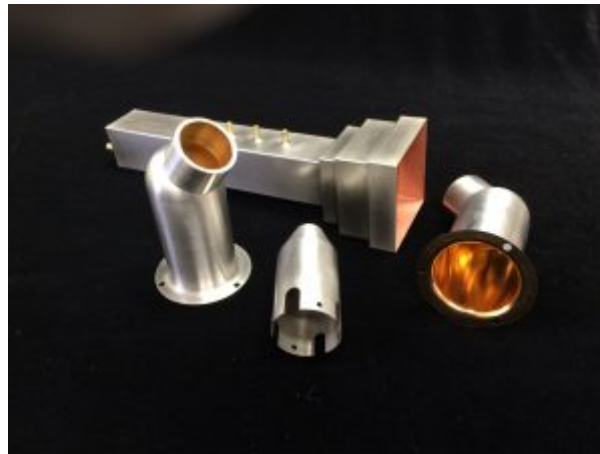


Figure 1.1: Lightweight satellite steering rocket nozzle heat shields and a lightweight satellite microwave antenna horn [28].

Much work has been done to develop nickel electroforming for the manufacturing of high aspect-ratio micro components through its combination with the LIGA (Lithographie (Lithography), Galvanoformung (Electroplating) and Abformung (Molding)) process [9]. These microdevices find applications in ultra-high-speed inkjet printers, wearable biomedical devices, resistors, capacitors, highly sensitive temperature transducers, and pressure sensors [45].

Table 1.1: Examples of nickel electroforming applications.

Industry sector	Product feature	Products	Ref.
Automotive	Complex cavity geometries	Tools for rotational moulding of door panels, truck cabs, dashboards, etc.	[6, 29, 30]
Aerospace	Complex shapes	Erosion shields for helicopter blades, aircraft engine shafts, bellows, RF/microwave devices	[6, 28, 31, 32]
Informational storage	Patterned surfaces	Stampers for injection molding of CDs and DVDs	[30]
Batteries	Highly porosity	Foam electrodes, mesh	[30, 33]
Electronics	High aspect ratios	Stencils for printed circuit boards	[34]
Energy	Complex shapes	Bipolar plates with micro-featured flow field, microlens array, foils	[35, 36]
Optical	Parabolic, ellipsoidal	reflectors, X-ray telescopes	[37–39]
Medicine	Complex shapes	Prism molds	[40, 41]
Screens for centrifuges, filters, razor foils, sieves, etc	Perforated with tiny hole diameters	Meshes	[6]
Textiles	Patterned	Rotary printing screens	[6]
Micro and nano manufacturing	Microstructures	Micro-mold inserts, micro-mesh, micro-optics	[20, 42]
Actuators and sensors-electromechanical systems (MEMS)	Patterned surfaces with high aspect ratio	Micro gears, microcantilevers, microprobes	[43–45]

## 1.4 Basic concepts of electrodeposition

Electrodeposition is a metal film growth process which involves the reduction of metal ions to atoms in an electrochemical reaction. The metal atoms are deposited onto a base material (electrode) surrounded by a liquid solution known as an electrolyte. The use of electrodeposition in the electroforming process allows for the production of free-standing, thicker, and more intricate metal structures [46].

A practical set-up for nickel electroforming is illustrated in Figure 1.2. The system mainly consists of two metal electrodes (cathode and anode) separated by an aqueous solution (electrolyte) containing ions of the desired metal ( $\text{Ni}^{2+}$  in this case) [47]. The term "cathode" refers to the electrode where the metal is plated, whereas the "anode" refers to the electrode where species are oxidised. In electroforming, the cathode is referred to as a mandrel. To create a complete electronic circuit, both electrodes are connected via external cables to a power supply. Charge is carried by mobile electrons and ions in the electrodes and electrolyte, respectively, to enable current flow in the system [48].

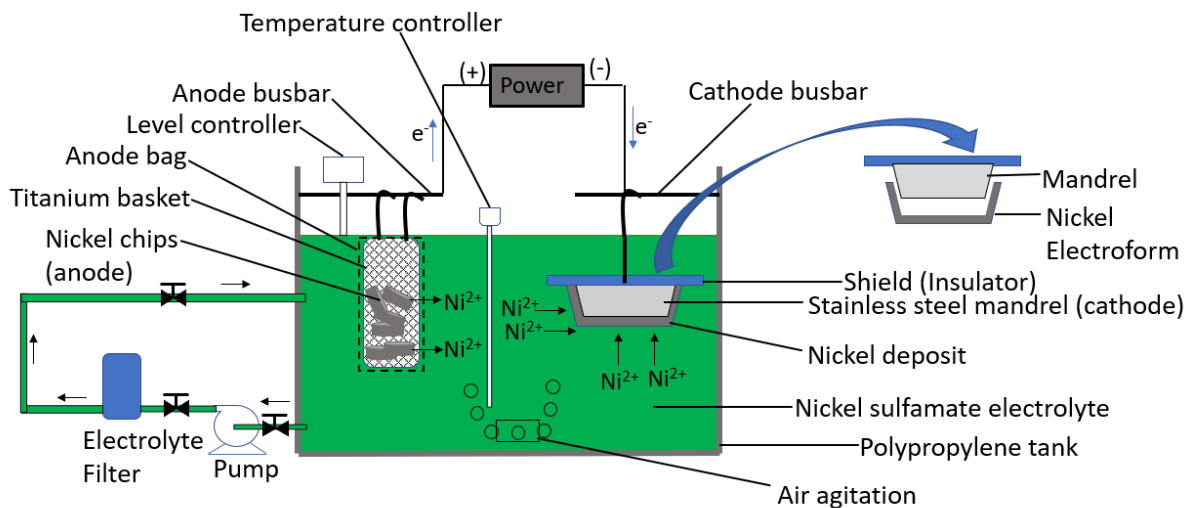


Figure 1.2: Schematic of a nickel electroforming set-up

It is noted that electrons do not flow through the electrolyte and ions cannot move through the electrodes. Therefore, current flow is only enabled in the system when charge is transferred between charge carriers across an electrode-electrolyte interface via an electrochemical reaction. For this type of reaction to occur, an elec-

tron or ion, must pass an electric double layer from one phase to another against a potential controlled activation energy barrier. Therefore, an electrochemical reaction, such as deposition or dissolution, cannot take place until sufficient potential is provided across the electrode-electrolyte interface to enable the reactive species to overcome this energy barrier. The same amount of charge is transported across the anode and cathode for a complete circuit. In this way, the consumption of electrons at the cathode balances out the release of electrons at the anode [48].

## 1.5 Nickel electrolytes

The main electrolytes that are used in nickel electroforming are the Watts, conventional sulfamate, and concentrated sulfamate baths (Table 1.2). Nickel plating was introduced commercially in the 1930s and for 30 years, electrodeposition of nickel was predominantly performed in the Watts bath which comprised of nickel sulfate as the main source of  $Ni^{2+}$ , nickel chloride to aid anode dissolution, and boric acid as a “buffer”.

Table 1.2: Composition of nickel electroforming solutions [26]

	Watts bath	Conventional sulfamate bath	Concentrated sulfamate bath
Nickel sulfate (g/L)	225-400	-	-
Nickel sulfamate (g/L)	-	300-450	500-650
Nickel chloride (g/L)	30-60	0-30	5-15
Boric acid (g/L)	30-45	30-45	30-45
pH	3-4.5	3-4	3-4
Temperature (°C)	44-66	32-60	32-60

Electroforming was first observed by Jacobi in 1837 during copper electrodeposition on a printing plate using copper sulfate solution. This attracted electroformers as copper deposits with low internal stress could be produced from acidic copper sulfate electrolytes which meant low chances of distortion [49].

The deposition of thick nickel deposits with low internal stress from the Watts bath intrigued researchers. These deposits could not be achieved without the use of organic sulfur-containing addition agents. These additives were not only effective at

reducing the stress in deposits but also refining the grain structure. This resulted in an increase in hardness, strength, and brightness while decreasing ductility of deposits. All commercial additives also led to the incorporation of sulfur in nickel deposits which decreased corrosion resistance. Incorporated sulfur greater than 0.01% [50] also limits the operating temperature of nickel as grain boundary embrittlement occurs when the electroform is exposed to elevated temperatures above 200 °C [49]. Embrittlement is not acceptable for some applications that use electroforming such as aerospace due to high-temperature exposure of metal parts. Nevertheless, the use of these commercial additives was inevitable if the Watts bath was going to be used for electroforming.

In 1938, Cambi and Pioletti developed the conventional sulfamate solution, the first industrial competitor to the Watts bath where nickel sulfate was replaced by nickel sulfamate [51]. However, it was not until 1950 that this sulfamate bath was made commercially viable by Barrett for the American electroplating industry [52]. The sulfamate bath attracted attention from researchers who sought to understand the effect of plating variables on the properties of electrodeposited nickel. Fanner and Hammond [53] reported that the optimal plating conditions in the sulfamate bath for low stress deposits were a pH of 4.0, temperature of 50 °C, and non-critical current density range of 20-60 mA cm<sup>-2</sup>.

Although nickel plating for decorative and engineering purposes continued in the relatively cheaper Watts bath, electroforming developed in the conventional sulfamate bath due to the relatively lower stressed and more ductile deposits that could be achieved without stress reducers. However, there was a limitation to the plating rates that could be used in this bath to achieve low internal stress. Another major limitation of the sulfamate bath was the finite lifetime of the bath due to the hydrolysis of sulfamate ions to ammonium ions (Equation 1.1) which increase deposit stress [21, 54]. The hydrolysis reaction is facilitated by an increase in acidity and temperature. Thus, the temperature at which the sulfamate bath could be operated safely was limited to 60 °C. This also limited the maximum permissible current density of the bath. Bulk decomposition of the sulfamate ion is a very slow process under normal operation [21, 54, 55] but high anodic current densities with accompanying pH decrease could propel runaway

hydrolysis [55].



Research continued to develop the sulfamate bath for rapid deposition that would increase throughput and reduce overhead. A breakthrough came in 1964 when Kendrick [21] reported the proprietary concentrated nickel sulfamate bath containing 600 g/l nickel sulfamate which led to the patenting of the “Ni-Speed” process by International Nickel Limited. Nickel sulfamate has a higher solubility (505 g/L at 19 °C [56]) than nickel sulfate (293 g/L at 19 °C [57]) such that it does not practically crystallise out of solution. Such high solubility means an exceptionally high amount of nickel salt can be used which means a higher concentration of nickel ions is available for deposition and higher current densities (plating rates) could be operated which offset the high costs of the sulfamate bath [58]. Higher current densities were possible in the concentrated sulfamate bath because the limiting current density (maximum permissible current density) was almost twice that of the conventional sulfamate solution. The concentrated bath allowed for nickel deposition over a wider current density range without organic additives whilst maintaining low internal stress and good mechanical properties.

Interestingly, by increasing the concentration of nickel sulfamate from 300 g/L to 600 g/L, the rate of increase in ammonium ion concentration due to hydrolysis reduced from  $2.8 \times 10^{-3} \text{ g L}^{-1} \text{ hr}^{-1}$  to  $0.5 \times 10^{-3} \text{ g L}^{-1} \text{ hr}^{-1}$ , respectively, at a pH of 4.0 and 70 °C [21]. This meant that a reasonable lifetime could be anticipated for the concentrated sulfamate solution when it was operated at temperatures above 60 °C.

Figure 1.3 shows the internal stress of deposits as a function of current density, bath composition, nickel ion concentration, and temperature. In the concentrated sulfamate bath, zero-stress deposits could be achieved at a higher current density ( $\approx 170 \text{ mA cm}^{-2}$ ) compared to the conventional sulfamate electrolyte ( $\approx 50 \text{ mA cm}^{-2}$ ) at 60 °C (Figure 1.3). Although, higher current densities make for shorter deposition times, nickel electroforming is usually performed at current densities in the range of 10 to 50  $\text{mA cm}^{-2}$  which provide good thickness uniformity, low internal stress, finer microstructure, and larger values of microhardness [24, 45, 59]. Nevertheless, a con-



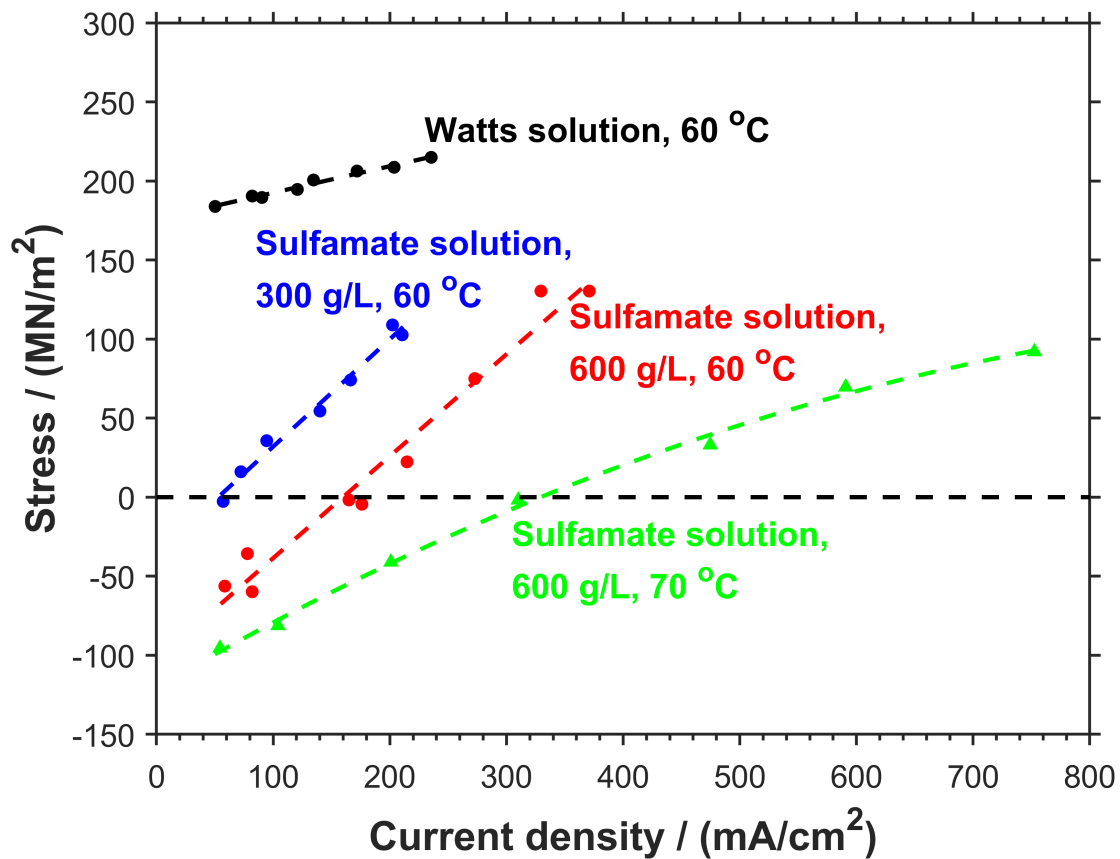


Figure 1.3: Variation of mean stress in 20  $\mu\text{m}$  electrodeposits from different nickel electrolytes. Adapted from [49].

concentrated nickel sulfamate bath (Table 1.2) is typically adopted industrially for electroforming, as zero stress deposits could be achieved by careful control of current density and temperature, without the use of addition agents [44]. In the conventional sulfamate solution, a high level of purity and elimination of chlorides is needed to achieve zero stress. Even with extreme care, zero stress may be difficult to maintain without the use of organic stress-reducers [44]. The reason for lower stressed deposits from the sulfamate electrolyte compared to the Watts bath has never been clearly elucidated but research debate focuses on products from the anodic decomposition of sulfamate ions which affect stress in deposits at the cathode.

## 1.6 Motivation

Since the pioneering work of Boettger [60], Cambi and Piontelli [51], and Barrett [52] in the 1930s–1950s to introduce a commercially viable electrolyte, i.e., the nickel sulfamate solution, electroforming has become an interesting growth technique for nickel parts. Since this landmark achievement, interest in laboratory research on nickel electroforming grew with the focus on identifying optimal conditions for the use of electroforming solutions.

Research has focused on identifying conditions that will generate electroforms of acceptable quality but limited attention has been paid to the electrodeposition mechanisms that determine the deposit characteristics. From an electroforming standpoint, the deposition must yield the desired microstructure, low internal stress, and good thickness uniformity. While these properties are of utmost importance, scarcely any work has been presented which simultaneously provides electrode kinetics accompanying electrodeposition, although Vincenzo and Cavallotti [61] have showed experimentally that growth structures in nickel electrodeposition from sulfamate electrolytes could be correlated to electrode kinetics.

Although electrodeposition kinetic studies have been performed in wide range of nickel electrolytes, kinetic data have not been provided under a systematic design of experiments in electroforming solutions. Due to the lack of adequate systematic data in the sulfamate electrolyte, knowledge about Ni deposition mechanism in this electrolyte has been observed from studies in the Watts bath [62–65]. However, evidence has shown that the stress of deposits from a Watts bath is an order of a magnitude higher than those from a sulfamate bath [21], which would indicate that the mechanisms are different. From the literature, a gap exists in fitting traditional kinetics models under typical electroforming variables (i.e. stirring rates, boric acid concentrations, temperatures, etc.). Since these parameters affect deposit properties, a better understanding of their influence is required to improve control, monitoring, and prediction of the electroforming process.

As can be seen from Table 1.2, electroformers recommend the addition of

boric acid to the electrolyte since it has been shown to maintain a constant pH close to the electrode surface [66–68] and result in current efficiencies near 100% [68]. There are several problems that have been encountered during nickel electrodeposition in the absence of boric acid: (1) significant hydrogen evolution [68], (2) a significant amount of oxygen (>28% atomic) was deposited with nickel [69], and (3) most deposits were cracked and therefore, not useful [70]. These problems are minimised or eliminated when boric acid is added to nickel plating electrolytes. Hence, the investigation into the function of boric acid in Watts-type and chloride solutions has been extensive but there remains a lack of consensus on its role. There is disagreement among studies that suggest that boric acid acts as a buffer as to where this effect comes from; some studies claim this is because polyborates form [71], while others propose this is due to the formation of nickel-borate complexes [66, 67, 72]. Because the calculated equilibrium constants for nickel-borate complexes are so small ( $\approx 10^{-11}$ ), it is doubtful that this weak complexation will have a significant impact [66, 72]. On the other hand, Raman spectroscopy confirms the formation of small quantities of polyborates (primarily triborate) in mixtures of boric acid and water at pH 4 and its increase with pH rise [71]. However, the participation of polyborates during nickel electrodeposition has never been proven.

According to other researchers [61, 73–79], boric acid adsorbs on iron-group metals and oxides which could decrease the electrode active surface area and inhibit cathodic reactions. This process could vary with the electrode surface material, applied potential, and electrolyte pH. On the other hand, Hoare [80] demonstrates that increasing the concentration of  $H_3BO_3$  in nickel sulfate solution results in an increase in the area of the nickel stripping peak evaluated from cyclic voltammograms measured on a Pt surface which could be correlated to the amount of nickel deposited. These results suggest that nickel deposition is enhanced in the presence of boric acid. The impact of boric acid on cathode current efficiency [68], kinetic data [61], and texture of electrodeposited nickel [61] suggests that it modifies the electrode surface and alters the rate of interfacial reactions which determine the morphology and properties of the nickel film but this has never been investigated for sulfamate electrolytes.

Electroforming is conventionally carried out using soluble nickel anodes which

have the advantage of replenishing the electrolyte with nickel ions throughout the process. Since the advent of the third industrial revolution, the use of titanium baskets has become critical to the viability of employing soluble anodes in the electroplating of nickel. Traditional nickel anodes, produced by casting, extruding, or rolling, had shortcomings in that the anode area constantly changed and became less efficient as the surface area decreased [81]. The anodes also contained significant quantities of additives to act as depolarisers but this presented a residue problem. Replacing worn anodes and cleaning anode bags represented a major maintenance expenditure in electroplating plants [81].

Since the introduction of titanium baskets in the 1960s, a large number of soluble nickel anode options have become commercially available for electrodeposition processes. Generalisations had been made to their performance in sulfamate solutions based on studies that were originally performed in the Watts bath. But subsequent research indicated that the anodic reactions in Watts and sulfamate solutions were different mainly due to differences in their anionic composition. Additionally, the relative performance of notionally similar products from different suppliers is uncertain due to variations in the mode of manufacture and precise composition. This thesis examines these features in the specific context of nickel electroforming from sulfamate electrolytes. Various commercially available soluble anodes are characterised by relating their elemental composition to their electrochemical behaviour, dissolution current efficiency, propensity to oxidise sulfamate ions, and impact on the cathodic electrochemical behaviour and current efficiency.

## **1.7 Aims and objectives of current work**

The first aim of this project was to investigate the effect of boric acid on the kinetics of nickel electrodeposition on a 304 stainless steel rotating-disc-electrode (RDE) under conditions of varying boric acid concentration (0-0.81 M), temperature (40-55 °C), and agitation (0-1600 rpm) typically employed for electroforming. To date, no experimental study considering all these variables has been reported for sulfamate electrolytes in the literature. This aim could be achieved by answering the following objectives:

- Determination of the total current-potential data in electroforming solutions from potentiodynamic measurements.
- Determination of the current efficiency and partial nickel current density-potential data from galvanostatic deposition and gravimetric measurements.
- Examination of the composition of nickel deposits to verify current efficiency data.
- Evaluation of kinetic parameters by fitting the Tafel equation to the partial nickel current density-potential data.

The second aim of this project was to employ Electrochemical Quartz Crystal Microbalance (EQCM) measurements to provide a dynamic description of the interface as a function of key variables: electrode potential, boric acid concentration, and electrode material in the absence and presence of nickel ions. The following objectives were completed:

- Determination of partial current-potential and current efficiency data on a 304 stainless steel quartz crystal electrode to verify the reproducibility of data obtained on the RDE.
- Determination of the effect of boric acid on the kinetics of hydrogen evolution reaction on Ni, Au, Cu, and 304 SS.
- Determination of the effect of boric acid on the initial stages of nickel electrodeposition on Au, Cu, and 304 SS.

The final aim of this project was to study the dissolution characteristics of some commercially available nickel anode materials in electroforming solutions by achieving the following objectives:

- Determination of the effect of chloride ions and agitation on the electrochemical behaviour of nickel anode materials.
- Examination of the dissolution potential and current efficiency of nickel anode materials.

- Determination of the effect of anode material and anode current density on the generation of sulfamate decomposition products.
- Investigation of the thermal decomposition of sulfamate products to verify the presence of azodisulfonate.
- Examination of the influence of sulfamate product build-up on cathode polarisation curves and current efficiencies.

## 1.8 Thesis organisation

This chapter reviews the advantages and principles of electroforming. Some applications of nickel electroforming are introduced. In chapter 2, current understanding of the nickel electrodeposition and hydrogen evolution reaction mechanisms are discussed and suggested roles for boric acid in sulfamate electrolytes are analysed. In addition, the history of nickel anodes and the mechanism and kinetics of the electrodisolution of nickel are reviewed.

Chapter 3 sets a foundation for the thesis by discussing relevant concepts such as thermodynamics, rate controlling mechanisms of kinetics such as charge-transfer (Tafel equation) and mass transfer processes, as well as electrocrystallisation. Chapter 4 details the chemicals, methods, and principles of the techniques used in this work.

Chapter 5 presents the results of nickel electrodeposition kinetics measured under electroforming conditions using potentiodynamic polarisation, galvanostatic deposition, and gravimetry techniques. Chapter 6 launches an investigation into the effect of boric acid on the interfacial processes that occur during nickel electrodeposition on different substrate materials using an Electrochemical Quartz Crystal Microbalance (EQCM). Chapter 7 presents the characterisation of nickel electrodisolution from different anode materials. Finally, conclusions and recommendations for future work are presented in chapter 8.

# Chapter 2

## Literature Review

### 2.1 Proposed mechanisms for the action of boric acid on the kinetics of interfacial processes

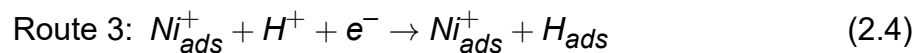
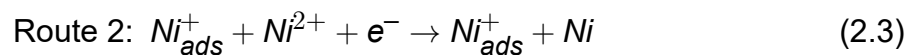
#### 2.1.1 Cathode reactions

##### 2.1.1.1 Nickel electrodeposition mechanism

The mechanism of nickel electroreduction has mostly been explored in nickel sulfate and nickel chloride electrolytes. As a result, the discussion of the mechanism has centred on these electrolytes. Numerous interpretations of the mechanism have been proposed because of the different experimental conditions adopted by researchers. Epelbion and Wiart [62] combined cathodic polarisation and electrochemical impedance measurements to study the nickel electrocrystallisation mechanism on a copper RDE in a Watts-type bath containing boric acid at 50 °C. Differing Tafel slopes, 118 and 43 mV/dec, were measured at low and high overpotentials, respectively. Additionally, the impedance spectra exhibited low frequency inductive features at low overpotentials. These results were concluded to support a faradaic electrodeposition process which occurs in several steps, during which  $(\text{NiOH})_{ads}$  acts as an intermediate which is consumed.

A later study performed by Epelbion, Jousselein, and Wiart [82] investigated the role played by protons and anions on electrode kinetics by evaluating impedance spectra measured on brass in unbuffered sulfate, chloride, and mixed electrolytes at 50 °C and pH 3 and 1.5. It was found that variations in pH did not significantly affect the low-frequency inductive features observed in chloride electrolytes but the promi-

nence of the low-frequency capacitive loop measured in sulfate media increased as the pH decreased. It is worth mentioning that these distinctive features are found in the impedance spectra below 0.1 Hz and at low polarisations, in addition to an inductive loop at frequencies close to 1 Hz which was ascribed to the relaxation of the electrode area corresponding to its coverage by  $Ni_{ads}^+$ . The researchers [82] proposed a set of reaction routes shown in Equations 2.1 to 2.4 which show the formation of  $Ni_{ads}^+$  as the key species which controls the rate of reduction of nickel ions (Equation 2.2 or 2.3) as well as hydrogen evolution (Equations 2.4, 2.5) or absorption (Equation 2.6). Therefore, occupation of reacting sites by  $Ni_{ads}^+$  can be a controlling species for  $Ni^{2+}$  and  $H^+$  reduction.



In a subsequent publication, Chassaing, Jousselein, and Wiert [83] investigated the effect of 2.4-4.8 M  $Cl^-$  concentration and pH between 0.5-1.5 on the low-frequency inductive loop observed on the impedance spectra measured in acidified nickel chloride electrolytes on a brass RDE. They found that these conditions had little to no effect on the inductive loop which had been related to the slow desorption of adsorbed anions by Epelboin and co-authors [82]. Therefore, Chassaing, Jousselein, and Wiert [83] suggested that the adsorbate probably resulted from the adsorption of chloride-containing complex rather than chloride ions. Consequently, the following model of interfacial reactions (Equations 2.7-2.8) was proposed for nickel chloride electrolytes where it was assumed that the adsorbate  $NiCl_{ads}$  could form on the nickel adions,  $Ni_{ads}^+$  (Equation 2.7) and is then reduced resulting in the desorption of the chloride ion (Equation 2.8) [83]:

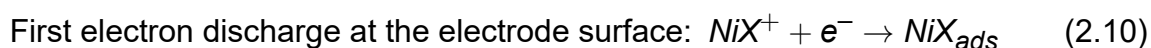






Potentiostatic transients measured by Saraby-Reintjes and Fleischmann [63] in a Watts bath on vitreous carbon at room temperature reveal that the rate of nickel electrodeposition has an order of 1 with respect to the concentration of nickel and chloride ions, which support propositions shown in Equations 2.1-2.2 and 2.7-2.8.

Given the numerous studies for Ni deposition from  $Cl^{-}$  or  $SO_4^{2-}$  baths, the main accepted mechanism for Ni electrodeposition follows the multistep reaction given in Equations 2.9 to 2.11 where  $X^{-}$  is an anionic species in solution ( $OH^{-}$  or  $Cl^{-}$ ) [63, 84, 85]. It is often assumed that Equation 2.10 is rate-determining to account for the slope of 120 mV/dec measured from Tafel plots [63].



This proposed sequence of reactions for  $Ni^{2+}$  reduction is summarised in Table 2.1 (Reactions 1-3). While most researchers have come to accept that nickel electrodeposition in acidic sulfate and chloride solutions occurs through two consecutive reactions (Reactions 2 and 3, Table 2.1), the debate has been whether the intermediate is  $NiOH^{+}$  or  $NiCl^{+}$  in baths containing both sulfate and chloride ions. Some studies have indicated that  $NiOH^{+}$  with a dissociation constant of  $8.71 \times 10^{-6}$ , is an important species in the charge transfer reaction in aqueous unbuffered sulfate electrolytes [84–88]. To explain changes in the potential of cathodic polarisation of nickel with pH, Matulis and Sližys [84] proposed that, in strongly acidified  $NiSO_4$  ( $pH < 4$ ),  $NiOH^{+}$  starts to form at  $pH \geq 4.0$  due to a decrease in acidity of solution close to the vicinity of the electrode surface following proton discharge, since its reversible potential is higher than that for  $Ni^{2+}$ . They also proposed that for solutions with  $pH \approx 4.0$ ,  $NiOH^{+}$  forms throughout the bulk solution [84].

Ji and Cooper [89] calculated nickel speciation data in aqueous chloride and

mixed sulfate-chloride solutions over a wide pH and  $\text{NiCl}_2$  concentration range. At  $\text{NiCl}_2$  concentrations above 0.01 M,  $\text{NiCl}^+$  was present in significant quantities (i.e. >12% of Ni(II) concentration) with  $\text{Ni}^{2+}$  in the acidic region ( $\text{pH} < \approx 6$ ). On the other hand, the concentration of  $\text{Ni(OH)}^+$  was negligible over the pH range 0-14 which dispute the propositions made by Matulis and Sližys [84]. Therefore, the participation of  $\text{NiOH}^+$  as an intermediate charge transfer species during  $\text{Ni}^{2+}$  reduction remains debatable due to the absence of direct experimental data.

Table 2.1: Cathode reactions proposed for nickel electrolytes.

Reaction number	Possible reactions Electrochemical	Chemical	Thermodynamic parameters	
			U° (V vs. SCE)	Reference
(1)	Ni deposition:	$\text{Ni}^{2+} + \text{X}^- \leftrightarrow \text{NiX}^+$		[63, 90]
(2)	$\text{NiX}^+ + \text{e}^- \rightarrow \text{NiX}_{ads}$ rate determining step (RDS)		-0.485	
(3a) or (3b)	$\text{NiX}_{ads} + \text{e}^- \leftrightarrow \text{Ni} + \text{X}^-$ $\text{NiX}_{ads} + \text{Ni}^{2+} + 2\text{e}^- \leftrightarrow \text{Ni} + \text{NiX}_{ads}$ where X <sup>-</sup> could be OH <sup>-</sup> or Cl <sup>-</sup> (if present in significant quantities)			
Proton reduction:				
(4)	$\text{Ni} + \text{H}^+ + \text{e}^- \leftrightarrow \text{Ni-H}_{ads}$		-0.245	[91]
(5a) or (5b)	$2\text{Ni-H}_{ads} \leftrightarrow 2\text{Ni} + \text{H}_2$ $\text{Ni-H}_{ads} + \text{H}^+ + \text{e}^- \leftrightarrow \text{Ni} + \text{H}_2$			
(6)	$\text{Ni-H}_{ads} \rightarrow \text{Ni}(\text{H}_{ads})$			
Oxygen reduction				
(7a) or (7b)	$\text{O}_2 + 2\text{H}_2\text{O} + 4\text{e}^- \leftrightarrow 4\text{OH}^-$ $\text{O}_2 + 4\text{H}^+ + 4\text{e}^- \leftrightarrow 2\text{H}_2\text{O}$		+0.984	[92]
Water reduction:				
(8)	$2\text{H}_2\text{O} + 2\text{e}^- \rightarrow \text{H}_2 + 2\text{OH}^-$		-0.589	[93]
Formation of nickel hydroxides and oxides				
(9)		$\text{Ni}^{2+} + 2\text{OH}^- \rightarrow \text{Ni}(\text{OH})_2$		[92]
Reduction of nickel hydroxides and oxides				
(10)	$\text{Ni}(\text{OH})_2 + 2\text{e}^- \rightarrow \text{Ni} + 2\text{OH}^-$		-0.96	[92]
(11)	$\text{NiOOH} + \text{H}_2\text{O} + 3\text{e}^- \rightarrow \text{Ni} + 3\text{OH}^-$		-0.88	
(12)	$\text{Ni}_3\text{O}_4 + 4\text{H}_2\text{O} + 8\text{e}^- \rightarrow 3\text{Ni} + 8\text{OH}^-$		-0.76	
Chemical Hydrolysis of sulfamate ions				
(13)		$[\text{H}_2\text{NO}_3\text{S}]^- + \text{H}_2\text{O} \rightarrow [\text{NH}_4]^+ + [\text{SO}_4]^{2-}$		
Chemical Equilibria of boric acid				
(14)		$\text{B}(\text{OH})_3(\text{aq}) + \text{H}_2\text{O} \leftrightarrow [\text{B}(\text{OH})_4]^- + \text{H}^+$ borate		[71]
(15)		$2\text{B}(\text{OH})_3(\text{aq}) \leftrightarrow [\text{B}_2\text{O}(\text{OH})_5]^- + \text{H}^+$ diborate		
(16)		$3\text{B}(\text{OH})_3(\text{aq}) \leftrightarrow [\text{B}_3\text{O}_3(\text{OH})_4]^- + \text{H}^+ + 2\text{H}_2\text{O}$ triborate		
(17)		$4\text{B}(\text{OH})_3(\text{aq}) \leftrightarrow [\text{B}_4\text{O}_5(\text{OH})_6]^{2-} + 2\text{H}^+ + 3\text{H}_2\text{O}$ tetraborate		
(18)		$5\text{B}(\text{OH})_3(\text{aq}) \leftrightarrow [\text{B}_5\text{O}_6(\text{OH})_9]^{3-} + 3\text{H}^+ + 3\text{H}_2\text{O}$ pentaborate		
(19)	Chemical Equilibria of Ni <sup>2+</sup> and boric acid	$\text{Ni}^{2+} + 2\text{B}(\text{OH})_3 \leftrightarrow \text{Ni}(\text{H}_2\text{BO}_3)_2 + 2\text{H}^+$ nickel-borate		[66]

### 2.1.1.2 Proton and water reduction on nickel electrodes

As mentioned in section 2.1.1.1, there is some controversy regarding Ni speciation in solution prompted by the decrease in acidity caused by proton or water discharge. These are called hydrogen evolution reactions (HER) as they both evolve hydrogen. Typically, HER occur in parallel with nickel electrodeposition as the standard electrode potentials for  $\text{Ni}^{2+}$  and  $\text{H}^+$  discharge (Table 2.1) differ by only 240 mV. For a long period, HER has been the topic of extensive studies in the search for materials to act as electrocatalysts for hydrogen production, such as nickel and some nickel alloys, platinum, etc. Bockris and Pentland [94] studied the mechanism of HER on copper in both aqueous 0.001-0.1 M HCl and 0.005-0.15 M NaOH solutions. It was suggested that the source of hydrogen liberated at an electrode could come from the proton (Equation 2.12) or water molecule (Equation 2.13) depending on the interfacial pH.



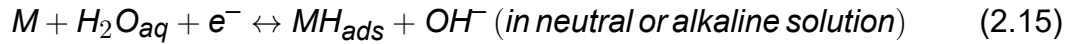
An earlier publication by Parsons and Bockris [95] noted that the discharge from water molecules was more probable in alkaline solutions where the concentration of water molecules is about  $10^{14}$  greater than that of hydroxonium ions as the rate of proton discharge would be limited by the supply of protons from the bulk solution to the electrode [95]. The bulk pH of nickel electroplating electrolytes is restricted to an acidic pH range of around 3-5, which would mean that the HER would commence with Equation 2.12 but the rise in interfacial pH due to the depletion of protons could create neutral or alkaline conditions in the vicinity of the electrode which would allow the transition from proton to water reduction (Equation 2.13).

Bockris and Pentland [94] proposed a mechanism for HER in acidic and alkaline aqueous solutions which comprises of the following steps (M = metal substrate):

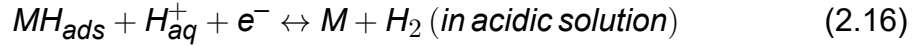
1. Electrochemical adsorption of protons (Volmer reaction)



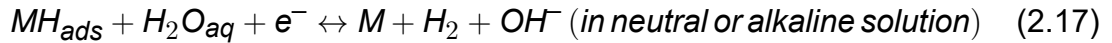
or



2. Electrochemical desorption (Heyrovsky reaction)



or

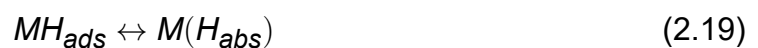


3. Chemical desorption (Tafel reaction)



It is considered that HER proceeds through the Volmer-Tafel reaction at low overpotentials while the Volmer-Heyrovsky mechanism is more probable at high overpotentials when the necessary rate is high [94, 96]. The Tafel slopes of 120, 40, and 30 mV/dec are expected if the Volmer, Heyrovsky, or Tafel step is the rate-determining step, respectively [97]. The rate determining step and reaction rate should depend on the energy of H adsorption on the given metal and the strength of the hydrogen bond with surface. Therefore, the mechanism is influenced by the materials and state of the electrode surface [98, 99]. Bockris and Potter [100] measured Tafel slopes for HER on Ni cathodes in aqueous solutions of HCl or NaOH at 0-40 °C. It was proposed that the most probable mechanism of HER on Ni is a rate determining Volmer reaction followed by rapid Tafel recombination due to low energy of desorption at high surface coverages. In a similar study by Bockris and Pentland [94], it was reported that the mechanism of HER on Cu in aqueous acid and alkaline solutions consists most likely of the Volmer adsorption reaction as the rate determining step followed by either electrochemical or chemical desorption.

As mentioned, whilst a major portion of adsorbed hydrogen reacts to generate H<sub>2</sub>, a small amount could be absorbed into the metal lattice (Equation 2.19) which could give rise to a mixture of interstitial hydrogen alloys of nickel in the deposits [70, 101].



Fleischmann and Saraby-Reintjes [101] measured anodic Linear Sweep Voltammetry scans of electrodeposited Ni on a glassy carbon electrode in a Watts bath. The scans displayed two active dissolution peaks which were suggested to correspond to the dissolution of two co-deposited nickel phases. These phases were identified as  $\alpha$ -Ni, a solid solution of hydrogen in nickel with H/Ni atomic ratio  $\leq 0.03$ , and  $\beta$ -Ni which is rich in interstitial hydrogen atoms (H/Ni  $\geq 0.06$ ). The formation of two types of nickel hydrides was also observed by other researchers [70, 98] using cyclic voltammetry in nickel chloride solution. On the other hand, Song et al. [65] studied the effect of HER on the initial stage of nickel electrodeposition on a Pt-coated quartz crystal electrode using an EQCM under potentiodynamic conditions and found that very little nickel hydride was co-deposited and most of the adsorbed hydrogen was desorbed as hydrogen gas.

### 2.1.2 Role of boric acid during nickel electrodeposition

The action of boric acid in nickel electrolytes has been investigated over the years [66–68, 73, 74, 99] by applying potentiometric titration, electrochemical techniques, gravimetry and microgravimetry measurements. Due to the key role played by boric acid in various electrodeposition applications, a variety of propositions have been made which can be summarised into the following views:

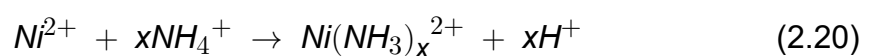
1. **Boric acid as a pH buffer.** As shown in section 2.1.1.2, hydrogen evolution, which could proceed via Reactions 4-5 or 8 in Table 2.1, is a concomitant process during nickel electrodeposition. The depletion of protons or production of hydroxyl ions during the HER leads to an increase in the pH of the electrolyte near the electrode surface. Findings have indicated that the addition of boric acid results in smaller pH variations at the cathode surface which led to speculations that boric acid functions as a pH buffer [66–68].

However, the role of boric acid as a pH buffer has been discounted as the practical pH range of a buffer is  $\text{pKa} \pm 1$ . At low concentrations, boric acid has a  $\text{pKa}$  of  $9.23 \pm 1$  at 25 °C but the pH of nickel electrolytes is around 4 [102]. The predominant forms of boric acid in acidic media (pH < 5) and alkaline media are the

undissociated molecule and borate ion (reaction 14 in Table 2.1), respectively. At high concentrations, boric acid could dissociate to form polymeric species according to reactions 15-18 (Table 2.1). Reaction 16 (Table 2.1) has a pKa of 6.8 [103]. Still, these dissociation reactions do not account for the buffer capacity at the low pH values of 3-4 encountered during nickel electrodeposition.

Rigsby and co-workers [71] collected Raman spectra for 0.65 M H<sub>3</sub>BO<sub>3</sub> in water. They detected polyborates (triborate and tetraborate) and borates at a pH of 4; it was found that peaks corresponding to these polyborates increased with increasing pH reaching a maximum at pH 7-8, whereas the peak for undissociated boric acid molecules, although still the predominant species, steadily decreased with increase in pH. Beyond a pH of 7-8, borate ions became the dominant species. The authors [71] proposed that though a low amount of polyborate ions could exist in bulk solution at the start of electrolysis, its concentration could increase due to local pH rise caused by hydrogen evolution. This formation of polyborate ions would lead to the release of protons (reactions 16-17, Table 2.1) which help to slow the rise in interfacial pH.

Ji et al. [67] considered the effect of H<sub>3</sub>BO<sub>3</sub> and NH<sub>4</sub>Cl on surface pH following 150 s of galvanostatic nickel deposition from a chloride electrolyte at 25 °C and a bulk pH of 2.5. In pure nickel chloride (0.937 M) electrolytes, the surface pH rapidly increased after a current density of 16 mA cm<sup>-2</sup> to a value of 6.7 at 26 mA cm<sup>-2</sup>. In the presence of H<sub>3</sub>BO<sub>3</sub> (0.485 M) or NH<sub>4</sub>Cl (1.31 M), the surface pH increased with current density to a value of about 3.5 at 58 mA cm<sup>-2</sup> indicating that these constituents effectively suppressed pH change during electrodeposition of nickel. Similar to boric acid, ammonium chloride is a known buffer in the region around pH 9.3 but it is also known for the formation of strong nickel-ammonia complexes, according to Eq. 2.20, which shift the buffering range to the acidic region starting around 3.2 [67]. This suggested to the authors that boric acid could have similar capabilities.



As shown from the reactions summarised in Table 2.1, there are two reasons for the suppression of surface pH increase during electrodeposition of nickel in

the presence of  $\text{H}_3\text{BO}_3$ : (i) proton donation or (ii) the prevention of reactions that either deplete protons or produce hydroxyl ions (Reactions 4-8, Table 2.1). Therefore, it is not possible to infer the role of boric acid from titration and surface pH measurements solely. Reliable electrodeposition current efficiency data is required to provide more information about the effect of boric acid on the rate of surface reactions which affect solution pH.

2. ***Boric acid promotes nickel deposition.*** Boric acid has also been suggested to promote nickel electrodeposition due to findings of decreased overpotential from cathodic current-potential data [80] and increased cathodic current efficiency from gravimetric measurements [68, 104] of deposits obtained in the presence of boric acid. Hoare's cyclic voltammetry experiments [80] indicated that the addition of boric acid to nickel sulfate electrolytes led to a decrease in overpotential, i.e. higher cathodic currents were achieved at less negative potentials. Additionally, it was discovered that the area of the Ni stripping peak grew with increasing boric acid concentrations, supporting theories that boric acid increased the rate of nickel electrodeposition [80]. Hoare [80] proposed that boric acid catalyses nickel electrodeposition. However, there is no conclusive evidence from its effect on measured nickel deposition partial current-potential curves or exchange current density data to back up this claim [105–107].

Tsuru et al. [68] provided evidence that nickel is deposited from sulfamate baths containing boric acid at current efficiencies approaching 100%. These findings indicate that nickel electrodeposition is accompanied by little to no side reactions (reactions 4-8, Table 2.1) and refute the initial claim that boric acid acts as a pH buffer. Tsuru et al. [68] measured the pH of the solution adjacent to the cathode surface during galvanostatic deposition at  $180 \text{ mA cm}^{-2}$ , using an antimony micro pH sensor. At boric acid concentration of 0.08 M, they observed a sharp increase in interfacial pH to a value of 5.75 with a measured current efficiency of 95%. On the other hand, the interfacial pH was maintained around 4.0 in a bath containing 0.81 M  $\text{H}_3\text{BO}_3$  and deposits were produced with cathode current efficiencies of 99% [68]. This finding supports the view that the suppression of surface pH rise in the presence of boric acid results from a decrease in the rate of hydrogen evolution rather than proton donation.



3. ***Boric acid suppresses hydrogen evolution.*** It is well known that hydrogen evolution before and during nickel deposition usually has deleterious effects on deposit quality [68, 108]. There are few studies on the effect of boric acid on HER kinetics in the absence of  $\text{Ni}^{2+}$  [74, 103], because it is typically added to nickel plating solutions to prevent surface pH rise and the precipitation of nickel hydroxide. However, these studies provide some evidence of the interaction of boric acid with the electrode surface.

Horkans [103] studied the effect of boric acid on hydrogen evolution kinetics on a Pt rotating disk electrode using potentiostatic linear sweeps in 0.75 M  $\text{Na}_2\text{SO}_4$  and 0.75 M NaCl solutions at pH 2.0. In the absence of boric acid, the limiting current for  $\text{H}^+$  reduction in  $\text{Na}_2\text{SO}_4$  was observed to be about 3.5 times greater than that in NaCl. It was concluded that the diffusion coefficient of protons was different for both solutions.

In the presence of 0.4 M  $\text{H}_3\text{BO}_3$ , the mass transport limiting current density ( $j_L$ ) for proton reduction decreased in  $\text{Na}_2\text{SO}_4$  and remained unaffected in NaCl. It was proposed that boric acid molecules adsorb on the surface of the cathode and reduce the area available for proton reduction, thereby decreasing  $j_L$  for proton reduction. The absence of a net decrease in active surface area in the chloride electrolyte was attributed to competitive adsorption of  $\text{Cl}^-$  and  $\text{H}_3\text{BO}_3$ . These findings were also substantiated by other studies [73, 74, 99]. However, Horkans [103] did not provide a clear explanation for the observed significant decrease in the overpotential of water reduction with the addition of boric acid.

Zech and Landolt [74] carried out investigations of the role of boric acid on hydrogen evolution in sulfate-, chloride- and perchloride-based electrolytes at pH 3.0 on a copper rotating cylinder electrode using Linear Sweep Voltammetry and obtained similar findings to Horkans [103]. Zech and Landolt [74] proposed the observed decrease in the overpotential of water reduction is not due to the acceleration of water decomposition but rather due to release of protons associated with the buffering action of boric acid in the potential region where water reduction is expected to occur.

This conclusion by Zech and Landolt [74] was drawn based on a shift in calcu-

lated surface pH values to more negative potentials under the influence of boric acid. These values were obtained from numerical simulation using a finite difference code based on transport processes and chemical equilibria. An interesting finding by Zech and Landolt [74] was a reduction in the current densities of proton reduction with increasing  $\text{H}_3\text{BO}_3$  concentration at pH 3.0, which they could not explain with mass transport and equilibria considerations. This observation was not made by Horkans [103] in similar studies at pH 2.0. Perhaps, the absence of this observation could be due to increased competitiveness between boric acid and  $\text{H}^+$  adsorption on the electrode surface at pH 2.0.

The hypothesis of  $\text{H}_3\text{BO}_3$  adsorption on the cathode and its influence on interfacial processes have also been supported by investigations involving deposit morphology and alloy electrodeposition. Karwas and Hepel [75] found evidence from scanning electron micrographs of Ni-Zn deposit surfaces that boric acid interferes with nucleation processes. The morphology changed from large porous globules to smooth, fine-grained deposits in the presence of boric acid indicating that the growth of adatoms was impeded. Significant increase in the primary nucleation rate coupled with suppressed secondary nucleation were also reported. Further evidence of the interaction of  $\text{H}_3\text{BO}_3$  with the Pt cathode surface during Ni-Zn electrodeposition was obtained from stripping voltammetry analysis. Karwas and Hepel [75] reported that as the  $\text{Ni}^{2+}/\text{Zn}^{2+}$  concentration ratio was increased from 0.25 to 3.3 in the presence of boric acid, the alloy composition shifted from Zn-rich to Ni-rich phases with lower hydrogen evolution, even though HER kinetics are more favourable on nickel than zinc. In the absence of boric acid, Zn-rich alloys were always obtained for  $\text{Ni}^{2+}/\text{Zn}^{2+}$  concentration ratios  $\leq 3.3$ . These results were attributed to the blocking of surface sites for hydrogen evolution and zinc deposition by weakly adsorbed boric acid molecules which offer "bridging effects" for nickel deposition. The adsorption of nickel-borate complexes on vitreous carbon electrodes was refuted by Abyaneh and Hashemi-Pour [109] who investigated the effect of ions and ionic strength on the kinetics of the initial stages of nickel electrocrystallisation in sulfate and chloride baths. They reported that the addition of boric acid increased both the outward and lateral growth rates of nickel deposition calculated from current-time transient curves. A

mechanism to explain these results, however, was not provided.

Literature research [110, 111] has indicated that the addition of boric acid suppressed crystal growth along the (200) direction and promoted growth along the (220) direction during nickel electrodeposition from sulfamate and Watts electrolytes which suggest an influence on electrocrystallisation. Although there are some published experimental works that have characterised the morphology of nickel coatings electrodeposited from sulfamate baths with and without  $\text{H}_3\text{BO}_3$ , most of these studies often took micrographs of the deposit surface which revealed large crystallites with pyramidal structures but provided little information about the influence of boric acid on the grain evolution of nickel as the film grows during electrodeposition [61, 68, 110, 112, 113]. It is proposed that the effect of boric acid on nucleation and growth will be better understood by taking cross-sectional micrographs of the deposits.

4. **Reduction of passive film formation.** Yin and Lin [73] reported that the steady state nickel partial current density measured in  $\text{H}_3\text{BO}_3$ -free sulfate electrolytes increased with increase in cathode potential but decreased after potentials of -1.25 V vs. SCE. They concluded that the electrode surface was passivated by  $\text{NiOH}_2$  which precipitated due to high interfacial pH (Reaction 9, Table 2.1). When boric acid was added to the electrolyte, higher nickel partial current densities were obtained which increased continuously with an increase in cathode potential. Yin and Lin [73] concluded that boric acid acts as a surface agent blocking certain active sites for HER while also stabilizing the nickel ion.
5. **Boric acid suppresses oxygen reduction.** Song et al. [65] calculated the deposited mass to charge ratio from a Linear Sweep Voltammogram obtained on a Pt-coated quartz crystal electrode in  $\text{NiSO}_4$  at room temperature using an EQCM. This was done to determine the species participating in charge transfer during nickel electrodeposition. It was determined that nickel co-deposited with  $\text{Ni(OH)}_2$  during the early stages of electrodeposition in the absence of  $\text{H}_3\text{BO}_3$  [65]. Cyclic Voltammograms (CVs) of the resulting deposits measured in 1 M KOH solution were found to be almost identical to those of the  $\alpha$  phase of  $\text{Ni(OH)}_2$ , which confirmed the formation of  $\text{Ni(OH)}_2$  during nickel electrodeposition. In the presence

of boric acid, although hydrogen evolution was initially dominant, it was superseded by nickel deposition at more negative potentials ( $< -0.9$  V vs. SCE). There was also no evidence of precipitated  $\text{Ni}(\text{OH})_2$  in the presence of boric acid [65]. Although Song and co-researchers [65] did not comment on how such a high pH could exist at the cathode surface as to allow the precipitation of  $\text{Ni}(\text{OH})_2$  before Ni deposition in the absence of boric acid, it could be hypothesised that oxygen reduction is the reaction most likely to precede  $\text{Ni}^{2+}$  reduction and cause such a high interfacial pH increase [24].

Oxygen reduction (Reaction 7, Table 2.1) cannot be avoided unless efforts are made to eliminate dissolved oxygen. Studies have indicated that the production of  $\text{Ni}(\text{OH})_2$  in aerated nickel electrolytes is most likely due to oxygen reduction which occurs prior to nickel deposition [70, 114]. Cui and Lee [114] compared voltammetric curves of nickel deposition in an unbuffered chloride bath in the presence and absence of dissolved oxygen (DO) at room temperature. In the presence of DO, they found that Ni deposition was preceded by an oxygen reduction current. Also, the first reduction peak, believed to be associated with the adsorbed nickel-hydroxyl intermediate ( $\text{NiOH}_{ads}$ ), disappeared and the nucleation overpotential of nickel deposition was shifted negatively. This was concluded to indicate that the adsorption of  $\text{NiOH}^+$  was suppressed by the competitive formation of  $\text{Ni}(\text{OH})_2$  on the electrode surface. However, as the concentration of  $\text{NiCl}_2$  was increased from 0.05 M to 0.5 M in the presence of DO, the reduction peak associated with  $\text{NiOH}_{ads}$  returned and an anodic shift in nickel nucleation potential was found indicating an increased adsorption of  $\text{NiOH}^+$  relative to  $\text{Ni}(\text{OH})_2$ .

Scanning electron micrographs indicated that deposits obtained from 0.25 M  $\text{NiCl}_2$  + 1 M KCl at -1.1 V vs SCE in the presence of DO had more pronounced cracks, improved uniformity, and finer grains which Cui and Lee [114] proposed were due to the presence of a stable layer of  $\text{Ni}(\text{OH})_2$  on the surface which curtailed nucleation and crystal growth.

Hoare [64] also reported that in the absence of dissolved  $\text{O}_2$ , nickel deposition from  $\text{N}_2$ -stirred  $\text{NiSO}_4$  on a Pt electrode without pre-electrolysis began at more anodic potentials than at pre-electrolysed Pt (i.e Pt with adsorbed oxygen). On a pre-electrolysed electrode, oxygen reduction preceded hydrogen evolution and

nickel deposition. It is therefore conceivable that elimination of dissolved  $O_2$  is crucial in cathodic electrochemical experiments to avoid the deleterious effects of local pH rise due to oxygen reduction which occur prior to nickel electrodeposition.

### 2.1.3 Effect of boric acid on charge transfer kinetics

As mentioned, boric acid was historically considered to act as a "buffering agent" which prevents the rapid change in interfacial pH that would accompany the evolution of hydrogen [66, 67]. However, current efficiencies near 100% measured in the presence of boric acid indicate that the rate of hydrogen evolution during nickel electrodeposition is minimal [68]. This finding along with thermodynamic information of the  $pK_a$  of boric acid dissociation have been used to refute the hypothesis that boric acid acts as a buffer.

Notably, deposits of good quality, high current efficiency, and negligible internal stress, are rarely produced in the absence of boric acid. Indeed, boric acid has been found to decrease the overpotential [80, 96] and change growth structures of nickel electrodeposition [61, 111]. These findings suggest that boric acid may operate by adsorbing on the electrode surface and modifying the kinetics and mechanism of charge transfer and electrocrystallisation of nickel deposition. Vincenzo and Cavallotti [61] indicated a correlation between growth structures and Tafel slopes, which were all affected by boric acid.

The kinetics of nickel electrodeposition in the presence of boric acid have been examined by a number of researchers [61, 63, 68, 115–122]. Despite the conflicting arguments, the experiments performed are inadequate for the purpose of examining the effect of  $H_3BO_3$  on nickel electrodeposition kinetics and mechanism during electroforming particularly for the following reasons: (i) that the working conditions do not correspond to those specified for electroforming conditions; (ii) that they are not compared against data in reference systems i.e simple unbuffered solutions, (iii) the solutions contain other chemical constituents which are capable of modifying charge transfer kinetics, (iv) that studies are focused on the low overpotential region of nickel

ion reduction (i.e.  $< 10 \text{ mA cm}^{-2}$ ) whereas electroforming proceeds at higher current densities, and (v) that there are limitations with the methodologies which are explored in the forthcoming paragraphs.

Only a few electrochemical systems (such as sulfate and chloride baths) are regularly used when discussing nickel electrodeposition kinetics, while sulfamate baths employed for nickel electroforming are discussed far less frequently. Electroforming conditions recommend using 500-650 g/L (1.55-2.01 M) of nickel sulfamate tetrahydrate, 5-15 g/L (0.021 - 0.063 M) of nickel chloride hexahydrate, and 30-45 g/L (0.49-0.73 M) of  $\text{H}_3\text{BO}_3$  and a temperature between 40-60 °C to enable low stress electroforms to be deposited [21, 123]. A few studies have measured kinetic parameters in these systems using a pH of about 4.0 similar to that encountered during electroforming; these are outlined in Table 2.2.

Three main techniques—chronopotentiometry [61,68], current pulse transient [61], and Linear Sweep Voltammetry (potentiodynamic) [118, 121, 122]—were used to measure the Tafel slopes listed in Table 2.2. The experimental Tafel slopes fall between 82 and 330.4 mV/dec, as can be seen in Table 2.2. A two-step charge transfer mechanism with a rate-limiting first step is typically predicted to have Tafel slopes between 118 and 128 mV/dec, corresponding to temperatures in the range of 25 to 50 °C; these values fall within the range of Tafel slopes determined experimentally (Table 2.2) suggesting a similar mechanism could be occurring in the sulfamate systems.

Notably, Tafel slopes of about 120 mV/dec are seen in sulfamate systems using both transient and chronopotentiometric methods. In chronopotentiometry, a constant current is applied for deposition while the corresponding potential is measured; the Ni partial current is calculated from the plated mass. The Tafel slope is evaluated from a plot of potential against log of the Ni partial current as determined from gravimetric measurements. In contrast, the transient approach superimposes a current pulse during deposition while measuring the corresponding potential transient. The asymptotic value attained following the charging transient is used to assess the transient Tafel slope [61].

The potentiodynamic technique shows a wider distribution of Tafel slopes be-

Table 2.2: Cathodic Tafel slopes obtained from nickel electrolytes reported in literature. The first six entries provide data on sulfamate-based electrolytes while the last two show a comparison with sulfate- and chloride-based systems.

Electrolyte composition (M) and substrate	Method	Temperature (°C)	Cathodic Tafel slope, $-b_c$ (mV/dec)	Reference
Ni(SO <sub>3</sub> NH <sub>2</sub> ) <sub>2</sub> , 1.55 + H <sub>3</sub> BO <sub>3</sub> , 0.81 Copper	Chronopotentiometry	50	120	[68]
Ni(SO <sub>3</sub> NH <sub>2</sub> ) <sub>2</sub> , 2 + H <sub>3</sub> BO <sub>3</sub> , 0.65 Brass/Nickel	Secondary current pulse technique	30	112 ± 3 (without boric acid)	[61]
	Chronopotentiometry		135 ± 5 (with boric acid)	
Ni(SO <sub>3</sub> NH <sub>2</sub> ) <sub>2</sub> .4H <sub>2</sub> O, 1.2 + NiCl <sub>2</sub> .6H <sub>2</sub> O, 0.11 + H <sub>3</sub> BO <sub>3</sub> , 0.6 Copper	Potentiodynamic	25	109	[118]
Ni(SO <sub>3</sub> NH <sub>2</sub> ) <sub>2</sub> , 2.4 + NiCl <sub>2</sub> .6H <sub>2</sub> O, 0.021 + H <sub>3</sub> BO <sub>3</sub> , 0.65 Indium-tin oxide glass plates	Potentiodynamic	41	87.4 (*calculated from digitised data)	[121]
Ni(SO <sub>3</sub> NH <sub>2</sub> ) <sub>2</sub> , 2 + NiCl <sub>2</sub> .6H <sub>2</sub> O, 0.028 + H <sub>3</sub> BO <sub>3</sub> , 0.57 (industrial grade without additives) 304 stainless steel	Potentiodynamic	50	330.4	[122]
Ni(SO <sub>3</sub> NH <sub>2</sub> ) <sub>2</sub> , 1.54 + H <sub>3</sub> BO <sub>3</sub> , 0.73 + SDS, 0.2 g/L + Saccharin (Na salt) 2 g/L Pt RDE	Chronoamperometry	50	82 (*calculated from digitised data)	[120]
NiSO <sub>4</sub> , 1 + H <sub>3</sub> BO <sub>3</sub> , 0.65 Brass/Nickel	Secondary current pulse technique	50	96 ± 3 (without boric acid)	[61]
	Chronopotentiometry		154 ± 10 (with boric acid)	
			90 (without boric acid)	
			110-120 (with boric acid)	
NiCl <sub>2</sub> , 1 + H <sub>3</sub> BO <sub>3</sub> , 0.65 Brass	Secondary current pulse technique	50	121 ± 3 (without boric acid)	[61]
			140 ± 2 (with boric acid)	

tween 87 to 330 mV/dec. In these studies, a potentiostat is used to monitor the current flowing between the counter and working electrodes as the potential between the working and reference electrodes is continuously varied in the cathodic direction (negatively). Tafel slopes are assessed from plots of potential against the log of the observed current. It is important to note that for all approaches mentioned, it is assumed that only Ni is plated during the experiment; the formation of oxides in the deposit or concurrent hydrogen evolution are not taken into account.

Tafel slopes measured in the sulfate and chloride systems, which range between 90 and 154 mV/dec as shown in the last two entries of Table 2.2, are comparable to those determined in the sulfamate system. Therefore, in the absence of robust data on the mechanism by which nickel electrodeposition occurs in sulfamate electrolytes, one could use the propositions regarding the mechanisms by which nickel electroreduction occurs in sulfate and chloride electrolytes [62, 63, 82, 83]. According to Equations 2.9 through 2.11 as stated in section 2.1.1.1, the accepted proposition entails two sequential charge transfers with the involvement of an anion  $X^-$ , which could be  $OH^-$  or  $Cl^-$ .

The first electron discharge step (Equation 2.10) has been demonstrated to be the rate-limiting step using impedance measurements [62, 82] and steady state polarisation measured using chronopotentiometry [63] mentioned earlier. Despite the similar Tafel behaviour observed in sulfamate, sulfate, and chloride electrolytes, the data in Table 2.2, however, suggest that Tafel slopes increase in the presence of boric acid and are greater than those predicted for a single electron transfer rate limiting step ( $\approx 120$  mV/dec). An industrial grade nickel sulfamate system containing boric acid is likewise shown to have an abnormally high Tafel slope (330 mV/dec) [24, 122]. Thus, there are still a number of unanswered questions: (i) why is there an increase in Tafel slopes when boric acid is added, as is observed by Vincenzo and Cavallotti [61], and is this a systematic increase? (ii) Why do deposits plated from solutions with and without boric acid differ as observed by Tsuru et al. [68]? (iii) What is the role of other chemical constituents (nickel chloride) on the charge transfer kinetics and deposit properties? and (iv) Can chronopotentiometry provide a reliable method to evaluate Tafel slopes, especially in light of the knowledge that nickel oxide and oxy-hydroxide can be deposited



from the electrolyte [96]?

These questions remain unanswered during nickel electrodeposition from electroforming baths. Whatever the exact role of  $\text{H}_3\text{BO}_3$  on nickel electroreduction, a measurement of exchange current densities derived from current-potential data as well as Tafel slopes gathered from solutions with different boric acid concentrations could be used to elucidate whether boric acid enhances or impedes charge transfer during Ni deposition.

## **2.2 Types of anode materials**

An anode's primary purpose is to balance the charge at the cathode by oxidising either itself or electrolyte components, completing the electronic circuit in an electrodeposition process. As a result, anodes can generally be split into two groups: soluble and insoluble (inert) materials [50]. According to the comparison of these anode materials in Table 2.3, there are benefits and drawbacks to employing each of these anode materials since they each behave differently in nickel sulfamate solution.

Table 2.3: Comparison of insoluble and soluble nickel anode materials. Soluble nickel anodes could be categorised into low sulfur and sulfur-activated materials.

	Insoluble anodes	Low sulfur anodes	Soluble nickel anodes	Sulfur-activated anodes
<b>Propensity to passivation</b>	-	High		Very low
<b>Oxidation reactions</b>	Oxidation of water molecules, sulfamate ions and chloride ions.	Nickel dissolution but could oxidise water and sulfamate ions during transpassive dissolution	Mainly nickel dissolution	
<b>Anode potential</b>	Greater than the equilibrium potential of water (+0.984 V vs SCE)	Close to the equilibrium potential of nickel (-0.485 V vs SCE) but could increase to higher potentials close to that of water oxidation.	Close to the equilibrium potential of nickel (-0.485 V vs SCE)	
<b>Electrolyte composition</b>	-Decrease in nickel ion concentration. -Generation of sulfamate decomposition products.	-Some nickel ion concentration maintenance. -Possible generation of sulfamate decomposition products.	-Nickel ion concentration is maintained. -Unlikely generation of sulfamate decomposition products.	
<b>Anode to cathode gap and area ratio</b>	Constant	Changes but could be kept constant by using a titanium basket.	Changes but could be kept constant by using a titanium basket.	
<b>Anode residue</b>	None	Nickel fines	Nickel fines and nickel sulfide residue	
<b>Anode bag</b>	Not required	Required	Required	
<b>Maintenance requirements</b>	-Frequent addition of nickel carbonate to maintain nickel ion concentration. -Electrolyte pH adjustment.	-Replenishment of nickel in anode baskets. -Changing of anode bags	-Replenishment of nickel in anode baskets. -Changing of anode bags	

### 2.2.1 Insoluble anodes

An anode can be constructed out of an insoluble material such as platinum, platinized titanium, carbon, or lead. In order to counterbalance the charge loss at the cathode, insoluble anodes receive electrons from the oxidation of electrolyte species, which often commences at more positive electrode potentials than the nickel oxidation reaction at soluble (nickel) anodes. This implies that compared to soluble anodes, insoluble anodes would typically operate with a greater cell voltage and incur a higher power consumption.

The principal advantage of using insoluble anodes is that they do not change shape during use. Therefore, the gap between the anode and cathode can be closely controlled and maintained. A small gap can be adopted to achieve a low electrolyte resistance and cell voltage in order to minimise power costs [124]. Another benefit is that chloride ions, which are typically added to electrolytes to enhance dissolution of soluble anodes, are not necessary. This is a crucial advantage for electroforming because, as Klingenmaier [125] noted, deposits experienced increased tensile stress when concentrations of  $\text{NiCl}_2$ , as low as 4.8 g/L, were present in a conventional nickel sulfamate bath.

The major downside of using an inert anode is that there is constant decrease in nickel ion concentration and pH as nickel is plated out. Variations in solution composition could change deposit properties, which is undesirable for a process such as electroforming where high repetitive forming accuracy is required for mass production [126]. Therefore, arrangements must be made for regular additions of nickel salts (nickel carbonate or nickel hydroxide) to the electrolyte to maintain the desired concentration when employing an insoluble anode [126]. This additional maintenance requirement could make the use of an insoluble anode more expensive compared to the process of using a soluble anode.

The unpredictability of the oxidation products and their rate of synthesis at an insoluble anode in an electrolyte with a complex chemical composition is another disadvantage that could make control of the electrodeposition process difficult. Re-

search on oxidation reactions at inert (Pt or C) electrodes in sulfamate-based solutions [127–129] has shown that, in addition to water oxidation, sulfamate ions could break-down in multi-step reactions giving rise to a plethora of sulfonated products such as azodisulfonate, hydrazinesulfonate, sulfites, etc. These sulfonated compounds could also undergo reduction at the cathode, increasing the sulphur content and compressive stress of nickel deposits [125, 127, 130]. Increase in bath acidity is another undesirable side effect of sulfamate oxidation reactions but this impact can be mitigated in the process of replenishing the bath with nickel ions. When present in solution, chloride ions could also oxidise at an insoluble anode to produce toxic chlorine gas which could destroy the anode [124].

Though insoluble anodes are advantageously applied in nickel electrowinning [131] where the replenishment of nickel ions defeats the purpose of the process, literature reporting the employment of insoluble anodes in industrial nickel electroforming processes is limited [132, 133]. In certain circumstances, insoluble materials may be used as conforming auxiliary anodes to plate complex electroforms with a uniform coating. The concentration of nickel ions in the solution does not decrease as rapidly when insoluble anodes are utilised to only plate certain portions of a part [126]. Nonetheless, most commercial nickel electroformers prefer the use of soluble nickel anodes to maintain a stable process.

### **2.2.2 Soluble anodes**

Ideal soluble anodes are ones which dissolve uniformly with high current efficiency and low polarisation, without forming solid residues [134] or introducing new compounds into solution that would adversely affect the deposit properties [55]. A soluble anode made of the metal being deposited is preferable in electrodeposition. For example, a nickel anode will dissolve when an electric current for nickel electroforming is applied to it, delivering Ni(II) ions to the electrolyte in order to maintain a desired Ni(II) concentration. Electrodeposition specifications place a high priority on anode purity; the nickel (plus cobalt) content must be at least 99 % [126]. Impure anodes may cause the electrolyte to become contaminated and the deposits to have undesirable physicochemical

Table 2.4: Anode reactions proposed for nickel sulfamate electrolytes.

Reaction number	Possible reactions	Thermodynamic parameters	Reference
	Electrochemical	$U^0$ (V vs. SCE)	
	Ni dissolution:		
(1)	$\text{Ni} \rightarrow \text{Ni}^{2+} + 2\text{e}^-$	-0.485	
	Water oxidation		
(2)	$2\text{H}_2\text{O} \rightarrow \text{O}_2 + 4\text{H}^+ + 4\text{e}^-$	+0.984	
	Chloride ion oxidation		
(3)	$2\text{Cl}^- \rightarrow \text{Cl}_2 + 2\text{e}^-$	+1.12	
	Sulfamate ion oxidation		
(4a)	$2\text{H}_2\text{NSO}_3^- \rightarrow (\text{N}_2\text{H}_2(\text{SO}_3)_2)^{2-}$ hydrazinedisulfonate + $2\text{H}^+ + 2\text{e}^-$		[129]
(4b)	$(\text{N}_2\text{H}_2(\text{SO}_3)_2)^{2-} \rightarrow (\text{N}_2(\text{SO}_3)_2)^{2-}$ azodisulfonate + $2\text{H}^+ + 2\text{e}^-$		

characteristics.

Table 2.4 lists possible oxidation reactions that could occur at the anode in nickel sulfamate electrolytes. The primary anode reaction at nickel anodes in sulfamate solutions is often nickel dissolution (Reaction 1, Table 2.4). However, anodes with low current efficiency could also oxidise water and sulfamate ions [125, 135] as shown in Table 2.4 (Reactions 2 and 4). In principle, the standard equilibrium potentials of nickel oxidation ( $U^0 = -0.485$  V vs SCE) and water oxidation ( $U^0 = +0.984$  V vs SCE) are sufficiently far apart to allow nickel dissolution to proceed at 100% efficiency. However, pure nickel has a strong propensity to passivate in aqueous electrolytes which is when an oxidising nickel surface becomes completely covered by a passive film, reducing the nickel dissolution current [136]. In this situation, the potential of the nickel anode may be raised in order to achieve and maintain the requisite electrodeposition current. In addition to increasing the cell voltage and energy consumption, sufficiently high anode potentials could permit the breakdown of species in the electrolyte.

As mentioned earlier, ideal anodes should dissolve uniformly. This is because undercutting of grains during non-uniform dissolution results in the production of nickel fines, which could increase the roughness of the deposit when incorporated at the cathode surface [126]. This was a major flaw of the electrolytic nickel strips used as the first soluble anode material in nickel electrodeposition. The strips had to be suspended from hooks to make contact with the solution because they were only available in specific lengths. The bottom and sides of the strip would dissolve quicker

than the rest of the strip, resulting in a constantly shifting anode area and rising anode current density. As a result, the strip would break down into fines and stubs before it was completely consumed because it dissolved unevenly and became fragile and spongy. Consequently, the plating procedure had to be interrupted to replace the electrolytic nickel strips before they were completely consumed. Additionally, Ni fines and stubs together made up a sizeable amount of scrap [134]. Anodes had to be contained in cotton or polypropylene bags to prevent the dispersion of metal fines into solution which caused roughness at the cathode [126].

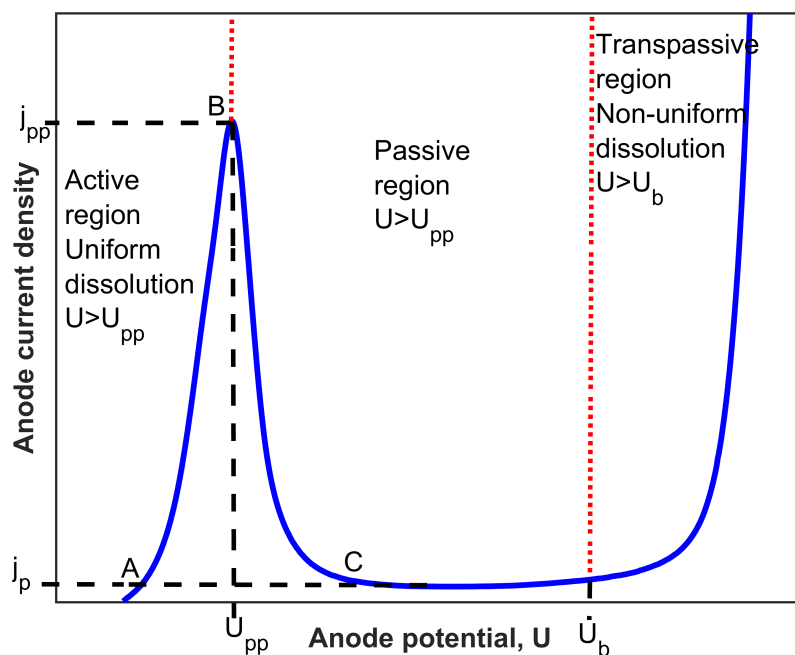


Figure 2.1: Idealised anodic polarisation curve obtained potentiodynamically in nickel electroforming solution [137]. Key:  $U_{pp}$ : principal or critical passivation potential,  $U_b$ : passive film breakdown potential,  $j_{pp}$ : critical passivation current density,  $j_p$ : the current density in the passive region. AB is the active region for dissolution and BC the active-to-passive transition region for dissolution. Adapted from [138]

Figure 2.1 shows an anode polarisation curve, where the "active region" denoted as AB refers to the period of nickel dissolution before complete coverage of the Ni anode by a passive film. Nickel anodes only dissolve uniformly in the active region, i.e., when their anode potential ( $U$ ) is lower than the critical passivation potential,  $U_{pp}$  or current density is less than the critical passivation potential,  $j_{pp}$ , as shown in

Figure 2.1. Anodes no longer dissolve uniformly once  $U_{pp}$  or  $j_{pp}$  is exceeded; this subject is covered in more detail in section 2.3. Ideal nickel anodes are those for which, regardless of the anions present,  $U_{pp}$  or  $j_{pp}$  is not exceeded under normal operating conditions. The different types of nickel anode materials that have been developed to produce this electrochemical activity are summarised in Figure 2.2 and are discussed in the forthcoming sections [126].

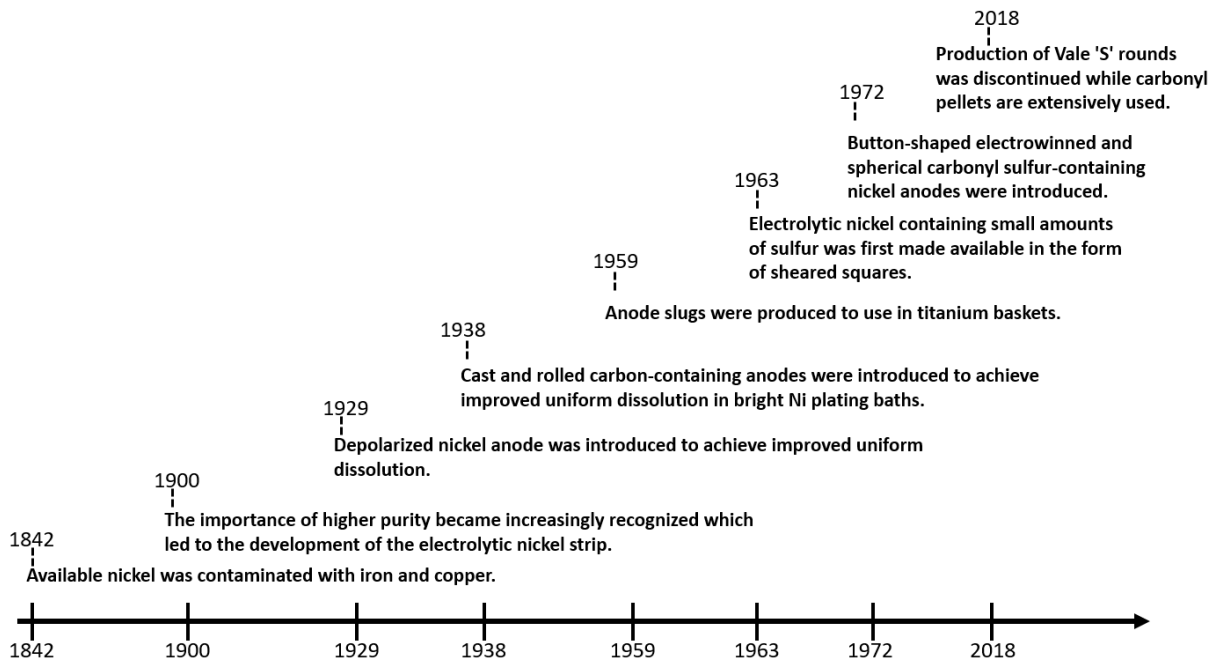


Figure 2.2: Historical development of soluble nickel anode materials.

### 2.2.2.1 Depolarised nickel

In 1929, the depolarised nickel anode was the first material developed to promote even dissolution. These rolled materials consisted of >99% nickel,  $\approx 0.5\%$  nickel oxide [134], and a carefully controlled inclusion and dispersion of a minute amount of sulfur (<0.01 wt%) [139]. Their microstructure was composed of fine grains with nickel oxide segregated at the grain boundaries [126]. Wesley [139] considered the effect of nickel oxide on S distribution to be the primary reason for the enhanced uniform dissolution of depolarised nickel; nickel oxide secured an optimum uniformity of S distribution, preventing the formation of nickel sulfide at grain boundaries, which would otherwise cause the anode to dissolve non-uniformly. The hot rolling production technique used to manu-

facture these anode materials allowed suitable lengths for commercial electroplating to be made, so there was no size limitation [138].

Depolarised nickel produced a brown film during dissolution, and therefore, had to be used in anode bags to prevent those residues from entering the solution and causing roughness at the cathode. Despite their uniform dissolution, it still maintained some limitations of the electrolytic nickel strip. Operations still had to be ceased to replace the depolarised nickel anodes since their anode area and current density changed during electrodisolution [134]. The use of this bar type depolarized anode has all but stopped due to these technical issues and their expense [126].

### **2.2.2.2 Carbon-containing nickel**

Introduced in 1938, cast and rolled nickel anodes contained a carbon and silicon content of  $\approx 0.25\%$  each [138]. Silicon is oxidised to silicic acid and protons which enhanced active dissolution by increasing acidity in the anolyte [140]. Silicic acid could then combine with carbon to form a thick, highly retentive, black film, which unlike the film formed on depolarised nickel, kept fine metallic particles in touch with the anode long enough for them to dissolve. Although carbon-containing anodes produced little to no metallic residue, they were nonetheless encased within anode bags to keep carbon and silicon residues out of the solution and avoid clogging the filters. Additionally, silicon oxidation decreased the efficiency of the anode below 100%, and this decrease was proportional to the silicon content [134]. Since the 1960s, the use of cast nickel anodes has been superseded by titanium baskets containing refined forms of primary nickel [141].

### **2.2.2.3 Primary nickel**

Primary nickel anodes are produced with high purity consisting of  $>99\%$  Ni. Due to their fairly high purity, the dissolution characteristics of primary nickel are not often ideal as they dissolve non-uniformly at high anode potentials. It is advised that they are used at a solution pH below 4.5 and with a chloride ion concentration of at least 6 g/L [126].



In addition to the pure (non-activated) grade, an activated grade that lowers the anode potential by incorporating low amounts of sulfur ( $\approx 0.01$  to  $0.04$  wt%), usually in the form of sulfides, is also commercially available [142]. First introduced in 1963 in the form of sheared squares [138], electrolytic sulfur-activated nickel dissolved uniformly at low potentials [50] and current efficiencies close to 100% [125], irrespective of the chloride content of the electrolyte. The ability of sulfur-activated nickel to dissolve uniformly even in the absence of chloride ions allowed for better control of deposit stress due to reduction/elimination of chloride ions in solution which benefited electroforming [134].

Sulfur-activated anodes meet the characteristics of an ideal anode in all but one aspect: a fine, insoluble, non-metallic nickel sulfide powder ( $\approx 0.1\%$  of the anode) is produced during the dissolution of sulfur-activated nickel anodes which necessitates the use of anode bags [134].

There is some debate about whether the comparatively low voltage dissolution measured for sulfur-activated nickel anodes in laboratory studies results in the anticipated long-term energy savings [143]. Following long-term rack plating with a sulfur-activated electrolytic nickel anode at constant anode and cathode current densities of  $30 \text{ mA cm}^{-2}$  in a pilot tank containing Watts solution, Whittington [144] reported that, at over  $4875 \text{ Ah/L}$ , the voltage had to be increased progressively to maintain a constant current. This was attributed to the accumulation of a non-conductive nickel sulfide powder during nickel dissolution which could increase the electrical resistance and drive up the voltage until the anode bags are removed and cleaned [58, 144]. Therefore, the use of sulfur-activated nickel anodes requires regular plant maintenance. In contrast, the dissolution of pure electrolytic nickel anodes produce less residue which is conductive, so a constant voltage could be maintained for long periods of time. Additionally, they do not require a cleaning procedure as frequent as that of sulfur-activated anodes [58, 144].

Modern primary Ni anodes come in small pieces because by containing them within titanium baskets, it is possible to maintain a nearly constant anode area and completely consume the anode which improves operational efficiency. Therefore, this procedure has made the use of heavy single-piece anodes obsolete. Additionally, bas-

kets can be made into a variety of sizes and shapes to suit requirements of the cathode [138].

There are several different forms of primary Ni anode materials available, including pellets and discs (chips) produced by the decomposition of nickel carbonyl in the Mond process, and square or button-shaped (rounds/crowns) pieces made by electrodeposition [138]. It is also important to note that both methods are capable of producing sulfur-activated nickel anodes. In fact, two forms of sulfur-activated nickel were made commercially available in 1972: a button-shaped material produced by electrowinning and a carbonyl spherical form [26].

Button and spherical shapes facilitate safe loading and settling of anodes in a titanium basket due to the absence of sharp, pointed corners. Pellets are attractive for automating the basket-loading process due to their flowability. They also have relatively high packing densities, which reduce regular basket maintenance requirements and save energy [145]. Consequently, spherical and circular forms of nickel, typically produced by the Mond process, have gained more popularity with electroplaters compared to nickel squares [134]. In addition to a variety of physical shapes, the different methods of production also lead to elemental compositional differences between electrolytic and carbonyl nickel anodes, which could be noted from the examples given in Table 2.5. Carbonyl nickel anodes contain relatively higher Ni and less Co, Cu, Pb, and Zn, as shown in Table 2.5. On the other hand, carbonyl anodes contain more carbon than electrolytic nickel which could likely lead to the production of more insoluble residue [144].

Electrolytic nickel anodes are produced by electroforming nickel onto flat metal mandrels to form rounds/crowns, or to form a rectangular sheet that can be cut into squares [144]. On the other hand, carbonyl nickel anodes are produced by the Mond process discovered by Ludwig Mond [146]. In this process, carbon monoxide is passed over impure solid nickel at a temperature of 50-60 °C to release carbonyl nickel gas ( $\text{Ni}(\text{CO})_4$ ). The gas is then heated to a temperature range of 200-280 °C where it decomposes to pure solid Ni pellets. In the industrial Mond process, "seed pellets" with diameters of 1 mm are preheated to the required decomposition temperature and then placed in a chamber containing  $\text{Ni}(\text{CO})_4$ . The surface of the seed pellets are coated

Table 2.5: Elemental composition of sulfur-activated nickel anode materials produced by the electrolysis and carbonyl processes as seen from the manufacturers' specification sheets.

<b>Chemical analysis (wt%)</b>	<b>Electrolytic rounds</b>	<b>Carbonyl pellets</b>
Ni	>99.0	>99.97
S	0.019-0.025	0.022-0.030
Co	<0.065	<0.00002
Cu	<0.0008	<0.0001
C	<0.0035	<0.005
Fe	<0.0003	<0.004
Pb	<0.0003	<10 <sup>-6</sup>
Zn	<0.0002	<0.00002

with a pure nickel film as the gas decomposes. Up to 300 repeats of this procedure are required to expand the pellets layer by layer to the ideal diameter of about 10 mm. Due to variations in the pellet temperature during Ni(CO)<sub>4</sub> decomposition in industrial settings, the completed pellets are inhomogeneous, exhibiting lamellar structures resembling an onion. The variations in each lamina's characteristics could cause the anodic dissolution behaviour of the pellets to change during electroplating [147]. Carbonyl discs are pellets which have been flattened by mechanical work and could also exhibit a similar inhomogeneity.

### 2.2.2.3.1 Titanium baskets

It is often necessary to maintain a constant cathode-to-anode size ratio and distance for stable operation. A non-uniform change in the cathode-to-anode distance could affect the throwing power and thickness uniformity of deposits [124, 126], while changes in cathode-to-anode size ratio could affect electrode reactions due to changes in the electrode current density and potential [135]. As mentioned earlier, single-piece nickel anodes decreased in size and became tapered during use, making it difficult to main-

tain a constant cathode-to-anode size ratio and distance [126]. This led to the development of baskets which could maintain a nearly constant anode area. The adoption of these anode baskets revolutionised anode procedures and sparked the use of unique varieties of primary nickel for electroforming [138].

Anode baskets are typically made out of titanium mesh to allow free flow of the electrolyte. To prevent the dispersion of insoluble residue which could result in roughness at the cathode, baskets are enclosed in anode bags. The bags are often snugly fitted so metallic residues can stay in contact with the Ti basket long enough for them to dissolve. To create an electrical connection, the anode basket is suspended by Ti hooks that are integrated into the basket and submerged in the electrolyte. Some baskets are supplied with hoopers to facilitate loading with refined forms of primary nickel [138].

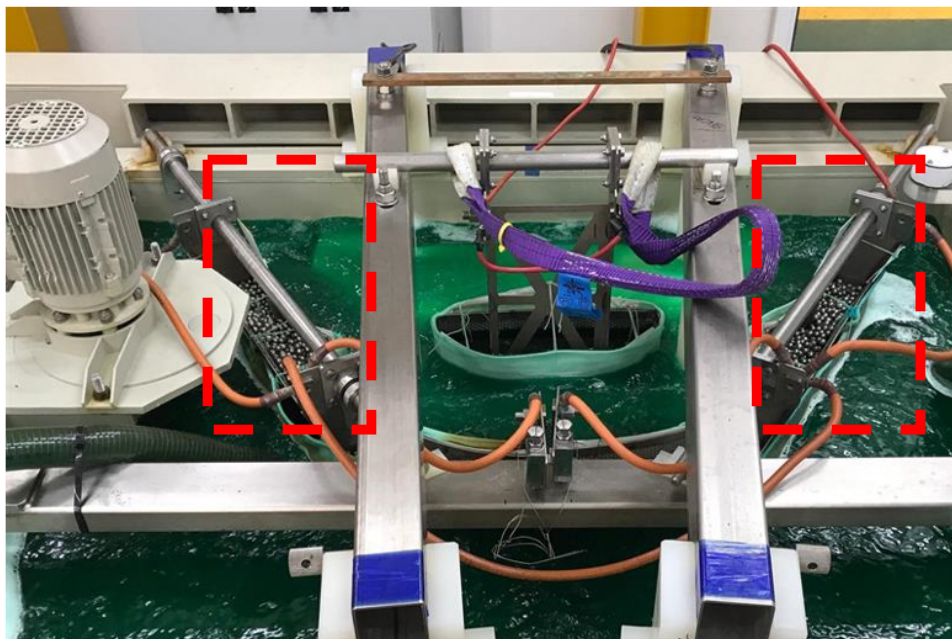


Figure 2.3: Industrial setup of nickel electroforming [148]. The red boxes highlight titanium baskets which are filled with nickel pellets

The top view of an industrial nickel electroforming equipment is shown in Figure 2.3 (courtesy of Doncasters [148]). The setup displays two titanium baskets containing nickel pellets that are encased in anode bags. Titanium is an ideal material for anode baskets because it delivers electric current to nickel pieces without self-oxidising. This is because titanium is protected by the preferential oxidation of nickel

which occurs at a lower equilibrium potential than titanium oxidation [138]. Therefore, the basket should always be kept full with nickel so good contact between titanium and nickel is maintained [126].

A well-designed basket, with proper maintenance, is large and unchanging, ensuring that a constant cathode-to-anode size ratio is maintained throughout the electrodeposition operation and repeat batches [126]. Additionally, baskets can be automatically loaded with nickel without interrupting plating operations. Conforming baskets can also be made in any shape and size to act as auxiliary anodes [138].

## 2.3 Kinetics and mechanism of nickel dissolution and passivity

As mentioned earlier, pure nickel has the tendency to become passive as it dissolves anodically in aqueous electrolytes. The anodic polarisation curve of nickel measured potentiostatically in nickel sulfamate solution (Figure 2.1) shows distinct active, passive, and transpassive regions which are discussed below. It is important to mention that studies of the mechanism of Ni dissolution and passivity in nickel electrolytes are very limited and information has been gleaned from studies made in acidic Ni(II)-free electrolytes.

### 2.3.1 Active dissolution

The kinetics of active dissolution of nickel has been widely studied in acidic sulfate [149–152], chloride [115, 151], and perchlorate [153] electrolytes. These studies have argued against a single step mechanism with divalent nickel ion acting as the charge carrier represented by Equation 2.21. This was mainly because pH was found to affect the anodic polarisation curves.



Sato and Okamoto [149] measured a steady state Tafel slope of  $\approx 30$  mV/dec for nickel oxidation in 0.5 M H<sub>2</sub>SO<sub>4</sub> at 40 °C and for current densities less than 3

$\text{mA/cm}^{-2}$  considered to be in the active region. The reaction rate was also found to be first order with respect to pH. This kinetic data was interpreted in terms of a consecutive mechanism of nickel dissolution with hydroxyl ions participating in the formation of intermediates, represented in Equations 2.22 to 2.24 [149].



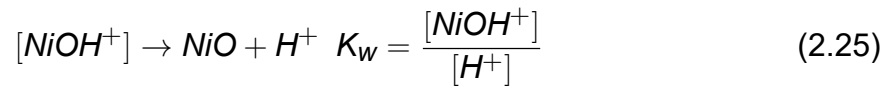
In later work, Piatti et al. [115] measured steady state Tafel slopes,  $b_{\text{SS}}$ , of  $55 \pm 5$  mV/dec in sodium chloride and sodium perchlorate electrolytes at 25 °C, Itagaki et al. [152] measured  $b_{\text{SS}}$  of 40 mV/dec in sulfate electrolytes at 25 °C, and Muralidharan et al. [154] measured  $b_{\text{SS}}$  of  $50 \pm 10$  mV/dec in  $\text{H}_2\text{SO}_4$  solution at 32 °C. The majority of these authors largely agreed with the consecutive charge transfer mechanism in Equations 2.22 to 2.24 and proposed Equation 2.23 to be the rate determining step.

### 2.3.2 Passivation

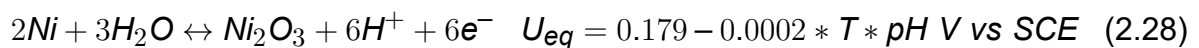
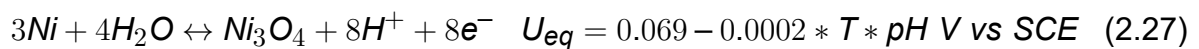
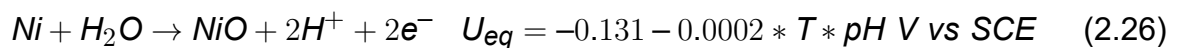
In some cases, more than one peak have been observed in the active region from potentiostatic and potentiodynamic studies of the anodic behaviour of nickel in acid solutions [151, 155–158]. It should be emphasised that in these situations, the critical passivation potential is the potential where the current density drops to a very low value that is maintained for an extended potential range. From literature review, there seems to be a general agreement that nickel dissolves anodically to form a soluble intermediate  $\text{NiOH}^+$ , which accumulates in the vicinity of the electrode surface until there is the precipitation of a precursor or pre-passive film. It was also suggested that the formation of this pre-passive film is characterised by the first of multiple peaks in the active region [155, 159] because this film does not render the electrode surface passive. However, there is some debate on the nature of this precursor film.

Sato and Okamoto [155] proposed that when the concentration of  $\text{NiOH}^+$  exceeds the saturated value which is determined by the solubility product,  $K_w$  of  $\text{NiO}$ ,

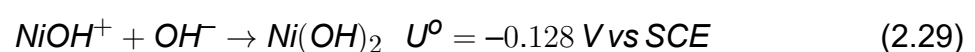
precipitation of a porous nickel oxide film occurs on the electrode surface, according to the reaction in Equation 2.25.



The researchers [155] also postulated that subsequent peaks following the formation of the precursor film could be attributed to the direct oxidation of Ni to NiO through pores in the film represented by Equation 2.26. In addition, the direct oxidation of Ni to higher nickel oxides such as Ni<sub>3</sub>O<sub>4</sub> and Ni<sub>2</sub>O<sub>3</sub> has also been proposed and is represented in Equations 2.27 and 2.28. Experimental values of peak potential obtained in the active dissolution region were found to correspond to the reversible potentials of Ni/Ni<sub>x</sub>O<sub>y</sub> reactions and were used to support these propositions [155, 160]. Passivation was attributed to the complete coverage of the electrode surface by a pore-free oxide film which caused the current to drop to a very small value [155].



An alternative to the precipitation reaction given in Equation 2.25 has been proposed by other researchers based on ellipsometric techniques applied to study nickel dissolution [159, 161, 162]. In this technique, an ellipsometer was used to evaluate the refractive index, thickness, and light absorption of the passive film under transient conditions. Reddy and Rao [161] argued, based on chronoellipsometric data and auxiliary assessments from the Pourbaix diagram, that Ni(OH)<sub>2</sub>, rather than NiO, is formed as the precursor film by a dissolution-precipitation mechanism. This precipitation reaction is given in Equation 2.29.



Bockris et al. [159] used absorption coefficients from ellipsometric studies of Ni oxidation in dilute H<sub>2</sub>SO<sub>4</sub> to investigate the mechanism of true passivation. They

used the relationship between the absorption coefficient of the film and its electrical conductivity at optical frequencies. Bockris et al. [159] found that the absorption coefficient decreased to a near-zero value until the critical passivation potential. This indicated that the precursor film was patchy because it was formed by precipitation and it was an electronic insulator. Hence, the precursor film permitted transport of ions and dissolution of the underlying metal. At the passivation potential, the absorption coefficient immediately increased to values which correspond to those of an electronic conductor. This meant that the precursor film was converted into a semiconducting passive film which inhibited high-field ion transport and dissolution. According to these researchers, the passive film is composed of a non-stoichiometric nickel oxide ( $\text{NiO}_x$ ,  $x \geq 1$ ) [159].

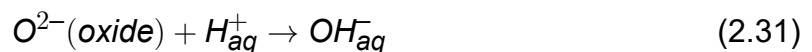
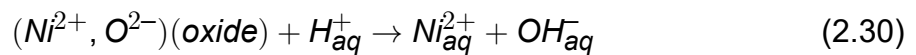
To explain the origin of the precursor film, Reddy and Rao [162] on the basis of automated ellipsometry results demonstrated that there was a time lapse called an induction time,  $\tau$ , during which the charge passed was used for an anodic process that did not build-up material on the nickel surface. This implied that the current is used for the generation of a soluble intermediate which has been proposed to be  $\text{NiOH}^+$ . Therefore, the accumulation of this product at the electrode surface is diffusion-controlled. Chronoellipsometric experiments by Reddy and Rao [161] demonstrated that  $j\sqrt{\tau}$  increased with current density,  $j$ , at low  $j$ 's but was independent of  $j$  at high  $j$ 's. They [161] concluded from these findings that the precursor film in the passivation of nickel in acid solutions was formed by a dissolution-precipitation mechanism because the absorption coefficient measured during  $\tau$  corresponded to that of a clean Ni surface. After  $\tau$ , the absorption coefficient dropped indicating film formation [162]. A plot of  $\tau$  against  $j$  provided a means of predicting the solubility product in the precursor film which was found to correspond to that of  $\text{Ni(OH)}_2$  [161].

Subsequent studies of passive films on Ni in acid and alkaline solutions using X-ray Photoelectron Spectroscopy and *in situ* scanning tunnelling microscopy demonstrated that a bilayer structure composed of an inner crystalline layer of NiO and an outer layer of  $\text{Ni(OH)}_2$  describe the characteristics of passive films on Ni better than a simple uniform oxide [163, 164]. This also provided additional evidence of the presence of  $\text{Ni(OH)}_2$  in the passive film. Passive films formed in acid electrolytes have been re-



ported to possess thicknesses ranging from 0.9 nm to 1.2 nm with larger values of 2.5 nm reported in alkaline solutions [164].

During passivation, the rate of passive film dissolution is counterbalanced by the rate of film formation. The rates of these reactions are not affected by the electrode potential of nickel, but controlled by the galvanic-potential difference across the oxide/electrolyte interface [155]. Ellipsometric studies also revealed that the film growth process came to a virtual stop after the passivation potential which was further indication that the rates of formation and dissolution of the passive film are exactly the same to maintain a constant film thickness [159]. The overall dissolution reaction of the passive film given in Equation 2.30 is a coupled reaction of two processes shown in Equations 2.31 and 2.32 [155].



### 2.3.3 Transpassive dissolution

There is a transpassive dissolution region shown in Figure 2.1 where the current density begins to increase after the passive region. This indicates that the passive film has been broken down in a process known as depassivation. In this process, grain boundaries of the oxide passive film play an important role on the redistribution of the potential across the metal/oxide and oxide/electrolyte interfaces. The grain boundaries in the oxide layer could exhibit ionic conductivities many orders of magnitude greater than those in the bulk layer. Hence, there is less resistance to ion transport at grain boundaries. Consequently, the potential drop at the oxide inter-granular boundaries is smaller compared to the rest of the bulk [165]. There are several reported mechanisms by which depassivation could occur depending on which interface controls the potential drop [165–167]:

#### 1. Local thinning and dissolution of the oxide layer

A significant potential difference across the oxide/electrolyte interface will cause an increased rate of transfer of metal cations from the oxide to the electrolyte, especially at inter-granular boundaries where metal cations are loosely bound. Therefore, one can expect an enhanced localised dissolution at the grain boundaries. This could trigger pit formation in these less resistive sites where local thinning of the passive film is not compensated by repassivation [165]. Pitting is typically autocatalytic in nature by developing conditions that would promote further pit growth. One of these conditions is the insufficient supply of  $\text{OH}^-$  to the pit compared to the bulk oxide surface which will shift repassivation to the exposed surface where  $\text{OH}^-$  is more plentiful and hinder repassivation in the pit [167].

## **2. Metal voiding and collapse**

The continuous formation of localised depressed areas (voids) at the metal surface underneath the oxide layer could develop stress in the non-supported oxide layer, eventually leading to its rupture, i.e local depassivation, revealing a pit as shown in Figure 2.4 [165]. Metal/oxide interfacial voiding is initiated by faster diffusion of new metal cations, formed by the metal oxidation reaction, across the inter-granular boundaries of the oxide layer to the electrolyte. Voiding will occur if metal cations do not diffuse towards the metal surface fast enough to fill the vacancies [165].

## **3. Stress-induced rupture of the oxide layer caused by particle growth at the metal/oxide interface**

Stress could also be induced in the oxide layer when transport through inter-granular boundaries of the oxide layer to the metal/oxide interface is dominated by anions ( $\text{O}^{2-}$  and  $\text{Cl}^-$ ). These anions could react with newly formed metal cations to form metal complexes beneath the oxide layer, halting voiding. Continuous growth of these metal complexes will generate osmotic stress at the metal/oxide interface and in the oxide film, eventually leading to local fracture and depassivation [165]. The mechanism of this process is shown in Figure 2.5.

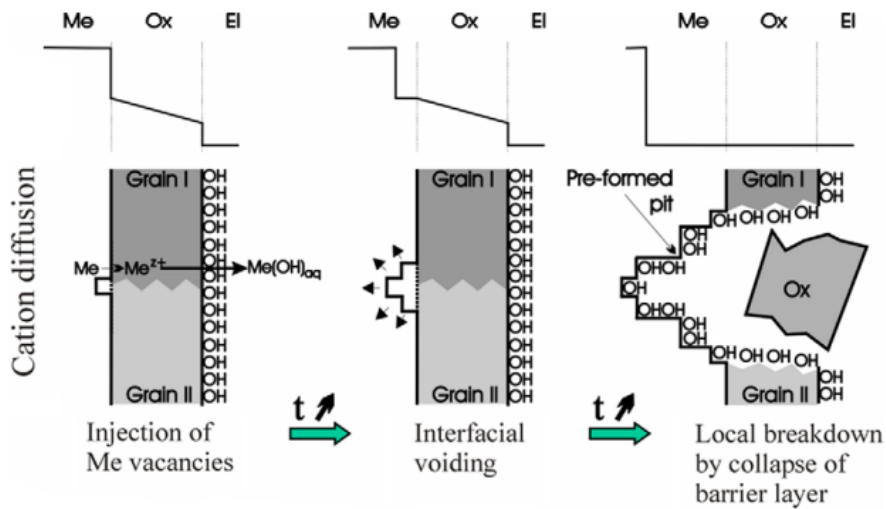


Figure 2.4: The mechanism of voiding and collapse of the oxide layer driven by the potential drop at the metal/oxide interface of an inter-granular boundary in the oxide layer [165].

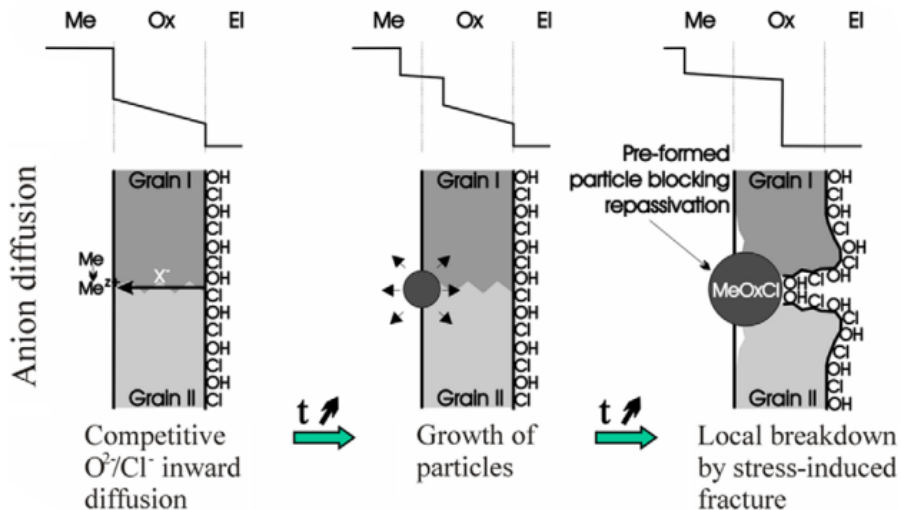
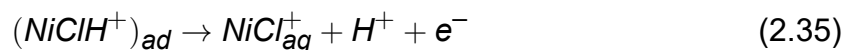


Figure 2.5: The mechanism of stress induced fracture driven by anion transport through an inter-granular boundary in the oxide layer [165]

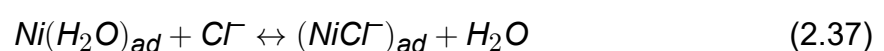
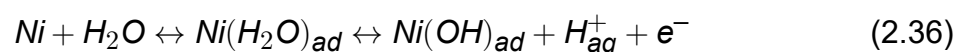
Sato and Okamoto [155] measured Tafel slopes of 121-131 mV/dec for transpassive nickel dissolution in acidic sulfate electrolytes which were greater than those measured for active dissolution (30-50 mV/dec). This indicated a change in the rate determining step of the nickel electrodisolution mechanism (Equations 2.22-2.24) from Equation 2.23 in the active region to Equation 2.22 in the transpassive region.

## 2.4 Effect of chloride ions on nickel dissolution and passivity

The problem of passivity in pure nickel anodes could be alleviated in two ways: (i) the incorporation of small amounts of sulfur (0.01 to 0.04 wt%) in the anode material which has been introduced in section 2.2.2.3 and is discussed in section 2.5 and (ii) the addition of chloride ions to the electrolyte. Chloride ions present in solution can play a significant role in the kinetics of nickel active dissolution indicated by a non-zero reaction order with respect to  $\text{Cl}^-$  reported in literature. Researchers have reported reaction orders of 0.5 and 1.0 with respect to  $\text{Cl}^-$  and  $\text{H}^+$ , respectively, in acidic chloride solutions leading them to propose the following mechanism [168, 169]:



Chloride ions could either promote or hinder active dissolution depending on its concentration and the pH of the electrolyte [158, 170]. According to experimental data, low concentrations of chloride ions decelerate the anodic dissolution reaction while high concentrations enhance dissolution [158, 170]. It is proposed that the inhibitive action of chloride ions on dissolution rate could be due to the chemical adsorption of these anions on the nickel surface which could prevent the reaction of metal atoms with  $\text{H}_2\text{O}$  or  $\text{OH}^-$  by displacing water dipoles and covering the surface as shown in Equations 2.36 and 2.37 [158, 168].



On the other hand, at high enough concentrations, chlorides promote active dissolution of nickel by forming adsorbed complexes with metal cations which dissolve into solution [158]. The formation of  $(\text{NiCl})_{ad}$  and  $(\text{NiClH}^+)_{ad}$  intermediates also interferes with the process in Equation 2.29 which hinders passive film formation [171].

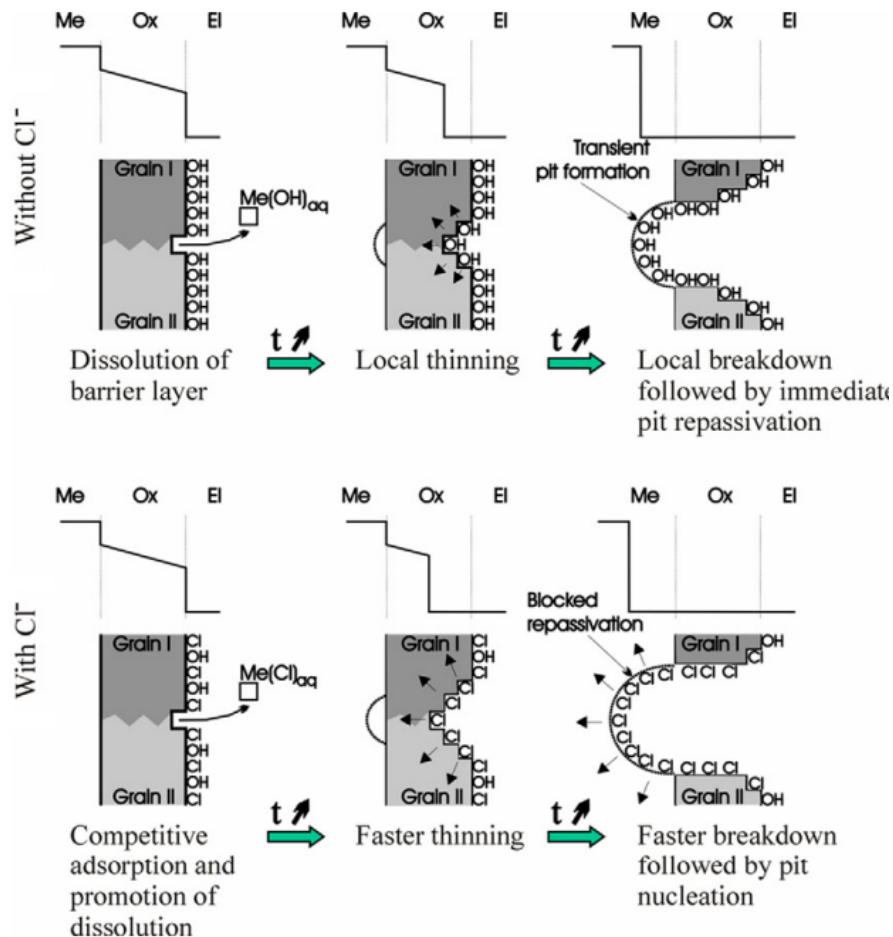


Figure 2.6: The effect of chloride ions on the mechanism of local thinning and breakdown of passivity driven by the potential drop at the oxide/electrolyte interface of an inter-granular boundary in the oxide layer [165].

Chloride ions could affect passivity by competing with  $\text{OH}^-$  for adsorption on oxide surface sites. Adsorbed metal chloride complexes,  $\text{Me-Cl}^-$  or  $\text{MeO(H)-Cl}^-$ , are loosely bound to the oxide surface and therefore require a smaller activation energy for their dissolution from the passive film. This increases the localised dissolution rate and poisons film growth. Consequently,  $\text{Cl}^-$  adsorption on the oxide surface promotes local thinning and depassivation. After local depassivation,  $\text{Cl}^-$  also compete with  $\text{OH}^-$  for adsorption at pits, which could deplete the supply of  $\text{OH}^-$  hindering repassivation and

enhancing pit growth as shown in Figure 2.6 [165]. Chloride ions could also penetrate the oxide film through oxygen vacancies and prevent repassivation [165].

The addition of chlorides to nickel sulfamate electrolytes dates back to the 1950s when Diggin [172] advocated for the addition of 30 g/L  $\text{NiCl}_2$  to the bath, similar to the concentration in a Watts bath. Diggin indicated that this was necessary to promote anode corrosion. Since then, the necessity for the addition of chloride ions to electroforming baths and the required  $\text{NiCl}_2$  concentration has been a point of controversy as regards to the internal stress of the deposit and anode corrosion.

Fanner and Hammond [53] stated that a chloride-free sulfamate bath could not be used with electrolytic and depolarised nickel anodes which were found to polarise rapidly even at current densities less than  $2 \text{ mA cm}^{-2}$ . The authors then investigated the incremental increase of chloride ion concentration in the bath on the internal stress and anode corrosion of bagged depolarised nickel anodes. They reported that a minimum  $\text{NiCl}_2 \cdot 6\text{H}_2\text{O}$  concentration of 0.014 M (3.3 g/L) was required for reliable anode corrosion at pH values less than 5.0 and current densities up to  $50 \text{ mA cm}^{-2}$ . In addition, they claimed that this chloride ion concentration did not increase the stress in deposits significantly. Internal stress data was not reported but was stated to be within the limits of sensitivity of the method used for measurement.

Researchers have reported an increase in nickel dissolution current efficiency to 100% [125], and a decrease in cell voltage [58] when 0.04 M (4.8 g/L)  $\text{NiCl}_2$  was added to a sulfamate bath. Hart, Wearmouth, and Warner [50] also found that increasing the  $\text{NiCl}_2$  concentration from 8 g/l (0.062 M) to 24 g/l (0.185 M) increased the active dissolution currents of a non-activated anode before passivity occurred and decreased the breakdown potential of the passive film.

However, chloride ions tend to raise the tensile stress of nickel deposits [125, 173–175]. Therefore, it is often preferable to operate chloride-free baths or keep the nickel chloride ( $\text{NiCl}_2 \cdot 6\text{H}_2\text{O}$ ) concentration to 5 g/L (0.021 M) for applications such as electroforming where control of the internal stress is critical. At such low concentrations, chloride ions are less effective at preventing the passivity of pure Ni anodes [50]. This led to a demand for additives that could prevent Ni passivation without the addition

of chlorides.

## 2.5 Effect of sulfur on nickel dissolution and passivity

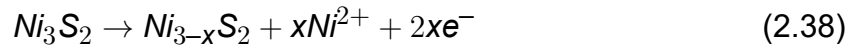
There are numerous reports of increased dissolution rate of nickel doped with small amounts of sulfur [50, 138, 176]. Although other additives such as silicon and phosphorus have been investigated, sulfur was found to be the sole additive that was practical to alleviate passivity in electrolytic nickel. Problems such as significant metal waste in the form of fines, low anode efficiency, changes in bath pH, and incorporation of the anode additive in the deposit emerged with other investigated additives [126].

There are propositions that the high dissolution rate in the presence of sulfur is due to its adsorption on the metal surface which poisons the sites usually available for the adsorption of oxygenated species, hindering the formation of the passive film [176]. This adsorption is achieved by surface segregation during dissolution in the active region to form an outermost nickel sulphide film which prevents the surface from being passivated while allowing nickel to dissolve at a rate that is noticeable. The passive film forms following the desorption of adsorbed sulfur [176].

The sulfur layer formed on sulfurised nickel during anodic dissolution has been identified by X-ray Photoelectron Spectroscopy (XPS) as  $\text{Ni}_3\text{S}_2$  [177]. It was also found that a nickel sample coated with 50 nm of  $\text{Ni}_3\text{S}_2$ , revealed by radiochemical measurements, supported current densities comparable to those observed with nickel-sulfur alloys [176]. Later work using XPS and Auger Electron Spectroscopy also confirmed the presence of sulfide on nickel in the active dissolution region [178].

Bear et al. [179] measured an anodic Tafel slope of 110 mV/decade in the active region for sintered and electroformed nickel anodes of different sulfur contents (0.035-0.17 wt%) in nickel sulfate solution at 21 °C. They suggested that the mechanism of sulfur-activated nickel dissolution followed that proposed by Sato and Okamoto [149] for transpassive pure nickel dissolution in  $\text{H}_2\text{SO}_4$  solutions, which was characterised by a 120 mV/decade Tafel slope. This mechanism is given in Equations 2.22 to 2.24.

Bear et al. [179] also found that the dissolution rates of sulfur-activated sintered and electroformed nickel anodes were comparable to those of synthetic heazlewoodite ( $Ni_3S_2$ ) electrodes. Based on their kinetic measurements along with evidence of the formation of a  $Ni_3S_2$  surface film from other reports [176–178], Bear et al. [179] concluded that nickel is extracted from the  $Ni_3S_2$  surface film leaving a sulfide of lower nickel content,  $Ni_{3-x}S_2$ , according to Equation 2.38.



The sulfide,  $Ni_{3-x}S_2$ , then interacts with the underlying elemental nickel to reconstruct the film [179]:



## 2.6 Review of the anodic behaviour of different materials in nickel plating electrolytes

One of the earliest reviews of the anodic behaviours of depolarised, carbon-containing, and primary nickel materials was obtained by Di Bari [137, 138, 140] in a Watts bath containing 14 g/L (0.11 M)  $NiCl_2$  and a chloride-free nickel sulfate solution at 60 °C (140 °F). The results are shown in Figure 2.7. As mentioned earlier, though depolarised and carbonised nickel materials are more active than pure electrolytic nickel in a Watts Bath, sulfur-activated nickel was found to be the most active anode material. Sulfur-activated nickel was also the only material that dissolved at a low potential in nickel sulfate in the absence of chloride ions.

Hart and other researchers [50] applied the potentiodynamic technique to compare the anodic polarisation curves of sulfur-free electrolytic nickel squares and sulfur-activated electrolytic nickel rounds (0.024% S) in nickel sulfate-based and nickel sulfamate-based solutions. Compared to the galvanostatic technique used by Di Bari [140], the potentiodynamic approach allowed clear differentiation between the active, passive, and transpassive dissolution regions as shown in Figure 2.8.

Hart [50] demonstrated that sulfur-activated nickel dissolved satisfactorily in



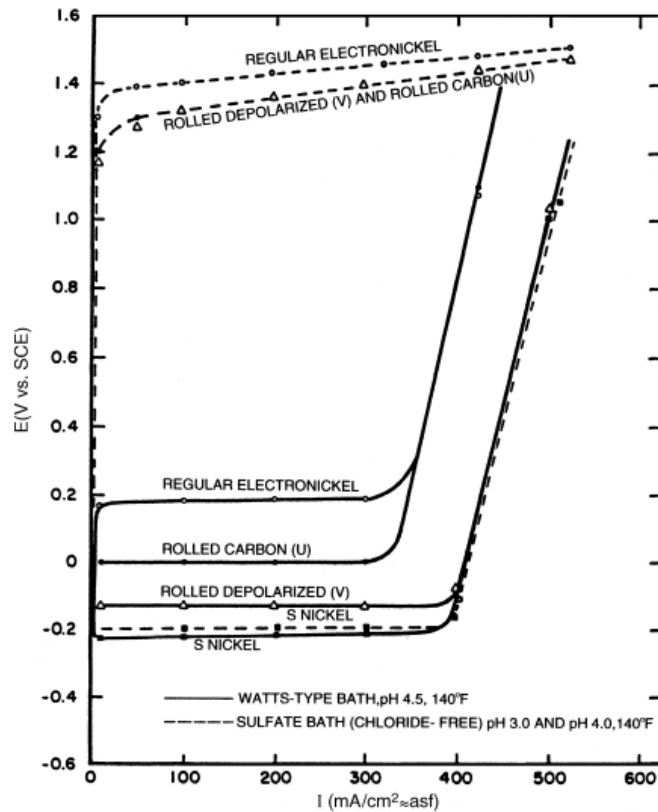


Figure 2.7: Anodic polarisation curves of different nickel anode materials obtained under galvanostatic conditions in Watts and chloride-free nickel sulfate electrolytes [138].

the active region with current densities above  $700 \text{ mA cm}^{-2}$  before passivating as shown in Figure 2.8. In contrast, non-activated nickel could not maintain current densities  $> 0.5 \text{ mA/cm}^2$  in the active region even when the concentration of  $\text{NiCl}_2$  in the bath was increased from  $0.037 \text{ M}$  to  $0.1 \text{ M}$ . In fact, sulfur-free Ni could only dissolve with appreciable current densities at potentials above  $0.8 \text{ V vs SCE}$ . It should be mentioned that an increase in the concentration of chloride ions barely affected the active dissolution currents but significantly decreased the breakdown potential of the passive film [50]. Thus, it would appear that the action of chloride ions on the depassivation of the passive film, rather than their ability to inhibit passivation, is what makes them useful in enhancing the dissolution of sulfur-free nickel. It should also be noted that the chloride concentrations employed in the investigations by Hart et al. [50] were greater than those commonly employed for electroforming operations where the chloride content is kept to  $0.021\text{-}0.025 \text{ M}$  to ensure a low tensile stress [24, 180].

The study by Hart et al. [50] also reported significant variations in the dis-

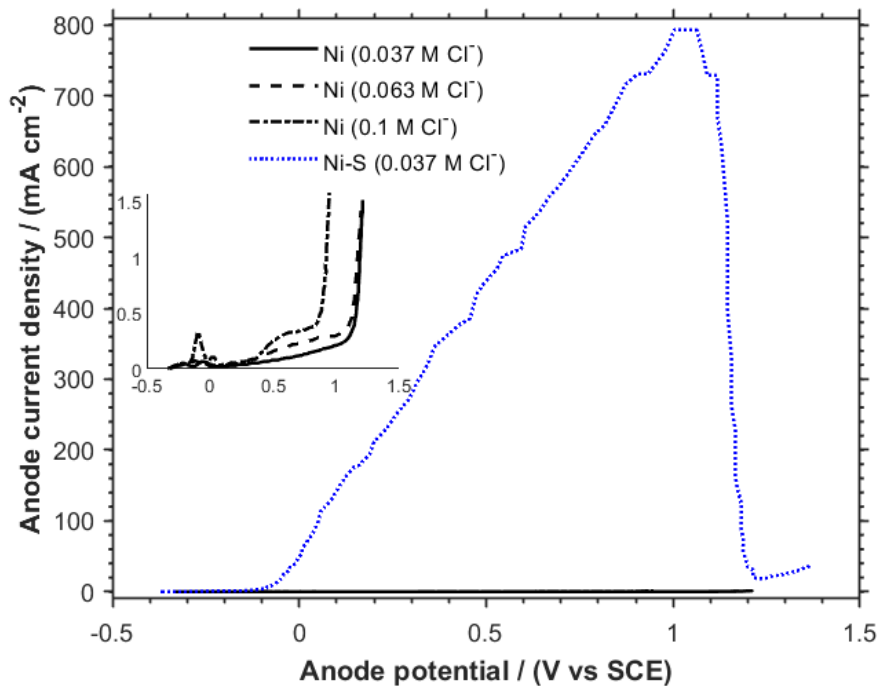


Figure 2.8: Anodic polarisation curves of different nickel anode materials obtained under potentiodynamic conditions in nickel sulfamate-based electrolytes at 60 °C and pH 4.0. The base electrolyte contained 1.86 M  $\text{Ni}(\text{SO}_3\text{NH}_2)_2 \cdot 4\text{H}_2\text{O}$  and 0.65 M  $\text{H}_3\text{BO}_3$ , plus 0.037-0.1 M  $\text{NiCl}_2 \cdot 6\text{H}_2\text{O}$ . Adapted from [50].

solution behaviour of sulfur-free nickel in Watts and nickel sulfamate electrolytes of comparable Ni(II) content. Transpassive dissolution of sulfur-free nickel occurred at less noble potentials in the Watts bath. An explanation for this phenomenon was not provided but it was clear that the action of  $\text{Cl}^-$  on passive film breakdown was also affected by other anions present in the solution. This suggests that there could be major differences between the anodic processes (anodic dissolution and passive film formation) in sulfate and sulfamate systems.

Watson [181] demonstrated that the use of sulfur-activated nickel (0.025% S [49]) in titanium baskets could maintain high dissolution rates up to  $500 \text{ mA cm}^{-2}$  around a potential of  $-0.2 \text{ V vs SCE}$  in 1.86 M  $\text{Ni}(\text{SO}_3\text{NH}_2)_2 \cdot 4\text{H}_2\text{O}$  solution containing 0.021 M  $\text{NiCl}_2 \cdot 6\text{H}_2\text{O}$ , which is slightly lower than the potential measured by Hart et al. [50] for sulfur-activated nickel in controlled electrochemical experiments. Similarly, it was also reported by Watson [181] that non-activated nickel in industrial practice could achieve dissolution rates up to  $150 \text{ mA cm}^{-2}$  at low potentials around 0.2 V vs SCE in

the same investigated electrolyte. These results are opposed to those reported by Hart et al. [50] who demonstrated that significant dissolution rates for non-activated nickel were only obtained above 0.9 V vs SCE. These findings suggest that different situations exist in laboratory and industrial environments. These differences were proposed to arise from the use of nickel in a titanium basket and the absence/presence of agitation [50]. The accumulation of sulfamate ion oxidation products in industrial electroforming baths which run for long durations without changing the electrolyte may be another cause for the discrepancies observed. These oxidation products could build up over time and alter the dissolution characteristics of nickel anodes.

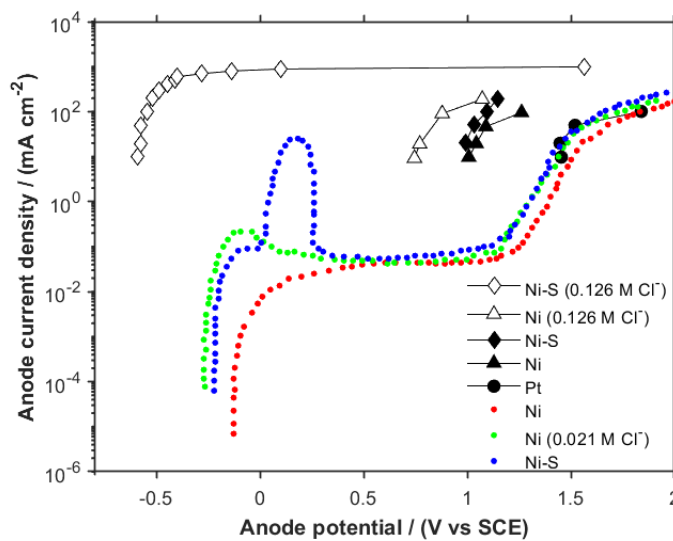


Figure 2.9: Anodic polarisation curves, obtained under galvanostatic (black and white markers) and potentiodynamic conditions (red, green, and blue markers), of different anode materials in nickel sulfamate-based electrolytes measured by Nakano et al. [130] and Yang et al. [180], respectively. The base electrolyte of Nakano et al. [130] contained 1 M  $\text{Ni}(\text{SO}_3\text{NH}_2)_2 \cdot 4\text{H}_2\text{O}$  plus 0.126 M  $\text{NiCl}_2$  at 50 °C and pH 4.0. The base electrolyte of Yang et al. [180] contained 1.39 M  $\text{Ni}(\text{SO}_3\text{NH}_2)_2 \cdot 4\text{H}_2\text{O}$ , 0.65 M  $\text{H}_3\text{BO}_3$ , and 1mL/L wetting agent (WT-400), plus 0.021 M  $\text{NiCl}_2 \cdot 6\text{H}_2\text{O}$  at 50 °C and pH 3.6. Adapted from [130] and [180].

More recent descriptions of the behaviour of different anode materials in nickel sulfamate solution measured under galvanostatic and potentiodynamic conditions have been given by Nakano et al. [130] and Yang et al. [180], respectively. The results are shown in Figure 2.9. Nakano et al. [130] studied the behaviour of Pt, non-activated

Ni, and sulfur-activated electrolytic Ni (0.019% S) in 1 M  $\text{Ni}(\text{SO}_3\text{NH}_2)_2 \cdot 4\text{H}_2\text{O}$  solution with and without 0.126 M  $\text{NiCl}_2$ . They performed galvanostatic experiments by applying anodic current densities between 10 and 1000  $\text{mA cm}^{-2}$ . Their results indicated that sulfur-activated Ni polarised in the absence of chloride ions, dissolving at potentials around 1 V vs SCE, similar to those of pure Ni. The addition of  $\text{NiCl}_2$  prevented passivation of sulfur-activated Ni but did not do so in the case of pure Ni. Instead, the presence of  $\text{NiCl}_2$  decreased the dissolution potential of Ni to around 0.8 V vs SCE. On the other hand, Yang et al. [180] showed that sulfur-activated nickel with a higher content of sulfur (0.04% S) dissolved in the absence of nickel chloride with a passivation current density of 25  $\text{mA cm}^{-2}$  at 0.2 V vs SCE. These results are at odds with those reported originally by Hart et al. [50] and Watson [181], who found that sulfur-activated nickel ( $\approx 0.024$  wt% S) dissolved in the active region with current densities above 400  $\text{mA cm}^{-2}$ . This suggests that the performance of sulfur-activated nickel may vary depending on the sulfur content of the nickel anode or the chloride content of the bath.

In summary, sulfur-activated nickel could typically maintain appreciable current densities in a chloride-containing electroforming bath but it is unclear if this is often the case in the absence of chloride ions. On the other hand, non-activated nickel anodes often dissolve with high overpotentials close to the equilibrium potential of water oxidation (+0.984 V vs SCE). Under such conditions, the oxidation of sulfamate ions could occur leading to changes in the electrolyte composition which is explored in the forthcoming section.

## 2.7 Oxidation of sulfamate ions

Anodic behaviour is more complex in a sulfamate electrolyte than it is in a Watts electrolyte. It has also been demonstrated that the choice of anode material and anode current efficiency could be correlated to variations in internal stress and sulfur content of electroformed nickel [125, 130, 173].

Klingenmaier [125] found that the type of anode material and dissolution ef-

efficiency had a significant influence on the sulfur content and residual stress of nickel deposits produced from sulfamate systems. Nickel electrodeposited from a bath containing 0.8 g/L (0.006 M)  $\text{NiCl}_2$  with a pure depolarised nickel anode had an increased sulfur content and decreased tensile stress compared to deposits produced from the same bath with a sulfur-depolarised nickel anode. It was noted that pure depolarised and sulfur-depolarised anodes dissolved at current efficiencies of 96% and 100%, respectively. Klingenmaier [125] stated that the increased sulphur in deposits could only have come as a result of the oxidation of sulfamate ions which occurred at anodes with low dissolution efficiency. This paper [125] paved the way for further investigations into anode reactions in the sulfamate bath.

Similarly, Marti [173] reported that internal stress data of consecutive nickel deposits showed increasingly compressive values when electrolytic Ni or Pt/C anodes were employed in nickel sulfamate solutions and suggested that this was caused by sulfite ( $\text{SO}_3^{2-}$ ) based on the effect of adding sulfite to the electrolyte on internal stress measurements. In a further report, Greene [127] stated that hydrazinesulfonate, azodisulfonate (ADS), sulfite, sulfate, and persulfate were consecutively produced at an inert (Pt/C) anode in nickel sulfamate solution based on UV-vis analysis which led to the disagreement that sulfite was the main stress-reducing oxidation product as insufficient quantities of this product (10-20 ppm) were measured in the electrolyte after electrolysis greater than 4 Ah/L. Instead, it was claimed that ADS, which showed a distinctive UV peak at 245 nm, was the main oxidation product affecting stress in the deposits since the conditions for its generation and removal paralleled those for creating and eradicating the electrolyte's ability to reduce stress [127]. A potentiostatic study by Novikov et al. [135] further demonstrated that, depending on the potential, a series of electrochemical reactions also occur at a non-activated nickel anode in nickel sulfamate solution based on the results of dissolution efficiency and gas chromatography used to identify gases evolved at the anode. The results suggest that sulfamate ion is oxidised to ADS at intermediate potentials between +1.055 and +1.355 V vs SCE explained by the absence of gas evolution and anode efficiencies less than 100%. Nitrogen gas was only detected at potentials greater than +1.355 V vs SCE which is co-generated with sulfate ions.

Zhang and Park [129] studied the UV spectra of sodium sulfamate following electrolysis with a platinum anode at pH 2 in an effort to identify other oxidation products besides ADS. Zhang and Park [129] proceeded to separate sulfite, hydrazinesulfonate, and ADS from the electrolysed sample by chemical methods and found that a product was present in this sample which gave rise to a distinct UV peak at 245 nm, similar to ADS [127]. Fast atomic bombardment mass spectroscopy (FAB-MS) and IR spectroscopy experiments were performed on the isolated product to identify its molecular weight and structure. Zhang and Park [129] concluded that the unknown compound was diimide-S-sulfonate (DSS,  $\text{H}_2\text{N}=\text{N}-\text{S}-\text{SO}_3$ ). The reduction of this compound at the cathode in sodium sulfamate solution was investigated using potentiostatic experiments with subsequent measurements of the absorbance of the 245 nm UV band. The absorbance showed a decrease at -1.644 V vs SCE. Although, the compound was shown to be reducible at the cathode, its exact effect on the stress of nickel deposits was not investigated.

The investigations by Zhang and Park [129] support an earlier study by Jiazhu et al. [128] which also found that dithionate ions and a compound denoted as AUP were produced at a Pt anode in addition to sulfite, hydrazinesulfonate, and ADS. AUP also gave rise to a UV peak at 245 nm and decreased the stress of nickel deposits [129].

Kendrick and Watson [182] reported that for concentrated nickel sulfamate solutions, a compound is produced at a non-activated nickel anode which is different from that produced at an insoluble anode. Although both decreased the tensile stress in deposits, the former retained little to no sulfur in nickel deposits (max. 0.006%) whilst the latter increased the sulfur content in the deposit up to 0.03%. Kendrick and Watson [182] proposed that the non-activated nickel anode could be operated at low current densities of 5-10  $\text{mA cm}^{-2}$  corresponding to an anode potential of 0.1 V vs SCE, in addition to a sulfur-activated nickel anode, to couple the advantages of this stress-reducer with the high dissolution rates of the activated nickel anode. This process was called a 'conditioning' treatment. Watson [49] claimed that the insoluble anode generated azodisulfonate which is unstable and could be destroyed by heating the solution to 65 °C or oxidation with potassium permanganate whereas the unidentified stress-reducer produced at low-sulfur nickel anodes is stable for extended periods at 70 °C. Klingen-

maier [125] had reported that deposits produced from sulfamate electrolytes using a platinized titanium anode had higher sulphur contents and compressive stresses than deposits generated from electrolytes using non-activated nickel anodes.

Nakano et al. [130] demonstrated that the UV spectra of oxidation products generated at Pt and non-activated Ni anodes in nickel sulfamate solutions showed a distinct peak and shoulder around 245 nm, respectively, which suggested that the products may be different. It is noted from previous reports discussed above [127–129] that it is unknown whether the oxidation product with an absorption peak at 245 nm is ADS, AUP, or some other compound. There have not been any prior reports on the outcomes of analytical analyses of ADS in nickel sulfamate baths electrolyzed using Pt and Ni anodes.

Nakano et al. [130] also demonstrated that the sulfamate oxidation product cannot be generated at sulfurised nickel anodes unless anode current densities  $> 700 \text{ mA cm}^{-2}$  were applied which far exceed practical dissolution rates ( $10\text{-}25 \text{ mA cm}^{-2}$ ) for an anode to cathode size ratio of 2:1. This has been attributed to the low dissolution potentials ( $< +0.14 \text{ V}$ ) of sulfurised nickel anodes in contrast to the high anodic potentials of non-activated Ni and Pt anodes which correspond to around 1.06 V and 1.46 V vs. SCE, respectively [130].

Table 2.6: Summary of sulfamate decomposition products detected in various studies.

Anode	Bath composition	Products detected	Anode potential (V vs SCE)	References
Pt or C	1.3 M nickel sulfamate, pH = 4	Azodisulfonate (ADS), hydrazinedisulfonate (HDS), bisulfite, sulfate, thiosulfate	-	[127]
Pt	1.0 M sodium sulfamate, pH = 2 and 12	Diimide s-sulfonate (ADS and HDS as intermediates)	+1.755 (pH=2), +1.156 (pH=12)	[129]
Pt	1.0 M sodium sulfamate, pH = 13	AUP, HDS, ADS, and dithionate	-	[128]
Pt, Ni	1.0 M nickel sulfamate, pH = 4	unassigned (245 nm peak)	1.06 (Ni), 1.46 (Pt)	[130]
Ni	1.4 M Nickel sulfamate, pH = 3.9	nitrogen gas (ADS and HDS as intermediates)	1.4	[135]

It is not possible to estimate the equilibrium potential for the oxidation of sulfamate ions and its products since there is a lack of thermodynamic data. The literature-reported sulfamate oxidation products and the anode potentials at which they were produced are summarised in Table 2.6. According to these reports, sulfamate oxidation is most likely to happen when nickel anodes dissolve transpassively and at potentials higher than the oxygen evolution equilibrium potential at  $45 \text{ }^{\circ}\text{C}$  and pH 4.0. ( $+0.73 \text{ V}$

vs SCE). While sulfamate ion breakdown has been qualitatively demonstrated, a quantitative understanding is still required. In particular, because potentiostatic techniques were employed in the majority of studies, it is uncertain if these sulfamate breakdown products, which certainly alter the internal stress in deposits, are generated under electroforming current densities. Secondly, there is no proof that the breakdown products produced at Pt and low-sulfur nickel anodes are different from one another. Finally, it is unknown how the long-term accumulation of these compounds would affect the deposit quality and cathode current efficiency.



# Chapter 3

## Fundamentals

### 3.1 An overview of electroforming

As mentioned, electroforming is a specialised use of electrodeposition. The key distinguishing feature of electroforming compared to electroplating is that it produces free-standing parts. To achieve this objective, the electrodeposited part must possess certain characteristics: (i) adequate thickness to provide sufficient mechanical strength to be self-supporting, (ii) easily separable from the mandrel, and (iii) zero internal stress to ensure its shape and dimensions are maintained following separation from the mandrel. Without proper control, high stress levels could distort the electroform, prematurely separating it from the mandrel, and causing cracks in the metal in extreme circumstances [25]. As a result, constituents of the electrolyte are carefully chosen to regulate the level of stress in deposits.

A thorough understanding of the electrodeposition process as well as the roles and behaviours of electrolyte constituents are required in order to optimise the bath composition to achieve desirable properties in the deposits. Numerous electrochemical phenomena, including charge transfer kinetics, electrocrystallization, and the mass transfer of electroactive species, could be affected by the electrolyte composition. Since a part of this research is focused on investigating the effect of boric acid during nickel electroforming, it is important that one first understands the principles behind electrochemical reactions in the electrodeposition process.

This chapter lays the groundwork for this thesis by discussing essential aspects of the electrochemical process and their relevance to the influence of  $\text{H}_3\text{BO}_3$  on electroforming. Important concepts such as thermodynamics, charge transfer kinetics, mass transfer, and electrocrystallisation are explored.

### 3.1.1 Laboratory studies of electrodeposition systems

An electrochemical system must be subject to some level of monitoring and control in order to be studied and evaluated. It is necessary to measure current and electrode potential since they are crucial physical variables that can be utilised to monitor and control the electrode process. The electrode potential ( $U$ ) is the Galvani potential difference ( $\Delta\varphi$ ) between the electrode and solution just outside the electrical double layer. The electrical double layer is a spatial finite region of equal and opposite charged layers at the interface between the electrode and the solution as shown in Figure 3.1. The electric potential of each electrode is a measure of the electron energy and could be used to change the rate of electrochemical reactions which is characterised by the amount of current flowing in the electrical circuit [47].

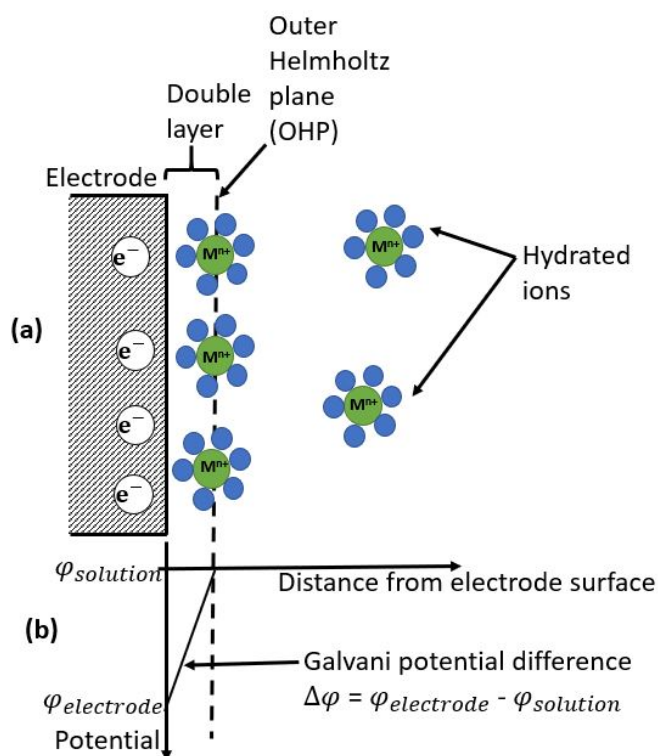


Figure 3.1: Schematic of (a) the Helmholtz electrical double layer model and (b) the potential drop across the double layer. Adapted from [183]

As was shown in Figure 1.2, industrial electrodeposition systems are performed using a two-electrode configuration. However, there are limitations to the amount

of information that can be gained from experiments performed using this configuration in laboratory studies. The two-electrode system is usually operated in galvanostatic mode where the current flowing in the electrical circuit is fixed and the overall potential difference between the cathode and anode defined as the cell potential is allowed to vary with time. This cell potential is a combination the anode and cathode potentials and the ohmic drop in solution. The cell potential can be used to monitor changing electrode and electrolyte conditions, but it is unable to pinpoint the precise process that is changing, specifically the critical process [48].

Alternatively, the two-electrode design can be operated with a constant cell potential while the electric current is allowed to vary. This mode is especially helpful when it is possible to carefully control the potential of the electrode of interest (working electrode) and, as a result, the driving force behind the electrode reaction [48]. However, it is frequently challenging to achieve a cell potential that closely resembles the potential of the working electrode because a significant portion of the applied cell potential is utilised to drive the electrochemical process at the counter electrode and overcome the ohmic drop in the electrolyte [48].

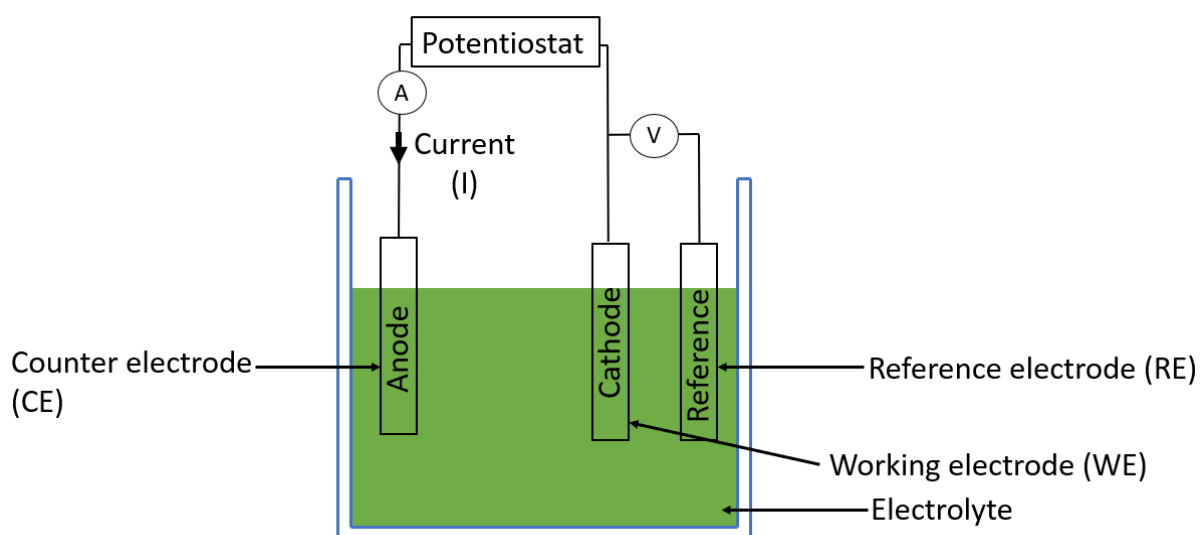


Figure 3.2: Schematic of an electrochemical cell with a three-electrode system employing a potentiostat. Current and voltage measurement devices are represented by A and V, respectively.

Many of the issues discussed above in the two-electrode system have been

resolved in lab-scale experiments by using a three-electrode configuration shown in Figure 3.2. The three-electrode cell consists of an additional electrode called a reference electrode immersed in the electrolyte. The potential of the working electrode is measured or controlled against the reference electrode which has a known, stable, and reproducible potential [46]. The reference electrode used for all experiments in this thesis is a saturated calomel electrode. Therefore, unless otherwise stated, all electrode potentials are referenced against that of a saturated calomel electrode (SCE).

The cathode is often referred to as the working electrode (WE) in three-electrode electrodeposition systems like that depicted in Figure 3.2 because it supports the reaction of interest (metal deposition). The three-electrode setup can be used in galvanostatic and potentiostatic modes where the rate and driving force of the electrodeposition reaction can be controlled, respectively using a potentiostat [48]. The ohmic drop between the working and reference electrodes presents a source of error which can be minimised in results by careful design of lab-scale experimental conditions [47, 48] which is addressed in chapter 4.

## 3.2 Thermodynamics of electrodeposition

### 3.2.1 Introduction

The metal (M) deposition reaction from its ions ( $M^{n+}$ ) can be represented as:



Aqueous electrolytes contain other species (e.g.  $H_2O$ ,  $H^+$ ) besides  $M^{n+}$  which could also react at the cathode surface and, as a result, affect the deposition reaction. If there are multiple viable faradaic reactions in a system, they proceed in a hierarchical manner depending on their thermodynamic characteristics [48]. The electrochemical thermodynamics of the species of interest is usually considered against those of other reacting species in order to ascertain the extent to which the desired process and the

side reactions will overlap. This degree of overlap could have an impact on the metal reduction current efficiency [48].

Electrochemical thermodynamics is characterised by the equilibrium potential which is important in identifying what electrochemical reactions are feasible under certain applied conditions (concentration, pH, and temperature) and understanding electrochemical kinetics which is defined relative to the equilibrium potential [48]. The following subsections provide a condensed discussion on the analysis of equilibrium potentials of electrochemical reactions. More comprehensive discussions can be found in standard textbooks [46–48, 184, 185].

### 3.2.2 Equilibrium potential

An electrochemical reaction at equilibrium can be written as:



where Ox is the oxidising species and Red, the reducing species. Under equilibrium conditions, the rates of the forward (cathodic/reduction) and reverse (anodic/oxidation) reactions across the phase boundary of the electrode are equal, so there is no net charge transfer across the interface and no detectable current in the cell. Under these conditions, the electrode potential is defined as the equilibrium or reversible potential ( $U_{eq}$ ) of that particular reaction [46]. Depending on the process conditions, electrochemical equilibrium is a dynamic process that can occur slow or fast. The rate of the partial reactions at equilibrium is expressed as an exchange current density ( $j_0$ ). Typically, a low energy barrier across the electrode-electrolyte interface will result in a large exchange current density [46].

The equilibrium potential is directly determined by the thermodynamic activity (a) of the electroactive species in solution and is described by Nernst equation, which in the simplest case of an equilibrium between Ox and Red takes the form [46]:

$$U_{eq} = U^0 + \frac{RT}{nF} \ln\left(\frac{a_{Ox}}{a_{Red}}\right) \quad (3.3)$$

where  $U^0$  is the standard electrode potential defined for standard conditions (25 °C,

pressure = 1 atm and unit activity for all species involved), R is the gas constant (8.3145 J/mol K), T is the absolute temperature (K), F is Faraday's constant (96485 C/mol), and a is the activity of species. Data of standard electrode potentials are extensively published in literature [48, 183].

For an electrodeposition process, equilibrium is met when the rates of metal deposition and dissolution at the cathode surface are equal. The corresponding Nernst equation takes the form:

$$U_{eq} = U^0 + \frac{RT}{nF} \ln\left(\frac{a_{M^{n+}}}{a_M}\right) \quad (3.4)$$

Since the activity of any pure metal is one by convention (i.e.  $a_M=1$ ), equation 3.4 yields:

$$U_{eq} = U^0 + \frac{RT}{nF} \ln(a_{M^{n+}}) \quad (3.5)$$

Ion activity is often difficult to measure and it is more convenient to work in terms of the concentration, c, of the species. Consequently, modified versions of Equations 3.3 and 3.5 have been formulated and are shown in Equations 3.6 and 3.7, respectively [48]:

$$U_{eq} = U^0 + \frac{RT}{nF} \ln\left(\frac{c_{Ox}}{c_{Red}}\right) = U^0 + \frac{2.303RT}{nF} \log\left(\frac{c_{Ox}}{c_{Red}}\right) \quad (3.6)$$

$$U_{eq} = U^0 + \frac{RT}{nF} \ln(a_{M^{n+}}) = U^0 + \frac{2.303RT}{nF} \log(c_{M^{n+}}) \quad (3.7)$$

Equations 3.6 and 3.7 are based off the assumption that  $a = c$  which is appropriate for very dilute solutions (i.e. concentrations < 0.001 M) [183]. However, this assumption does not hold for higher concentrations similar to those used in nickel electroforming solutions (where  $c_{Ni^{2+}} > 1.55$  M). Nonetheless, it can be noted from Equation 3.3 that a large change in activity will result in a relatively small error in the potential because the activity appears only in the logarithm term [48]. For example, the reversible potential ( $U_{eq}$ ) for  $Ni^{2+}/Ni$  in 1 M  $Ni(SO_3NH_2)_2$  at 298 K assuming an activity of  $a_{Ni^{2+}} = 1$  (given that  $c_{Ni^{2+}} = 1$  M and  $U^0 = -0.485$  V) is calculated to be -0.485 V from equation 3.7 [183]. The corresponding  $U_{eq}$  for a case where  $a_{Ni^{2+}} = 0.05$  is -0.523 V giving an error of 7.3% for a relative activity change of 95%. Given the relatively small amount of error, Equations 3.6 and 3.7 could be employed to obtain estimates of the equilibrium potential.

It should be mentioned that the equilibrium potential of a certain reaction can only be determined experimentally in the absence of external current flow, when it is possible to disregard the impact of side reactions on the reaction of interest. Under real conditions, a macroscopic (mixed) equilibrium of multiple electrode reactions may exist [46]. The condition of a cell where the external current is zero is termed open circuit, and the associated potential is the Open Circuit Potential (OCP) which corresponds to a mixed equilibrium potential [47]. The relevant reactions involved and characteristics of the electrode surface, such as roughness, the presence of adsorbed species, or the existence of a film, all affect OCP value [46].

### 3.2.3 Thermodynamic considerations in nickel sulfamate electrolytes

Table 3.1 shows equilibrium potential formulations for some relevant reduction and oxidation reactions in nickel sulfamate electrolytes determined using Equations 3.6 and 3.7. It is noted from Table 3.1 that interfacial reactions are influenced by the concentration of metal ions, temperature, and pH of the solution. For better representation, a diagram of equilibrium potential against pH at 298 K is shown in Figure 3.3 which has been constructed based on the thermodynamic equilibrium of the reactions given in Table 3.1.

Table 3.1: Relevant electrochemical reactions and their equilibrium potentials in nickel sulfamate electrolytes. The last entry gives the chemical equilibria of nickel hydroxide precipitation and its corresponding pH. Calculations were based on  $U^0$  values found in [136]

Electrochemical process	Electrochemical reactions	Equilibrium potential (V vs SCE)
(1) Nickel deposition and dissolution	$Ni^{2+} + 2e^- \leftrightarrow Ni$	$U_{eq} = -0.485 + (9.923 \times 10^{-5}) * T * \log(c_{Ni^{2+}})$
(2) Proton reduction	$2H^+ + 2e^- \leftrightarrow H_2$	$U_{eq} = -0.245 - (1.985 \times 10^{-4}) * T * pH$
(3) Ni oxidation	$Ni + 2H_2O \leftrightarrow Ni(OH)_2 + 2H^+ + 2e^-$	$U_{eq} = -0.135 - (1.985 \times 10^{-4}) * T * pH$
(4) Water oxidation	$2H_2O \leftrightarrow O_2 + 4e^- + 4H^+$	$U_{eq} = +0.984 - (1.985 \times 10^{-4}) * T * pH$
(5) Nickel hydroxide precipitation	$Ni^{2+} + 2OH^- \leftrightarrow Ni(OH)_2$	$pH = 0.5 * (12.18 - \log(c_{Ni^{2+}}))$ at 298 K

The potential-pH diagram shown in Figure 3.3 indicates that in order to convert  $Ni^{2+}$  to metallic Ni under the ascertained conditions, an electrode potential more negative than -0.478 V and a pH less than 6 are required. At greater pH values,  $Ni^{2+}$

is converted to  $\text{Ni(OH)}_2$  which, in addition to reducing the concentration of free  $\text{Ni}^{2+}$ , could deposit with the nickel metal. For this reason, nickel electrodeposition is only performed from acidic electrolytes.

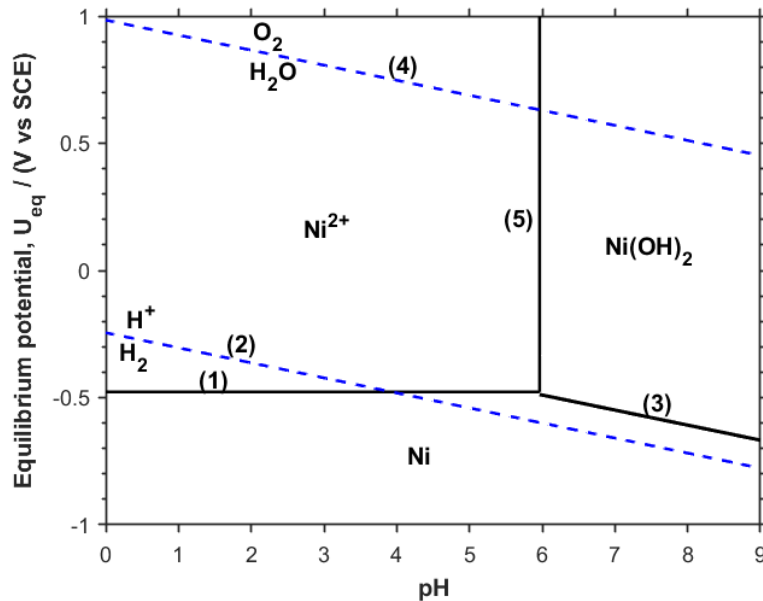


Figure 3.3: Potential-pH diagram for a pure aqueous  $\text{Ni}^{2+}$  system at 25 °C, 1 atm. and a total  $\text{Ni}^{2+}$  concentration of 1.785 M. The numbers in the figure correspond to the reactions given in Table 3.1

In the pH region between 0 and 6, hydrogen evolution occurs via the reduction of protons indicated by the blue dashed line (2) in Figure 3.3. The hydrogen evolution reaction (HER) is a parasitic reaction which not only reduces the amount of charge supplied for nickel electrodeposition but also negatively impacts deposit properties.

Since faradaic reactions during electrodeposition proceed in a hierarchical manner based on their equilibrium potential, i.e., reactions with the least negative equilibrium potential will occur first followed by a reaction with a more negative  $U_{eq}$  [48]. Figure 3.3 indicates that the equilibrium potential of proton reduction is less negative compared to that of  $\text{Ni}^{2+}$  reduction in the pH range between 0 and 4 which suggests that proton reduction will commence prior to nickel electrodeposition. The degree of  $U_{eq}$  separation between the two processes will affect the proportion of charge lost to HER prior to the commencement of nickel electrodeposition. For example, a higher proportion of charge could be lost to hydrogen evolution in a pure nickel electrolyte at



pH 2 than at pH 4 due to the greater degree of potential separation between HER and nickel electrodeposition. For this reason, nickel electrodeposition is often performed at a pH of 3-4 to mitigate the impact of hydrogen evolution and avoid  $\text{Ni(OH)}_2$  precipitation. In this selected pH range, proton reduction occurs simultaneously with nickel electrodeposition. To resolve this issue, boric acid is added to the nickel electrolyte which reduces the relative rate of hydrogen evolution.

Figure 3.3 also demonstrates that the equilibrium potentials for nickel dissolution and water oxidation are sufficiently far apart at the pH range of 3 to 4 such that nickel anodes can dissolve without the interference of the oxygen evolution reaction. In summary, this section has shown the importance of thermodynamics in selecting appropriate conditions for nickel electroforming.

### 3.2.4 Current efficiency

As mentioned, undesired reactions (such as HER) occur concurrently with nickel electrodeposition, as was covered in the section above. Consequently, the total current supplied for electrodeposition is partially consumed by these side processes. The fraction of the total current that drives the desired reaction (nickel electrodeposition) is defined as the current efficiency (CE) and is given by [47]:

$$\text{CE}(\%) = \frac{\text{current of desired reaction}}{\text{total current}} \times 100 = \frac{\text{measured deposit mass}(w)}{\text{theoretical mass}(m)} \times 100 \quad (3.8)$$

Experimentally, the current efficiency can be determined from the ratio of the measured deposit mass,  $w$ , against the theoretical mass ( $m$ ) calculated using Faraday's Law (Eq. 3.9) [186]:

$$m = \frac{IMt}{nF} = \frac{QM}{nF} \quad (3.9)$$

where  $m$  is the theoretical deposited mass (g),  $Q$  the amount of charge passed (C),  $I$  the applied current (A),  $t$  the duration of electrolysis (s),  $n$  the number of electrons involved in the reaction,  $F$  the Faraday's Constant ( $96,485 \text{ C mol}^{-1}$ ),  $CE$  the current

efficiency of the process (CE), and  $M$  the atomic weight of the metal ( $\text{g mol}^{-1}$ ). For predictive calculations using Equation 3.9, the current efficiency is taken to be 1 based on the assumption that the total charge transferred at the electrode surface is solely consumed in the desired reaction. However, the mass plated in nickel electrodeposition experiments has been found to be less than the mass predicted from Faraday's law indicating a CE less than 1 [68].

To calculate the current efficiency for a certain current density,  $j$  ( $\text{I/A}$ ), Equations 3.8 and 3.9 can be combined to give Equation 3.10.

$$\text{current efficiency (\%)} = \frac{wnF}{jAtM} \times 100 \quad (3.10)$$

In electroforming, a current efficiency of 100% is required to improve dimensional fidelity, provide an efficient and reliable process, and produce deposits with desirable qualities. Furthermore, at a given current density, an increased current efficiency means that a greater amount of the charge passed is used in carrying out the desired reaction. An important aspect of electrodeposition is that the amount of charge utilised in carrying out the desired reaction is directly related to the mass plated and hence, the thickness of the deposited layer. The expected (theoretical) thickness of the deposited layer could be related to the expected mass plated as follows [47]:

$$h = \frac{m}{\rho A} = \frac{MQ}{\rho AnF} \quad (3.11)$$

where  $h$  is the expected thickness of the deposit ( $\text{cm}$ ),  $\rho$  the bulk density of the metal ( $\text{g cm}^{-3}$ ), and  $A$  the area of the electrode ( $\text{cm}^2$ ). If a greater proportion of the charge passed is used to carry out the desired reaction (i.e current efficiency is high), less time is needed to deposit the desired thickness of nickel which enhances production throughput.

## 3.3 Electrochemical kinetics

### 3.3.1 Introduction

Electrochemical thermodynamics quantifies process energetics and provides information regarding possible overlaps between reactions at equilibrium. However, electroforming is carried out very far from equilibrium where the rates of charge and mass transfers are important. Electrochemical kinetics describe the response of each reaction's rate to changes in the electrode potential from equilibrium. For example, if we consider the proton and nickel ion reduction reactions at pH 3 shown in Figure 3.3, the rate of the former reaction may change much more slowly compared to that of the nickel ion reduction reaction in response to a certain change in the electrode potential from equilibrium. Hence, a nickel ion reduction current efficiency close to 100% could still be achieved despite thermodynamic indications that  $H^+$  reduction commences prior to nickel electrodeposition. Reaction kinetics are influenced by reactant concentrations in the charge transfer reaction and conditions of the electrode surface and electrolyte.

The paragraph above introduces two important points: (i) a change in electrode potential from equilibrium is required for a net reaction to occur, and (ii) this change controls the rate of the overall reaction. These points are explored in the forthcoming sections.

### 3.3.2 Departure from equilibrium: overpotential

The electrodeposition reaction is not simply a charge transfer reaction but involves a number of complex sequential steps outlined below [187]:

1. Diffusion of ions in solution to the electrode surface
2. Chemical reactions preceding charge transfer, which may be homogeneous reactions in the solution or heterogeneous reactions at the surface e.g. ion dehydration or ligand dissociation

3. Charge transfer at the cathode surface (i.e reduction of ions to form adsorbed atoms (ad-atom)).
4. Formation and growth of metal crystals from ad-atoms (crystallisation)

These four processes possess activation energies which need to be overcome for a net deposition reaction to occur. This is achieved by applying a high current or potential sufficiently greater in magnitude than that of the equilibrium potential [48]. It is noted that the potential of an electrode through which current flows,  $U(I)$ , differs from the equilibrium potential,  $U_{eq}$  [188]. The departure of the electrode potential from the equilibrium value caused by the passage of a constant current is called polarization. Overpotential ( $\eta$ ) measures the extent of electrode polarisation and is considered the difference between these potentials as given in Equation 3.12 [188, 189].

$$\text{Overpotential, } \eta = U(I) - U_{eq} \quad (3.12)$$

The sign of  $\eta$  affects the direction of the electrode reaction. Making the potential of an electrode more positive than the equilibrium potential ( $+\eta$ ) lowers the energy of electrons in the electrode making it easier for molecules or atoms to lose electrons to the electrode. Thus, positive overpotentials promote oxidation reactions and the flow of an anodic current. Negative overpotentials increase the energy of electrons in the electrode and promote the loss of electrons from the electrode surface to a chemical species in solution (reduction) prompting the flow of a cathodic current [47]. This is depicted in Figure 3.4.

As mentioned, the overpotential,  $\eta$ , is required to overcome the hindrance of the overall electrode reaction which is usually composed of four processes. Thus, the measured value of overpotential can be divided into several parts [183]:

$$\eta = \eta_{ct} + \eta_d + \eta_r + \eta_c \quad (3.13)$$

where  $\eta_{ct}$ ,  $\eta_d$ ,  $\eta_r$ , and  $\eta_c$  are the overpotentials associated with charge transfer, diffusion, chemical reactions, and crystallisation, respectively. The rate of the deposition reaction is largely dependent on two processes: diffusion and charge transfer, and is

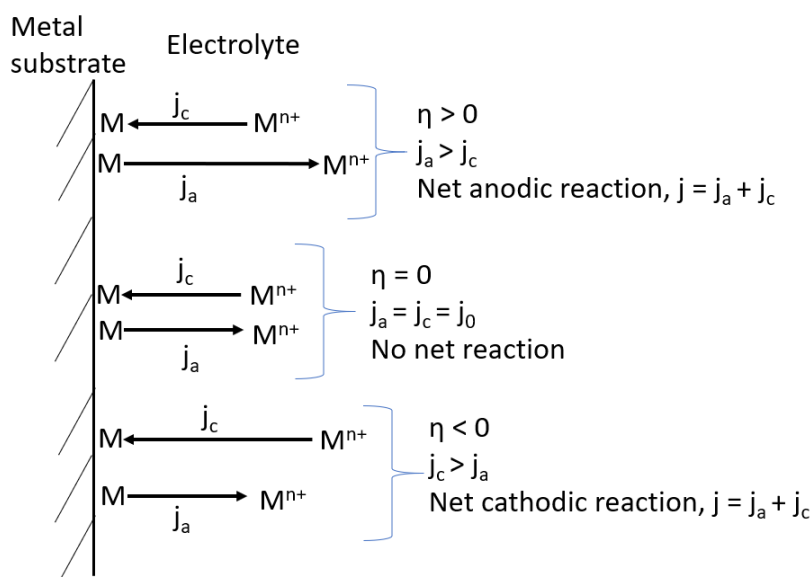


Figure 3.4: Metal/metal ion electrode showing anodic and cathodic currents at equilibrium and during application of an overpotential (subscript a=anodic and c=cathodic). Adapted from [183]

determined by the rate of the slower process. For example, an electrochemical reaction is considered to be kinetically controlled when the rate of charge transfer is slow compared to that of mass transfer. Under these circumstances,  $\eta \approx \eta_{ct}$ . Likewise for a diffusion controlled system,  $\eta \approx \eta_d$ . For a system controlled by both charge transfer and diffusion,  $\eta \approx \eta_{ct} + \eta_d$ .

### 3.3.3 Charge transfer kinetics

Electrochemical reactions involve the transfer of charge across the electric double layer which could occur via one of two ways: electron transfer or ion transfer which are depicted in Figure 3.5. Both processes involve the transfer of electroactive species in the form of complexes or hydrated ions from bulk solution to the outer Helmholtz plane (OHP) of the electric double layer. In the case of electron transfer, an electron is directly transferred from the electrode to the ion at the OHP. Subsequently, the reduced ion is transported from the electrode surface to the bulk solution [48].

For ion transfer processes, the ion at the OHP moves across the double layer

so that it is adsorbed on the electrode surface as an ad-ion during which it may lose its ligand or hydrated sheath. The ad-ion is then neutralised by an electron to form an ad-atom which is then incorporated in a growing lattice. Metal deposition and dissolution reactions are typically ion transfer processes [48].

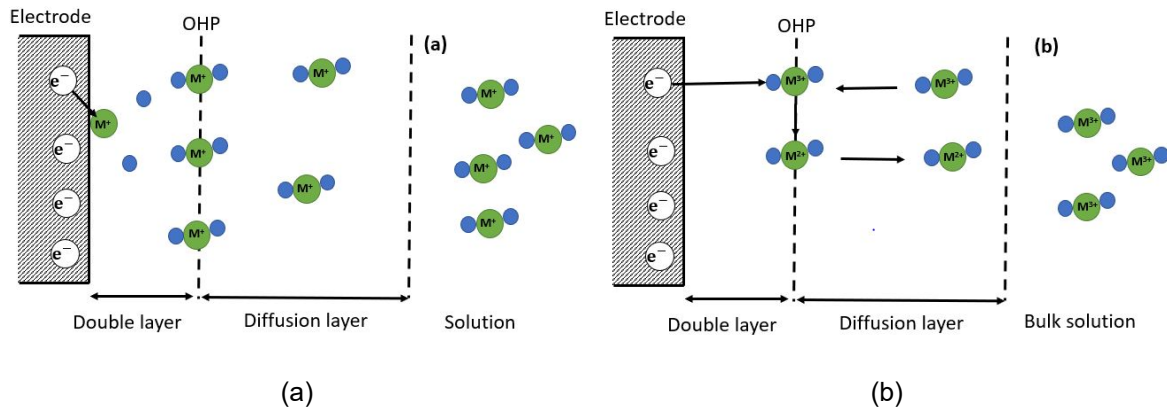


Figure 3.5: Schematic diagram showing (a) ion transfer and (b) electron transfer processes. Adapted from [48]

Equations that describe the response of the rate of reaction (characterised by the current density,  $j$ ) to the overpotential for ion transfer and electron transfer reactions are given in Equations 3.14 and 3.15, respectively:

$$\text{ion - transfer equation : } j = j_0 \left( \exp \left( \frac{\beta n F \eta}{RT} \right) - \exp \left( \frac{-(1 - \beta) n F \eta}{RT} \right) \right) \quad (3.14)$$

$$\text{Butler - Volmer equation : } j = j_0 \left( \exp \left( \frac{\beta F \eta}{RT} \right) - \exp \left( \frac{-(1 - \beta) F \eta}{RT} \right) \right) \quad (3.15)$$

where  $j$  is the current density,  $j_0$  the exchange current density, and  $\beta$  the symmetry factor for the anodic reaction. It should be mentioned that both equations are only applicable for kinetically controlled reactions where mass transport (diffusion) control is negligible.

The derivation of Equation 3.14 is given in Appendix A. Notably, Equation 3.14 is similar to the Butler-Volmer equation developed for electron transfer except that the latter does not include the charge transfer valency,  $n$ . This arises from differences between the underlying assumptions of Equations 3.14 and 3.15 which have been summarised in Table 3.2 [48]. Although, it has been assumed in Equation 3.14 that multivalent ions such as  $\text{Ni}^{2+}$  can travel the electrode double layer in a single step,

Table 3.2: Differences between the underlying principles of the ion transfer equation and the Butler-Volmer equation for electron transfer [48].

<b>Ion-transfer equation</b>	<b>Butler-Volmer equation (electron transfer)</b>
Multiple elementary charge units (e.g. divalent ion) can be transferred at a time	Single electron transfer at a time
$\beta$ lies between 0 and 1	$\beta$ is assumed to be 0.5

this is high unlikely as it will require a complete loss of its hydration sheath in a single step which is energetically unfavourable [48]. Therefore, equation 3.14 should be used cautiously in the determination of nickel electrodeposition kinetics.

### 3.3.4 Charge transfer kinetics of multistep processes

As noted earlier, it is more energetically favourable for multivalent ion transfer reactions to occur in a series of discrete steps than in a single step. The current-potential behaviour for a multistep electrode reaction scheme has been derived by Bockris and Nagy [190] which is given in Equation 3.16. For this derivation, a pseudo-equilibrium approach was used where it is assumed that one step in the sequence is slower than the rest and it alone controls the rate of the reaction while the other steps are in equilibrium. This slow step is called the rate determining step (rds).

$$j = j_0 \left( \exp \left( \frac{\alpha_a F \eta}{RT} \right) - \exp \left( \frac{-\alpha_c F \eta}{RT} \right) \right) \quad (3.16)$$

where  $\alpha_c$  and  $\alpha_a$  are transfer coefficients for the cathodic and anodic reactions, respectively, given by:

$$\alpha_c = \frac{s}{v} + r(1 - \beta) \quad (3.17)$$

and

$$\alpha_a = \frac{n - s}{v} - r(1 - \beta) \quad (3.18)$$

where  $r$  is the number of electrons exchanged in the rds,  $s$  the number of electrons exchanged before the rds,  $n$  the total number of electrons exchanged in the overall reaction,  $\beta$  the symmetry factor, and  $v$  the stoichiometric coefficient which is the number

of times the rds has to occur for the overall electrode reaction to occur once.  $\alpha_c + \alpha_a = n/v$  holds true for Equation 3.16. While the symmetry factor is only concerned with the fraction of the potential imparted to the system that changes the activation energy for single step reactions, the transfer coefficient includes other parameters relating to the mechanism of multistep reactions, for example the number of electrons which precede the rds [190].

### 3.3.5 Charge transfer kinetics: Tafel equation

Nickel deposition and dissolution reactions are typically carried out at high overpotentials,  $\eta$ . Therefore, equation 3.16 can be further simplified for high negative and positive overpotentials. For metal deposition processes which involve large negative overpotentials, i.e.,  $\eta < 0$  and  $\eta \gg \frac{RT}{F}$ , Equation 3.16 becomes:

$$j_c = j_0 \exp\left(\frac{-\alpha_c F \eta}{RT}\right) \quad (3.19)$$

and

$$\log|j_c| = \log j_0 - \frac{\alpha_c F}{2.303 RT} \eta \quad (3.20)$$

which can be rearranged for  $\eta$  as follows:

$$\eta = \frac{2.303 RT}{\alpha_c F} \log j_0 - \frac{2.303 RT}{\alpha_c F} \log|j_c| \quad (3.21)$$

Similarly, for large positive overpotentials, i.e.,  $\eta > 0$  and  $\eta \ll \frac{RT}{F}$ , Equation 3.16 becomes:

$$j_a = j_0 \exp\left(\frac{\alpha_a F \eta}{RT}\right) \quad (3.22)$$

and

$$\log|j_a| = \log j_0 + \frac{\alpha_a F}{2.303 RT} \eta \quad (3.23)$$

which can be rearranged for  $\eta$  as follows:

$$\eta = -\frac{2.303 RT}{\alpha_a F} \log j_0 + \frac{2.303 RT}{\alpha_a F} \log|j_a| \quad (3.24)$$

Both equations 3.21 and 3.24 express a linearised Tafel form:

$$\eta = a + b \log|j| \quad (3.25)$$

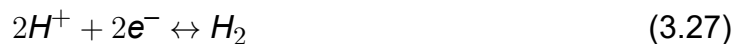


where  $b$  represents the Tafel slope which is equivalent to  $-\frac{2.303RT}{\alpha_c F}$  and  $\frac{2.303RT}{\alpha_a F}$  for cathodic and anodic processes, respectively. The Tafel slope is usually expressed in mV per decade to emphasise the use of a decadic scale and not a natural log scale [48].

As mentioned, the Tafel equation is only valid for conditions where charge transfer is rate limiting, i.e the surface concentration of the reacting species remains close to its bulk concentration and its mass transport can be neglected. Under these conditions, a linear Tafel plot is obtained. Sulfamate electrolytes employed for nickel electroforming contain a high concentration of  $Ni^{2+}$  and are operated at very low current densities between 5-50 mA/cm<sup>-2</sup> where it is expected that electrodeposition is kinetically controlled.

### 3.3.6 Application of kinetics to understanding reaction mechanisms in nickel plating electrolytes

Now that the steady state current-potential relationships for anodic and cathodic reactions have been developed, the purpose for this section is to examine its application to elucidating reaction mechanisms in nickel plating electrolytes. The overall electrode reactions for nickel ion and proton reduction could be written as:



Nickel electrodeposition kinetics was analysed by Epelboin and Wiart [62] in a Watts bath. Firstly, they found different Tafel slopes at low (118 mV/dec) and high (43 mV/dec) overpotentials. Secondly, an inductive character was identified at low frequencies and low overpotentials from impedance measurements in  $NiSO_4$  and  $NiCl_2$  media which was attributed to an adsorption process by nickel species. These findings substantiated the non-integer reaction orders with respect to  $Ni^{2+}$  measured by other researchers [63, 115] in sulfate (0.875) and chloride (0.5-1.1) electrolytes. These collective observations discounted a single step mechanism as shown in Equation 3.26

and pointed to mechanisms comprised of a series of charge transfer reactions, with some related to adsorption processes.

Consequently, Equation 3.16 proposed by Bockris and Nagy [190] has been generally accepted for nickel electrodeposition. According to the authors, a reaction mechanism is defined by the rate determining step which in turn define the kinetic parameters. Hence, values of the Tafel slope could serve as a diagnostic criteria of which step occurs more slowly. Table 3.3 presents calculated values of  $b_c$  and  $b_a$  (assuming  $\beta=0.5$ ,  $\nu=1$ ,  $T = 298$  K) for different rate limiting steps of possible reaction schemes in nickel plating electrolytes.

Table 3.3: Calculated cathodic and anodic Tafel slopes,  $b_c$  and  $b_a$  (mV/dec) for multistep electrode reactions in nickel plating electrolytes (assuming  $\beta=0.5$ ,  $\nu=1$ ,  $T = 298$  K).

Mechanism	Reaction steps	rate determining step		
		(1)	(2)	(3)
Deposition and dissolution of uncomplexed nickel	(1) $\text{Ni}^{2+} + \text{e}^- \leftrightarrow \text{Ni}_{ads}$	$b_c = -118$ mV/dec	$b_c = -39$ mV/dec	-
	(2) $\text{Ni}_{ads} + \text{e}^- \leftrightarrow \text{Ni}$	$b_a = 39$ mV/dec	$b_a = 118$ mV/dec	-
Deposition and dissolution of complexed nickel	(1) $\text{Ni}^{2+} + \text{X}^- \leftrightarrow \text{NiX}^+$			
	(2) $\text{NiX}^+ + \text{e}^- \leftrightarrow \text{NiX}_{ads}$	$b_c = \infty$ mV/dec	$b_c = -118$ mV/dec	$b_c = -39$ mV/dec
	(3) $\text{NiX}_{ads} + \text{e}^- \leftrightarrow \text{Ni} + \text{X}^-$ where $\text{X}=\text{OH}$ or $\text{Cl}$	$b_a = 30$ mV/dec	$b_a = 39$ mV/dec	$b_a = 118$ mV/dec
Hydrogen evolution reaction (Volmer-Heyrovsky)	(1) $\text{M} + \text{H}^+ + \text{e}^- \leftrightarrow \text{M-H}_{ads}$	$b_c = -118$ mV/dec	$b_c = -39$ mV/dec	-
	(2) $\text{H}^+ + \text{M-H}_{ads} + \text{e}^- \leftrightarrow \text{M} + \text{H}_2$	$b_a = 39$ mV/dec	$b_a = 118$ mV/dec	-
Hydrogen evolution reaction (Volmer-Tafel)	(1) $\text{M} + \text{H}^+ + \text{e}^- \leftrightarrow \text{M-H}_{ads}$	$b_c = -118$ mV/dec	$b_c = -30$ mV/dec	-
	(2) $\text{M-H}_{ads} + \text{M-H}_{ads} \leftrightarrow \text{M} + \text{H}_2$	$b_a = 39$ mV/dec	$b_a = \infty$ mV/dec	-

From the calculations in Table 3.3, it can be seen that different mechanisms, such as the deposition of uncomplexed and complexed nickel, can generate the same Tafel slope (118 mV/dec). Therefore, experimental Tafel slopes cannot be solely used as a diagnostic for a specific mechanism but could prove helpful for the elucidation of the mechanism. For example, a Tafel slope value of 118 mV/dec measured for an electrochemical reaction involving a multivalent ion usually indicates a multistep mechanism where the first charge transfer step is rate-limiting. Additional information such as the reaction order with respect to participating species ( $\text{OH}^-$  and  $\text{Cl}^-$ ) is required to identify the mechanism. AC impedance, steady state, and transient electrochemical

methods are typically used to provide additional mechanistic information about nickel deposition and dissolution. These studies have been explored in chapter 2.

It should be mentioned that there are certain limitations with the simplified kinetic approach proposed by Bockris and Nagy [190] because there is not always a clear rds and because the authors' arguments also assume that the electrode surface is relatively free of adsorbed species (i.e. fractional coverages ( $\theta$ ) are less than 0.1). So, deviations from the theoretically Tafel slopes in Table 3.3 are likely. Tafel slopes for higher coverages of  $\text{Ni}_{ads}$  ( $\theta > 0.2$ ) have been calculated by Saraby and Fleischmann [63]; these values were found to be different from those for lower coverages but still no greater than 120 mV/dec.

Tafel slopes of 80 mV/dec to 330 mV/dec measured in nickel electrochemical systems (sulfate and sulfamate) [61, 68, 118, 120, 122] lend some support to the mechanisms involving the multistep deposition of nickel shown in Table 3.3. Despite the similar Tafel behaviour of nickel deposition from  $\text{Ni}_{ads}$  and  $\text{NiX}_{ads}$ , researchers [63, 115] have demonstrated reaction orders of 0.8-1.2 for  $\text{OH}^-$  and  $\text{Cl}^-$  which suggested that these anions participated in charge transfer. Electrochemical impedance spectra obtained in 1.22 M  $\text{NiCl}_2$  indicated an inductive loop below 6 mHz which was absent in the spectra measured in  $\text{NiSO}_4$  solution or Watts-type electrolytes (where the  $\text{Cl}^-$  concentration was an order of magnitude lower). These observations were rationalised to indicate the presence of a chloride-containing nickel adsorbate ( $\text{NiCl}_{ads}$ ) [62, 82, 83]. Researchers have thus come to the consensus that nickel electrodeposition proceeds from a complex,  $\text{NiX}_{ads}$ .

Cathodic Tafel slopes significantly greater than 118 mV/dec have been measured during nickel electrodeposition by some researchers [61, 122] which could be rationalised in terms of a low transfer coefficient (i.e.  $\alpha_c < 0.5$ ) which can be observed when the symmetry factor for the cathodic process ( $\beta_c = (1-\beta)$ ) is less than 0.5. Usually, it is assumed that  $\beta_c$  is equivalent to 0.5 for electron transfer processes but values less than this could be encountered in ion transfer processes. Alternatively, high values of the Tafel slope could arise due to the presence of an oxide film layer [191] or adsorbed species [192] on the electrode surface. It has been found that kinetic parameters ( $j_0$  or Tafel slopes), are functions of the electrode material when an adsorbed intermedi-

ate is involved as has been observed for the hydrogen evolution reaction from proton reduction [193]. However, the effect of electrode materials on nickel electrodeposition kinetics has received limited attention from researchers although literature research indicates different Tafel slopes measured under similar conditions on different substrates [61, 68, 194].

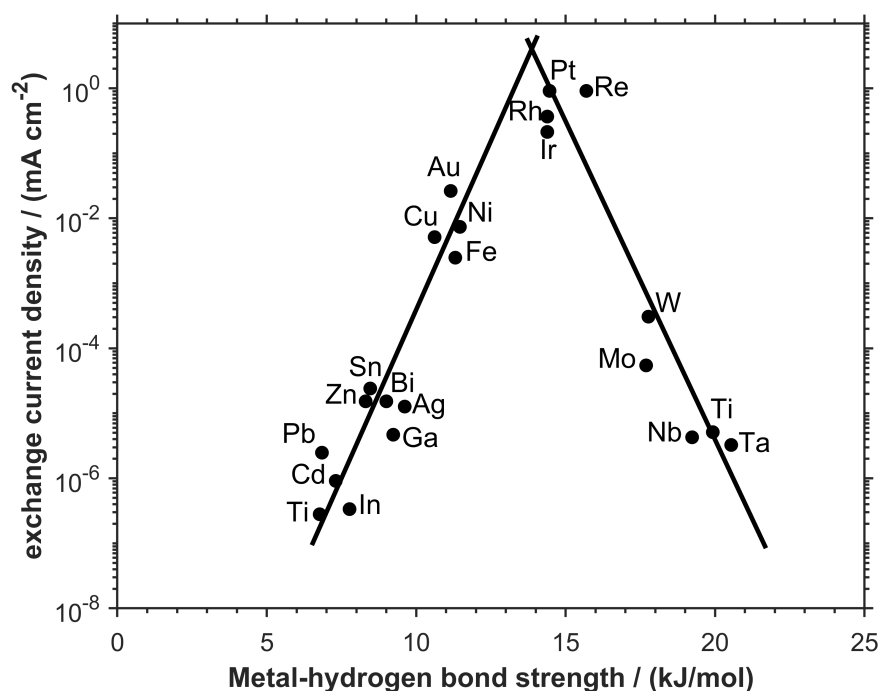


Figure 3.6: Dependence of exchange current density for hydrogen evolution reaction on the strength of the metal-hydrogen bond formed in the electrode reaction. Adapted from [193]

If we consider the HER mechanisms in Table 3.3, it is shown that the adsorbed hydrogen atom plays a key role in the mechanism and kinetics. The electrode material (M) is important in determining the properties of the surface bond M-H. Hence, selecting a cathode material with a low free energy of adsorption will favour the formation of  $H_{ads}$  but have the opposite effect on the desorption steps in the overall process. This is observed from Figure 3.6 which shows a "volcano plot" of exchange current density for HER vs. the free energy of H adsorption for a series of cathodes [193]. Experimental studies of hydrogen evolution at different substrates have shown a wide range of exchange current densities as well as different Tafel slopes [193, 195, 196]. Hence, the main point to be emphasised is that the choice of electrode material could influence the

exchange current density and Tafel slope and could also lead to different conclusions for nickel electrodeposition kinetics performed on different substrates.

### 3.3.7 Overall importance of kinetics in electroforming

In summary, electrochemical kinetics provide a quantitative measurement of the rate of reactions (in terms of exchange current density) as well as insight into the dependence of these rates on variables such as concentration and temperature. Tafel slopes evaluated from kinetic measurements could corroborate or contradict postulated reaction mechanisms and support mathematical modelling of the electroforming process.

It is essential to study the kinetics of nickel electroreduction in sulfamate systems used for electroforming because charge transfer kinetics affect the quality of the electroform. Such information is vital for assessing the secondary current distribution, which characterises the thickness and homogeneity of an electrodeposited coating as well as the cathode's shape evolution during electroforming [197]. The current distribution is a function ( $F(x)$ ) of the relative local current density defined by a ratio of the current density at any point  $x$  on the electrode surface and the average current density across the metal-solution interface as given in Equation 3.28 [48].

$$F(x) = \frac{j_x}{j} \quad (3.28)$$

In practice, the current distribution may be identified by a thickness variation over the surface of the cathode. Current tends to concentrate at edges and protrusions leading to thicker deposits at these points [183], as shown in Figure 3.7.

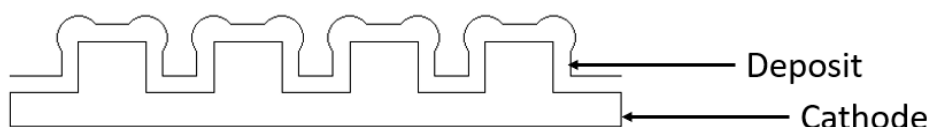


Figure 3.7: Schematic showing the effect of surface features on the thickness distribution. Thicker deposits are obtained at the edges due to relatively higher currents at these points.

The current distribution during electrodeposition is dependent on the cell geometry (primary current distribution), charge transfer kinetics (secondary current distribution), and mass transfer (tertiary current distribution) [48, 197]. The prevailing type of current distribution is dictated by the applied current density. Applied current densities in nickel electroforming are usually about 10% of that dictated by mass transfer limitations and it could be expected that the deposition reaction is mainly influenced by the charge transfer reaction [122]. Additionally, the electroforming electrolyte typically contains a high concentration of nickel sulfamate, so the influence of mass transport could be neglected. Therefore, secondary current distribution could be assumed to prevail in the system. Under such circumstances, the Wagner number ( $Wa$ ) is a critical parameter used for estimating the uniformity of the deposit and is given by:

$$Wa = \frac{R_p}{R_\Omega} = \frac{\kappa}{L} \cdot \frac{\delta\eta}{\delta j} = \frac{\kappa}{L} \cdot \frac{b}{j} = \frac{\kappa}{L} \frac{RT}{\alpha F j} \quad (3.29)$$

where  $R_p$  is the polarisation resistance ( $\frac{\delta\eta}{\delta j}$ ),  $R_\Omega$  the ohmic resistance,  $\kappa$  the specific conductivity of the electrolyte,  $j$  the current density,  $b$  the Tafel slope ( $\frac{RT}{\alpha F}$ ) and  $L$  the characteristic length of the system. The Wagner number should be high in order to achieve a uniform deposit thickness. A Wagner number much lower than 1.0 would likely produce poor uniformity in deposits.

$Wa \gg 1$  for uniform thickness distribution

$Wa \ll 1$  for non-uniform thickness distribution

$Wa \rightarrow 0$  for non-uniform thickness distribution where ohmic losses dominate

$Wa \rightarrow \infty$  where mass transport control dominates

Secondary current distribution is required for the design of accurate models for the simulation of an electroforming system which could prove to be a significant asset in efforts to optimise the process [122, 194]. Up till now, the optimisation of electroforming has mostly relied on empirical knowledge which has constraint transformation into high volume manufacturing [24, 194]. In the advent of a new industrial revolution, there is increased demand for faster time-to-markets and a digital-first approach to the design of increasingly complex final parts, placing pressure on businesses to deliver and remain

competitive. Reliable kinetic data obtained in electroforming systems is required for the design of modelling tools that will facilitate this approach [194].

As already mentioned, a deeper analysis of the role of chemical constituents in the sulfamate system may be achieved by assessing the Tafel slopes and exchange current densities in solutions with different concentrations of the constituents to reflect how much the concentration of an individual reactant either accelerates or slows down the reaction or changes the reaction mechanism. By testing and identifying how variables affect the rate of a reaction, nickel electrodeposition could be optimized and side reactions reduced. Such information could also help to establish a systematic correlation between the electrolyte characteristics and deposit properties.

### **3.4 Mass transport during electrodeposition**

Sulfamate systems used for electroforming often contain high concentrations of  $\text{Ni}^{2+}$  where transport limitations of these ions to the electrode surface could be neglected at the low current densities employed [122]. In this thesis, studies were conducted to investigate the effect of boric acid on the initial stages of nickel electrodeposition and hydrogen evolution reaction. For these investigations, a dilute electrolyte (ten-fold dilution factor) was employed so that potentials for nickel electrodeposition and HER could be distinguishable [198] with the help of an EQCM. Under these conditions, it is expected that the rate of adsorption of the nickel ion intermediate will be limited by its diffusion to the electrode surface. Therefore, for better understanding of these experiments, this section provides a brief discussion of nickel electrodeposition under diffusional transport control.

At equilibrium, the concentration of reactant,  $\text{Ni}^{2+}$  in the solution at the electrode OHP is equivalent to its bulk concentration. When a current is applied for nickel electrodeposition to occur,  $\text{Ni}^{2+}$  is consumed at the electrode and its concentration at the interface decreases developing a concentration gradient ( $dc_{\text{Ni}^{2+}}/dx$  where  $x$ =distance from the electrode OHP) in the solution layer at the OHP. This concentration gradient will initiate the diffusional transport of  $\text{Ni}^{2+}$  towards the electrode surface.

As electrodeposition proceeds, there is progressive depletion of  $Ni^{2+}$  at the OHP of the electrode. This decrease in  $Ni^{2+}$  concentration extends farther away into solution increasing the depletion layer thickness. If the rate of consumption of  $Ni^{2+}$  is sufficiently high compared to the rate at which  $Ni^{2+}$  is replenished by diffusion, the concentration of  $Ni^{2+}$  at the OHP will drop to zero. At this point, the concentration gradient assumes a maximum value. Thereafter, the depletion layer continues to increase, thereby decreasing the concentration gradient and flux of the species [48].

The flux ( $N$ ) of a reacting species,  $i$ , from the bulk to electrode surface is a combination of diffusion, migration, and convection.

$$N_i = N_{diffusion} + N_{migration} + N_{convection} \quad (3.30)$$

Migration arises from the transport of charged species due to the electric field. The supporting (non-reacting) electrolyte provides the major contribution towards the migration flux. In this case, the flux of the reacting species is mainly due to diffusion and convection which are its responses to concentration gradients and bulk solution stirring, respectively [48].

In quiescent solutions (such as those employed for EQCM experiments) where there is no practical means of applying convection, diffusion is considered as the only means of transport. Therefore, since the flux of  $Ni^{2+}$  is given by Fick's law,

$$N_{diffusion} = D_{Ni^{2+}} \left( \frac{dc_{Ni^{2+}}}{dx} \right) \quad (3.31)$$

the rate of the reaction at the surface is given by:

$$j = nFN_{diffusion} = -nFD_{Ni^{2+}} \left( \frac{dc_{Ni^{2+}}}{dx} \right) \quad (3.32)$$

where  $D_{Ni^{2+}}$  is the ionic diffusion coefficient,  $c$  the concentration of reacting species, and  $x$  the distance from the electrode. The concentration gradient,  $dc_{Ni^{2+}}/dx$  is approximated using the Nernst diffusion-layer model which is given by:

$$j = -nFD_{Ni^{2+}} \frac{dc_{Ni^{2+}}}{dx} \approx -nFD_{Ni^{2+}} \frac{c_{Ni^{2+},x=bulk} - c_{Ni^{2+},x=OHP}}{\delta} \quad (3.33)$$

This model assumes that the electrolyte has a bulk concentration  $c_{Ni^{2+},x=bulk}$  up to a distance  $\delta$  from the electrode OHP and then falls off linearly to the concentration



at the OHP,  $c_{Ni^{2+},x=OHP}$ . The Nernst diffusion-layer model is illustrated in Figure 3.8 [183]. Beyond  $\delta$ , stirring by natural convection which arises due to density gradients (depletion of reactants at the surface may reduce the local density of the solution) is assumed to be dominant maintaining the concentration at a value equivalent to that of the bulk solution. This limits variations in concentration to the depletion layer of thickness,  $\delta$ . Reacting species must diffuse through this depletion layer to reach the electrode surface [183].

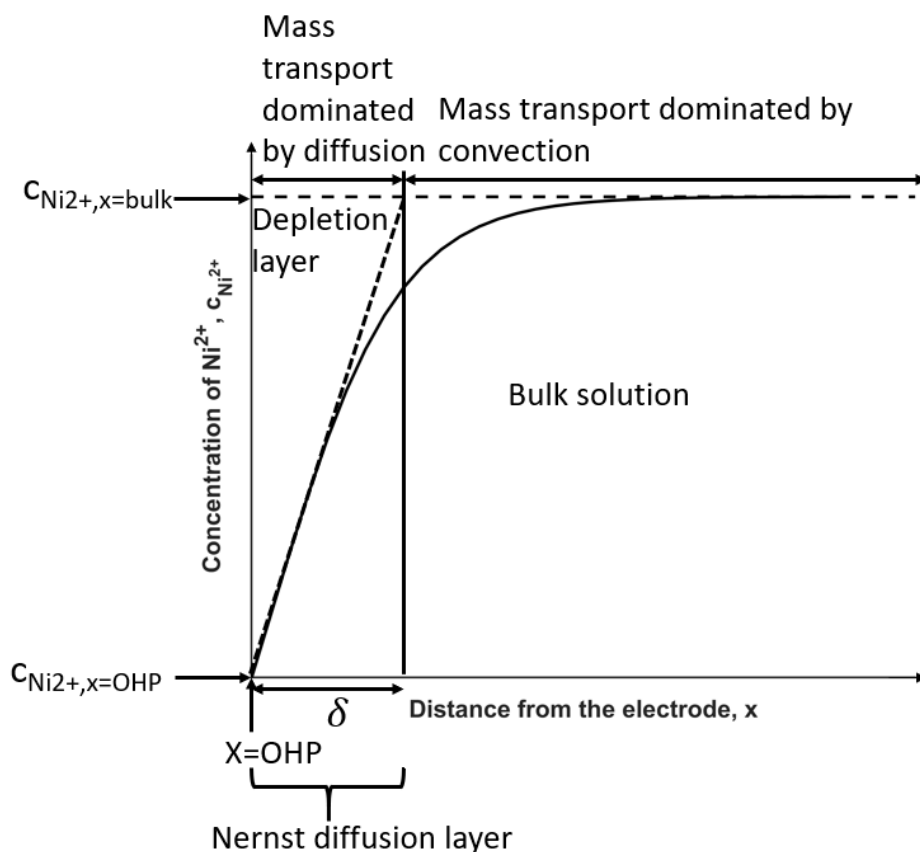


Figure 3.8: Schematic showing the reactant ( $Ni^{2+}$ ) concentration profile which describes the concentration distribution of  $Ni^{2+}$  around the electrode surface where the bulk concentration drops to a lower value at the OHP. The thickness of the depletion layer is approximated using the Nernst diffusion layer thickness ( $\delta$ ). Adapted from [183].

The maximum value of the concentration gradient and hence the current density is achieved when  $c_{Ni^{2+},x=OHP} = 0$ . The value of current density under these conditions is defined as the limiting current density  $j_{lim}$ , where

$$j_{lim} = \frac{nFD_{Ni^{2+}}c_{Ni^{2+},x=bulk}}{\delta} \quad (3.34)$$

Under limiting current conditions,  $Ni^{2+}$  is reduced as soon as it arrives at the surface so electrodeposition is occurring at the maximum rate possible in the system. At this point, electrodeposition is solely limited by mass transport of  $Ni^{2+}$  to the electrode [183].

If an external current greater than the limiting current of a reacting species is applied to the cathode, the potential of the cathode will change until some other species in solution can be reduced. It is often not advisable to operate at conditions close to the limiting current density as mass transport control leads to roughened, dendritic, or powdery deposits which are unsatisfactory. Therefore, electroforming is typically performed at only a fraction (<10 %) of the limiting current density for  $Ni^{2+}$  reduction [122].

In the absence of bulk stirring, the value of  $\delta$  in aqueous solutions is  $\approx 0.03$ - $0.05$  cm, depending on the viscosity and density of the solution, electrode geometry, and electrochemical conditions. Agitation of the electrolyte increases the supply of fresh reactant from the bulk to the electrode, thereby decreasing the depletion layer (down to  $0.001$  cm) and reducing the distance through which  $Ni^{2+}$  ions have to diffuse to the electrode OHP [46]. Convection will never reduce the diffusion layer thickness to 0 due to a "no-slip" condition at the electrode surface where the velocity is zero. Therefore, an increase in the rotation speed of the cathode is predicted to increase the current density.

### 3.5 Electrocrystallisation

In the case of nickel electroforming, electrocrystallisation refers to the electrochemical process that leads to the formation of a metallic overlayer on a surface [199]. There are two aspects to electrocrystallisation: (i) *deposition* which involves the transport of reacting species to the electrode surface and its electroreduction to form an adsorbed

atom (ad-atom) and (ii) *crystallisation* which involves the incorporation of ad-atoms into the metal lattice [187, 200]. While both aspects influence the crystallographic and morphological characteristics of the deposit, this section is mainly concerned with introducing the physical processes involved in the latter aspect to provide a basis for understanding deposit morphologies that are observed in practice.



There are two ways a metal ion can be discharged and incorporated into the metal lattice according to Equation 3.35 (where X is a water dipole or an anion): (i) it can be discharged at the electrode OHP to an ad-atom that will diffuse at the surface towards a growth site or (ii) it might be directly incorporated from the OHP at the growth site after charge transfer (without surface diffusion). These processes are shown in Figures 3.9 a and b, respectively. It has been determined that real metal crystal surfaces (substrates) contain microscopic imperfections (kinks and steps) which are energetically favourable for growth (i.e the energy requirements for incorporation of a new atom are relatively low compared to the flat portion of the surface) [201, 202].

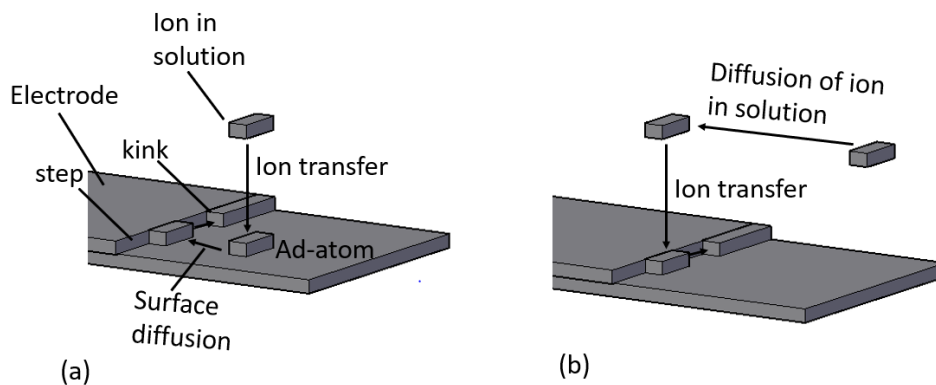


Figure 3.9: Schematic of electrocrystallisation steps: (a) charge transfer to form an ad-atom and its subsequent surface diffusion towards a growth site (steps or kink); and (b) charge transfer directly at a growth site. Adapted from [48].

Two competing processes will occur at the electrode surface after an ad-atom is formed: (i) the ad-atom might form a nucleus with other ad-atoms in close proximity (nucleation) from which growth can occur or (ii) the ad-atom might diffuse towards an

existing (and growing) nucleus and be incorporated there (crystal growth) [48]. It must be mentioned that for growth to occur from a new nucleus, it must achieve a critical cluster size. The morphology of the deposit largely depends on the nucleation rate and growth rate of existing nuclei (crystallites) as they determine the number of crystals in the deposit. Conditions that favor a higher growth rate compared to the nucleation rate will result in deposits with larger grains, while conditions that favor a relatively higher rate of nucleation will yield fine-grained deposits [47].

From a practical perspective, the role of nucleation and growth in influencing deposit morphology is a strong function of the surface overpotential, and therefore, the current density. At low overpotentials, deposition is limited by surface diffusion of ad-atoms to energetically favourable sites (kinks) as there is insufficient energy for nucleation. Under these conditions, deposits are almost always polycrystalline, although crystal sizes can be large; crystal structures are usually well-formed [47]. If the overpotential is increased to sufficiently high values, nucleation becomes favored as the critical size for stable growth decreases. Nucleation occurs at multiple sites and resulting crystallites coalesce to form the deposit [47]. Non-uniformities in the growth rate of different crystal planes could result in the formation of larger crystals as the deposit thickens, producing columnar deposits [47].

# Chapter 4

## Experimental

This chapter is divided into three sections which each describe the experiments conducted to: (i) identify the role of boric acid on nickel electrodeposition kinetics under electroforming conditions; (ii) investigate the effect of boric acid on electrode reactions which occur during nickel electrodeposition; and (iii) characterise anode materials for nickel electroforming. Each section is further broken down into three main sub-sections which detail: (i) the preparation of the electrolytes, (ii) the equipment and experimental set-up, and (iii) the procedure and conditions adopted in the experiments. In some cases, the apparatus and set-up used for experiments detailed in one section have also been applied to similar experiments described in another section. As such, references have been used to avoid content duplication.

### 4.1 Nickel Electrodeposition Kinetics

This section presents the experiments used to examine the kinetics of nickel electrodeposition from sulfamate solutions, employed for electroforming, on a 304 stainless steel substrate. The findings of these experiments are presented in chapter 5. The experiments were designed to investigate the effects of bath constituents, nickel chloride and boric acid ( $\text{H}_3\text{BO}_3$ ), as a function of bath temperature and cathode rotation speed. Emphasis was placed on the effect of  $\text{H}_3\text{BO}_3$  which has been highlighted in chapter 2 as a crucial bath component. Hence, Tafel slopes and exchange current densities of Ni electrodeposition were measured from baths with different concentrations of  $\text{H}_3\text{BO}_3$ . It was anticipated that the results of these experiments would show whether or not boric acid had an impact on the electrodeposition mechanism and whether it improved or hindered charge transfer kinetics.

The objective of these experiments was to measure current-potential (polarisation) curves for nickel electrodeposition from which reliable kinetic data could be obtained. First, polarisation curves were measured under potentiodynamic conditions which allowed quicker data acquisition compared to transient techniques. As mentioned in the previous two chapters, nickel electrodeposition proceeds simultaneously with hydrogen evolution reaction (HER). Therefore, it was important to correct for concurrent HER current in the measured potentiodynamic polarisation curves. This was done using current efficiency measurements from the galvanostatic deposition of nickel, which were subsequently verified using Energy Dispersive X-ray Spectroscopy performed with a Scanning Electron Microscope (SEM).

#### 4.1.1 Electrolyte preparation

All solutions were prepared with deionised water and analytical grade chemicals. Nickel sulfamate tetrahydrate ( $\text{Ni}(\text{SO}_3\text{NH}_2)_2 \cdot 4\text{H}_2\text{O}$ ) (Assay  $\geq 98\%$ ), nickel chloride hexahydrate ( $\text{NiCl}_2 \cdot 6\text{H}_2\text{O}$ ) (Assay  $\geq 99\%$ ), and boric acid ( $\text{H}_3\text{BO}_3$ ) (Assay  $\geq 99.5\%$ ) were obtained from Sigma-Aldrich. Chemicals were used as received.

Table 4.1: Composition and initial pH of nickel sulfamate solutions employed to study nickel electrodeposition kinetics.

Bath Composition (M)	A	B	C	D	E (Electroforming)	F
$\text{Ni}(\text{SO}_3\text{NH}_2)_2 \cdot 4\text{H}_2\text{O}$	1.78	1.78	1.78	1.76	1.76	1.78
$\text{NiCl}_2 \cdot 6\text{H}_2\text{O}$	0	0	0	0.02	0.02	0
$\text{H}_3\text{BO}_3$	0	0.49	0.65	0	0.65	0.81
pH at 40 °C	4.83	3.34	3.13	4.75	3.40	-
pH at 45 °C	4.74	3.38	3.12	4.49	3.26	3.06
pH at 55 °C	4.46	3.35	3.08	4.21	3.00	-

The composition and pH of sulfamate solutions used in this study are presented in Table 4.1. The concentration of nickel sulfamate tetrahydrate was selected in accordance with recommended settings for electroforming baths in literature [21, 138].

The different solutions were used to determine the different roles of the bath constituents with emphasis on boric acid. Electrolyte A which constituted of only nickel sulfamate tetrahydrate provided a baseline for all nickel electrolytes. Baths B, C, and F were used to understand how increasing amounts of boric acid affected electrodeposition kinetics; concentrations were chosen based on those which have been used by other researchers [61, 68]. Electrolyte D was used to determine the effect of chloride addition to a sulfamate system, and E is a typical electroforming solution used in industry containing all three constituents. It was expected that analysing the electrochemical behaviour using such a systematic manner would provide a basis to understand their individual influences on nickel deposition.

It is known that oxygen reduction could cause electrodeposited nickel to passivate [92, 114] which could affect the kinetics of nickel electrodeposition. Therefore, dissolved oxygen was removed from electrolytes by gently sparging with nitrogen gas (99.99% purity) at the beginning of all experiments. The electrolytes were deoxygenated in the glass cell used for the experiments which was sealed with the lid containing ground glass joints and/or glass threads. A sparger connected to a nitrogen gas tank was submerged through one of the lid joints to the base of the cell and used to gently sparge nitrogen gas through the electrolyte. A rubber stopper with a  $0.008 \text{ cm}^2$  hole was placed in one of the lid joints to provide an outlet through which the purged gas could escape. The rest of the glass joints and threads were sealed with glass stoppers and threaded caps, respectively, to ensure an airtight cell was established and to prevent any influx of air from the outside of the cell. Sparging was maintained for 20 and 30 minutes at the beginning of polarisation and deposition experiments, respectively, to allow full evacuation of dissolved oxygen from the cell. A nitrogen atmosphere was maintained during data collection to prevent oxygen influx. This was done by raising the orifice of the gas sparger just above the electrolyte surface.

#### **4.1.2 Equipment**

All measurements were conducted with a PGSTAT101 potentiostat/galvanostat (Metrohm Autolab) interfaced with NOVA 2.1.4 software for automated control of current or poten-

tial and real-time data acquisition. The system was set up in the potentiodynamic and galvanostatic modes to carry out polarisation and deposition experiments, respectively.

#### 4.1.2.1 Polarisation Experiments

A schematic of the electrochemical glass cell and set-up for the polarisation experiments is presented in Figure 4.1. The glass cell was filled with 72 ml of electrolyte and a standard three-electrode configuration was employed. The set-up consists of a working electrode where the reaction of interest occurs, which in this case is nickel electrodeposition. A potentiostat was used to control the potential of the working electrode against a reference electrode while the current flowing between the counter and working electrodes was measured. A description of each electrode used for these experiments is given in the forthcoming paragraphs.

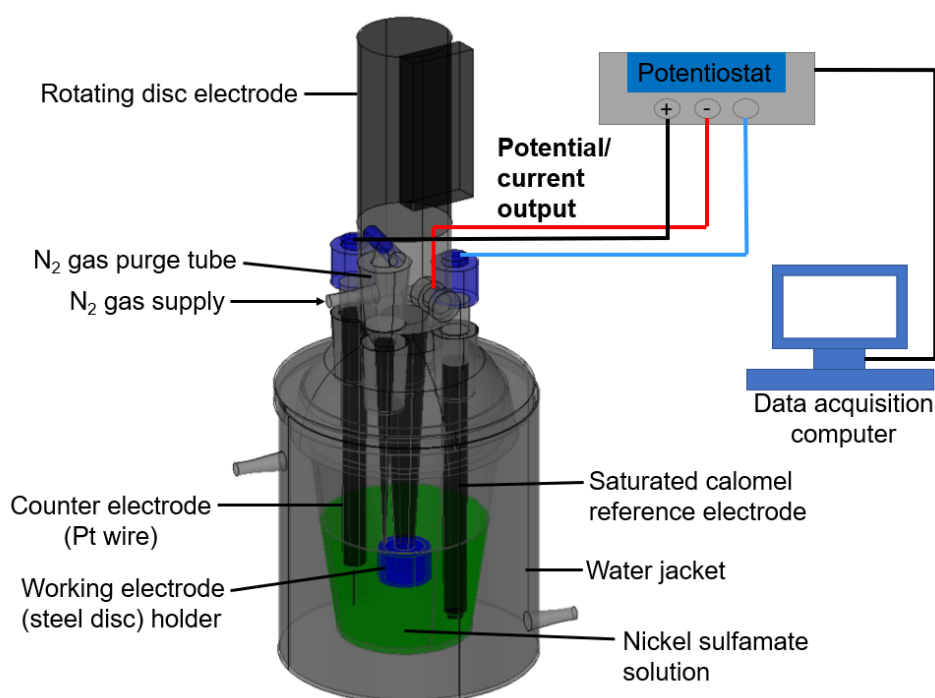


Figure 4.1: Schematic of the electrochemical glass cell used for polarisation experiments showing a three-electrode configuration. The potential of the 304SS rotating disc electrode (RDE), which acts as the working electrode, is controlled by the potentiostat against a saturated calomel reference electrode while the current flowing between the RDE and Pt counter electrode is measured.



A radiometer ED101 rotating disc electrode (RDE) with the tip serving a 304 stainless steel (SS) disc (composition: 8 wt% Ni, 18 wt% Cr, and 67 wt% Fe) was employed as the working electrode (WE). 304 SS was chosen as a substrate because it is a common mandrel material choice in the electroforming industry due to its reusability and the ease of deposit separation it offers after electrodeposition. To prevent electrolyte leakage into the RDE setup, the disc was lodged within a PTFE holder with an O-ring, exposing a surface area of  $1.35 \text{ cm}^2$ . The disc is recessed into the holder with a recess depth of about 1 mm. This has the advantage of providing a more uniform current distribution compared to a cathode without a recess [203]. The components and assembly of the RDE are shown in Figure 4.2. The rotation speed of the RDE was controlled by a CTV101 Speed Control Unit (Radiometer Analytical).

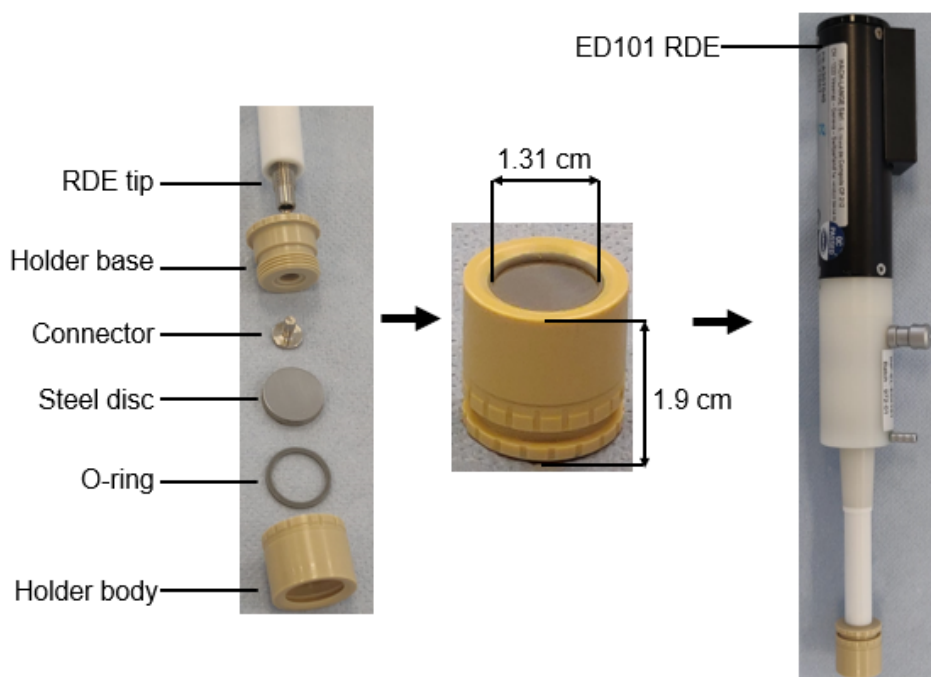
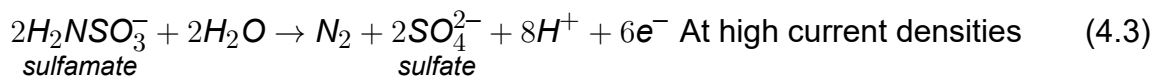
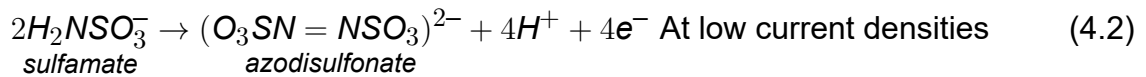


Figure 4.2: Components and assembly of the rotating disc electrode (RDE).

A platinum wire sealed within a glass tube with an exposed length of 0.92 cm and diameter of 0.1 cm (surface area =  $0.3 \text{ cm}^2$ ) was employed as the counter electrode (CE); all potentials in this work are reported against a saturated calomel electrode (SCE).

It has been reported that using a Pt anode can lead to the oxidation of sulfate ions, the products of which could change the electrolyte composition [129]. The

bulk pH was taken before and after each polarisation experiment and it was found that the pH dropped by 0.1 and 0.2 units at 40-45 °C and 55 °C, respectively. This slight acidification after polarisation could be due to water oxidation (Equation 4.1) or sulfamate ion oxidation reactions (Equations 4.2 and 4.3) at the Pt counter electrode.



An estimation was done to determine the maximum amount of azodisulfonate or sulfate that could be generated from sulfamate ion oxidation during each polarisation experiment if Equation 4.2 or 4.3 occurred with a current efficiency of 100% as follows:

$$m_{\text{anode product}} = \frac{Q_{\text{total}} \times M}{nF} \quad (4.4)$$

where  $m_{\text{anode product}}$  is the mass of azodisulfonate or sulfate generated (g),  $Q_{\text{total}}$  the total charge passed in each polarisation experiment,  $M$  the molar mass of azodisulfonate (188.14 g/mol) or sulfate (96.06 g/mol),  $n$  the number of electrons required to generate one mole of azodisulfonate ( $n = 4$ ) or sulfate ( $n = 3$ ) ions, and  $F$  the Faraday's constant (96485 C/mol).  $Q_{\text{total}}$  is approximately 9 C for each polarisation experiment which is equivalent to 0.004 g (0.021 mmol) of azodisulfonate ions and 0.003 g (0.031 mmol) of sulfate ions. The generation of these predicted amounts of azodisulfonate and sulfate ions required  $\leq 0.02\%$  of the initial quantity of sulfamate ions (0.25 mol), given that  $\approx 0.07$  L of electrolyte was used. Due to the low quantity of charge passed, it was expected that the products produced by sulfamate ion oxidation would not significantly alter the electrolyte composition during the polarisation experiments.

The depletion of Ni(II) in solution during polarisation experiments was also evaluated from gravimetric measurements of the working electrode. It was found that Ni(II) concentration typically decreased by 0.03% for each experiment. Therefore, 16 polarisation experiments could be performed in a single batch of solution before Ni<sup>2+</sup> concentration dropped to 0.5% of its initial value.

To avert experimental errors arising from  $\text{Ni}^{2+}$  depletion and sulfamate ion oxidation during polarisation measurements, 6 experiments were performed using a single batch of solution at a time and a fresh solution was used perform repeats. To verify the accuracy of the results, experiments were performed in triplicate. Kinetic data in the results section is reported as an average of the measurements obtained along with the standard deviation.

#### 4.1.2.2 Deposition Experiments

As mentioned earlier, galvanostatic deposition was performed to determine the current efficiency of nickel electrodeposition which corresponds to the ratio of the mass plated at a particular current to the theoretical mass expected; this has been discussed in chapter 3. Deposition was performed using the same working and counter electrodes described in section 4.1.2.1.

To achieve a measurable deposit mass and thickness that could also be characterised using the SEM, the charge passed during the deposition experiments was 8 times greater than that passed during polarisation experiments which would increase experimental errors arising from changes in electrolyte composition due to  $\text{Ni}^{2+}$  depletion and sulfamate ion oxidation at the Pt counter electrode. To avoid these errors, the electrolyte volume was increased to 450 mL and the CE was separated from the main bulk electrolyte by means of a bridge tube with a porous glass frit (P4 with pore size of 10-16  $\mu\text{m}$ ) to limit the diffusion of anodic reaction products to the bath. A schematic of the custom-built glass cell and set-up showing the bridge tube used for galvanostatic deposition is presented in Figure 4.3. A bridge tube, filled with 16 mL of electrolyte, was employed in all deposition experiments.

In order to estimate how quickly the anolyte entered the catholyte chamber, a bridge tube containing nickel sulfamate solution was placed in the cell (Figure 4.3) filled with deionised water, and the rate of solution leakage through the frit of the tube was studied. The water in the cell remained clear for over 8 hours which indicated that no leakage of solution had occurred during this time period. Hence, one could assume that no changes in the anode compartment were transferred into the catholyte during

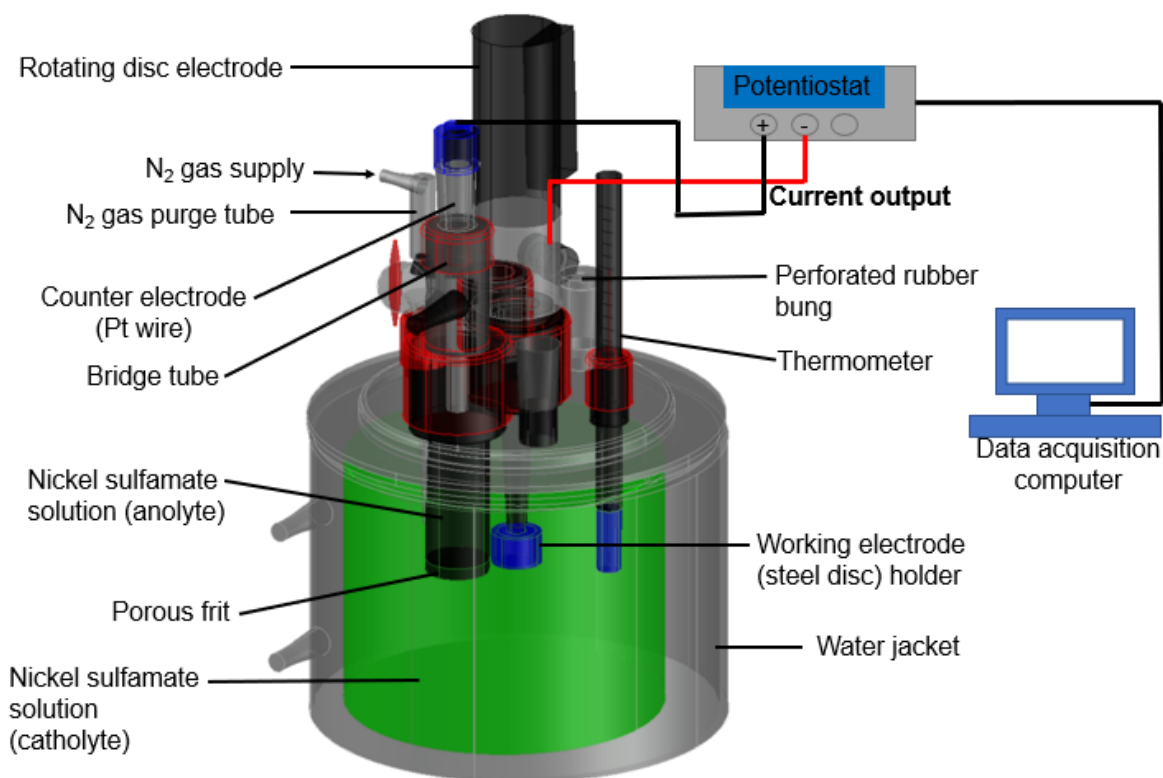


Figure 4.3: Schematic of the electrochemical glass cell used for galvanostatic deposition experiments showing a two-electrode configuration. A constant current was applied between the RDE working electrode and Pt counter electrode using a potentiostat to electrodeposit Ni for a desired period of time. Pt was placed in a bridge tube to limit diffusion of anode reaction products to the catholyte.

deposition experiments which were of a much shorter duration than 8 hours.

#### 4.1.2.3 Working electrode preparation for polarisation and deposition experiments

Prior to all experiments, the surface of the steel disc was mechanically polished sequentially with grades P#1200, P#2400, and P#4000 silicon carbide grit paper lubricated with tap water to achieve a mirror-like finish. Each polishing cycle was done for 2 minutes at 125 rpm using a two-speed polisher (Struers Dap-7). In between each polishing cycle, the steel disc was rinsed with deionised water to remove polishing residues. Finally, the steel disc was rinsed once again with deionised water and dried with nitrogen gas.

#### 4.1.2.4 Material characterisation: Scanning Electron Microscopy (SEM) and Energy Dispersive X-ray Spectroscopy (EDS)

A Scanning Electron Microscope (SEM) combined with Energy Dispersive X-ray Spectroscopy (EDS) was used to perform elemental analysis of deposit samples obtained from galvanostatic deposition in order to verify current efficiency measurements.

##### 4.1.2.4.1 SEM instrumentation

The Scanning Electron Microscope consists of several components which are shown in Figure 4.4 [204] and are described in the forthcoming paragraphs.

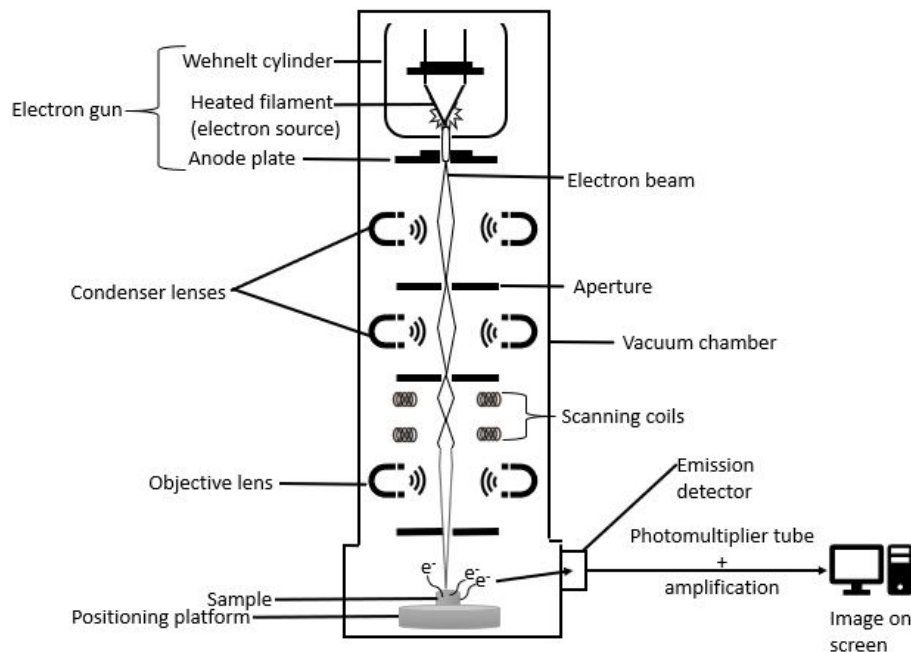


Figure 4.4: Schematic of major components of a Scanning Electron Microscope (SEM). Adapted from [204].

A sufficiently high current is supplied to a Tungsten filament to generate temperatures on the order of 2700-2900 K. The provision of energy in excess of the work function of Tungsten (4.7 eV) results in the thermionic emission of electrons which are focused by a negatively charged Wehnelt cylinder and drawn toward an aperture in a positively charged anode. The electrons that escape through the pinhole generate an electron beam which is directed down the SEM column toward the sample. The voltage

difference between the filament and the anode plate is defined as the accelerating voltage and is directly proportional to the energy of the electron beam. The voltage range for an SEM varies from 200 V to 40 kV [204]. A high accelerating voltage enhances the resolving power of the image, but very high values could charge and damage the sample [205].

Low energy and non-directional electrons are filtered through aperture strips with tiny holes of various diameters. For high resolution imaging, a small aperture is necessary, but very small diameters could result in dark images because fewer electrons contact the sample surface [205]. Condenser lenses above the aperture strip control the electron concentration and diameter of the beam while objective lenses converge and focus the beam to collide with sample surface. Two pairs of scan coils are used to deflect the electron beam in both horizontal and vertical directions, so that it scans in a raster fashion across the sample surface. The scan coils determine the magnification of the instrument by controlling the scanning area on the sample [205]. The SEM must be operated under extremely high vacuum conditions, to create an insulating medium between the filament and anode, prolong the lifespan and efficiency of the electron gun, and enable sharper beam focusing [204].

Interaction of the electron beam with the sample produces a variety of emissions (backscattered electrons, secondary electrons, and X-rays) which are recorded at their respective detectors and converted into images which reveal structural and elemental compositional information about the sample [204]. The phenomenon behind these interactions is discussed in the forthcoming section.

#### **4.1.2.4.2 Operating principle of the SEM and EDS**

The electron beam interacts with a teardrop-shaped region of the sample defined as the interaction volume, which extends from 500 nm to  $\approx 2 \mu\text{m}$  into the surface [204]. As previously stated, these interactions result in different emissions via three mechanisms as shown in Figure 4.5:

- **Inelastic scattering to yield secondary electrons (SE):** The electron beam

interacts with electrons in sample atoms and are inelastically scattered. In this case, the source electrons displace core electrons from filled shells of the sample atoms. The resulting atom is left in an energetic excited state, with a missing inner shell electron(s). Often, detected SE are released from atoms at the sample surface; electrons ejected from deeper regions of the sample are likely to be reabsorbed by the material before they reach the surface. Hence, SE imaging is useful for the inspection of the sample's surface topography as protrusions release more SEs compared to a flat surface [204].

In order to obtain information from underlying portions of the sample (i.e. increase the interaction volume of the sample with the electron beam and produce more energetic emissions that will reach the surface from lower depths of the sample), the intensity (accelerating voltage) of the electron beam must be increased or the sample density decreased [204].

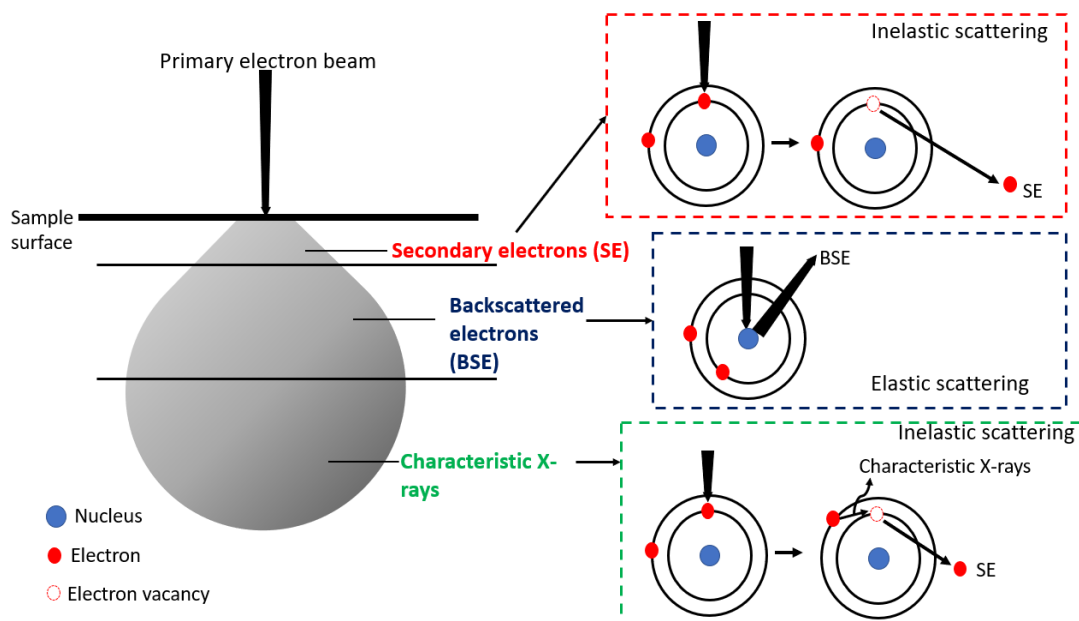


Figure 4.5: Illustration of the sample interaction volume of the SEM, the corresponding emissions from various depths, and their respective mechanisms of emission resulting from the interaction of the electron beam with sample atoms. The exact interaction volume will depend on the accelerating voltage of the electron beam and sample composition. Adapted from [204].

- **Inelastic scattering to yield X-rays:** In this case, the vacancies in an excited

atom formed following SE generation are filled with electrons from its outer shells which return the excited atom to ground state. This post-ionisation atomic relaxation produces excess energy that may be released as characteristic X-rays. In Energy Dispersive X-ray Spectroscopy (EDS), all characteristic X-ray energies reaching the detector are measured simultaneously which provides rapid data acquisition. Using this technique, it is possible to ascertain the chemical composition of the surface under investigation both qualitatively and quantitatively (using appropriate standards) by counting the quantity and energy of X-rays produced by electrons interacting with the sample [204].

- **Elastic scattering to yield Backscattered Electrons (BSE):** The electron source may also be elastically scattered through interactions with the nucleus of surface atoms. In this case, the trajectory of the electron source changes with little or no energy loss to produce backscattered electrons (BSE). The number of BSE that are produced from a given material is proportional to its atomic number, i.e., materials with a high density of large atoms, such as metals, would backscatter more electrons, resulting in brighter tones in the SEM image relative to less dense materials like organic solids. Accordingly, it is easier to inspect cross-sectional images of metal deposits in a support material by their varying contrasts. Hence, images obtained using the detection of BSE are related to the sample's composition, providing both spatial and chemical information [204].

In certain instances, the electron beam will follow its initial path through the atomic structure without scattering. This is frequently seen in molecules that contain light atoms, such as H, Li, etc [204]. Therefore, hydrogen in deposit samples cannot be detected by EDS.

#### **4.1.2.4.3 Sample preparation for SEM and EDS analysis**

For analysis of the deposit elemental composition,  $\approx 20 \mu\text{m}$  thick nickel films were deposited from sulfamate solutions with varying boric acid concentration and current density. The surface of deposit samples were preliminary observed using a YenWay



optical microscope. Afterwards, the samples were cross-sectioned and embedded in a slow setting epoxy resin. Figure 4.6 shows an image of the epoxy resin containing the deposit samples.

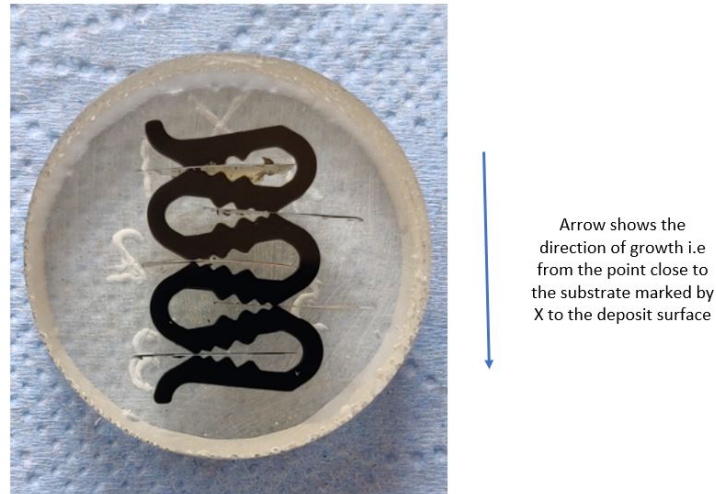


Figure 4.6: Image of the epoxy resin containing 5 cross-sectioned Ni deposits held in place by black clippers.

The surface of the deposit-containing resin shown in Figure 4.6 was coated with a thin gold film (<10 nm) to create a conductive surface. The Au-coated sample was then mounted onto the top of an adhesive fastened to an aluminium stub holder. A conductive gold tape was used to sequester the sample and to create a conductive path between the sample and the aluminium holder. The employment of a conductive surface film and conductive mounting materials are important to prevent charging, i.e. the build-up of electrons on the sample surface, which affects the imaging ability of the SEM [204].

## 4.1.3 Procedure

### 4.1.3.1 Polarisation Measurements

#### 4.1.3.1.1 Polarisation technique: Linear Sweep Voltammetry (LSV)

The current-potential relationship for nickel electrodeposition is required to determine its kinetic parameters. In chapter 2, some applied electroanalytical techniques (chronopotentiometry, chronoamperometry, and Linear Sweep Voltammetry) to ascertain this relationship were discussed. In some cases, these approaches produced similar results. In the transient techniques described, a current-potential curve is constructed from a set of potential measurements for certain applied currents (chronopotentiometry) or current measurements for certain applied potentials (chronoamperometry) [183]. In Linear Sweep Voltammetry, current-potential curves are recorded directly in a single experiment which offers quicker data acquisition. In earlier literature, this procedure was referred to as a potentiodynamic technique to differentiate from the potentiostatic technique which has a similar setup [200].

In Linear Sweep Voltammetry, the potential of the working electrode is varied linearly with time from an initial potential to a stop potential at a constant rate called the scan rate,  $\nu$  ( $\text{mV s}^{-1}$ ), while the current flowing through the working electrode is measured. The potential of the working electrode at time  $t$ ,  $U_t$  in the cathodic polarisation is given by [183]:

$$U_t = U_{t=0} \pm \nu t \quad (4.5)$$

where  $U_{t=0}$  is the initial potential (mV), typically the Open Circuit Potential. For the purpose of measuring kinetic parameters, it is required to perform the LSV experiment at a slow scan rate ( $\leq 5 \text{ mV s}^{-1}$ ) so that the recorded currents are obtained under steady state conditions [200]. In this way, the equations developed for charge transfer kinetics, discussed in chapter 3, could be applied to the polarisation measurements.

One caveat of the LSV technique is that current density is measured for all reactions at the electrode surface, not just the desired reaction. Concepts for charge transfer kinetics are developed for a single reacting species. For multiple reactants,

these concepts remain the same, but have to be applied to each individual species. To measure the kinetics of nickel ion electroreduction, the fraction of the total current consumed by this reaction could be determined using the current efficiency calculated from gravimetric measurements (see section 4.1.3.2).

It is important to state that current efficiency calculations from the mass plated are based on the assumption that the nickel electroreduction reaction is the only reaction capable of producing a mass change at the cathode surface (i.e the deposit is composed of metallic nickel only). In reality, nickel hydroxides, oxides, and oxyhydroxides could also be included in the deposit if water reduction increases the pH at the cathode to sufficiently high levels. Therefore, additional characterisation methods such as Energy Dispersive X-ray Spectroscopy (EDS) and EQCM are required to validate gravimetric measurements which are discussed in sections 4.1.2.4 and 4.2, respectively.

#### **4.1.3.1.2 Polarisation procedure**

Current-potential (polarisation) data was collected by conducting a slow Linear Sweep Voltammetry (LSV) at a scan rate of  $0.005 \text{ V s}^{-1}$  on a steel disc. The potential was swept from the Open Circuit Potential (OCP), which was typically  $-0.25 \pm 0.1 \text{ V}$ , to  $-1.7 \text{ V}$ . Above  $-1.7 \text{ V}$ , significant hydrogen evolution occurred.

Polarisation experiments were performed in the different electrolytes outlined in Table 4.1 at 40, 45, and 55 °C, the temperature regime of electroforming operations. The solution temperature was controlled to  $\pm 1 \text{ }^\circ\text{C}$  using a water jacket and circulator water bath (Thermo Haake DC10-B3). An attempt to carry out experiments at lower temperatures was made, but it was found that boric acid crystallised out of solution at 35 °C and concentrations above 0.65 M (40 g/L). Although the solubility of boric acid in aqueous solution at 30 °C (62 g/L) is higher than the concentrations of  $\text{H}_3\text{BO}_3$  used in these experiments ( $\approx 30\text{-}50 \text{ g/l}$ ), it is also known that the nature of other dissolved ions affects its solubility [206], which could account for the lower-than-expected solubility of boric acid in nickel sulfamate solutions, also observed by Kelly et al. [207].

The polarisation curves were recorded using different RDE rotation speeds of 0, 900, and 1600 rpm to study the effect of agitation on electrodeposition. These rotation speeds are identical to those employed by Tsuru et al. [68] and Kelly et al. [208] to measure nickel electrodeposition kinetics, so that the results from these experiments could be compared directly with their findings. These sets of experiments were expected to reveal the influence of temperature and agitation on the action of  $\text{H}_3\text{BO}_3$  during electrodeposition.

#### 4.1.3.1.3 Determination and correction of ohmic drop

In an electrochemical cell with a three electrode set-up, such as that employed for these polarisation experiments, the potentiostat is able to apply a desired potential between the working electrode (WE) and the reference electrode (RE) by adjusting the current flow at the WE surface. An equivalent circuit representation of this situation is shown in Figure 4.7. The placement of the RE away from the WE introduces an error in the measured potential due to the additional resistance between the WE and RE. This resistance is called the uncompensated resistance,  $R_U$ . [47, 209], which causes a control error in the working electrode potential called ohmic drop or IR of magnitude: current  $\times R_U$ . Hence, the true potential of the working electrode will either be higher or lower than the measured potential depending on the direction of current as given by Equation 4.6:

$$U_{true} = U_{measured} - (I \times R_U) \quad (4.6)$$

where  $U_{true}$  is the true working electrode potential (V),  $U_{measured}$  the measured potential (V),  $I$  the current (A), and  $R_U$  the uncompensated resistance ( $\Omega$ ). The signs of the potential and current are negative for cathodic reactions. Hence,  $U_{true}$  will be less negative compared to  $U_{measured}$  for electrodeposition experiments.

The findings of electrochemical polarisation measurements could be significantly distorted by ohmic drop, and conclusions drawn from measurements taken at various temperatures may not only reflect the influence of temperature on reaction ki-

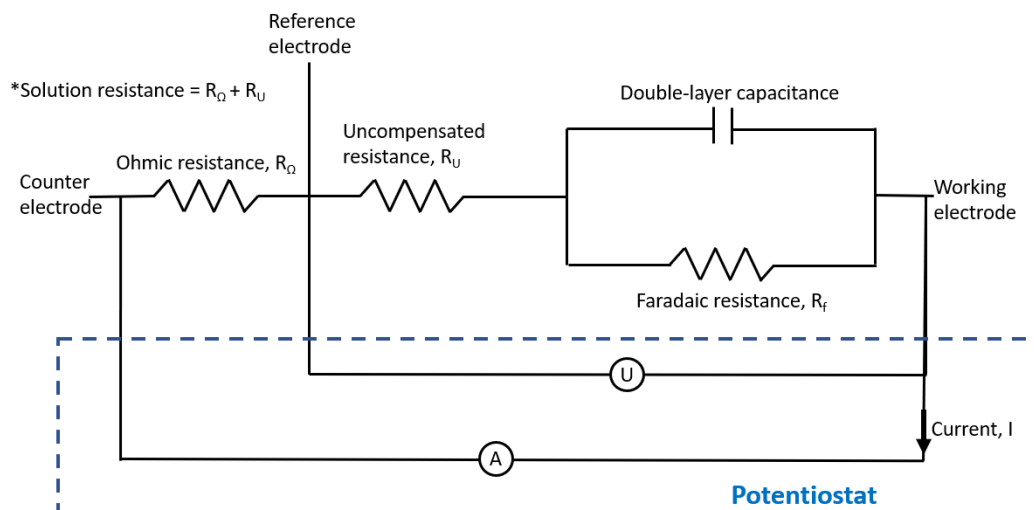


Figure 4.7: Equivalent circuit for the working electrode in a three-electrode configuration. Adapted from [47]

netics but also variations in electrolyte conductivity which affect  $R_U$  [210]. Therefore, it is important to correct measurements for this potential (ohmic) drop.

The approach to dealing with ohmic drop is first to minimise it as much as possible, and then compensate or correct for any potential drop that cannot be eliminated [47]. It is often suggested to use a Luggin capillary to move the tip of the reference electrode close to the working electrode surface in order to minimise ohmic drop [47]. However, this geometry is not always practical for RDE experiments because the capillary tip could alter hydrodynamic flow [47]. The potentiostat employed for these polarisation experiments could not perform IR compensation. Hence, values of  $R_U$ , measured using Electrochemical Impedance Spectroscopy (EIS) prior to each experiment, were used to correct the polarisation curves for ohmic drop, retrospectively using Equation 4.6.

Electrochemical Impedance Spectroscopy (EIS) was used to determine  $R_U$  using the identical three-electrode arrangement shown in Figure 4.1. The cell was connected to a Palmsens4 impedance analyser interfaced with PSTrace 5.6 software. An ac signal amplifier of  $\pm 10$  mV vs. OCP was applied with frequencies starting at 10 kHz and ending at 5 Hz on a logarithmic scale. The complex impedance of the electrochemical system was determined by recording the corresponding current re-

sponses. In Figure 4.8, the Nyquist plot of an EIS measurement performed in Bath E at 45 °C is shown. The value of  $R_U$  was determined from the x-axis intercept (real part of measured impedance) of the Nyquist plot at high frequencies. Measurements were performed thrice and the average value of  $R_U$  was obtained. The arrangement and

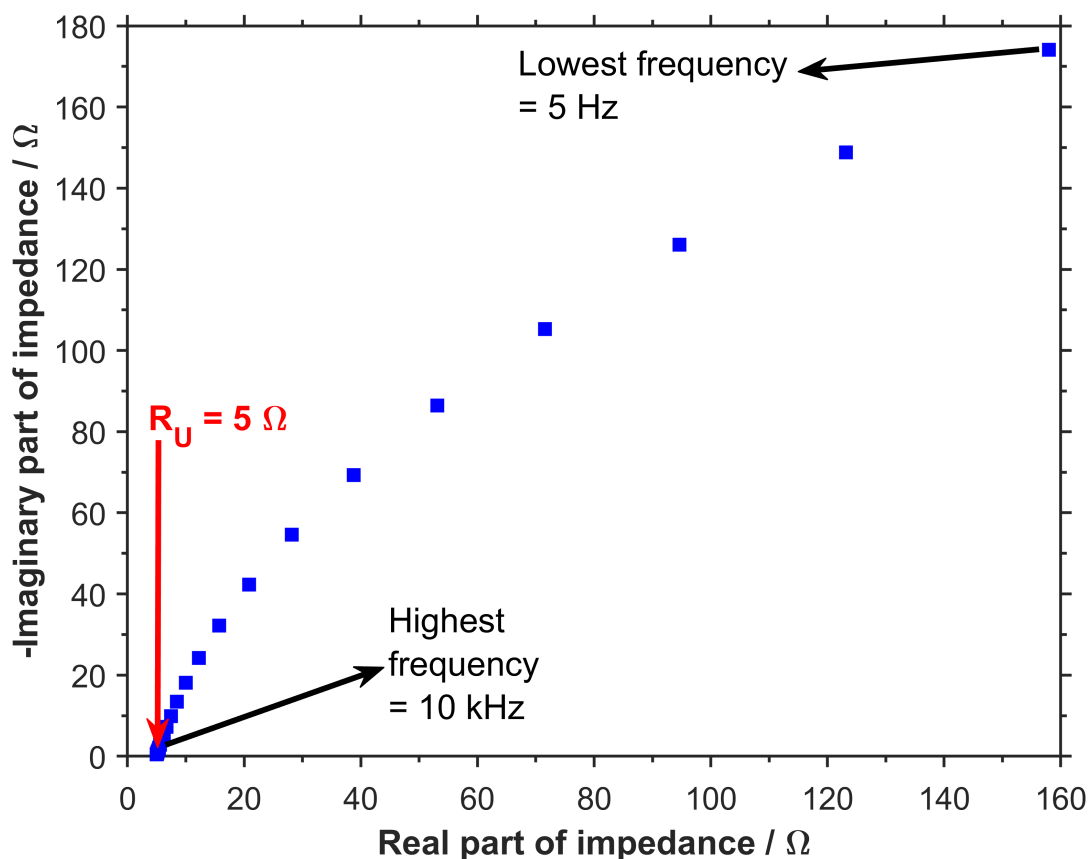


Figure 4.8: Example of a nyquist plot measured in Bath E at 45 °C showing how the uncompensated resistance,  $R_U$  can be determined from the real part of the impedance at the highest frequency.

distances between electrodes were kept the same for each polarisation experiment, to ensure that the uncompensated resistance remained approximately the same. Distance between the RE and WE was maintained at 2.5 mm in all experiments.

The uncompensated resistance between the WE and RE could be experimentally determined by impedance spectroscopy because the working electrode system is analogous to the equivalent circuit shown in Figure 4.7. The interface between the WE and electrolyte represents a double layer capacitance arising from charge separation at the surface, in parallel with a charge transfer resistance, both in series with the elec-

trolyte resistance. When a potential amplitude is applied at the highest frequency, the capacitor acts as a “short” due to the voltage oscillating at a rate much faster than the time it takes to charge the double layer. Because the double layer is never sufficiently charged, the capacitor offers negligible resistance to the oscillating current. Thus, all of the current flows through the double layer capacitor. Thereby, at the highest frequency, the resistance measured between the WE and RE is equivalent to the uncompensated resistance,  $R_U$  [47,210]

The uncompensated resistance,  $R_U$  could also be estimated from equation 4.7 for a disk electrode [47]:

$$R_{U, disk} = \frac{1}{4r\kappa} \quad (4.7)$$

where  $r$  is the radius of the working electrode (0.65 cm), and  $\kappa$  the specific conductivity of the electrolyte ( $\Omega \text{ cm}^{-1}$ ). Table 4.2 compares values for  $R_U$  measured from EIS to those calculated from equation 4.7. There are some differences between estimated and measured  $R_U$  values in Table 4.2 which are of the magnitude  $0.9 \pm 0.3 \Omega$ . The lead and contact resistances in the RDE unit, which are included in the measured  $R_U$  values and are typically measured to be approximately  $1.0 \pm 0.5 \Omega$ , could explain these differences. Therefore, resistances within the WE unit are also taken into account when correcting the IR drop using  $R_U$  values from EIS measurements.

Table 4.2: Estimated  $R_U$  from Equation 4.7 and measured  $R_U$  obtained from Nyquist plots of EIS measurements performed in deoxygenated nickel sulfamate electrolytes at 0 rpm and 45 °C

Electrolyte	Conductivity ( $\Omega \text{ cm}^{-1}$ )	Estimated $R_U$ ( $\Omega$ )	Measured $R_U$ ( $\Omega$ )	Difference ( $\Omega$ )
A	0.0954	4.03	5.15	1.11
B	0.0940	4.09	4.90	0.81
C	0.0902	4.26	4.7	0.44
D	0.1018	3.78	5.31	1.53
E	0.0950	4.05	5.00	0.95

Figure 4.9 presents polarisation plots to illustrate the magnitude of the effect of ohmic drop (IR) on polarisation measurements. It can be seen from Figure 4.9 that

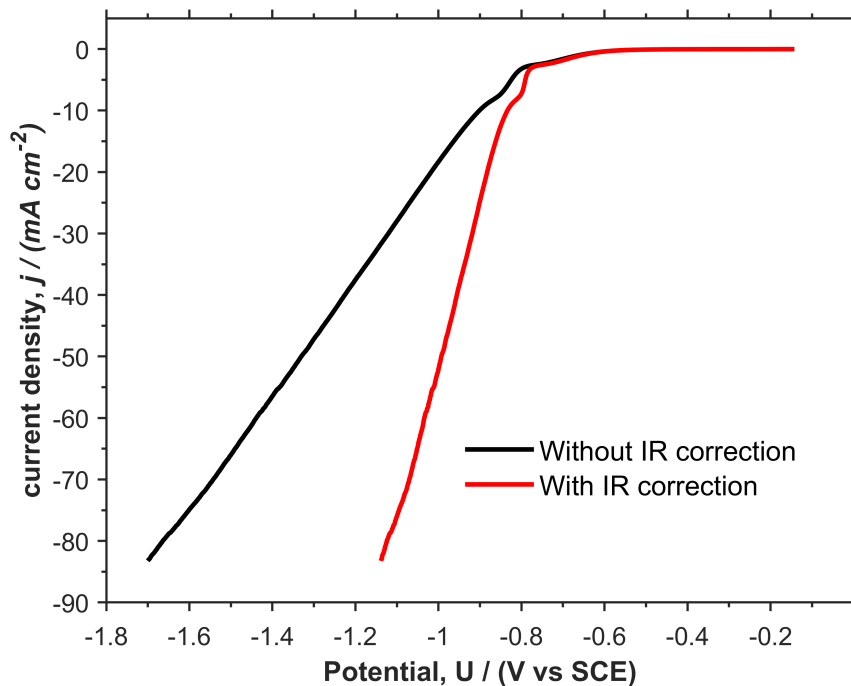


Figure 4.9: The effect of ohmic drop (IR) correction on the polarisation curve measured from Bath E at 45 °C and 0 rpm;  $R_U = 5 \Omega$

the difference in potential between the two plots at a certain current density increases with increase in current density. Therefore, neglect of IR correction would result in substantial error at high current densities. Additionally, it can be seen that failing to account for IR drop could lead to higher cathodic Tafel slopes ( $\frac{dU}{d \log |j|}$ ). As a result, this section emphasises the importance of ohmic drop correction for obtaining accurate kinetic measurements.

#### 4.1.3.2 Galvanostatic deposition experiments

Deposition experiments were conducted in the baths outlined in Table 4.1 under the same temperature, agitation, and inert conditions as has been described previously in section 4.1.3.1.2.

In galvanostatic deposition, a constant current is applied between the WE and CE for a certain duration. Five current densities (10-50 mA cm<sup>-2</sup>) were selected, which cover conditions usually employed for electroforming.



For all current densities, the deposition time was adjusted to obtain deposits with a thickness of 20  $\mu\text{m}$  using Equation 4.8 with the assumption of 100% current efficiency:

$$t(\text{s}) = \frac{h\rho nF}{10000Mj} \quad (4.8)$$

where  $t$  is the deposition time (s),  $h$  the film thickness ( $\mu\text{m}$ ),  $\rho$  the density of the bulk nickel metal ( $8.907 \text{ g/cm}^3$ ),  $n$  the number of electrons required to discharge one atom of Ni (2),  $F$  the Faraday constant ( $96,485 \text{ C mol}^{-1}$ ),  $M$  the atomic weight of Ni ( $58.69 \text{ g/mol}$ ),  $j$  the total current density passed ( $\text{A cm}^{-2}$ ), and  $A$  the surface area of the cathode ( $1.35 \text{ cm}^2$ ). The selected thickness corresponds to  $\approx 79 \text{ C}$  of electricity passed for each experiment.

To determine current efficiency from deposition, the mass of the deposit was calculated gravimetrically, i.e. from the difference between the initial and final mass of the cathode steel discs, which were measured using an electronic balance (KERN, ABJ-NM/ABS-N) with capability of measuring down to  $\pm 0.1 \text{ mg}$ . Each deposit was carefully removed from the cathode using a scalpel, rinsed with deionised water, and dried in a stream of nitrogen gas before its weight was measured.

The current efficiency for nickel deposition was calculated using equation 3.10, already given in chapter 3. In addition, the partial current density ( $\text{A cm}^{-2}$ ) of Ni deposition was also calculated from the measured mass of the deposit using Faraday's Law [186]:

$$-j_{\text{Ni}} = \frac{wnF}{AtM} \quad (4.9)$$

#### 4.1.3.3 Data Interpretation for polarisation and deposition

Current-potential data gathered from polarisation and deposition measurements were used to determine the effect of each constituent on kinetics. Tafel lines were drawn from the Ni partial current density-potential ( $j_{\text{Ni}}-U$ ) curves as described by the Tafel Equation given below:

$$\eta_c = U - U_{\text{rev}} = \frac{2.303RT}{\alpha_c F} \log|j_o| + \frac{2.303RT}{\alpha_c F} \log|j_{\text{Ni}}| \quad (4.10)$$

where,  $\eta_c$  is the charge transfer overpotential (V);  $U$  the electrode potential (V);  $U_{rev}$  the reversible potential (V);  $\alpha_c$  the transfer coefficient;  $j_o$  the exchange current density of Ni/Ni<sup>2+</sup> (mA cm<sup>-2</sup>);  $j_{Ni}$  the Ni partial current density (mA cm<sup>-2</sup>);  $R$ ,  $T$ , and  $F$  are the gas constant (8.314 J/mol.K), temperature (K), and Faraday constant (96485 C/mol), respectively.

From Tafel lines, values of electrokinetic criteria, Tafel slope,  $-b_c$  (V decade<sup>-1</sup>) and transfer coefficient,  $\alpha_c$  are evaluated as follows:

$$-b_c = \frac{dU}{d\log|j_{Ni}|} \quad (4.11)$$

$$\alpha_c = -\frac{2.303RT}{nF} \frac{d\log|j_{Ni}|}{dU} \quad (4.12)$$

The exchange current density of Ni/Ni<sup>2+</sup> describes the rates of Ni deposition and dissolution at the reversible potential, i.e., when the charge transfer overpotential is zero. For a plot of  $U - \log|j_{Ni}|$ , charge transfer overpotential,  $\eta$  is zero where the Tafel line meets with the reversible potential. At this point of intersection,  $\log|j_{Ni}| = \log|j_o|$ . The reversible potential of nickel ion reduction was estimated using Equation 1 in Table 3.1 given in Chapter 3.

#### 4.1.3.4 SEM and EDS

Images of the deposit cross-sections were collected using a tungsten (W) filament SEM (Hitachi S-3700N) wherein an accelerating voltage of 10 kV was applied. Images were taken using the backscattered electron (BSE) mode of the SEM to improve contrast between nickel and the epoxy. The electron micrographs were imaged using a magnification of X1000.

EDS was used to assess the elemental distribution in the deposit at points near the substrate, near the midpoint, and near the surface of the deposit cross-section as shown in Figure 4.10. These experiments were expected to reveal the influence of boric acid on the initial stages of nickel electrodeposition (i.e. electrodeposition of the first few monolayers) versus its action during multilayer deposition.

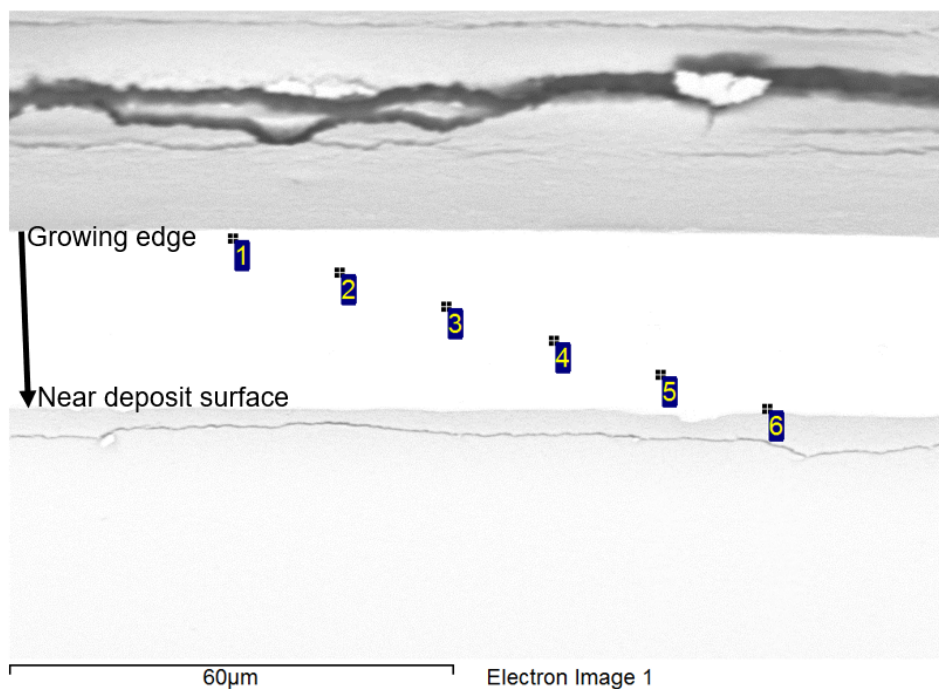


Figure 4.10: A micrograph of Ni electrodeposited from Bath E at 45 °C showing EDS measurements mapped over 6 areas of the deposit cross-section. The arrow in the Figure indicates the direction of growth of the deposit.

## 4.2 EQCM studies of interfacial processes during nickel electrodeposition

This section describes the experiments performed using an Electrochemical Quartz Crystal Microbalance (EQCM). The results are presented in Chapter 6. Studies in literature [68] demonstrate that current efficiencies of nickel electrodeposition are increased in the presence of boric acid which indicate that nickel deposition rates are increased while the rates of HER are decreased. This gives two possible explanations for the action of boric acid: (i) it increases Ni deposition rates (i.e. reduces its overpotential) and (ii) it adsorbs on the cathode surface to interfere with reactions (such as HER, formation of nickel oxides, hydroxides, or oxy-hydroxides) that modify the interfacial pH and co deposit products that could impede nickel electrodeposition. Both of these processes involve mass changes at the cathode surface which cannot be gleaned from total current-potential data. Hence, experiments were performed with an EQCM, which could be used to obtain *in-situ* electrode mass changes during electro-

chemical reactions.

A principal aim of these experiments was to verify current efficiency values measured by galvanostatic deposition on the disk electrode. These experiments also investigated the effect of boric acid on nickel plating rates. A second series of experiments were conducted to understand the effect of boric acid and substrate materials on the initial stages of nickel electrodeposition. Prior to this, it was necessary to understand how boric acid affected the kinetics of hydrogen evolution and electrode mass changes in the absence of  $\text{Ni}^{2+}$ . Results on different substrate materials (304SS, Nickel, Gold, and Copper), typically employed in the electroforming industry were compared.

#### 4.2.1 Electrolytes

A series of experiments were performed in Baths A, B, C, and F outlined in Table 4.1 using the EQCM to verify current efficiency data measured by galvanostatic deposition on disc electrodes. It was also expected that these experiments will reveal the effect of increasing boric acid concentration on the deposition rate of nickel which in addition to the measured exchange current densities, could demonstrate whether boric acid enhances or impedes charge transfer during Ni deposition.

Another series of experiments were performed in the electrolytes G, H, I and J given in Table 4.3. These solutions were found to be alkaline and were adjusted to pH 4.0 using reagent grade sulfamic acid and potassium hydroxide. Bath G which constituted of only potassium sulfamate provided a baseline for the study of HER in the absence of nickel ions. Bath H was used to study the effect of boric acid on HER in the absence of  $\text{Ni}^{2+}$ . To study the effect of boric acid on the initial stages of nickel electrodeposition, Baths I and J were prepared by dissolving  $\approx 18$  mM  $\text{Ni}(\text{SO}_3\text{NH}_2)_2 \cdot 4\text{H}_2\text{O}$  in supporting electrolytes containing 0 M and 0.65 M boric acid, respectively.

All solutions were purged with nitrogen gas to remove dissolved oxygen before the experiments, and the same gas was used to maintain an inert atmosphere during the experiments.

Table 4.3: Composition of sulfamate solutions used in EQCM studies.

Bath Composition (M)	G	H	I	J
$\text{Ni}(\text{SO}_3\text{NH}_2)_2 \cdot 4\text{H}_2\text{O}$	0.0	0.0	0.018	0.018
$\text{H}_3\text{BO}_3$	0.0	0.65	0.0	0.65
$\text{KSO}_3\text{NH}_2$	3.57	3.57	3.57	3.57
pH at 45 °C	4.0	4.0	4.0	4.0

## 4.2.2 Equipment

### 4.2.2.1 Operating principle of an EQCM

A Quartz Crystal Microbalance (QCM) consists of a thin quartz crystal sandwiched between metal electrodes that establishes an alternating electric field across the crystal, causing a vibrational motion of the crystal at its resonant frequency,  $f_0$  [211]. The result of this vibrational motion at  $f_0$  is the establishment of a transverse acoustic wave that propagates across the crystal thickness ( $t_q$ ) with the surfaces serving as anti-nodes for the acoustic wave. A standing wave is established when the wavelength ( $\lambda$ ) is equivalent to  $2t_q$  so the resonant frequency ( $f_0$ ) is given by Equation 4.13:

$$f_0 = \frac{v_{tr}}{\lambda} = \frac{\sqrt{\frac{\nu_q}{\rho_q}}}{2t_q} \quad (4.13)$$

where  $v_{tr}$  is the velocity of the shear wave which is essentially the transverse velocity of sound in quartz,  $\nu_q$  the shear modulus, and  $\rho_q$  the density of quartz [211].

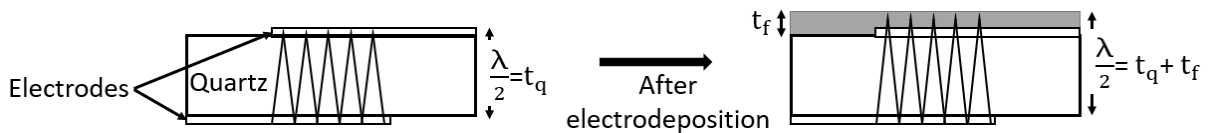


Figure 4.11: Schematic representation of the transverse acoustic wave in a quartz crystal and a composite resonator comprising the quartz crystal and a layer of foreign material. Adapted from [211]

As demonstrated in Figure 4.11, the acoustic wave will propagate through a uniform layer of foreign material. This implicitly assumes that the foreign material is

rigidly coupled to the quartz crystal surface such that the particle displacement and shear stress are continuous across the interface between the two materials [211]. For example, under conditions of the electrodeposition of thin metal layers and a monolayer adsorption of small molecules [212]. If the acoustic characteristics of the quartz and layer are similar, this system can be treated as a "composite resonator" where a change in thickness caused by the foreign layer is viewed as being similar to a change in the quartz crystal thickness [211]. Thus, a fractional change in thickness causes a fractional change in frequency as expressed in Equation 4.14 [211] given that  $t_q^{-1}$  is equivalent to  $2f_0/v_{tr}$  from Equation 4.13:

$$\frac{\Delta f}{f_0} = -\frac{\Delta t}{t_q} = -2f_0 \frac{\Delta t}{v_{tr}} \quad (4.14)$$

The negative sign is included because the wavelength of the composite resonator lengthens as its thickness increases and as a result, the resonant frequency of the composite resonator is lower than that of the unloaded QCM [211].

Appropriate substitutions can be made in Equation 4.14 for  $\Delta t (= \Delta m / (A \rho_q))$  and  $v_{tr} (= \sqrt{\frac{\nu_q}{\rho_q}})$  to give the well-known Sauerbrey equation (Equation 4.15):

$$\Delta f = \frac{-2f_0^2}{A \sqrt{\nu_q \rho_q}} \Delta m = -C_f \Delta m \quad (4.15)$$

where  $\Delta f$  is the change in frequency (Hz),  $f_0$  the resonant frequency of the quartz crystal (Hz),  $A$  the piezoelectric active area ( $0.196 \text{ cm}^2$ ),  $\rho_q$  the density of quartz ( $2.648 \text{ g cm}^{-3}$ ),  $\nu_q$  the shear modulus of quartz ( $2.947 \times 10^{11} \text{ g cm}^{-1} \text{ s}^{-2}$  for an AT-cut crystal),  $C_f$  the sensitivity factor ( $\text{Hz g}^{-1}$ ), and  $\Delta m$  the change in mass of the deposit. The Sauerbrey equation could be used to convert measured frequency changes ( $\Delta f$ ) to mass changes ( $\Delta m$ ) if the sensitivity factor ( $C_f$ ) is known. To determine the value of  $C_f$ , a calibration experiment is necessary which is discussed further in section 4.2.3.1.

The ability to employ one side of the QCM as a working electrode in an electrochemical cell to measure current in response to changes in the potential while simultaneously measuring mass changes is a powerful approach that could be used to investigate interfacial plating processes (deposition, adsorption, and desorption) [211]. In this case, the technique is called Electrochemical Quartz Crystal Microbalance (EQCM).

It should be stressed that the EQCM is not a mass sensor and the measured

frequency change may also be affected by other environmental factors such as temperature changes, roughness evolution which entrap liquid molecules, and compressive stress [211]. There are many ways a quartz wafer can be cut from a quartz rod, each resulting in a unique vibrational mode. An AT-cut quartz resonator, which consists of a thin quartz wafer cut from the rod at an angle of  $\approx 35^\circ$  with respect to the crystalline x-axis, was employed in the experiments in this thesis because it possesses a low temperature coefficient, i.e. small changes in temperature have a minimal effect on the frequency [211]. Furthermore, a temperature-controlled cell is employed in the EQCM experiments to limit temperature variations. The stress generated in films plated from sulfamate electrolytes is reportedly low [49, 181]. The evolution of roughness is assumed to be negligible for films that are only a few nanometres thick [213]. Additionally, the effect of liquid that is rigidly coupled to the oscillatory motion of the quartz crystal is usually acknowledged to be minimal and constant for a deposition experiment once a coherent film has developed [214].

#### **4.2.2.2 Substrate materials**

Commercially purchased 304 stainless steel (SS) and Au AT-cut quartz crystals with nominal resonance frequencies of 9 MHz and 8.93 MHz, respectively, were employed as working electrodes in certain cases. SS crystals have been prepared by sputtering a 304 stainless steel overcoat onto a piezoelectric quartz crystal wafer and thereby, could bear slightly different compositions from 304 SS rods.

*Preparation of nickel electrodes* - Nickel was electrodeposited on a Au quartz crystal electrode from a solution containing 1.785 M  $\text{Ni}(\text{SO}_3\text{NH}_2)_2$  and 0.65 M  $\text{H}_3\text{BO}_3$  at 55 °C; a current density of 5  $\text{mA}/\text{cm}^2$  was applied for 300 s. A freshly prepared Ni-coated Au electrode was used for each experiment.

*Preparation of copper electrodes* - Copper was electrodeposited on a Au quartz crystal electrode from a solution containing 0.5 M  $\text{CuSO}_4$ , 0.5 M  $\text{H}_2\text{SO}_4$ , and 1.1 M Ethanol at 55 °C; a current density of 20  $\text{mA}/\text{cm}^2$  was applied for 75 s. A freshly prepared Cu-coated Au electrode was used for each experiment.

The prepared crystal was fixed between two Viton O-rings and assembled in a well crystal holder as shown in Figure 4.12 which exposed an active surface area of  $0.196 \text{ cm}^2$  in the final assembly (Figure 4.12g).

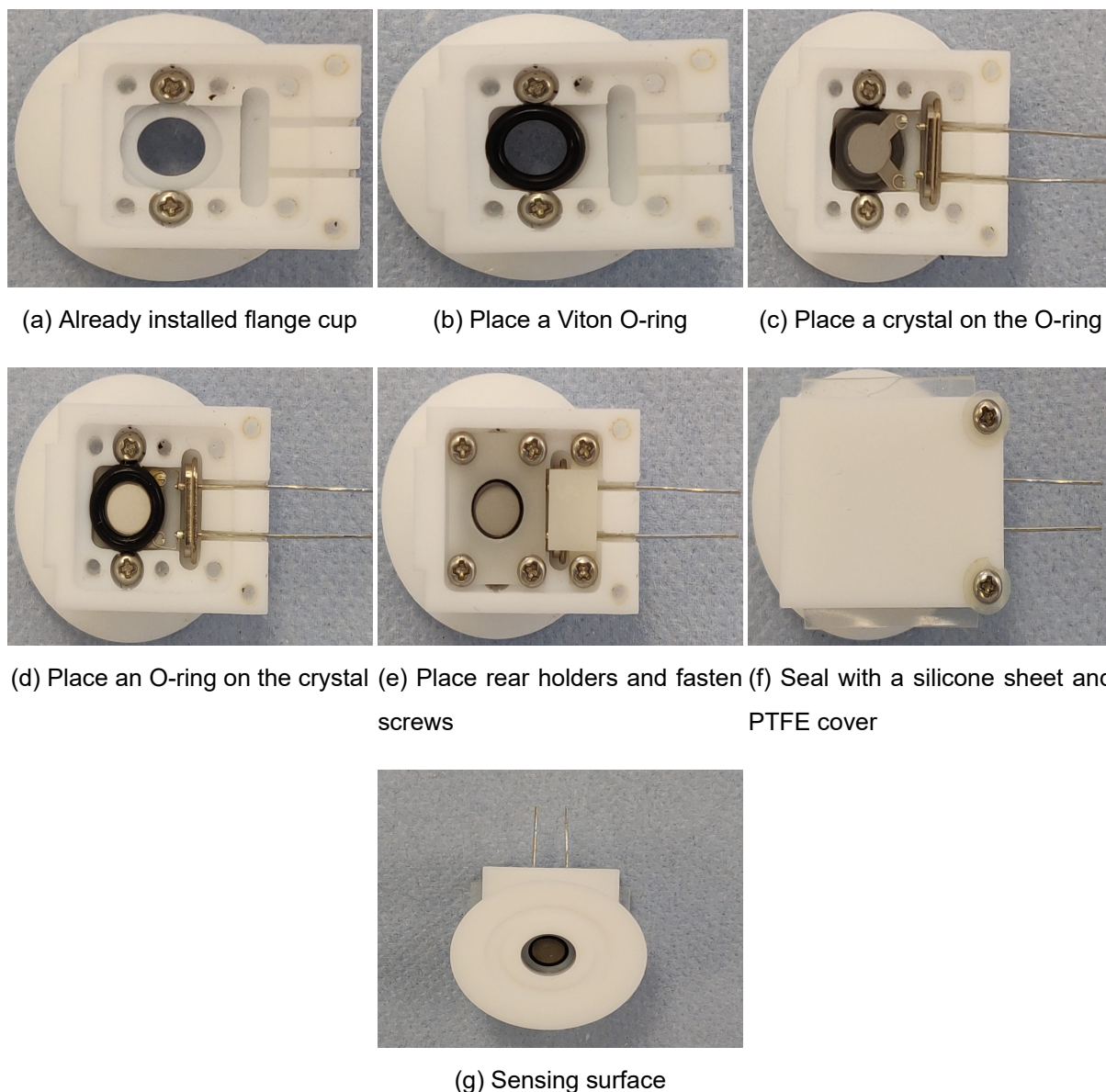


Figure 4.12: Step-by-step assembly of the quartz crystal into the well cell holder

#### 4.2.2.3 Preparation and re-usability of 304 SS quartz crystals

Before each experiment, a fresh (unused) quartz crystal (QC) surface was rinsed with deionised water and gently dried with nitrogen gas. Electrodeposited nickel produced following each experiment was dissolved from the substrate using a dilute solution of



nitric acid (0.1 M) so as not to etch or passivate the steel surface [215]. The cleaned steel crystals could then be reused.

EQCM polarisation experiments were performed in Bath B to compare errors associated with fresh (intercrystal replicates) and reused (intracrystal replicates) crystals; the results are shown in Figure 4.13. The standard deviations for four replicate measurements on fresh and reused crystals were equivalent and within  $\pm 15\%$  of the average current and frequency changes. Therefore, the crystals could be reused while accounting for an experimental error of 15%.

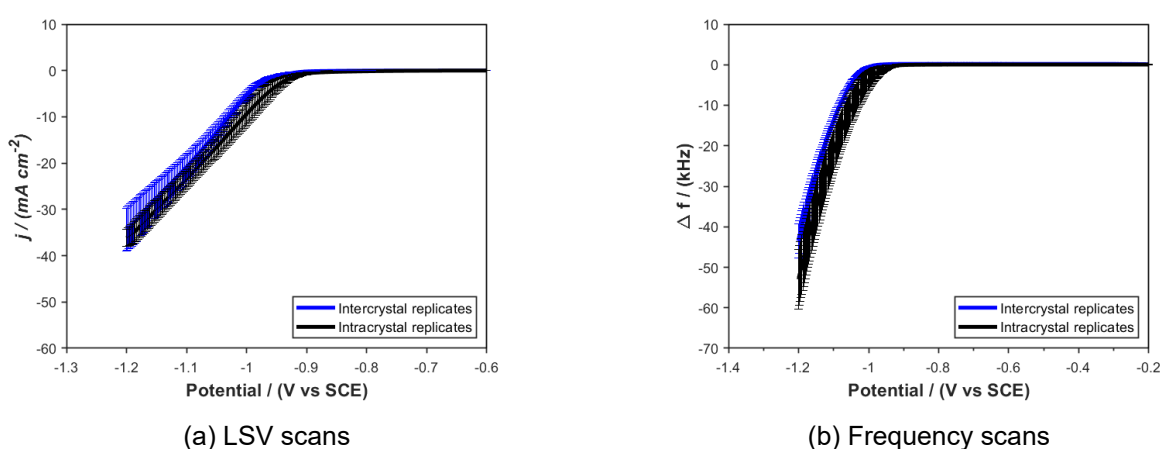


Figure 4.13: Measured polarisation and frequency scans performed in 1.78 M  $\text{Ni}(\text{SO}_3\text{NH}_2)_2 \cdot 4\text{H}_2\text{O}$  + 0.49 M  $\text{H}_3\text{BO}_3$  at  $0.005 \text{ V s}^{-1}$  and  $45^\circ\text{C}$  on fresh (intercrystal) and used (intracrystal) 304 SS quartz crystal surfaces.

#### 4.2.2.4 EQCM equipment

For the EQCM experiments, a bespoke electrochemical cell was filled with an electrolyte volume of  $\approx 100 \text{ mL}$  and setup as shown in Figure 4.14. A Seiko EG&G Quartz Crystal Analyser (Model: QCM922A) was used in the experiments to measure frequency changes. The Quartz Crystal Analyser (QCA) has a built-in digital to analogue converter (DAC) which can output the measured frequency as an analogue voltage signal. The QCA main unit is connected to the PGSTAT101 potentiostat via a BNC and monitor cable. The voltage change sensed by the QCA is read off in-situ by the potentiostat and converted to a frequency change ( $\Delta f$ ) using Equation 4.16. The ab-

solute oscillation frequency of the quartz crystal (working electrode) at the beginning of experiments is set as the initial baseline frequency. The output range is set to  $\pm 200$  kHz.

$$\Delta f(\text{Hz}) = \text{measured freq.} - \text{initial baseline freq.} = \frac{\text{output voltage} \times \text{output range}}{10} \quad (4.16)$$

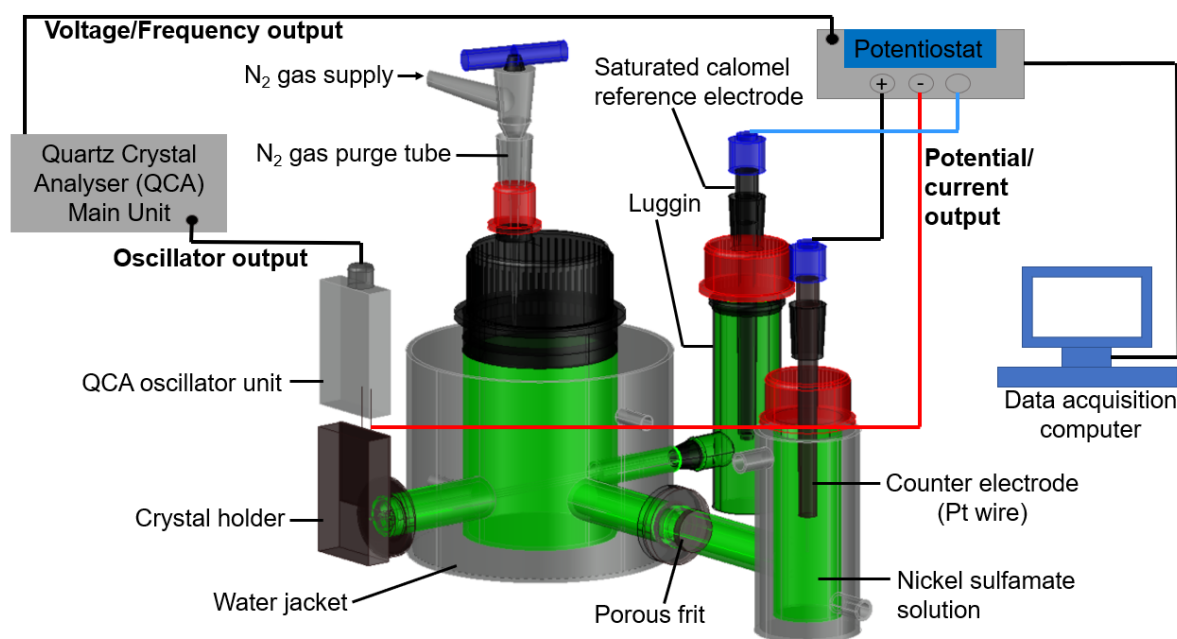


Figure 4.14: Electrochemical Quartz Crystal Microbalance apparatus.

The well crystal holder was positioned vertically enabled by the custom built electrochemical cell shown in Figure 4.14. It has been reported that with this positioning, stable and reproducible values of frequency are often obtained [216]. In all experiments, the initial baseline frequency, after placing the quartz crystal in nickel sulfamate solution, was found to stabilise at approximately 9.07 MHz.

The platinum wire earlier described in section 4.1.2.1 was employed as the counter electrode. It was placed in an anode compartment separated from the cathode by a porous glass frit (P4 with pore size of 10-16  $\mu\text{m}$ ) to limit the diffusion of anodic reaction products to the bulk solution at the cathode. The reference was a saturated calomel electrode placed in a luggin capillary; the tip of the luggin was placed at a distance of 7 mm from the quartz crystal surface to minimise the effects of uncompensated electrolyte resistance and compensate for ohmic drop.

## 4.2.3 Procedure

### 4.2.3.1 EQCM Calibration procedure

As mentioned earlier, a mechanical load on the surface of the quartz crystal causes a decrease in its resonant frequency. A metal depositing on the crystal, which is employed as the working electrode, would change the resonant frequency according to Sauerbrey equation [217, 218] given in Equation 4.15. It must be mentioned that this equation is only valid for rigid materials and for mass loadings <2% of the original QCM mass, i.e  $\Delta f$  should be  $< 0.02f_0$ . Excessive mass loadings, surface roughness, and stress could alter the crystal sensitivity [219].

Sauerbrey equation reveals that the change in frequency is inversely proportional to changes in mass. Thus, a metal depositing will cause a decrease in the oscillation frequency. Due to its ability to convert frequency changes to mass changes, the Quartz Crystal Microbalance (QCM) is a useful quantitative tool to combine with electrochemical techniques for in-situ examination of adsorption/desorption, current efficiencies for metal deposition, and oxide film formation. The sensitivity factor is required to quantitatively relate measured frequency changes to mass changes. For 9.07 MHz SS crystals, Equation 4.15 predicts a sensitivity of  $9.5 \times 10^8 \text{ Hz g}^{-1}$ . However, the theoretical  $C_f$  predicted by Equation 4.15 corresponds to a crystal vibrating in a vacuum [218]. When the crystal is placed in solution, the liquid couples to the crystal surface affecting its shear mode and decreasing  $f_0$ . Additionally, the crystal's surface roughness and electrochemical double layer also play a role in decreasing  $f_0$  [218]. Therefore, the EQCM needs to be calibrated in solution for accurate and reliable measurements.

In this study, a standard calibration method was used to determine the sensitivity and stability of the quartz crystal. An electrolyte where metal deposition is known to proceed at 100% current efficiency is used for calibration as the deposit mass ( $\Delta m$ ) can be predicted using Faraday equation (Equation 4.17) by monitoring the charge consumed. The sensitivity factor is then calculated from the experimental frequency change. Equation 4.18 for the calculation of experimental  $C_f$  has been derived by sub-

stituting Equation 4.17 in Equation 4.15.

$$\Delta m(g) = \frac{QM}{nF} \quad (4.17)$$

$$C_f = \frac{-\Delta f n F}{QM} \quad (4.18)$$

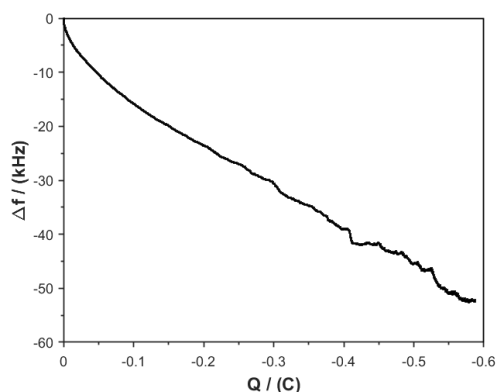
where  $n$  is the number of electrons transferred per mole of the metal deposited,  $F$  the Faraday constant (C/mol),  $Q$  the charge consumed (C), and  $M$  the atomic weight of the metal (g/mol).

#### 4.2.3.1.1 EQCM calibration with Cu electrodeposition

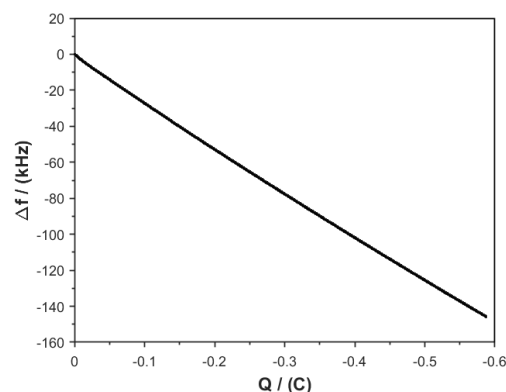
A current density of  $10 \text{ mA cm}^{-2}$  was applied for 300 s to plate copper on a 9 MHz 304 SS quartz crystal from a degassed solution of 0.1 M  $\text{CuSO}_4$  in 0.5 M  $\text{H}_2\text{SO}_4$  at 45 °C. This solution was chosen because Cu deposition from acidified solutions is known to proceed at 100% current efficiency [216] and therefore, Equation 4.18 is expected to hold true. For comparison, an 8.93 MHz gold (Au) AT-Cut crystal was also calibrated under the same condition. This is because successful calibrations with Cu electrodeposition from this solution have been reported on Au quartz crystals [216,220]. Figures 4.15a and 4.15b show the frequency decrease with charge passed measured under galvanostatic deposition conditions for 304 SS and Au crystals, respectively.

The value of  $C_f$  for the 304 SS crystal was found to be  $2.71 \times 10^8 \text{ Hz g}^{-1}$ . This value is 64% lower than the  $C_f$  value ( $7.52 \times 10^8 \text{ Hz g}^{-1}$ ) found for the 8.93 MHz Au quartz crystal calibrated under the same condition as given in Table 4.4. This is unexpected as according to Equation 4.15, the sensitivity factor of the crystal is proportional to the square of the resonant frequency which means crystals with higher resonant frequencies are expected to show higher sensitivities. However, this is not the case for 9.07 MHz 304 SS crystals calibrated using copper deposition indicating that the  $C_f$  value could be inaccurate.

The measured  $C_f$  values were compared to the ones predicted by Equation 4.15:  $C_{f,theoretical}$  (9.07 MHz) =  $9.5 \times 10^8 \text{ Hz g}^{-1}$  and  $C_{f,theoretical}$  (8.93 MHz) =  $9.21 \times 10^8 \text{ Hz g}^{-1}$ . Gold shows better agreement with the predicted value than stainless steel.



(a) 9.07 MHz 304 SS crystal



(b) 8.93 MHz Au crystal

Figure 4.15: Variation of the resonant frequency change as a function of charge passed for galvanostatic Cu deposition on (a) 304 SS and (b) Au quartz crystal electrodes from 0.1 M  $\text{CuSO}_4$  + 0.5 M  $\text{H}_2\text{SO}_4$  at  $-10 \text{ mA cm}^{-2}/45 \text{ }^\circ\text{C}$ .

Table 4.4: Sensitivity factors for Au and 304 SS crystals found using copper deposition EQCM experiments.

Electrolyte	Experiment	Substrate	Temperature ( $^\circ\text{C}$ )	Theoretical $C_f$ ( $\text{Hz ng}^{-1}$ )	Experimental $C_f$ ( $\text{Hz ng}^{-1}$ )
0.1 M $\text{CuSO}_4$ + 0.5 M $\text{H}_2\text{SO}_4$	Galvanostatic deposition ( $-10 \text{ mA cm}^{-1}$ )	9.07 MHz 304 SS	45	0.950	0.271
0.1 M $\text{CuSO}_4$ + 0.5 M $\text{H}_2\text{SO}_4$	Galvanostatic deposition ( $-10 \text{ mA cm}^{-1}$ )	8.93 MHz Au	45	0.921	0.752

This provides additional evidence that 304 SS crystals were not properly calibrated using copper deposition.

A second calibration procedure was conducted to see if calculated current densities from the frequency (or mass) changes agreed with measured current densities. Cyclic voltammetry experiments between 0.6 and  $-0.6 \text{ V}$  were performed in degassed solutions containing 0.1 M  $\text{CuSO}_4$  and 0.5 M  $\text{H}_2\text{SO}_4$  on 304 SS and Au crystals. The results from these experiments are shown in Figures 4.16 a and b, respectively. The arrows in the Figures show the potential scan direction. The current density is calculated using Equation 4.19 by combining Sauerbrey and Faraday equations for 100% current efficiency:

$$j_{calc} = \frac{nF}{C_f M A} \frac{d\Delta f}{d(t)} \quad (4.19)$$

where  $j_{calc}$  is the calculated current density ( $A\ cm^{-2}$ ),  $n$  the number of electrons involved in the reaction,  $F$  the Faraday constant ( $C\ mol^{-1}$ ),  $C_f$  the sensitivity factor ( $Hz\ g^{-1}$ ),  $M$  the atomic weight of the metal ( $g\ mol^{-1}$ ),  $\Delta f$  the frequency change (Hz), and  $t$  the time duration (s). As stated earlier, Sauerbrey Equation is only valid for frequency changes less than 2% of the resonant frequency in solution. Therefore, for crystals oscillating at 9.07 MHz, Equation 4.19 is only valid up to -181.4 kHz. The frequency changes during copper and nickel plating experiments were much lower than this.

It should also be noted that the differential of  $\Delta f$  with respect to time produces noisy  $j_{calc}$  signals. For clearer analysis, the data was smoothed in MATLAB R2018b using a moving average formula with a smoothing factor of 0.11 as shown by the green plot in Figure 4.16. It was found from Figure 4.16a that there was poor agreement between the calculated and measured current densities on 304 SS, whereas,  $j_{calc}$  for Au followed the measured current densities closely (Figure 4.16b).

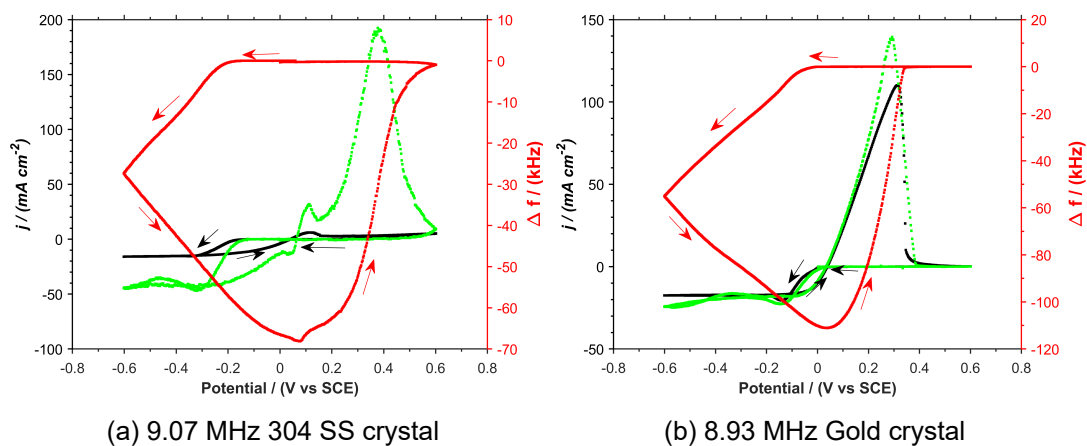
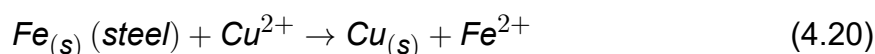


Figure 4.16: Cyclic voltammograms of 0.1 M  $CuSO_4 + 0.5\ M\ H_2SO_4$  solution on (a) 304 SS and (b) Au at  $10\ mV\ s^{-1}/45\ ^\circ C$ , showing the measured current (black), smoothed calculated currents (green), and frequency change (red). Sensitivity factors ( $C_f$ ) derived from calibrations with copper deposition from the same electrolyte are used to calculate currents.

The poor agreement observed between experimental and theoretical  $C_f$  val-

ues, as well as between measured and calculated current densities for a 304 SS crystal calibrated using copper deposition could be explained by the nearly instant displacement reaction between more reactive Fe in steel and less reactive  $\text{Cu}^{2+}$  (Equation 4.20) giving rise to precipitated copper which prevents adhesion during copper electrodeposition. No such displacement reaction occurs on the gold electrode because Au is less reactive than copper.



The effects of this copper precipitate on steel could be discerned from Figure 4.15 as frequency changes observed on Au are twice those observed on steel for the same amount of charge passed. This indicates that there is a higher deposition rate on Au compared to steel. This also means that the current efficiency of Cu deposition on steel could be less than 100%. Therefore, the EQCM system which utilises a steel crystal could not be properly calibrated using copper electrodeposition.

#### 4.2.3.1.2 EQCM calibration with Ni electrodeposition

At this point, the current efficiencies of nickel electrodeposition have been computed using the method described in section 4.1.3.2. The findings indicated that nickel could be electrodeposited with 100% current efficiency from a solution containing 1.78 M  $\text{Ni}(\text{SO}_3\text{NH}_2)_2 \cdot 4\text{H}_2\text{O}$  and 0.49 M  $\text{H}_3\text{BO}_3$  at an applied cathode current density of  $10 \text{ mA cm}^{-2}$  at 45 and 55 °C. Therefore, this solution was selected for calibration of the 304 stainless steel quartz crystal at 45 and 55 °C. It is also known that nickel electrodeposition from sulfamate systems give rise to smooth deposits with low internal stress, so stress and roughness effects could be ignored [49].

For EQCM calibration, galvanostatic deposition was conducted at  $10 \text{ mA cm}^{-2}$  for 300 s. The change in frequency as a function of charge passed at 45 °C and 55 °C are shown in Figures 4.17 a and b, respectively. It was found that both plots give good linear fits with regression coefficients of 0.9999 which is in accordance with the linearity predicted by Equation 4.15.

For each temperature, calibration measurements were performed in dupli-

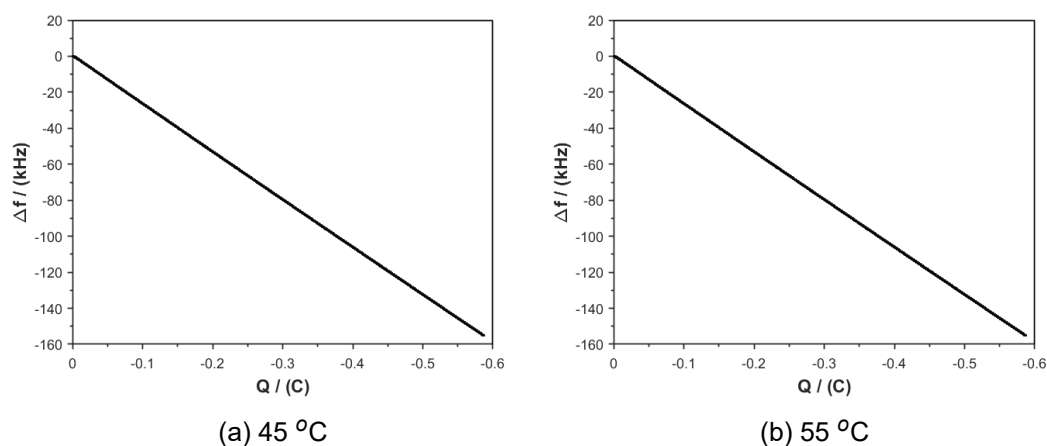


Figure 4.17: Variation of the resonant frequency change of the steel quartz crystal electrode as a function of charge passed for galvanostatic Ni deposition from 1.78 M  $\text{Ni}(\text{SO}_3\text{NH}_2)_2 \cdot 4\text{H}_2\text{O}$  + 0.49 M  $\text{H}_3\text{BO}_3$  at 10  $\text{mA cm}^{-2}$ / (a) 45 °C and (b) 55 °C.

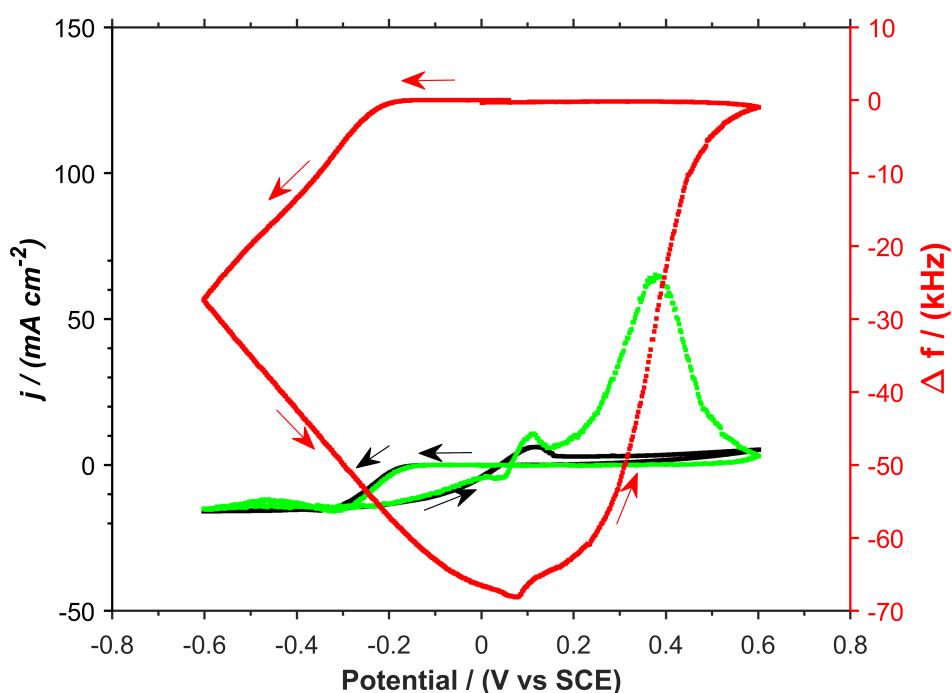


Figure 4.18: Cyclic voltammograms of 0.1 M  $\text{CuSO}_4$  + 0.5 M  $\text{H}_2\text{SO}_4$  solution on 304 SS at 10  $\text{mV s}^{-1}$ /45 °C, showing the measured current (black), smoothed calculated currents (green), and frequency change (red). The sensitivity factor ( $C_f$ ) derived from calibrations with nickel deposition from a solution containing 1.78 M  $\text{Ni}(\text{SO}_3\text{NH}_2)_2 \cdot 4\text{H}_2\text{O}$  and 0.49 M  $\text{H}_3\text{BO}_3$  is used to calculate currents.



cate. The sensitivity factors were found to be  $8.67 \times 10^8 \text{ Hz g}^{-1}$  (with a standard deviation of  $5.18 \times 10^6 \text{ Hz g}^{-1}$ ) and  $8.24 \times 10^8 \text{ Hz g}^{-1}$  (with a standard deviation of  $1.94 \times 10^7 \text{ Hz g}^{-1}$ ) for Ni deposition at 45 and 55 °C, respectively, which are within 15% of the theoretical calibration constant calculated from Equation 4.18.

With  $C_f = 8.67 \times 10^8 \text{ Hz g}^{-1}$ , currents were recalculated from the frequency change for the cyclic voltammogram measured in the solution containing 0.1 M  $\text{CuSO}_4$  + 0.5 M  $\text{H}_2\text{SO}_4$  as shown in Figure 4.16a. The results are shown in Figure 4.18. It was observed that the measured and calculated current densities are in excellent agreement over most of the potential range except between 0.05 and 0.6 V in the anodic direction where excess current densities for copper dissolution were calculated. This could be due to the break down of the deposit which begins at 0.05 V, permitting the release of Cu at 0.2 V which does not occur by electrochemical oxidation. Nonetheless, the excellent agreement between calculated and measured cathodic currents in Figure 4.18 indicates that the EQCM system could be properly calibrated with nickel electrodeposition.

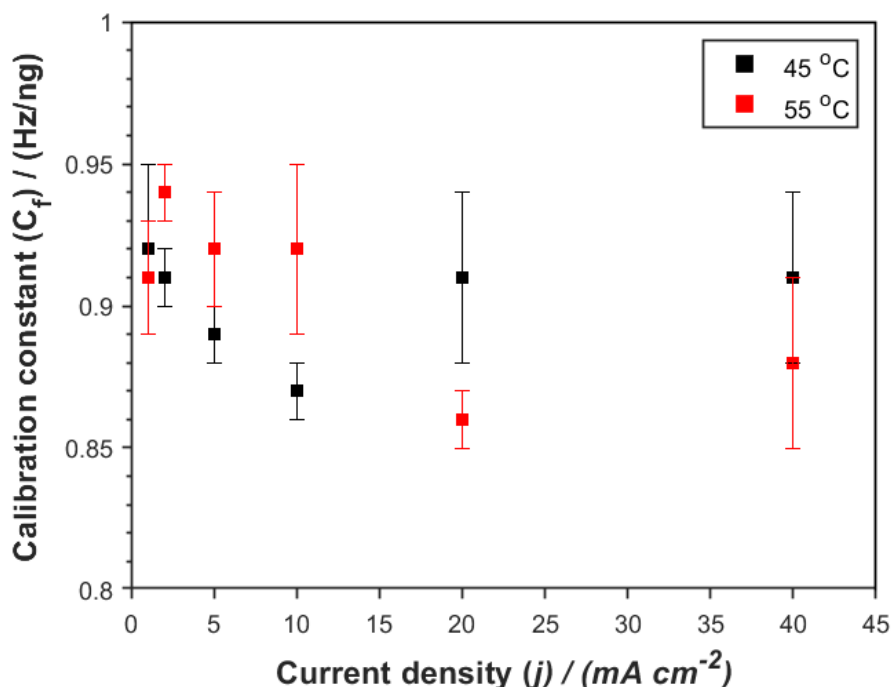


Figure 4.19: Calibration constants (sensitivity factors) of 304 SS crystals obtained from Ni electrodeposition at different applied cathode current densities and temperatures.

A series of experiments were conducted to understand the effect of applied

current densities on the calibration constants at 45 and 55 °C; the results are shown in Figure 4.19. A constant charge of 0.588 C was applied in all experiments. Calibration constant values were scattered between 0.85 and 0.95 Hz/ng with error within 5%. For analysis in this thesis,  $C_f$  values obtained at 2 mA cm<sup>-2</sup> were employed as low stress in deposits could be guaranteed at such low cathodic current densities [49].

#### **4.2.3.2 EQCM experimental procedure**

Each experiment was commenced after the crystal was allowed to resonate in the electrolyte for at least 30 minutes so as to achieve a baseline frequency signal which does not fluctuate  $> \pm 10$  Hz for 15 mins; so the frequency shift per minute was less than 1 Hz. All experiments were performed under a nitrogen atmosphere.

##### **4.2.3.2.1 Effect of boric acid on nickel electrodeposition rates and current efficiencies**

Slow Linear Sweep Voltammetry experiments were performed in Baths A, B, C, and F (Table 4.1) at 45 and 55 °C by scanning the potential from OCP (typically  $0.2 \pm 0.1$  V) to -1.2 V, at a scan rate of 0.005 V s<sup>-1</sup>. More negative potentials were not employed so as not to lead to excessive mass loadings on the crystal. As mentioned earlier (section 4.2.2.4), the current and frequency changes of the crystal were measured simultaneously by the potentiostat. The potential data was not corrected for ohmic drop as compensation had been provided by a Luggin capillary and measured currents were low (<12 mA). Additionally, the QCM lacked mass transfer regulation and therefore, all experiments were unagitated and thereby, comparable to experiments performed in unstirred systems on disk electrodes.

#### **4.2.3.2.2 Effect of boric acid on HER kinetics and the initial stages of Ni electrodeposition**

Slow Linear Sweep Voltammetry experiments were performed in Baths G, H, I, and J (Table 4.3) at 45 °C by scanning the potential from OCP to -1.7 V at a rate of 0.005 V s<sup>-1</sup>. Results were reported on different substrate materials (304 SS, Au, Ni, and Cu).

### **4.3 Characterisation of anode materials for nickel electroforming**

This section describes experiments conducted to characterise soluble nickel anode materials for electroforming whose performance remain unreported. The results are reported in Chapter 7. Given that there is little information available on these commercially employed anode materials, there are a number of unanswered questions: (i) do these materials undergo active or transpassive dissolution and what effect does this have on their current efficiency values?; (ii) are chloride ions or agitation required for their dissolution?; (iii) do sulfamate ions breakdown at these anodes?; and (iv) how does anodic behaviour influence cathodic deposition and the usage time of the electrolyte?

To answer the questions mentioned above, a set of experiments were conducted to investigate the dissolution behaviour of nickel anodes by collecting polarisation, chronopotentiometric, and chronoamperometric data; anodic current efficiency values were evaluated from gravimetric measurements following dissolution. The amount of chloride ions in the electrolyte and the electrode rotation speeds were varied to determine the effect of these parameters on the dissolution behaviour.

Ultra-violet Visible (UV-Vis) spectroscopic spectra of the electrolytes before and after nickel electrodisolution were collected to investigate the presence of electrogenerated species resulting from sulfamate ion oxidation at the anode. This is because sulfamate breakdown products have been reported to produce new absorbance bands in the UV-Vis spectra of nickel electrolytes [127–130]; the absorbance of these bands could be used to monitor concentration changes of these products and thereby,

the rate of sulfamate ion oxidation in response to changing conditions.

A final series of experiments were carried out to investigate the impact of nickel anodes and their processes on cathodic polarisation curves and the stability of bath operational parameters (cathodic and anodic current efficiencies and anode potentials) during extended electrolysis. The performance of soluble anodes is also compared with that of insoluble platinum, which is employed in the industry on a much smaller scale to enhance the thickness uniformity of complex-shaped and hollow-shaped electroforms [126, 221]. Research along these lines should reveal conditions that favour the efficient use of soluble anodes as well as factors to consider when selecting anodes for specialised electroforming applications.

### **4.3.1 Electrolytes**

To determine if chloride ions are required in the electrodisolution of nickel anodes, chloride-free and chloride-containing solutions were prepared for the experiments. The compositions of these solutions correspond to those of Bath C (pH = 3.12) and Bath E (pH = 3.26), respectively, which have been outlined in Table 4.1. The concentration of chloride ions employed was selected to reflect those in typical chloride-containing electroforming solutions [24].

Additional experiments compared the performance of chloride ions in Bath C to that in a sulfate-based solution which comprised of 1.764 M Nickel sulfate hexahydrate ( $\text{NiSO}_4 \cdot 6\text{H}_2\text{O}$ ) (Assay  $\geq 98\%$ ), 0.021 M nickel chloride hexahydrate ( $\text{NiCl}_2 \cdot 6\text{H}_2\text{O}$ ) (Assay  $\geq 99\%$ ) and 0.65 M boric acid ( $\text{H}_3\text{BO}_3$ ) (Assay  $\geq 99.5\%$ ) obtained from Sigma-Aldrich. The ionic strength of  $\text{Ni}^{2+}$  was kept the same in both baths.

### **4.3.2 Equipment**

All experiments were carried out with a computer-controlled potentiostat (PGSTAT101 from Metrohm Autolab) interfaced with NOVA 2.1 software for data collection.

#### **4.3.2.1 Anode materials employed**

It is often attractive to employ soluble anodes in industry because they replenish  $\text{Ni}^{2+}$  during the electrodeposition process. Commercially available anodes can be categorised as non-activated (pure) nickel and sulfur-activated nickel, depending on their chemical composition [50].

Table 4.5: Summary of chemical composition (in wt%), forms, and manufacturing process of nickel anode materials employed in electrochemical dissolution characterisation studies (Information taken from the technical datasheet for each material).

	Pure Ni Anodes				Sulphurised Ni Anodes					
	Vale Ni plating chips		Goodfellow Pure Ni		Vale Ni S-rounds		Vale Ni S-pellets		Xstrata D-crowns	
	>99.98	99.98	>99.98	>99.98	>99.90	>99.97	>99.97	>99.95		
Ni	>99.98	99.98	>99.98	>99.98	>99.90	>99.97	>99.97	>99.95		
S	<0.0002	0.001	<0.0002	<0.0002	≈0.019-0.025	≈0.022-0.03	0.022	0.022 (0.0175-0.03)		
C	<0.007	0.007	<0.011	<0.011	<0.0035	<0.005	<0.002	<0.002		
Co	<0.00002	0.0008	<0.00002	<0.00002	<0.065	<0.00002	<0.0002	<0.0002		
Cu	<0.0001	0.001	<0.0001	<0.0001	<0.0008	<0.0001	<0.0001	<0.0001		
Fe	<0.004	0.001	<0.004	<0.004	<0.0003	<0.004	<0.001	<0.001		
Pb	<0.000003	-	<0.00001	<0.00001	<0.0003	<0.000001	<0.0002	<0.0002		
Zn	<0.00002	-	<0.00002	<0.00002	<0.0002	<0.00002	<0.0002	<0.0002		
As	-	-	-	<0.0015	-	-	-	-		
Cr	-	0.0008	-	-	-	-	-	-		
Mg	-	0.001	-	-	-	-	-	-		
Mn	-	0.001	-	-	-	-	-	-		
Si	-	0.0008	-	-	-	-	-	-		
Ti	-	0.001	-	-	-	-	-	-		
Manufacturing process	carbonyl	carbonyl	carbonyl	carbonyl	electrodeposition	carbonyl	carbonyl	electrodeposition		
Form	plate	rod	spherical	spherical	button	spherical	spherical	button		

Table 4.5 outlines the chemical composition of some commercially available Ni anodes which have been studied in this thesis. Sulfur-activated nickel differs from pure nickel in that it contains small amounts of sulfur inclusions (0.0175 - 0.03 wt%) which influence its dissolution characteristics.

Table 4.5 also highlights that the nickel anodes are produced using different techniques, each resulting in a unique composition. S-rounds and D-crowns are the only anodes produced by electrodeposition with sulfur-containing additives [180]. The rest are produced by the carbonyl (Mond) process which has been described earlier in chapter 2 [146,222]. Although it is unclear from literature how the different manufacturing processes influence the electrochemistry of the anode materials, one can deduce from Table 4.5 that carbonyl anodes contain greater and lesser amounts of carbon and impurities (such as Co, Cu, Pb, and Zn), respectively, compared to electrolytic anodes.

The different manufacturing processes, which have been outlined in Table 4.5, produce anodes in various shapes as shown in Figure 4.20. It would appear that the technical benefits of pellets have rendered the S-rounds obsolete (which was once commonly used) by major manufacturers such as Vale [223]. Hence, electroformers have sought S-pellets and D-crowns as alternatives but there are limited studies on the electrochemistry of these anodes. A series of experiments were also performed with the platinum wire (surface area = 0.3 cm<sup>2</sup>) acting as the anode.

#### **4.3.2.2 Anode preparation**

Disk specimens were cut out of plating chips, Goodfellow Ni rod, S-rounds, and D-crowns. The specimens were cleaned using the procedure described in section 4.1.2.3 and assembled in the RDE illustrated in Figure 4.2, which exposes an active surface area of 1.35 cm<sup>2</sup>.

Threaded holes were drilled in P- and S-pellets, and a titanium wire with a screw tip was inserted to form an electrode with low electrical resistance of <0.1  $\Omega$  (Figure 4.21) to mimic the industrial processes where Ni and Ti are in contact with each other. The pellets were polished sequentially with grades P#1200, P#2400, and



Figure 4.20: Forms of Ni anode materials.

P#4000 silicon carbide grit paper, rinsed with deionised water, and dried with  $N_2$  gas. Before each experiment, the surface areas of polished spherical pellets were calculated from five diameter measurements taken from multiple locations on the pellet using a vernier caliper and were used to report current densities. The surface areas of Ni P- and S-pellets were around  $3.95 \pm 0.22 \text{ cm}^2$  and  $4.24 \pm 0.52 \text{ cm}^2$ , respectively.



Figure 4.21: Photograph of a Ni P-pellet assembly.



#### 4.3.2.3 Polarisation and current efficiency measurements

The three-electrode cell setup depicted in Figure 4.1 was used to measure polarisation curves and current efficiencies of the electrodisolution of nickel anodes by performing Linear Sweep Voltammetry and chronopotentiometry/chronoamperometry experiments, respectively. The nickel materials outlined in Table 4.5 were employed as working electrodes; a Pt wire (surface area = 0.3 cm<sup>2</sup>) served as the cathode or counter electrode, while a saturated calomel electrode (SCE) was used as a reference. The rotational speed of the ED101 RDE was controlled by a CTV101 Speed Unit (Radiometer analytical).

The one-compartment glass cell was filled with 70 mL of electrolyte. The solutions in these experiments were not deoxygenated, and an inert environment was not maintained during the measurements because anodic reactions were the main interest of these experiments. Furthermore, this mimicked industrial conditions where dissolved oxygen is typically present [24].

#### 4.3.2.4 Sulfamate ion oxidation studies

It is reported that sulfamate ions are oxidised when insoluble or passive soluble anodes are used [127–130]. Under these conditions, the UV-Vis spectra of the electrolysed sulfamate systems were found to show absorption bands that were not visible in the UV-Vis spectra of the fresh (non-electrolysed) bath [127–130]. These absorption bands were proposed to be the result of products generated from sulfamate breakdown. However, the issue of sulfamate ion oxidation at Ni pellets used for electroforming is largely unresolved with regards to: (i) the conditions under which the process occurs, (ii) the rate of anode product formation, (iii) the identity of the electrogenerated products, and (iv) the impact of these products on nickel electrodeposition.

Experiments to investigate sulfamate ion breakdown at Ni pellets were performed by using an ultraviolet spectrophotometer to collect the UV-Vis spectra of nickel sulfamate solutions before and after electrolysis. The operating principle of this instrument is discussed in the following section.

A set of galvanostatic deposition experiments in which the P-pellet anode was used were carried out in a cell with separate cathode and anode compartments (Figure 4.3) to verify that any electrogenerated products detected were produced as a result of the anode process. An RDE with 304 SS disc functioning as the cathode was put into the cell containing 450 mL of catholyte, while the anode was put in a bridge tube carrying 16 mL of anolyte. The UV-Vis spectra of catholyte samples were taken at regular intervals during electrolysis; these results were compared to those collected from experiments performed without separating the anode. It was anticipated that electrogenerated products of anodic processes will no longer be detected in the catholyte under conditions where the anode was separated.

A second series of chronopotentiometry experiments were performed in the cell setup shown in Figure 4.3 to investigate changes in the concentration of electrogenerated anode product(s) (qualitatively assessed from its absorbance) in response to changes in electrolysis conditions (type of anode material and anode current density); the concentration of an absorbing species is proportional to the absorbance which is explored in section 4.3.2.4.1. The cell was filled with 60 mL of electrolyte. Different anode materials with comparable surface areas were employed as the working electrode: P-pellet, S-pellet, and a Pt wire spiral (surface area =  $4.77 \text{ cm}^2$ ). An RDE containing a 304 SS disc was used as the counter electrode while SCE was used as a reference. Before each experiment, the electrolyte was purged with  $\text{N}_2$  gas to remove dissolved oxygen which could have deleterious effects on Ni electrodeposition. An inert atmosphere was also maintained during the experiments.

#### **4.3.2.4.1 Operating principle of Ultraviolet Visible spectrophotometer**

Figure 4.22 shows an illustration of a single beam spectrophotometric experiment used in this thesis. Light from a continuous source is passed through a monochromator (a prism, grating, or filter) to produce light of a narrow band of wavelengths from the incident beam. Thereafter, the monochromatic light with irradiance (i.e. energy per unit time per unit area,  $\text{W/m}^2$ ),  $P_0$  is allowed to travel through a sample-containing cuvette of pathlength,  $d$ . The irradiance of the beam emerging from the other side of

the cuvette is  $P$ . Some of the light may be absorbed by the sample, so  $P \leq P_0$  [224].

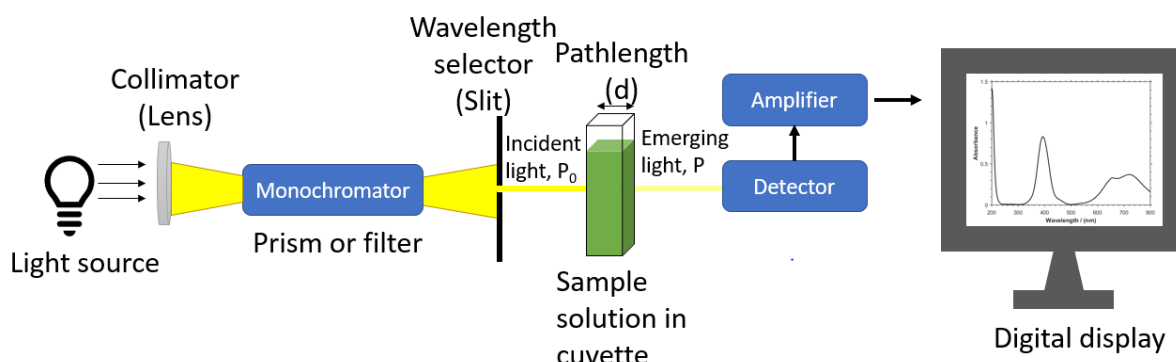


Figure 4.22: Diagram of a single beam spectrophotometric experiment showing the basic instrumentation. Adapted from [224]

The incident irradiance,  $P_0$ , is not directly measured in the single-beam experiment shown in Figure 4.22. Instead,  $P_0$  is determined from the irradiance of light that has travelled through a cuvette filled with a reference or baseline solution (pure solvent or a reagent blank). Next, the sample is inserted in place of the baseline solution to determine  $P$  from the irradiance of light that strikes the detector after passing through the sample. A baseline solution is employed to compensate for light reflection, scattering, and adsorption by the cuvette and solvent [224].

The fraction of the light that passes through the sample is defined as Transmittance,  $T$  which ranges from 0 to 1 [224].

$$T = \frac{P}{P_0} \quad (4.21)$$

Absorbance,  $A$  is defined from the Transmittance according to equation 4.22 [224]:

$$A = \log \left( \frac{P_0}{P} \right) = -\log T \quad (4.22)$$

Based on Beer's law, the absorbance is directly proportional to the concentration,  $c$ , of the light-absorbing species in the sample [224]:

$$A = \epsilon dc \quad (4.23)$$

where  $\epsilon$  is the molar absorptivity ( $M^{-1} \text{ cm}^{-1}$ ).

Typically, the equipment determines the true absorbance of a sample at each wavelength by deducting the absorbance of the baseline spectrum from the measured absorbance of the sample. [224].

#### 4.3.2.4.2 UV-Vis spectroscopy equipment

A Varian Cary 5000 UV-Vis spectrophotometer was used to obtain UV-Vis spectra of nickel sulfamate solutions. A quartz cuvette with a pathlength of 1 mm was used; a longer pathlength of 10 mm produced high absorption signals distorted by background noise as shown in Figure 4.23. This could be attributed to the high concentrations of  $\text{Ni}^{2+}$  species (1.78 M) present in nickel sulfamate solutions. The 1 mm pathlength cuvette was placed in a cuvette adapter, which was then inserted into the spectrophotometer's 10 mm cuvette holder. Deionised water was employed as the baseline solution.

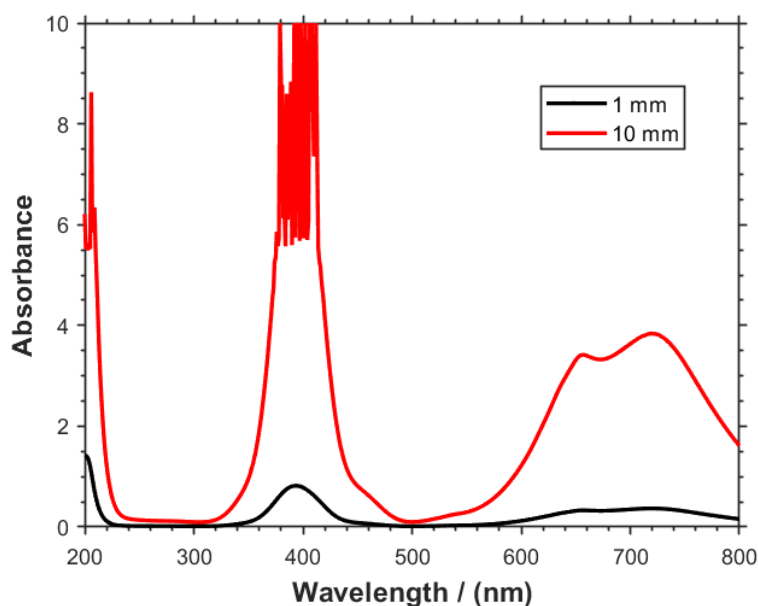


Figure 4.23: UV-Vis spectra of fresh Bath E acquired with cuvettes of 1 mm and 10 mm pathlengths.

#### **4.3.2.5 Influence of anodic processes on electrodeposition and long-term stability of the electrolyte**

Initial studies were performed to investigate the effect of anodic processes on nickel electrodeposition by measuring cathodic polarisation curves in the absence and presence of sulfamate decomposition products. Polarisation measurements were performed in the cell shown in Figure 4.1 with a 304 SS RDE acting as the working electrode, a Ni S-pellet counter electrode, and a saturated calomel reference. Sulfamate decomposition products were introduced into the electrolyte by performing galvanostatic dissolution experiments with a Ni P-pellet working electrode and 304 SS counter electrode.

In the next set of experiments, anode and cathode current efficiencies, as well as their potentials, were measured during extended electrolysis to characterise the stability of nickel sulfamate electrolytes. Chronopotentiometry experiments were conducted in a sealed one-compartment glass cell (Figure 4.1) containing 60 mL electrolyte volume, with a 304 stainless steel working electrode and a saturated calomel reference electrode. The materials employed as counter electrodes were Ni P-pellet, Ni S-pellet, and Pt (surface area =  $0.3 \text{ cm}^2$ ); the Pt anode was studied to allow a comparative evaluation of insoluble anode materials. A multimeter was used to record the anode potential during electrodeposition while the potentiostat monitored the cathode potential. Solutions were deoxygenated using nitrogen gas and an inert atmosphere was maintained during the experiments as described in section 4.1.1.

### **4.3.3 Procedure**

#### **4.3.3.1 Polarisation and current efficiency measurements**

Linear Sweep Voltammetry experiments to measure dissolution polarisation curves were performed by sweeping the potential of the working electrode from Open Circuit Potential to +1.6 V, at a slow scan rate of  $5 \text{ mV s}^{-1}$ . These experiments were conducted in Bath C, Bath E (Table 4.1), and a Watts-type electrolyte at  $45 \text{ }^\circ\text{C}$  under

quiescent conditions to study the influence of chloride ions on dissolution characteristics. Another set of experiments were performed to investigate the effect of various RDE rotation speeds (0, 300, 600, and 900 rpm) on the polarisation behaviours of non-activated (plating chips) and sulfur-activated (D-Crowns) Ni anodes in Bath C.

The uncompensated resistance was determined by impedance spectroscopy as detailed in section 4.1.3.1.3. Positive feedback was applied by the potentiostat (PG-STAT101, Methrom Autolab) to compensate for ohmic drop during the measurement. In this case, a correctional voltage proportional to the current,  $I$ , flowing through the working electrode is fed back to the input of the potentiostat and added to the applied potential to compensate the ohmic drop. As a result, the positive feedback mechanism automatically adapts for changes in cell current. In principle, the potential of the working electrode is controlled at the preset applied value. Although, this technique assumes that  $R_U$  is constant for the duration of the experiment, this is often not the case, as the electrolyte conductivity could change, and bubbles or surface layers could form on the WE. This could lead to overcompensation errors which could cause the potentiostat control circuit to oscillate or become unstable and fail [225]. Therefore, it is recommended to use 80-90% of the measured uncompensated resistance ( $R_U$ ), to avoid oscillations and damage to the potentiostat, WE, and electrolyte [226]. For the anode polarisation experiments, it was found that 90%  $R_U$  could be used for ohmic drop compensation without oscillations or instabilities.

Chronopotentiometry experiments were carried out from quiescent Bath E solutions at 45 °C and applied anode current densities in the range of 1.6 to 8.6 mA/cm<sup>2</sup> using two different soluble nickel working electrodes: P-pellets and S-pellets. In the chronopotentiometry technique, a constant current is applied to the working electrode using a potentiostat while its potential is simultaneously measured against a reference electrode. The duration of each experiment was determined by the time it took to pass a charge of 43.7 C. Potential measurements from these experiments could be used to determine whether nickel dissolved actively or transpassively.

Current efficiencies of active and transpassive dissolution were compared by carrying out chronoamperometry experiments from quiescent solutions of Bath E at 45 °C using P-pellet and S-pellet working electrodes. In these experiments, a constant

potential reflective of active or transpassive dissolution as determined from polarisation measurements was applied to the working electrode while the current flowing through was measured using a potentiostat. A charge of 43.7 C was applied to all experiments by employing a charge cutoff signal in the NOVA software.

The current efficiency (the percentage ratio of the experimental to theoretical Faradaic metal dissolution rates) was determined by weighing the anode before and after each chronopotentiometry/chronoamperometry experiment using the same procedure described in section 4.1.3.2. The dissolved mass of Ni,  $w$ , was used to assess the dissolution efficiency using Equation 3.10 given in Chapter 3.

It is worth noting that when Ni anodes were immersed in the test electrolyte at Open Circuit Potential for durations longer than those employed in the experiments, there were no discernible mass changes measured in the anodes. This indicates that anodes did not chemically dissolve in solution and any mass decrease measured from the experiments was solely due to electrochemical dissolution.

#### **4.3.3.2 Sulfamate ion oxidation studies**

Electrodissolution experiments were carried out in the galvanostatic mode from Bath E solutions at 45 °C and applied current densities in the range of 5 to 25 mA/cm<sup>2</sup> using a 0.1 L undivided cell and different working electrodes: an insoluble Pt spiral anode as well as soluble Ni P- and S-pellets. A charge of 500 C was passed in every experiment. Additionally, potentials of the anode and cathode against a saturated calomel reference electrode were monitored using a potentiostat and multimeter, respectively.

A series of galvanostatic dissolution experiments were performed in divided and undivided cells at a fixed current density of 25 mA cm<sup>-2</sup> using Ni P-pellet anode with varying amounts of charge between 75 C and 1000 C. These tests confirmed whether newly formed species during dissolution were produced at the anode in an electrochemical reaction, as was anticipated. All solutions were agitated by rotating the 304 SS cathode at 450 rpm.

For all experiments discussed in this section, samples were collected before

and after electrodisolution for analysis by UV-Vis spectroscopy to identify samples which contained new species generated during the experiments.

#### 4.3.3.2.1 UV-Vis spectroscopy test procedure

The spectrophotometer was used to measure the UV-Vis spectra of samples between wavelengths of 200 to 800 nm. The data interval and integration time were set to 1 nm and 0.1 s, respectively, resulting in a scan rate of  $600 \text{ nm min}^{-1}$ .

To warm up the UV-Vis lamps, the spectrophotometer was turned on 30 minutes before measurements were to be taken. Baseline correction was done in water to subtract environmental effects (humidity, temperature, pressure, etc). Notably, the baseline correction did not need to be repeated before each measurement performed on the same day because the Cary WinUV programme automatically stored and subtracted the baseline. Nonetheless, baseline correction was repeated on a daily basis.

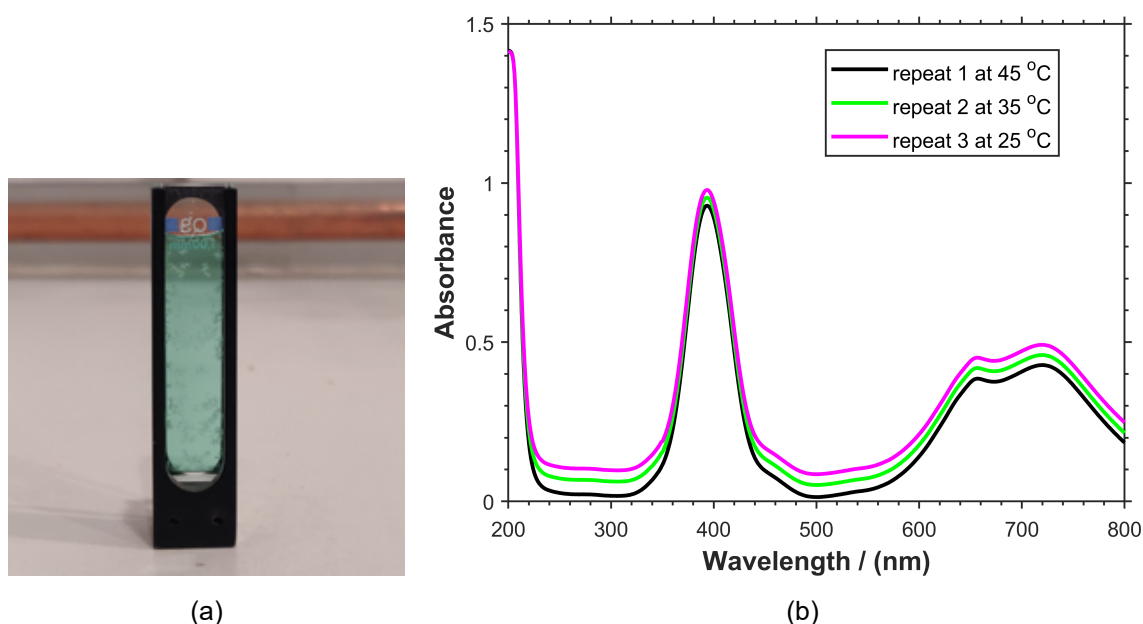


Figure 4.24: (a) Boric acid crystallisation in the cuvette taken at  $25 \text{ }^{\circ}\text{C}$  and (b) UV-Vis spectra of non-electrolysed Bath E acquired at different temperatures, which were not reproducible due to boric acid crystallisation.

Before each measurement, the cuvette was meticulously washed several times



with DI water and twice with the solution sample. The surface of cuvette was wiped dry before assembly into the cuvette adapter. Thereafter, 300  $\mu\text{L}$  of the solution sample was transferred into the quartz cuvette using an automatic pipette (range 20 to 200  $\mu\text{L}$ ), ensuring that no bubbles were trapped in the compartment.

As mentioned earlier, boric acid crystallised out of solution at temperatures below 35  $^{\circ}\text{C}$  which has been illustrated in Figure 4.24a. This produced irreproducible absorbances shown in Figure 4.24b; repeat 1 was taken from a sample at 45  $^{\circ}\text{C}$ , where no visible boric acid crystals could be observed. The same sample was allowed to cool down to 35  $^{\circ}\text{C}$  and 25  $^{\circ}\text{C}$  before measurements for repeats 2 and 3 were taken, respectively. To attain reproducible UV-Vis spectra data for nickel sulfamate electrolytes containing boric acid, solutions were stirred and heated to  $48 \pm 2$   $^{\circ}\text{C}$  using a hotplate stirrer before being placed in the cuvette. This resulted in reproducible absorbances within  $\pm 2\%$ .

#### **4.3.3.3 Influence of anodic processes on electrodeposition and long-term stability of the electrolyte**

Cathodic polarisation curves in the absence and presence of sulfamate decomposition products were measured in Bath E at 45  $^{\circ}\text{C}$  by performing Linear Sweep Voltammetry from OCP to -1.4 V at a slow scan rate of 5  $\text{mV/s}^{-1}$ . The 304 SS working electrode was set to rotate at a speed of 450 rpm. Galvanostatic dissolution experiments to introduce sulfamate decomposition products were performed by applying a constant current density of 25  $\text{mA cm}^{-2}$  to the P-pellet working electrode while the 304 SS counter electrode was set to rotate at 450 rpm. Different quantities of charge were passed (250 and 500 C) to change the amount of sulfamate decomposition products in solution. Changes in the concentration of decomposition products were investigated by collecting UV-Vis spectra of electrolyte samples before and after dissolution, as described in section 4.3.3.2.1.

Long-term electrodeposition experiments were performed in Bath E at 45  $^{\circ}\text{C}$  to determine the degree of instability that could be encountered when Pt, Ni P-pellet, and Ni S-pellet materials are used as anodes. The degree of instability was charac-

terised by changes in anode and cathode current efficiencies and potentials in successive plating experiments in the same solution. For each electrodeposition experiment with a different anode material, a fresh electrolyte was used. In the experiment, a fixed cathode current density of  $40 \text{ mA cm}^{-2}$  was applied to the stainless steel working electrode rotating at 450 rpm, while the charge was increased from 157.69 C to 316.17 and 632.33 C. These values of charge were selected to successively plate out 40, 80, and 160 microns of Ni deposit. Additionally, the potentials of the cathode and anode were monitored using a potentiostat and multimeter, respectively, while the deposition process proceeded. The cathode and anode were removed from solution, after plating out a desired thickness, for weight measurements that were used to compute the efficiency values as described in section 4.3.3.1.

Changes in  $\text{Ni}^{2+}$  concentration during extended electrolysis of the electrolytes were monitored from gravimetric measurements of the anode and cathode; variations were found to be within 5% of the initial bulk concentration (1.785 M). A pure solution of 2.1 M nickel sulfamate tetrahydrate was used to adjust the concentration of  $\text{Ni}^{2+}$ .

# Chapter 5

## Effect of boric acid on nickel electrodeposition under electroforming conditions

Electroforming conditions recommend the use of electrolytes which contain nickel sulfamate, small amounts of nickel chloride, and boric acid ( $\text{H}_3\text{BO}_3$ ). The addition of boric acid to the electroforming bath is reportedly critical to the production of electroforms with low internal stress [68]. This constituent has been demonstrated to have significant improvements on the electrodeposition current efficiency [68, 104, 121] and deposit morphology [75, 108, 227]. Undoubtedly, boric acid plays a major role in the success of the electroforming process but the nature of this role remains largely unresolved.

As mentioned before, Ji et al. [67] found that adding boric acid to the electrolyte prevented the rise in cathode surface pH that is typically encountered during nickel electrodeposition, which was later confirmed by Tsuru et al. [68]. Ji et al. [67] speculated that boric acid acts as a pH buffer. Typically, the practical pH range of a buffer is equivalent to its  $\text{pK}_a \pm 1$ . Thus, it is not understood how  $\text{H}_3\text{BO}_3$ , which has a  $\text{pK}_a$  of  $9.23 \pm 1$  [102], can act as a buffer in typical nickel electroforming baths which often have pH ranges of 3-4. Moreover, reports of current efficiencies greater than 96% for nickel electrodeposition from sulfamate solutions containing boric acid [68, 121] suggest that the rate of side reactions (oxygen, proton, and water discharge), which cause a rise in electrode surface pH, is marginal. Therefore, it appears that boric acid affects the relative rates of nickel deposition and other reactions, which have been reported to influence deposit characteristics [61].

The principal aim of this chapter is to understand how boric acid affects nickel deposition kinetics during electroforming. The first step was to establish the effect of individual constituents in the electroforming bath on the electrochemical behaviour of nickel electrodeposition, described by partial Ni current density-potential data obtained

from polarisation and gravimetric measurements. This is important in order to delineate the role of boric acid in the full electroforming bath. Data was collected from solutions with different amounts of boric acid, and in some cases with nickel chloride only. To ascertain whether boric acid affects the electrodeposition mechanism and whether it enhances nickel ion reduction, Tafel slopes and exchange current densities are evaluated from the partial Ni current density-potential data. Changes in temperature and cathode rotation speed are also known to affect surface processes, thereby the dependence of kinetic parameters on these variables is presented to provide additional insight.

The results presented in this chapter will advance current understanding of the roles of boric acid, temperature, and bath agitation during the electroforming process. Results were obtained on a 304 stainless steel disk electrode using commercially applicable nickel sulfamate electrolytes, which contain 1.78 M  $\text{Ni}^{2+}$ , to ensure that the information acquired is pertinent to the electroforming industry.

## **5.1 Nickel electrodeposition from solutions without agitation**

### **5.1.1 Total vs. partial polarisation curves**

During the electrodeposition of nickel, four main reactions occur at the cathode :  $\text{Ni}^{2+}$ ,  $\text{O}_2$ ,  $\text{H}^+$ , and  $\text{H}_2\text{O}$  electroreduction. The cathode process could be characterised by polarisation curves i.e. the dependence of the current density on the cathode potential ( $j=f(U)$ ). However, the total polarisation curve characterises a complex phenomena occurring at the cathode and does not give specific information about the process of  $\text{Ni}^{2+}$  discharge. The method of resolving the total polarisation curve into partial polarisation curves for nickel deposition and hydrogen evolution (i.e. a combination of  $\text{H}^+$  and  $\text{H}_2\text{O}$  electroreduction) is discussed in this section. Information that could be gleaned from comparing the partial polarisation data with the total polarisation data for nickel electrodeposition is also examined.

Figure 5.1 presents total polarisation curves,  $j$ - $U$  (solid lines) for Bath A and

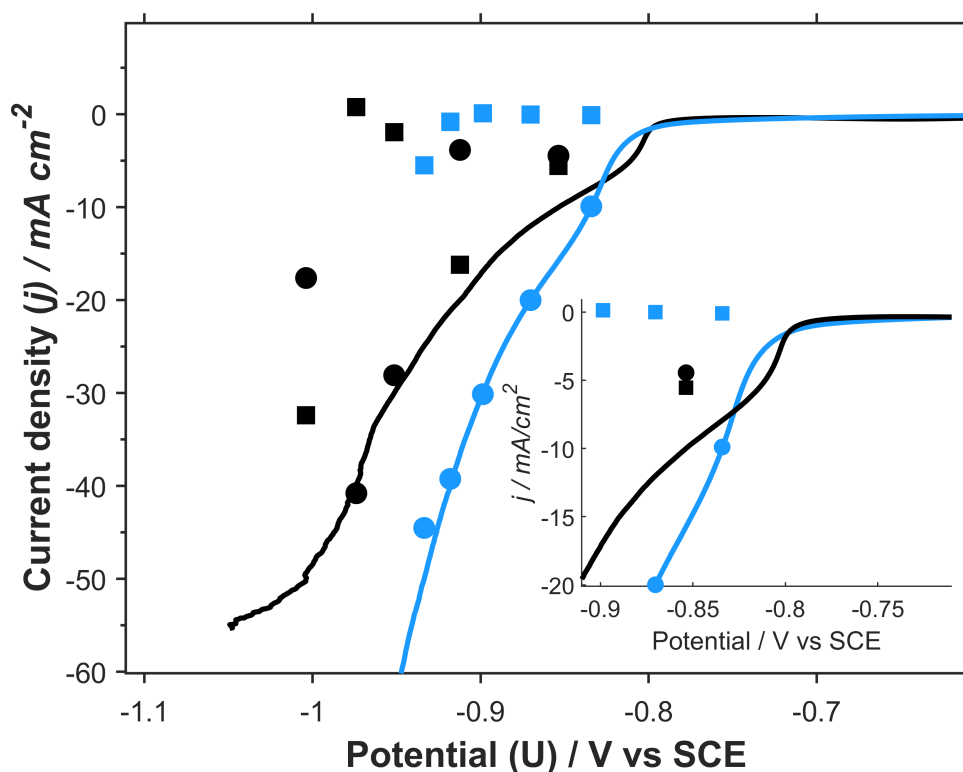


Figure 5.1: Polarisation curves: total current densities ( $j$ , solid lines) and partial current densities for Ni deposition ( $j_{Ni}$ , circles) and hydrogen evolution reaction ( $j_{H_2}$ , squares) in quiescent Bath A (black) and Bath B (lightblue) at 40 °C. This data shows the effect of boric acid on the rates of nickel electrodeposition and hydrogen evolution reactions. The Figure inset shows the effect of boric acid on the current breakthrough potential.

Bath B, i.e. solutions containing nickel sulfamate only (solid black line) or nickel sulfamate and 0.49 M boric acid (solid lightblue line), respectively. These data were obtained at 40 °C on a stationary 304 stainless steel (SS) electrode and shows the effect of boric acid on the total polarisation curves. In the presence of boric acid, there is a slight change in the potential at which a current breakthrough is observed, going from -0.8 V to -0.81 V (zoom inset, Figure 5.1). However, further inspection of the polarisation data shows that the addition of boric acid decreases the overpotential where significant current densities (i.e.  $>7 \text{ mA cm}^{-2}$ ) are observed. This indicates an increase in the rate of cathode reactions in the presence of boric acid, but as stated earlier, it is not clear if this increased rate pertains to that of nickel electrodeposition or the side reactions, unless the partial current densities are inspected.

As mentioned in the experimental section, current densities ( $j$ ) selected from the total polarisation curves are used for galvanostatic deposition of nickel and current efficiency (CE) data measured by gravimetry of the deposits is used to resolve the total polarisation curves into partial polarisation data, which is also depicted in Figure 5.1. For this purpose, the partial current density for Ni<sup>2+</sup> discharge,  $j_{Ni}$ , is determined using Equation 5.1.

$$j_{Ni} = CE * j \quad (5.1)$$

Notably, deposits obtained from H<sub>3</sub>BO<sub>3</sub>-free solutions were loose and observably possessed high levels of internal stress, unlike their counterparts obtained from electrolytes containing boric acid which were compact and coherent. Therefore, care had to be taken during handling to prevent the loss of deposits. Visual inspection of the electrolyte after electrodeposition showed a clear solution and it was assumed that deposits did not deadhere during the experiments. Plated nickel was carefully removed from the electrolyte, rinsed with deionised water, and left to dry for a couple of days at room temperature in a storage box before weight measurements were taken. Weekly weight measurements of deposits were taken for two weeks and it was found that weights remained constant which indicated that deposits had completely dried and the weights taken were solely that of the deposit. Some experiments were repeated thrice to check reproducibility and it was found that  $j_{Ni}$  could be measured to within  $\pm 1.5\%$  ( $\pm 0.6 \text{ mA cm}^{-2}$ ). This low standard deviation indicated that the deposit did not deadhere from the electrode during experiments and subsequent handling.

The partial current density for hydrogen evolution (which is presumably the only side cathodic reaction),  $j_{H_2}$ , is determined from the difference between the total current density,  $j$ , and  $j_{Ni}$ :

$$j_{H_2} = j - j_{Ni} \quad (5.2)$$

Although oxygen reduction is also reported to precede Ni deposition [92, 114], all solutions were de-oxygenated in the presented experiments, and hence the oxygen reaction would be suppressed. The partial current densities,  $j_{Ni}$  and  $j_{H_2}$ , are denoted in Figure 5.1 as circles and squares, respectively.

Generally speaking, the difference between  $j_{Ni}$  and the total current density ( $j$ )

at any potential could be used to determine whether Ni deposition is the sole reaction (i.e.  $j_{Ni} = j$ ) or if there are side reactions occurring alongside nickel deposition (i.e.  $j_{Ni} < j$ ). This principle is applied in the interpretation of the data shown in Figure 5.1.

The data in Figure 5.1 reveals that nickel electrodeposition from sulfamate-only solution (Bath A) occurs with low current efficiency. At low overpotentials, i.e. between -0.85 and -0.91 V,  $j_{Ni}$  is only 4.4 mA cm<sup>-2</sup> and 3.8 mA cm<sup>-2</sup>, which constitutes 45 and 19% of the total current density, respectively. One may conclude that at these potentials, hydrogen evolution reactions occur simultaneously with Ni deposition, according to Equations 2.12 and 2.13 given in section 2.1.1.2, Chapter 2. Such a behaviour has been observed in previous studies on Ni electrodeposition in the absence of boric acid [64, 65, 101, 108].

At intermediate potentials between -0.95 and -0.97 V, still in Bath A, there is a sharp increase in the partial current density for nickel up to 40.8 mA cm<sup>-2</sup>, such that the  $j_{Ni}$ -U plot converges with the  $j$ -U curve. At this point, Ni deposition seems to be the dominant reaction and  $j_{H_2}$  is reduced to  $< 2 \pm 0.6$  mA cm<sup>-2</sup>. Further increase in electrode potential (between -0.97 and -1.0 V) shows a drop in the nickel ion reduction current density, presumably due to the onset of water reduction. In effect, this data demonstrates that the use of an all-sulfamate system at 40 °C provides a very narrow window for nickel deposition, and hydrogen evolution is the more significant reaction at low and high overpotentials enabled via H<sup>+</sup> reduction or H<sub>2</sub>O discharge. Consequently, a second issue with hydrogen evolution is the alkalization at the electrode surface which may reach a degree that promotes the formation of nickel hydroxides and oxides [65, 108]. However, one needs to recall that the electrode is cathodic, and the data shows that high currents for nickel deposition are achieved at intermediate potentials, and hence the passive film may either not be permanent or formed.

When boric acid is present (bath B), the partial Ni polarisation curves converge with the total polarisation curves over the current density range examined in Figure 5.1 while the partial current density for hydrogen evolution remains suppressed to negligible levels of 0.7 mA cm<sup>-2</sup> and appears to increase only at more negative potentials < -0.95 V. Therefore, it is reasonable to conclude from Figure 5.1 that the overpotential for Ni<sup>2+</sup> reduction is decreased while HER is suppressed nearly completely in the

presence of boric acid.

This data clearly shows that the presence of  $\text{H}_3\text{BO}_3$  in Ni-sulfamate solution has two effects: (1) that  $\text{H}_2$  evolution at the electrode surface is obviated - which can occur via  $\text{H}^+$  reduction at low overpotentials and  $\text{H}_2\text{O}$  discharge at high overpotentials and (2)  $\text{Ni}^{2+}$  reduction is facilitated at the electrode surface. However, it is not clear whether these key observations are due to the inability of  $\text{H}^+$  or  $\text{H}_2\text{O}$  to adsorb on the electrode surface or the synergistic effect of  $\text{Ni}^{2+}$  adsorption in the presence of  $\text{H}_3\text{BO}_3$ .

### 5.1.2 Current-potential data from polarisation and deposition

To interrogate these questions further, the influence of boric acid on Ni deposition in an electroforming bath was examined by measuring total polarisation curves for electrolytes C, D, E, and F, and determining the partial Ni current densities using current efficiencies, summarised in Table 5.1, which were measured from deposition experiments. Electrolytes C and D contain 0.65 M boric acid or 0.021 M  $\text{NiCl}_2$ , respectively, while bath E is similar to an electroforming solution typically used in industry, containing both  $\text{H}_3\text{BO}_3$  (0.65 M) and  $\text{NiCl}_2$  (0.021 M). The experimental conditions, such as temperature and current density for each electrolyte is tabulated in Table 5.1. The summary of these experiments at 40, 45, and 55 °C are shown in Figures 5.2a, 5.2b, and 5.2c, respectively, which reveal a few trends about the effect of boric acid, chloride ions, and temperature which are discussed in the forthcoming sections.

#### 5.1.2.1 Effect of boric acid

In all solutions containing boric acid (Baths B, C, E, and F), partial Ni polarisation plots ( $j_{\text{Ni}}-U$ , circles) are convergent with the corresponding total polarisation plots ( $j-U$ , solid lines) when the bath is operated at temperatures between 40 °C and 55 °C (Figures 5.2a-c). This signifies that the current density observed in polarisation measurements and that calculated using gravimetric measurements from deposition experiments are nearly the same (within experimental error) in the presence of  $\text{H}_3\text{BO}_3$ , irrespective of the temperature employed. Table 5.1 shows that boric acid-containing electrolytes



Table 5.1: Current efficiencies (%) for 20  $\mu\text{m}$  thick nickel deposits from quiescent sulfamate baths (Table 4.1) as a function of cathode current density and bath temperature. Seven experiments were repeated three times and the standard deviations were found to be within 1.5%.

Baths	Cathode current density ( $\text{mA cm}^{-2}$ )					
	10	20	30	40	50	65
Temperature: 40 °C and Rotation rate: 0 rpm						
A	44.6	19.2	93.8	101.5	35.3	-
B	99.2	100.0	99.9	98.2	89.2	-
C	100.0	100.0	99.6	96.3	81.5	-
D	103.6	108.2	97.2	96.7	85.7	-
E	100.0	100.0	100.0	99.1	91.3	-
Temperature: 45 °C and Rotation rate: 0 rpm						
A	99.4	91.0	<b>21.9</b>	100.7	90.7	-
B	100.0	100.0	99.0	100.1	90.4	-
C	99.4	99.7	99.2	99.9	85.7	-
D	99.7	97.4	99.6	<b>16.3</b>	90.4	-
E	99.7	100.0	99.7	99.8	90.4	-
F	100.0	100.0	100.3	100.1	87.2	86.4
Temperature: 55 °C and Rotation rate: 0 rpm						
A	100.0	100.0	73.5	49.6	100.5	-
B	100.1	99.9	99.3	99.9	96.9	-
C	100.0	100.0	99.2	99.9	97.9	-
D	99.4	99.7	41.0	40.3	31.5	-
E	98.8	99.3	100.0	99.1	97.8	-

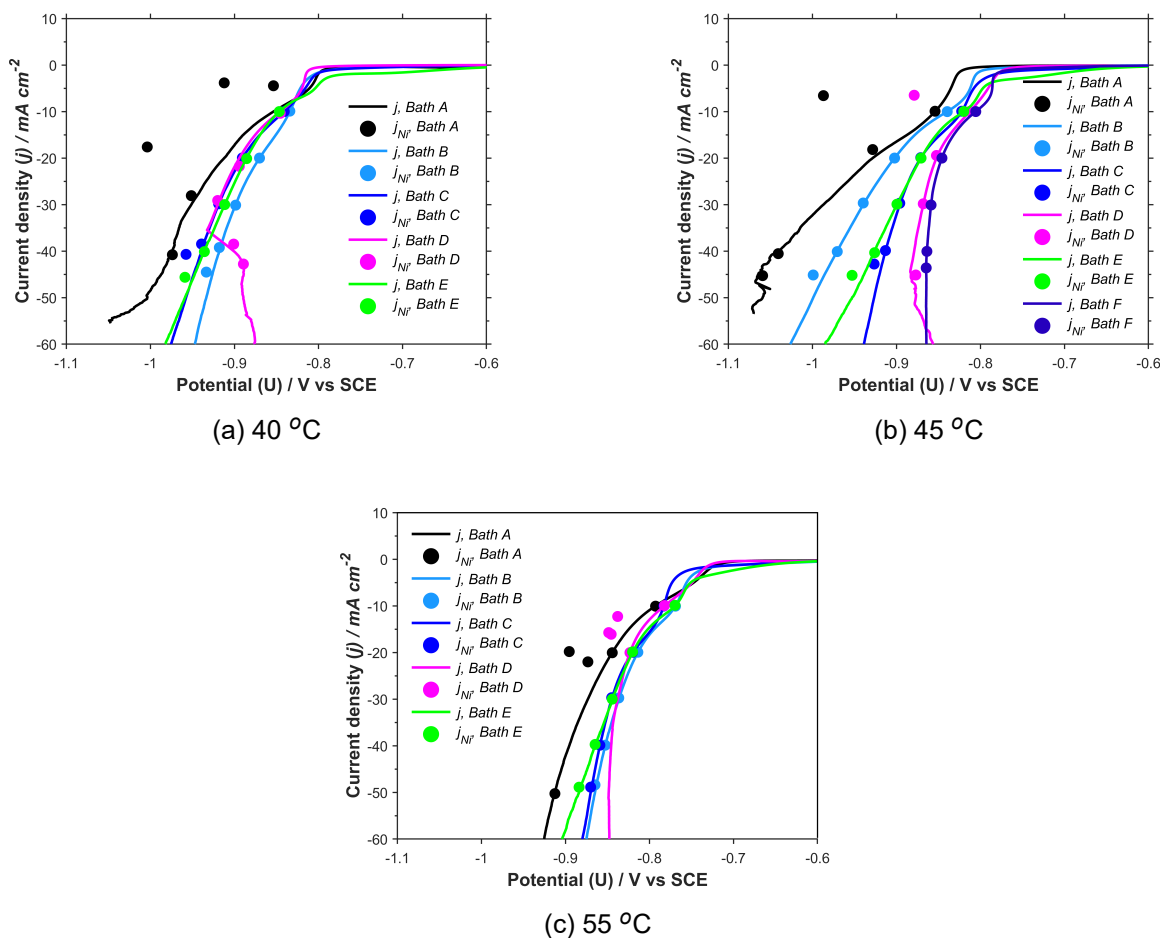


Figure 5.2: Polarisation curves: total current densities (solid lines) and Ni current densities (circles) for electrodeposition in quiescent Bath A (●); Bath B (●); Bath C (●); Bath D (●); Bath E (●); and Bath F (●) at different temperatures.

nearly always deposit nickel with current efficiencies  $>98\%$ , except at a current densities of  $50\text{-}65\text{ mA cm}^{-2}$ , where values drop to  $\approx 90\%$ , presumably because mass transfer limitations are approached, similar to that noted by other researchers [175, 228]. The presented results show good agreement with earlier studies which have also reported current efficiencies close to  $100\%$  in nickel sulfamate solutions containing boric acid [68, 121].

In the absence of boric acid (i.e. in solution A and D), Table 5.1 shows that there is a significant degree of variability in current efficiency with current density, with values ranging between 19 and  $100\%$ . Therefore, high current efficiencies approaching  $100\%$  in the presence of boric acid mean that this constituent effectively suppresses

hydrogen evolution.

Additional evidence of the suppression of hydrogen evolution could be gleaned from the effect of boric acid on the surface appearances of the deposit observed from the optical micrographs given in Figure 5.3. The film plated in the absence of boric acid (Bath A) consisted of a stressed deposit, with many cracks; the micrograph shown in Figure 5.3a is representative of the appearance of most films plated from sulfamate baths which do not contain boric acid (Baths A and D). More representative optical micrographs of nickel deposited from Baths A-E at 40-55 °C are included in Table 9.1, Appendix B.

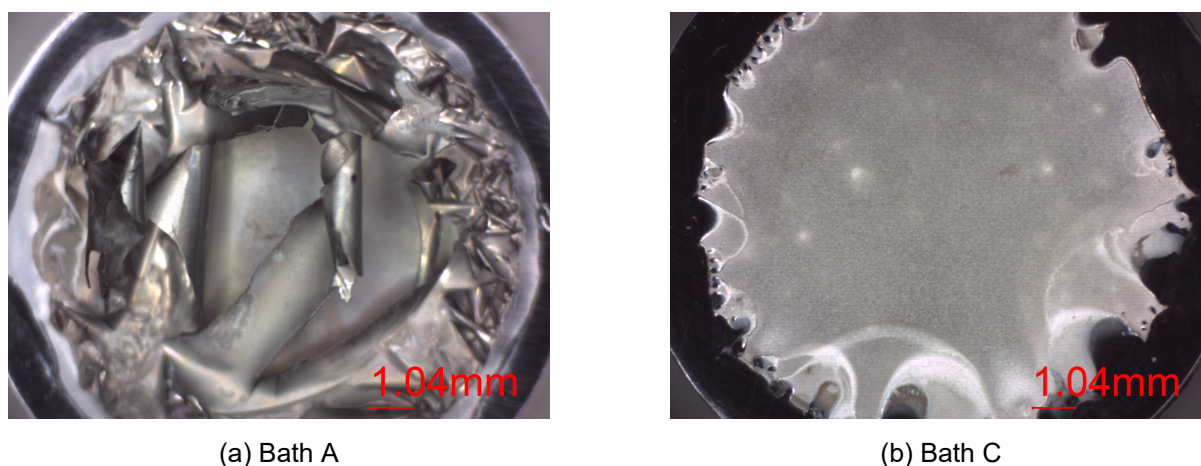


Figure 5.3: Effect of boric acid on the appearance of the nickel films plated at 30 mA cm<sup>-2</sup> and 40 °C from: (a) Bath A (without boric acid) and (b) Bath C (containing 0.65 M boric acid).

The nickel film plated from Bath C (0.65 M H<sub>3</sub>BO<sub>3</sub>) was flat, compact, and crack-free; the micrograph shown in Figure 5.3b is representative of the appearances of all deposits obtained from sulfamate baths which contain boric acid (Baths B, C, E, and F). These results remain in agreement with those reported by Tsuru et al. [68] who found that the addition of boric acid prevented the formation of cracks in nickel plated from sulfamate baths. According to Tsuru et al. [68], cracks appear when the tensile stress in the deposit exceeds its yield strength. Therefore, the crack manifestation in deposits from baths without H<sub>3</sub>BO<sub>3</sub> (Figure 5.3a) could be an indication of high levels of internal stress in the deposit and the absence of these cracks in deposits obtained in the presence of boric acid indicates decreased levels of internal stress in the deposits.

There are a number of reasons why stress may develop in deposits. As noted from Table 5.1, nickel electrodeposition from pure sulfamate baths is accompanied by the reduction of protons or water into atomic hydrogen. The codeposition and subsequent desorption of hydrogen has been linked to the development of tensile stress in Ni films [229,230]. Table 5.1 indicates that as the concentration of boric acid is increased in the bath from 0 M (Bath A) to 0.65 M (Bath B) at 40 °C, the current efficiency of plated nickel at a cathode current density of 30 mA cm<sup>-2</sup> (cf. Figure 5.3) rises from 93.8% to 99.6%. The decrease in internal stress in the presence of boric acid could be correlated to this increase in the current efficiency, indicating that boric acid decreases the rate of hydrogen evolution via either proton or water reduction, and, consequently suppresses an increase in the internal stress in the nickel deposit.

### 5.1.2.2 Inclusion of chloride ions

Chloride ions are added to commercial Watts, Woods, and sulfamate baths to facilitate the dissolution of soluble nickel anodes [53]. These ions are also useful in increasing electrolyte conductivity [175] which could decrease the electrolyte resistance, cell voltage, and power costs during Ni electrodeposition [124]. Additionally, chloride ions have been reported to participate in the electrodeposition reaction mechanism [103, 115].

Some evidence of the influence of chloride ions during the electrodeposition of nickel could be gleaned by comparing the total polarisation curves of Bath A and Bath D in Figures 5.2a-c which indicate that a lower overpotential is required for cathodic reduction in the presence of Cl<sup>-</sup>. This reduction in overpotential would be expected to increase  $j_{Ni}$  which is indeed observed from the merging of total and partial Ni polarisation curves in the presence of Cl<sup>-</sup>, at solution temperatures of 40-45 °C. At these temperatures, whilst Bath A exhibits low current efficiency at both low ( $\leq 20$  mA cm<sup>-2</sup>) and high ( $\geq 40$  mA cm<sup>-2</sup>) current densities, Bath D exhibits current efficiencies close to 100% in most cases except at a current density of 40 mA cm<sup>-2</sup> at 45 °C. This shows that the inclusion of Cl<sup>-</sup> may facilitate Ni deposition via the adsorption of the NiCl<sup>+</sup> species, which allows for high current efficiency at low overpotentials. At high overpotentials (or high currents) and at 55 °C, however, this is not the case where water

reduction lowers current efficiency as shown in Figure 5.4.

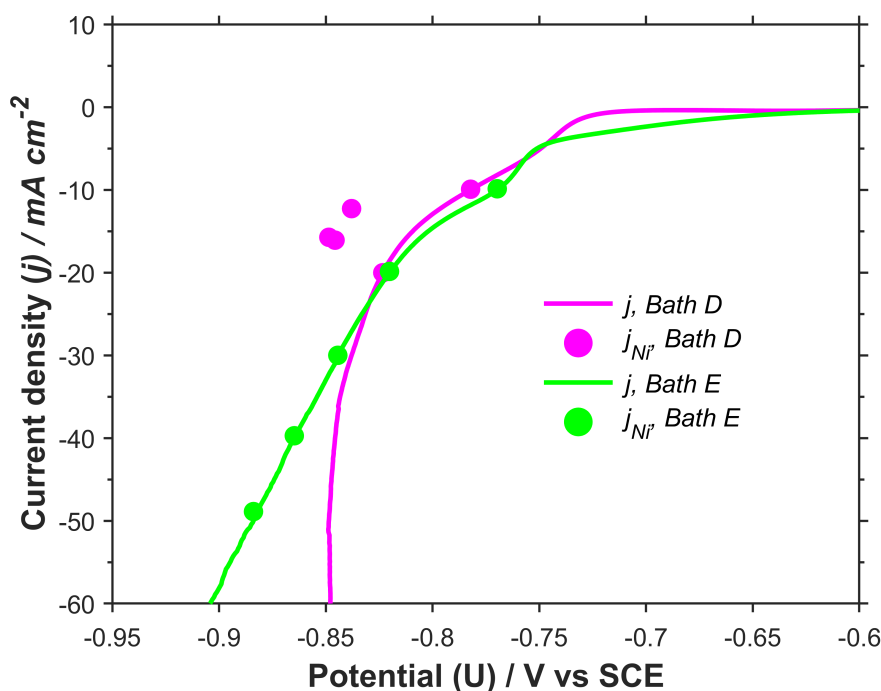


Figure 5.4: Polarisation curves: total current densities (solid lines) and Ni current density (○) for electrodeposition in quiescent Bath D (●) and Bath E (●) at 55 °C.

The presented results are consistent with those reported by Horkans [103] who demonstrated lower overpotentials and higher Ni deposition currents are obtained when the anion of the electrolyte is changed from  $\text{SO}_4^{2-}$  to  $\text{Cl}^-$ . This was attributed to a bridging mechanism involving the formation of a nickel-chloro complex ( $\text{NiCl}^+$ ) which facilitates the discharge of Ni(II) ions. Under this scheme,  $\text{Cl}^-$  enters the hydration sphere of  $\text{Ni}^{2+}$ , replacing one of the associated water molecules. This forms the  $[\text{Ni}(\text{H}_2\text{O})_5\text{Cl}]^+$  complex which moves the nickel ion closer to the electrode surface to engage in charge transfer [103]. It should be noted that as a convention, all coordinated water molecules are usually omitted in writing [89]. Therefore,  $[\text{Ni}(\text{H}_2\text{O})_5\text{Cl}]^+$  is usually written as its simplified version,  $\text{NiCl}^+$ . Earlier studies [103, 175, 231, 232] have also reported higher current efficiencies close to 100% in the presence of  $\text{Cl}^-$  and attributed this to the formation of a chloro-hydroxylated nickel complex which facilitates the transfer of charge between the electrode surface and  $\text{Ni}^{2+}$ .

Ji and Cooper [89] studied nickel ion speciation in aqueous solutions at 25 °C over a wide  $\text{NiCl}_2$  concentration and pH range. They found that  $\text{NiCl}^+$  started to

appear as one of the dominant species in the acidic region ( $\text{pH} < 6$ ) at  $\text{NiCl}_2$  concentrations above 0.01 M. The concentration of  $\text{NiCl}_2$  employed in these experiments is 0.02 M (Bath D). From that account, it is conceivable that the observed accelerating effect of  $\text{Cl}^-$  on  $\text{Ni(II)}$  reduction could be attributed to the formation and adsorption of a  $\text{NiCl}^+$  complex which facilitates the electroreduction of  $\text{Ni}^{2+}$  via the reaction sequence proposed in Equations 2.9-2.11.

Notably, the films deposited from sulfamate solutions with chloride ions only at 40 °C were all highly stressed and similar to those shown in Figure 5.3a. As was previously mentioned, the existence of such cracks could be partially explained by the codeposition and desorption of interstitial hydrogen [68, 233]. On the other hand, the observed increase in current efficiency to values close to 100% with chloride ion addition at 40 °C must be considered as it suggests that the rate of hydrogen evolution is minimal. Seo et al. [234] have also reported that highly stressed Ni-Fe-P deposits could be produced from a sulfamate bath with a high current efficiency of 95%. Earlier researchers have suggested that the occlusion of impurities (H, O, and S) during deposition from sulfamate baths could be responsible for high tensile stresses in deposits [234, 235]. Therefore, the presence of high stress in deposits produced with high current efficiencies from Bath D could be explained by the codeposition of  $\text{Ni(OH)}_2$  or NiO during nickel electrodeposition which is promoted by hydrogen evolution. This is supported by the measurement of current efficiencies of 104-108% at 10-20  $\text{mA cm}^{-2}$  in Bath D at 40 °C. Measured current efficiencies above 100% indicate that the mass of the deposit is greater than the mass expected for the deposition of metallic nickel given the charge passed during deposition, suggesting that other elements, besides Ni, are present in the deposit. Indeed, the incorporation of  $\text{Ni(OH)}_2$  at the cathode surface during nickel electrodeposition in the absence of boric acid has been demonstrated by researchers using an EQCM [65, 108].

The conclusion drawn from this section is that, while the addition of chloride ions (Bath D) and boric acid (Baths B and C) to a sulfamate-only system (Bath A) at 40 °C results in higher  $j_{\text{Ni}}$  values and current efficiencies, sound deposits with lower stress levels are only produced in the presence of boric acid. Thus, boric acid is the only constituent responsible for inhibiting hydrogen evolution as well as the accompanied

precipitation of  $\text{Ni}(\text{OH})_2$  or  $\text{NiO}$  in the electroforming bath.

### 5.1.2.3 Influence of temperature

Temperature is known to increase the rate of charge transfer as well as raise the diffusion coefficients of species in solution by increasing conductivity and lowering viscosity of the electrolyte, and in doing so decreases the concentration overpotential. Temperature could also change the equilibrium of solution complexes [236] and adsorption-desorption characteristics of surface processes [237–240].

It was found that as the temperature is increased from 40 °C to 55 °C (Figure 5.2a vs. 5.2c), a lower overpotential is generally required to initiate Ni deposition which leads to higher total current densities. This could be explained by an increase in the rates of charge transfer and diffusion which respectively decrease activation and concentration overpotential of nickel deposition and/or hydrogen evolution. By observing the effect of temperature increase on  $j_{\text{Ni}}$ , one could determine which partial reaction is favoured.

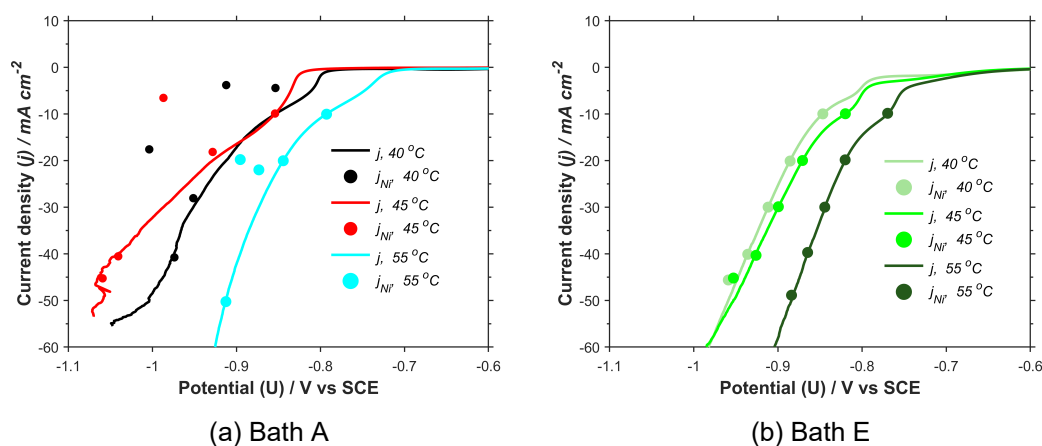


Figure 5.5: Total polarisation (solid lines) and partial Ni polarisation (circles) plots in quiescent (a) Bath A and (b) Bath E at 40 °C, 45 °C, and 55 °C.

The influence of temperature increase on  $j_{\text{Ni}}$  could be considered for two instances: (i) in the absence of boric acid (Baths A and D), and (ii) in the presence of boric acid (Baths B, C, and E). For example, Figures 5.5 a and b show the effect of increasing

solution temperature from 40 °C to 55 °C on the total and partial Ni polarisation curves obtained from a sulfamate-only system (Bath A) and a typical electroforming system which consists of boric acid and chloride ions (Bath E).

### 5.1.2.3.1 In the absence of boric acid

As the temperature is increased from 40 to 55 °C in a sulfamate-only system (Figure 5.5a), it is observed that at total current densities  $\leq 20 \text{ mA cm}^{-2}$ , Ni deposition currents increase such that the current density observed in polarisation measurements and that calculated using gravimetric measurements from deposition are the same (within experimental error) at 45-55 °C which means that  $\text{Ni}^{2+}$  reduction is the dominant reaction at 45-55 °C and current densities  $\leq 20 \text{ mA cm}^{-2}$  in Ni-sulfamate only systems (Bath A, Figures 5.2a-c). This is clearly summarised in Table 5.1 where an increase in temperature in Baths A and D leads to electrodeposition of nickel with close to 100% current efficiency at current densities  $\leq 20 \text{ mA cm}^{-2}$ . These results indicate that an increase in temperature favours Ni(II) discharge and suppresses the rate of  $\text{H}^+$  reduction at low current.

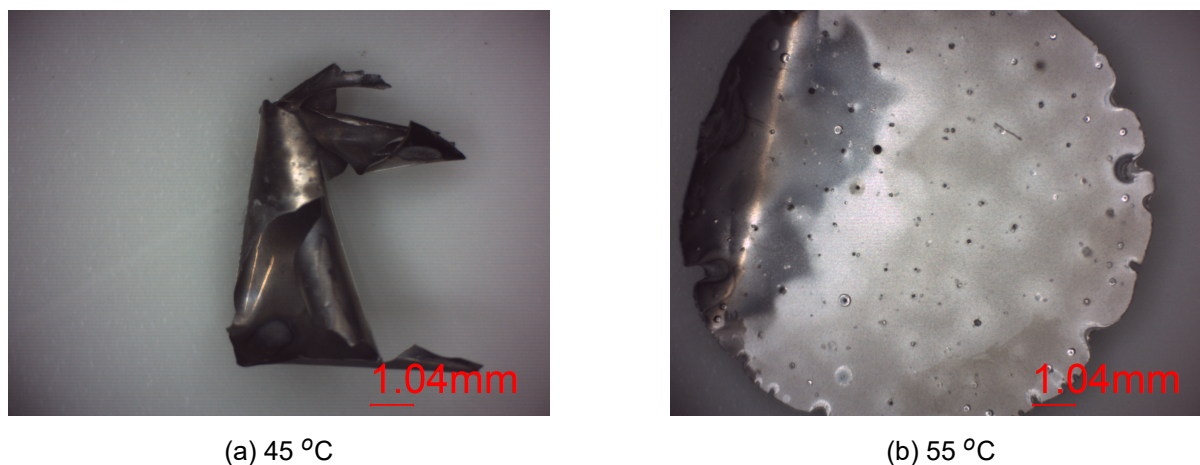


Figure 5.6: Effect of temperature on the appearance of the nickel films plated at  $20 \text{ mA cm}^{-2}$  from Bath A (no boric acid): (a) 45 °C and (b) 55 °C.

The appearance of the deposits from Bath A produced at  $20 \text{ mA cm}^{-2}$ , as shown in Figure 5.6, also provides evidence of the suppression of hydrogen evolution at high temperatures. As the temperature rises from 45°C to 55 °C, the appearance



of the deposit taken from Bath A changes from curled with cracked edges to a semi-curved surface with less cracks. This improved deposit appearance with temperature rise could be correlated to an increase in current efficiency from 91% to 100% as the temperature is raised from 45 to 55 °C in Bath A. Additionally, it should be highlighted that the improved deposit appearance with temperature increase observed in Bath A and Bath D is limited to cathode current densities  $\leq 20 \text{ mA cm}^{-2}$ .

In contrast, at current densities  $>20 \text{ mA cm}^{-2}$  in Baths A and D,  $j_{Ni}$ -U plots shift away from  $j$ -U curves as temperature is increased from 40 °C to 55 °C. This indicates that  $j_{Ni}$  becomes lower than  $j$  which suggest that the rate of hydrogen evolution is increased with temperature rise at current densities above  $20 \text{ mA cm}^{-2}$ . This is particularly significant in Bath D at 55 °C which is shown Figure 5.4.

#### 5.1.2.3.2 In the presence of boric acid

Temperature has a minimal influence on current efficiency in baths containing boric acid (Baths B, C, and E). Current efficiencies close to 100% are obtained at still higher temperatures of 55 °C and nickel deposition seems to be the sole reaction occurring. Perhaps, the most significant effect of temperature rise in sulfamate systems which contain boric acid is that the  $\text{Ni}^{2+}$  reduction potential becomes less negative which has also been previously observed [234]. This is clearly shown in Figure 5.5b which is representative of other baths which contain boric acid.

In conclusion, it appears that the main benefits of operating an electroforming bath at higher temperatures of 50-55 °C is that a lower overall cell voltage could be applied to electrodeposit nickel with current efficiencies close to 100% due to a reduction in  $\text{Ni}^{2+}$  reduction overpotential. Other points to consider while planning to operate at a higher temperature are that energy savings obtained from operating at a lower cell voltage could be offset by two factors: (i) the process's increased thermal energy requirements; and (ii) the comparatively high rate of water evaporation that occurs at higher temperatures, which could affect the pH of the solution and the deposit characteristics.

### 5.1.3 Kinetics of nickel electrodeposition

To study the effect of boric acid on the kinetics of nickel electrodeposition from electroforming solutions, kinetic parameters were evaluated from the partial current density-potential plots for Ni deposition (Figures 5.2a-c) using the Tafel analysis method discussed in chapter 4 in section 4.1.3.3. A summary of this analysis is presented in Figure 5.7 which shows Tafel plots for Ni reduction, which are typical for sulfamate solutions, in the absence and presence of boric acid,  $\text{Cl}^-$ , or their combination at (a) 40 °C, (b) 45 °C, and (c) 55 °C. It must be mentioned that Tafel plots for bath A were difficult to construct due to the variability in current efficiency (c.f. Appendix C/Figure 9.2). However, enough data points were available to obtain a good fit for all solutions.

Tafel analysis provides information on the rate of nickel electrodeposition (via exchange current density data) and mechanism (via Tafel slope data). As discussed in chapter 3, the experimental Tafel slopes could be compared to calculated ones to elucidate differences in the rate determining step of nickel electrodeposition. Cathodic Tafel slopes,  $-b_c$ , are obtained from the slopes of the Tafel lines (broken lines) drawn in Figure 5.7. The exchange current density ( $j_o$ ) is the absolute value of current flowing across the interface in both directions at the equilibrium potential (i.e. zero overpotential). It is obtained from the x-intercept of the Tafel line at the equilibrium potential which is depicted as the solid black line in Figure 5.7.

The kinetic parameters ( $-b_c$  and  $j_o$ ) obtained for nickel electrodeposition from quiescent nickel sulfamate solutions are summarised in Table 5.2 and reveal information about the effect of chloride ions, boric acid, and temperature on the electrodeposition mechanism and the rate of nickel electrodeposition which is discussed in the forthcoming sections.

#### 5.1.3.1 Effect of chloride ions

The Tafel slopes measured in pure nickel sulfamate solution (Bath A) and nickel sulfamate solution containing chloride ions (Bath D) at 40 °C are  $106 \pm 11$  and  $140 \pm 16$ ,

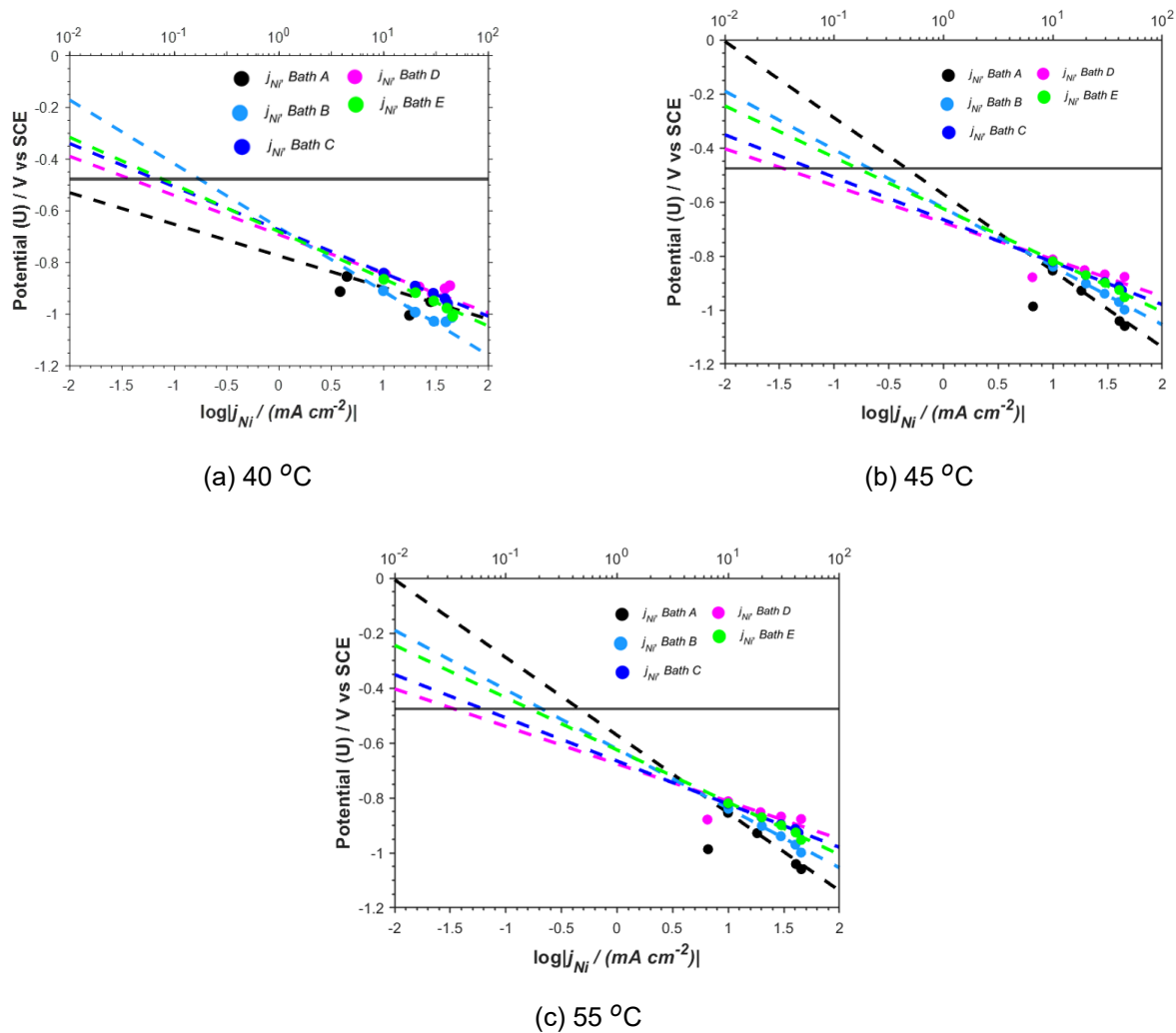


Figure 5.7: Tafel plots and reversible potential (thick black line) in quiescent Bath A (●); Bath B (●); Bath C (●); Bath D (●); and Bath E (●) at 40, 45 and 55 °C.

respectively. These Tafel slopes in Baths A and D are the same within error which indicates that electrodeposition from both solutions at 40 °C follow similar mechanisms. The generally accepted mechanism for Ni deposition from sulfate and chloride solutions is proposed to involve two consecutive single-electron transfer steps involving a nickel ion complex ( $NiX^+$ ) as given in Equations 5.3-5.5 [62, 63, 115]:



where  $X^-$  is the anion, which could be  $OH^-$  or  $Cl^-$ , that complexes with  $Ni^{2+}$ . This mechanism with Equation 5.4 as the RDS would result in a calculated Tafel slope of 120

Table 5.2: Kinetic parameters for nickel deposition obtained in quiescent sulfamate baths at different temperatures.

Baths	$-b_c$ mV decade <sup>-1</sup>	$j_0$ mA cm <sup>-2</sup>
Temperature: 40 °C and Rotation rate: 0 rpm		
A	106 ± 11	0.0017 ± 0.0013
B	197 ± 54	0.093 ± 0.063
C	177 ± 5	0.094 ± 0.01
D	140 ± 16	0.023 ± 0.021
E	171 ± 19	0.072 ± 0.036
Temperature: 45 °C and Rotation rate: 0 rpm		
A	319 ± 46	0.626 ± 0.225
B	166 ± 50	0.102 ± 0.101
C	171 ± 27	0.092 ± 0.51
D	138 ± 5	0.036 ± 0.01
E	189 ± 20	0.148 ± 0.056
F	160 ± 40	0.084 ± 0.064
Temperature: 55 °C and Rotation rate: 0 rpm		
A	166 ± 13	0.103 ± 0.038
B	144 ± 24	0.085 ± 0.046
C	185 ± 62	0.245 ± 0.224
D	133 ± 3	0.05 ± 0.007
E	162 ± 13	0.241 ± 0.191

mV decade<sup>-1</sup> as discussed in chapter 3. Earlier studies have also demonstrated Tafel slopes around 120 mV decade<sup>-1</sup> for nickel deposition from sulfate [62, 63], chloride [115], and in some cases, sulfamate [68] electrolytes, which have been used as a corroboration of the aforementioned mechanism. The Tafel slopes measured in Bath A and Bath D at 40 °C are within range of this value indicating that the mechanism of nickel deposition in these electrolytes could be similar to that presented in Equations 5.3 to 5.5. It is also noted that the addition of Cl<sup>-</sup> (Bath D) to a sulfamate-only system (Bath A) at 40 °C results in a higher nickel exchange current density which support the

findings of higher partial current densities for Ni deposition measured in the presence of  $\text{Cl}^-$ , as mentioned in section 5.1.2.2.

### 5.1.3.2 Effect of boric acid

In general, Tafel slopes for sulfamate solutions without boric acid were lower than those measured when boric acid was added. In the presence of  $\text{H}_3\text{BO}_3$ , Tafel slopes are consistently greater than  $140 \text{ mV decade}^{-1}$  and in many cases are close to or above  $200 \text{ mV decade}^{-1}$ . The Tafel slopes ( $135 \pm 15 \text{ mV decade}^{-1}$ ) in the presence of  $\text{Cl}^-$  are quite different from those in boric acid-containing systems, but similar to those observed by other researchers [61, 115]. The difference in Tafel slopes in the presence of boric acid and  $\text{Cl}^-$  indicate that the reduction reaction in the presence of  $\text{Cl}^-$  only could be proceeding through a different route from those in solutions containing boric acid.

The Tafel slopes, observed in the presence of boric acid, are considerably greater than the calculated Tafel slope of  $120 \text{ mV/decade}$  for the presumed electrodeposition mechanism in Equations 5.3 to 5.5. As such, more overpotential is required to increase the rate of reaction (current density) as shown in Figure 5.7a. Certain factors could lead to high Tafel slopes: (i) adsorbed species [192], or (ii) precipitation of an oxide/hydroxide film on the cathode surface [191].

The suppression of hydrogen evolution and consequently, the prevention of  $\text{Ni}(\text{OH})_2/\text{NiO}$  formation in the presence of boric acid are supported by measured current efficiencies close to 100% and deposits of sound quality obtained from  $\text{H}_3\text{BO}_3$ -containing baths. Therefore, adsorption of either sulfamate ions or boric acid or their combination is the most probable contribution to the charge transfer overpotential at the cathode surface and therefore responsible for high Tafel slopes in boric acid-containing systems. The kinetic influence of boric acid could be ascribed to surface interaction by adsorbed  $\text{H}_3\text{BO}_3$  molecules which could stabilise nickel ion complexes at the electrode surface. Possible formation of nickel-boric acid complexes at the surface of the electrode has been proposed in other systems [61, 64, 66, 241]. A previous study by Vincenzo and Cavallotti [61] measured higher transient Tafel slopes during nickel elec-

trodeposition from sulfate and chloride systems containing boric acid and to a lesser extent for nickel deposition from sulfamate electrolytes. However, their earlier study for cobalt deposition from sulfamate solutions [77] had reported that boric acid clearly increased the Tafel slopes. Vincenzo and Cavallotti [61] proposed that this observation in nickel plating electrolytes was due to a "weak surface complexation of the nickel cation or intermediate discharging species". The same proposition had been made for cobalt electrolytes [77]. However, it was not clear from their statements whether this complexation reaction was heterogeneous (i.e. occurred at the electrode surface) or homogenous (i.e. occurred in the electrolyte adjacent to the electrode surface) in nature.

It should be noted that when a low Tafel slope is observed, such as those in the presence of  $\text{Cl}^-$  or at 40 °C for Bath A, the current efficiency was low. This shows that a low Tafel value may not be necessarily useful for electroforming. This is supported by the fact that the addition of boric acid increased the Ni exchange current density in the absence of chloride ions at 40 °C and in the presence of  $\text{Cl}^-$  at 40-55 °C.

### 5.1.3.3 Effect of temperature

Figure 5.8 shows Tafel plots for electroforming solutions at the three temperatures in this study. This figure is typical of other solutions, in that Tafel slopes decrease with temperature for all sulfamate based solutions with and without  $\text{H}_3\text{BO}_3$  – except for solution A where the lowest slope is calculated at 40 °C.

For pure nickel sulfamate solution, Tafel slopes at 45 and 55 °C are similar to values in boric acid-containing systems, although at 40 °C, the Tafel slope is lower than  $117 \text{ mV decade}^{-1}$ . This indicates that the surface resistance increases at the cathode during electrodeposition from pure nickel sulfamate at high temperatures of 45-55 °C. This could be attributed to the possible formation of an oxide or hydroxide surface film promoted by an increased rate of hydrogen evolution with the rise in temperature at current densities  $> 20 \text{ mA cm}^{-2}$ .

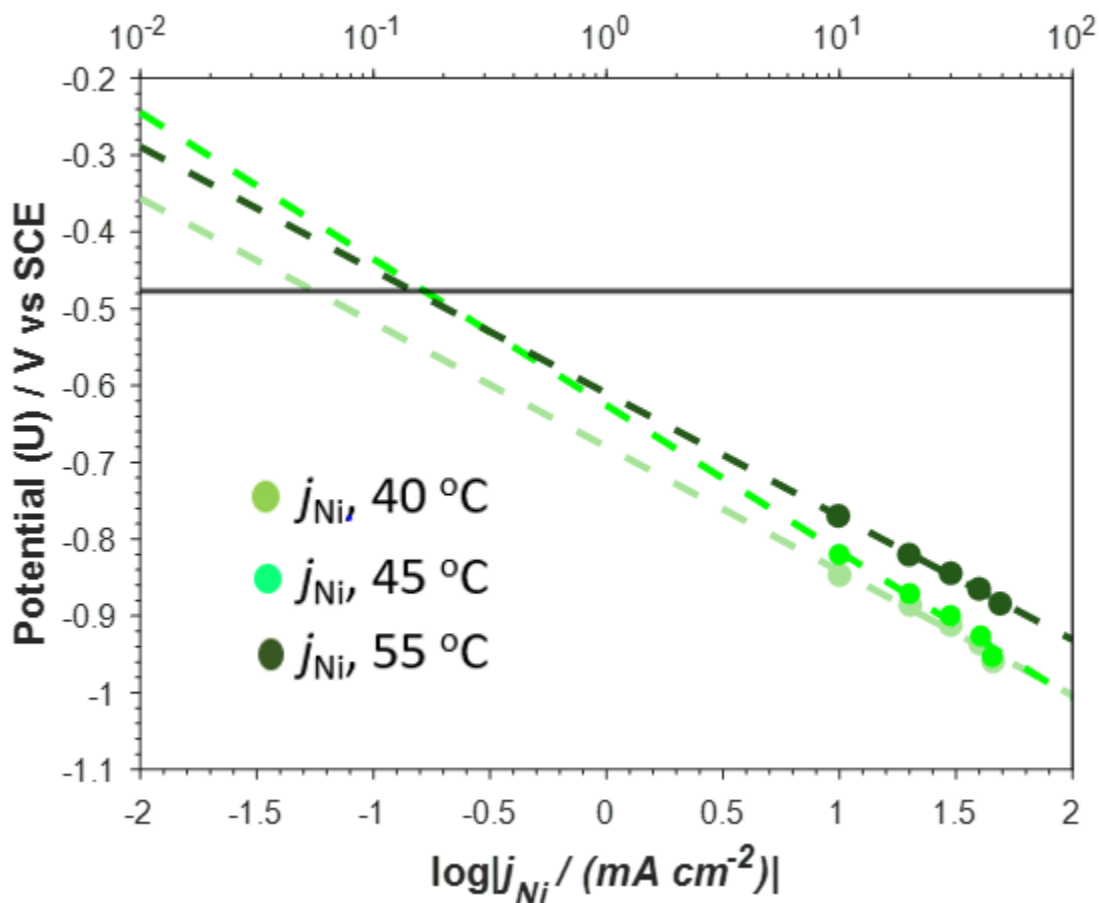


Figure 5.8: Tafel plots in quiescent Bath E at 40 °C (●); 45 °C (●); and 55 °C (●).

An increase in temperature from 40 °C to 55 °C generally increased  $j_o$  which remains in agreement with the findings in section 5.1.2.3 where higher values of  $j_{Ni}$  are obtained with increased temperatures. A higher temperature causes an increased supply of nickel ions to the electrode surface, a decreased overpotential for charge transfer, and an increased rate of discharge of the metal complex [237].

#### 5.1.4 Material analysis: SEM and EDS

It is presumed that flat, coherent, and crack-free deposits generated from sulfamate baths - such as those produced in the absence of boric acid (at high temperatures of 45-55 °C and low current densities  $\leq 20 \text{ mA cm}^{-2}$ ) and in the presence of  $\text{H}_3\text{BO}_3$  (at all temperatures and current densities) - consists mainly of metallic nickel. This is because these deposits are produced with high current efficiencies close to 100% which

suggests that the rate of HER is minimal and consequently, stress which would result from the codeposition of hydrogen and NiO/Ni(OH)<sub>2</sub> is minimised. To confirm these presumptions, cross-sections of sound deposits produced from chloride-containing baths in the absence and presence of boric acid at different current densities with faradaic efficiencies of 99.4-99.9% were characterised using Scanning Electron Microscopy (SEM) and Energy Dispersive X-ray Spectroscopy (EDS).

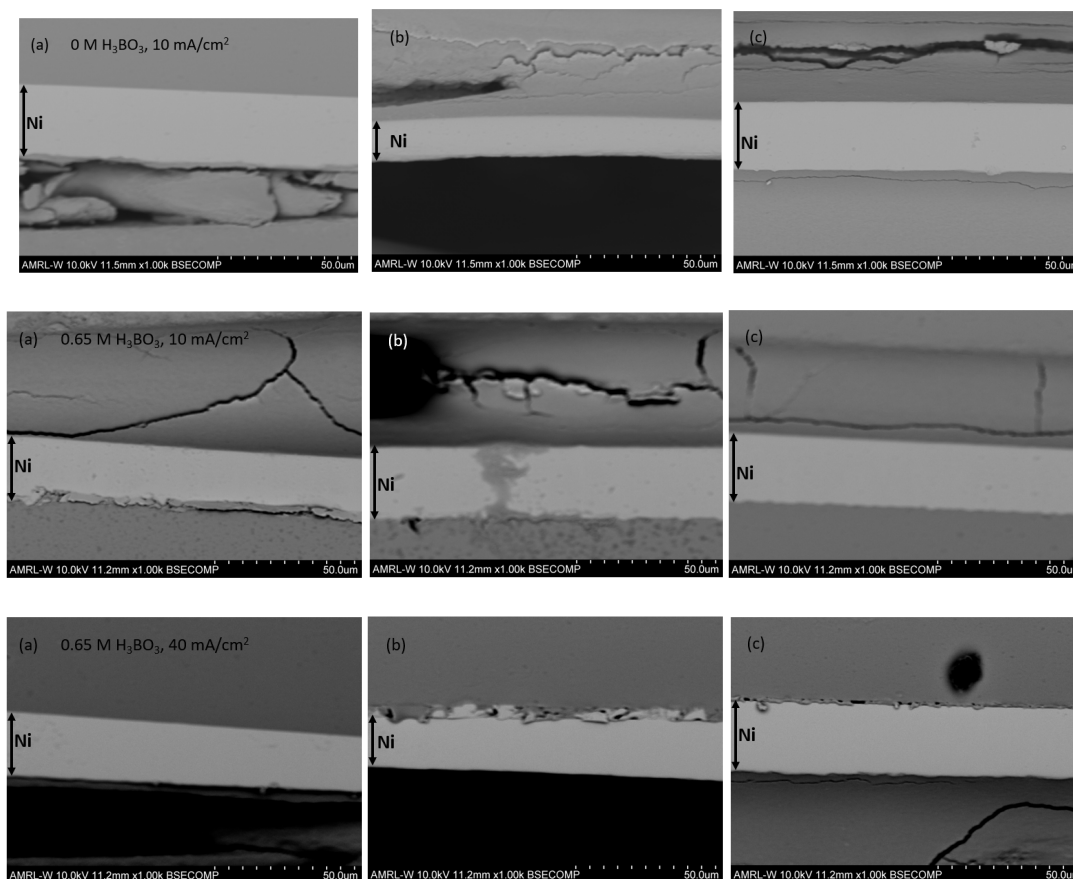


Figure 5.9: W-SEM cross-sectional images of Ni deposited from 1.764 M nickel sulfate + 0.021 M nickel chloride + xM boric acid at 45 °C as a function of the radial position on the RDE. a) near edge, b) mid-point, c) near centre.

SEM images of the deposit cross-sections as a function of the radial position on the RDE, shown in Figure 5.9, indicate that the sound deposits produced with high current efficiencies in the absence and presence of boric acid are indeed dense and compact without cracks.

Next, the elemental compositions of the deposits were examined using EDS. In certain instances, EDS point analysis was performed on the centre and edge of the



deposit because, in some deposits such as shown in Figure 5.3b, the centre appeared denser while the borders were pitted which could be attributed to non-uniform current distribution on the surface of the RDE. Some evidence of thinner edges and thicker centres could be gleaned from the SEM images of deposits produced from Bath E (i.e. containing 0.021 M NiCl<sub>2</sub> and 0.65 M H<sub>3</sub>BO<sub>3</sub>) at 10 mA cm<sup>-2</sup> (c.f. Figure 5.9).

A summary of the elemental composition for the centre and edge of deposits produced from Bath D (containing 0 M H<sub>3</sub>BO<sub>3</sub>) and Bath E (containing 0.65 M H<sub>3</sub>BO<sub>3</sub>) is given in Table 5.3; the standard deviation indicates the difference between the average elemental content and the lowest and highest elemental content across the deposit's thickness i.e. from the deposit's base close to the substrate to the deposit surface. EDS analysis confirms that the deposits consists mainly of metallic nickel (>96 wt%). The data also points to a homogeneous composition throughout the deposit, as evidenced by the small standard deviations and little variation in composition between the deposit's centre and margin.

Table 5.3: EDS results of Ni electrodeposited from 1.764 M nickel sulfamate + 0.021 M nickel chloride + xM boric acid at 45 °C.

Composition (wt%)	0 M H <sub>3</sub> BO <sub>3</sub> , 10 mA cm <sup>-2</sup>		0.65 M H <sub>3</sub> BO <sub>3</sub> , 10 mA cm <sup>-2</sup>		0.65 M H <sub>3</sub> BO <sub>3</sub> , 40 mA cm <sup>-2</sup>
	Near edge	Near centre	Near edge	Near centre	Near edge
Ni	97.52 ± 0.18	97.39 ± 0.32	96.58 ± 0.21	96.86 ± 0.42	97.75 ± 0.08
N	2.06 ± 0.12	2.18 ± 0.27	2.48 ± 0.24	2.41 ± 0.51	1.89 ± 0.15
O	0.42 ± 0.11	0.43 ± 0.10	0.94 ± 0.18	0.72 ± 0.09	0.37 ± 0.06

Within the detection limits of the EDS, sulfur and boron were not detected while oxygen (<1 wt%) and nitrogen (<3 wt%) impurities were identified in the deposits. Absence of sulfur in deposits suggests that anode reaction products of the Pt counter electrode employed have been successfully prevented from entering the catholyte by using the bridge tube. This is because such products have been reported to increase the sulfur content of deposits [125]. The low levels of oxygen detected could likely arise from adsorption of Ni(OH)<sup>+</sup> which has been suggested as a charge transfer intermediate [62, 82] during nickel electrodeposition.

Perhaps, the most interesting impurity is nitrogen which has rarely been re-

ported in deposits produced from additive-free sulfamate baths [235]. This impurity could likely result from the adsorption of sulfamate ions at the cathode. There are numerous reports about the decomposition of sulfamate ions at passive soluble and insoluble anodes [125, 127–130, 135] but its adsorption and subsequent decomposition at the cathode has only been considered in a limited number of studies [242, 243].

The presence of nitrogen in the deposit is consistent with the involvement of sulfamate anion at the cathode surface, either through: (i) hydrogen bonding between the amino group (-NH<sub>2</sub>) in sulfamate ions and the negatively charged electrode, or (ii) complexation of Ni<sup>2+</sup> by sulfamate ions through the lone pair of electrons on the amino group (-NH<sub>2</sub>) and the subsequent reduction of the generated nickel-sulfamate complex. The second mechanism seems more likely as the solution complexation of Ni<sup>2+</sup> by NH<sub>3</sub> has been previously reported [67].

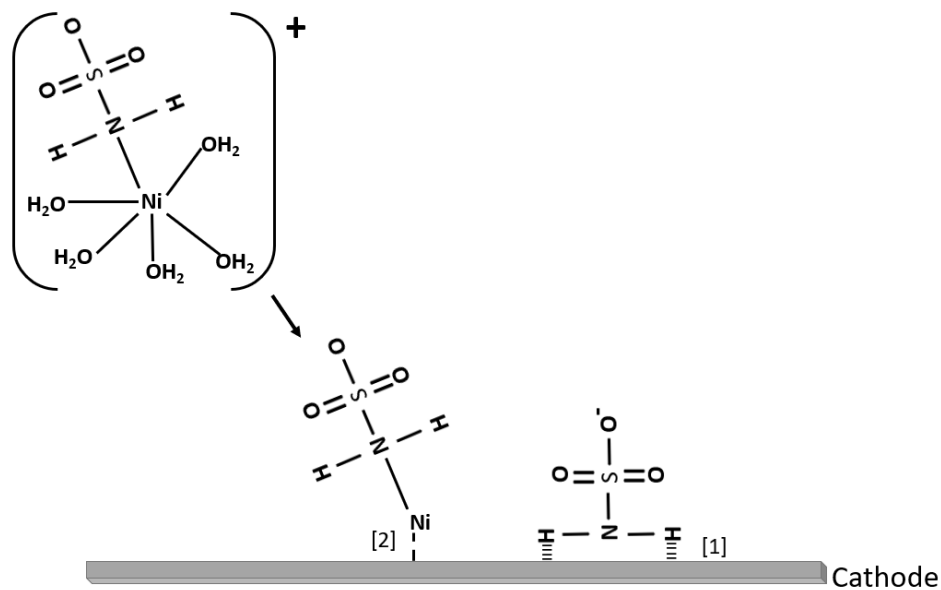


Figure 5.10: Schematic representation of the possible interaction of sulfamate anion with the cathode during nickel electrodeposition via [1] chemical interactions or [2] adsorption of a nickel-sulfamate complex.

### 5.1.5 Discussion

In the presented results, nickel electrodeposition from sulfamate systems at 40 °C in the absence of boric acid and stirring are often characterised by the generation of highly stressed deposits with current efficiencies which range from 19% to 100%. This has been attributed to the hydrogen evolution reactions which involve the parasitic reduction of protons and water molecules via the reaction mechanism clearly outlined in Equations 2.14 to 2.18 (c.f. chapter 2, section 2.1.1.2). These reactions could also affect deposit characteristics in the following ways: (i) absorption and desorption of adsorbed hydrogen which could cause tensile stress in deposits [65, 68, 229, 230], and (ii) alkalization of the electrolyte at the cathode surface where sufficient pH increase could allow the codeposition of Ni(OH)<sub>2</sub>/NiO which could also increase stress levels in the electrodeposited film [234, 235] while masking as high current efficiencies. The extensively cracked nature of deposits produced in the absence of boric acid and stirring made analysis via SEM and EDS difficult. Thereby, the formation of Ni(OH)<sub>2</sub>/NiO under these conditions could not be confirmed in these experiments but is investigated in the forthcoming chapter.

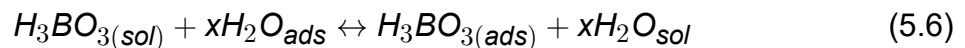
Temperature rise from 40 °C to 45-55 °C in unstirred boric acid-free sulfamate systems was effective at increasing faradaic current efficiencies and improving deposit appearance, but its beneficial effects were limited to low current densities <20 mA cm<sup>-2</sup>. Polarisation measurements indicated that higher partial nickel currents were obtained at elevated temperatures which suggested that the relative rate of nickel electrodeposition was enhanced by increasing temperature in agreement with earlier studies which reported that higher temperatures suppressed the rise in cathode surface pH [67].

Similar to increasing solution temperature, the addition of boric acid (0.49-0.81 M H<sub>3</sub>BO<sub>3</sub>) to unstirred sulfamate systems led to the generation of flat and crack-free deposits with high current efficiencies close to 100% which suggest that electrodeposition in the presence of H<sub>3</sub>BO<sub>3</sub> occurs with little to no hydrogen evolution. The beneficial effects of boric acid extended over a wide current density (10-50 mA cm<sup>-2</sup>) and temperature (40-55 °C) range. Current efficiencies have been verified using EDS analysis, which indicated that sound deposits produced with high current efficiencies were mainly

composed of metallic nickel (>96 wt%) with very low levels of oxygen (<1 wt%) and nitrogen (<3 wt%) impurities. Therefore, the presented faradaic efficiencies obtained in the presence of boric acid corroborate values reported by previous researchers [68]. Polarisation measurements and Tafel analysis indicate that higher partial nickel currents and exchange current densities are obtained in the presence of boric acid which suggest that  $H_3BO_3$  acts to enhance the relative rate of nickel electrodeposition rather than buffering of the electrolyte.

The addition of  $H_3BO_3$  to unstirred sulfamate systems produced higher Tafel slopes (120-251 mV/decade) than those measured in unstirred boric acid-free sulfamate baths in the absence ( $106 \pm 11$  mV/decade, 40 °C) and presence ( $130 \pm 15$  mV/decade, 40-55 °C) of chloride ions. This indicated that the electrodeposition mechanism in the presence of boric acid is different from that in its absence, presumably a two-step electron transfer process controlled by the adsorption of a nickel hydrolytic or chloride complex species (Equations 5.3-5.5).

Increase in Tafel slopes in the presence of boric acid suggests the development of an additional resistance at the electrode surface, which contributes to the activation overpotential during nickel electrodeposition. The formation of a nickel oxide/hydroxide film on the electrode surface in the presence of boric acid could be dismissed based on the EDS analysis results. Thereby, the high Tafel slopes measured in the presence of boric acid could be explained by the presence of adsorbed species on the cathode surface. It is proposed that boric acid molecules adsorb on the cathode surface during the electrodeposition of nickel, replacing one or more adsorbed water molecule at the surface:



The change in Tafel slopes also suggest a shift in mechanism where the intermediate species is no longer a simple hydrolytic or chloride complex. In this instance, adsorbed boric acid molecules may then combine with nickel hydrolytic or chloride ions from solution to form a weak complex which stabilises the adsorbed nickel cation and facilitates nickel ion reduction while blocking out other reactions, such as those for  $H_2$  evolution from  $H^+$  and  $H_2O$  discharge. Detected nitrogen impurities in nickel deposits

from the EDS analysis also provide some evidence that the sulfamate anion could interact with the electrode surface during charge transfer which could be via: (i) direct adsorption or (ii) a nickel complex ( $[\text{NiNH}_2\text{SO}_2\text{O}]^+$ ).

As mentioned earlier, Vincenzo and Cavallotti [61, 77] found that the addition of boric acid increased transient Tafel slopes measured during electrodeposition of nickel from sulfate and chloride electrolytes and cobalt from sulfamate solutions which led to the proposition that boric acid forms weak surface complexes with  $\text{NiOH}^+$  or  $\text{CoOH}^+$  which stabilise the metal cation. However, it was unclear from their paper [77] whether these claims applied to heterogeneous complexes or the adsorption of homogeneous complexes.

High Tafel slopes in the presented results could be correlated to high exchange current densities and current efficiencies. Therefore, the surface resistance responsible for the high Tafel slopes is required to produce deposits with high current efficiencies. In the presence of boric acid, this resistance has been proposed to result from the adsorption of  $\text{H}_3\text{BO}_3$  on the electrode surface which could inhibit the adsorption of protons or water molecules while stabilising nickel ion charge transfer intermediates at the surface.

## 5.2 Nickel electrodeposition from agitated solutions

Agitation is introduced in electroforming baths to dislodge adsorbed hydrogen bubbles from the mandrel surface that would otherwise cause "pitting" in deposits. Agitation also increases the convection of ions from the bulk solution to the cathode surface to replenish ions that are being reduced. Thus, the thickness of the diffusion layer and consequently, concentration overpotential decreases. On the other hand, agitation increases the turbulent flow of electrolyte at the electrode surface which could affect the adsorption of ions (such as those in Figure 5.10) [244]. Therefore, agitation could have considerable effects on nickel electrodeposition.

To understand the effect of electrode rotation on the action of boric acid during nickel electrodeposition, the rotation speed of the disc electrode was increased from 0

rpm to 900 rpm at 45 °C in each of the studied baths. This electrode rotation speed has been employed by earlier researchers, Kelly and Yang [208], to measure current-potential data from nickel sulfamate solution which could allow direct comparison of the experimental results to the results they reported.

### 5.2.1 Current-potential data from polarisation and deposition

Figure 5.11 presents the results of polarisation and galvanostatic experiments performed at 900 rpm and 45 °C in Baths A-F.

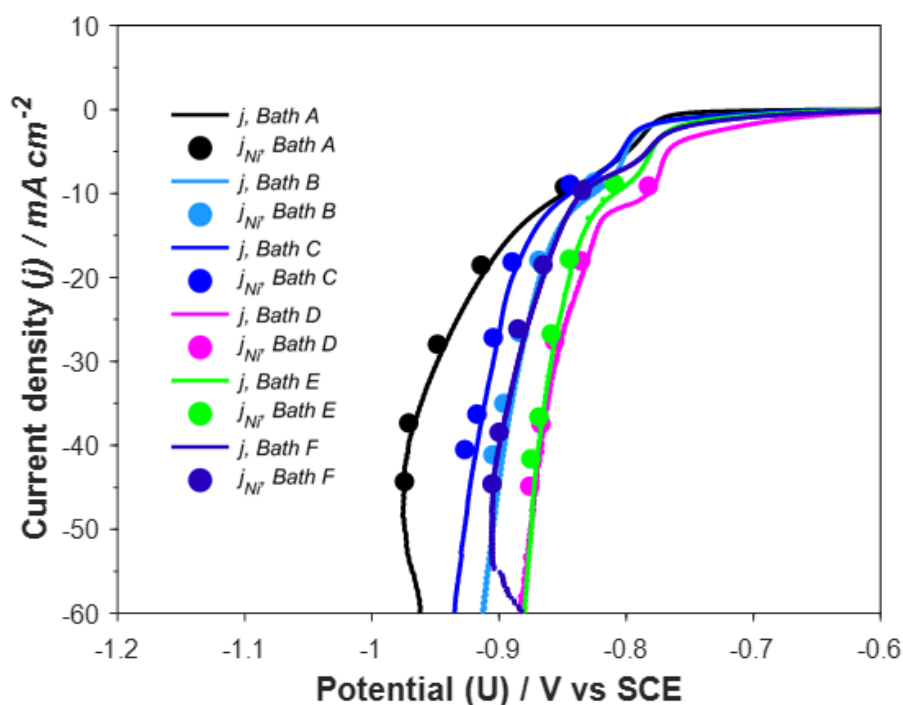


Figure 5.11: Polarisation curves: total current densities (solid lines) and Ni current density ( $\circ$ ) for electrodeposition in Bath A ( $\bullet$ ); Bath B ( $\circ$ ); Bath C ( $\bullet$ ); Bath D ( $\circ$ ); Bath E ( $\bullet$ ); and Bath F ( $\bullet$ ) at 45 °C and WE rotation speed of 900 rpm.

Comparison of the resulting  $j_{Ni}$ -U plots in Figure 5.11 with those in Figure 5.2b reveals that both  $Ni^{2+}$  reduction and HER begin at less negative potentials in all stirred baths. It is also observed that  $j_{Ni}$ -U plots lie close to the measured  $j$ -U curves which indicate high current efficiencies.

Table 5.4 summarises the faradaic efficiencies obtained from galvanostatic deposition under stirred conditions, which can be compared to the current efficiencies obtained under still conditions given in Table 5.1. Similar to previous reports [227,245], change in rotation speed from 0 rpm to 900 rpm during deposition at 45 °C slightly decreased the current efficiency in all baths, presumably due to an increased convection of protons to the cathode surface which increases the rate of HER. However, increased rotation speed also shows enhancement in Ni(II) transport to the electrode; for example, the very low current efficiencies which are marked in bold in Table 5.1 show a significant improvement when the RDE is rotated at 900 rpm. Use of agitation also seems particularly useful at high current densities, between 50-65 mA cm<sup>-2</sup> where Ni<sup>2+</sup> mass transfer could be an issue.

Table 5.4: Effect of deposition current densities and temperature on current efficiency for 20 μm thick nickel deposits from stirred sulfamate baths.

Baths	Current efficiency (%)					
	10 mA cm <sup>-2</sup>	20 mA cm <sup>-2</sup>	30 mA cm <sup>-2</sup>	40 mA cm <sup>-2</sup>	50 mA cm <sup>-2</sup>	65 mA cm <sup>-2</sup>
Temperature: 45 °C and Rotation rate: 900 rpm						
A	92.4	92.8	93.3	93.5	88.8	-
B	86.7	89.9	88.6	87.6	82.4	-
C	89.0	90.8	90.7	90.8	81.1	-
D	91.1	90.1	92.1	93.8	89.9	-
E	88.5	89.2	89.2	91.7	83.3	-
F	96.7	92.6	97.2	96.3	91.9	91.7
Temperature: 45 °C and Rotation rate: 1600 rpm						
F	89.2	91.1	91.5	92.4	89.2	89.2

It is expected that the increase in hydrogen evolution with increase in rotation speed will lead to deposit degradation due to codeposition and desorption of interstitial hydrogen and the alkalization at the electrode surface which could cause the occlusion of nickel hydroxides/oxides. However, it was found that stirring improved the deposit appearance in all baths especially those which do not contain boric acid. This resulted in flat and coherent deposits similar to those obtained in the presence of boric acid under still conditions as shown in Figure 5.3b. The improvement in deposit appearance in the presence of stirring, which has also been reported in earlier studies performed in

sulfate and chloride baths [227,232], could be attributed to the renewal of the electrolyte at the cathode surface which reduces or eliminates local pH variations and prevents sufficient rise in local pH to produce nickel hydroxides/oxides.

Under hydrodynamic conditions, the addition of 0.49-0.65 M  $\text{H}_3\text{BO}_3$  to nickel sulfamate solution with or without  $\text{Cl}^-$  decreased current efficiencies. An example of this observation is clearly shown in Figure 5.12 for a cathode current density of  $10 \text{ mA cm}^{-2}$ ; faradaic efficiencies at a rotation speed of 0 rpm and 900 rpm are depicted as black squares and red squares, respectively. To increase current efficiencies using boric acid, a concentration of 0.81 M (Bath F) is required at 900 rpm, but further increase in rotation speed to 1600 rpm decreases the current efficiencies (c.f. Table 5.4). Therefore, electrode rotation negatively affects the performance of boric acid in increasing current efficiencies in nickel sulfamate solutions. It is shown that to achieve high current efficiencies, stirred solutions require higher concentrations of boric acid than quiescent solutions.

## 5.2.2 Kinetics of nickel electrodeposition

Kinetic data measured from potential- $\log(j_{\text{Ni}})$  plots at 900 rpm are included in Table 5.5. Comparing the data for 45 °C in Tables 5.2 and 5.5, agitation seems to decrease the Tafel slopes for all electrolytes. As before, the Tafel slope for chloride containing solutions are within range of the cathodic Tafel slope value (120 mV/dec) used to corroborate the Ni electrodeposition mechanism outlined in Equations 5.3-5.5, which indicates that nickel electrodeposition could be controlled mainly by the adsorption of the  $\text{NiCl}^+$  complex. Tafel slopes for boric acid-containing electrolytes are similarly lower when a higher electrode rotation speed is employed, suggesting that agitation may reduce the resistance at the electrode surface.

Agitation also decreases the Ni exchange current density,  $j_o$  in Baths A-F by an order of magnitude. Since  $j_o$  is a function of the surface concentration of nickel ions [47], it is expected that it should increase when agitation is applied since there would be increased transport of Ni(II) to the electrode surface. The results are contrary to



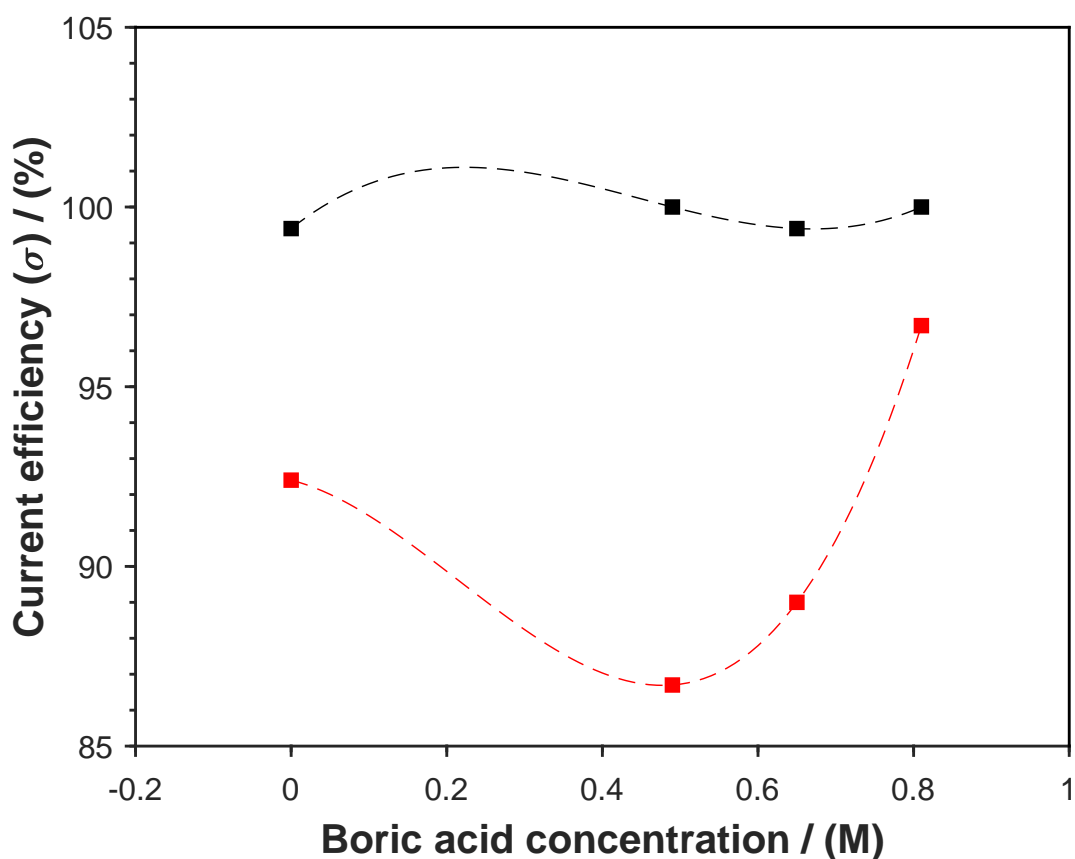


Figure 5.12: Effect of boric acid concentration on current efficiency of pure nickel sulfate solution for galvanostatic deposition at 45 °C and 10 mA cm<sup>-2</sup> with working electrode rotation speed of 0 rpm (black squares) and 900 rpm (red squares).

Table 5.5: Kinetic parameters for nickel deposition obtained from stirred sulfate baths.

Baths	$-b_c$ mV decade <sup>-1</sup>	$j_0$ mA cm <sup>-2</sup>
Temperature: 45 °C and Rotation rate: 900 rpm		
A	193 ± 41	0.147 ± 0.115
B	114 ± 5	0.011 ± 0.004
C	113 ± 4	0.008 ± 0.002
D	129 ± 7	0.052 ± 0.039
E	140 ± 37	0.083 ± 0.074
F	104 ± 6	0.004 ± 0.001

this which shows a reduction in  $\text{Ni}^{2+}$  at the electrode surface leading to a lower  $j_0$ . Looking at the overall results, it often seems that high Tafel slopes are coupled with higher values of  $j_0$  and faradaic efficiencies, in the presence of boric acid under still conditions.

### 5.2.3 Discussion

Stirring could have opposing effects on the deposition of nickel and the performance of boric acid:

1. Flow could enhance convection of boric acid molecules and nickel ions to the electrode surface which would increase their surface concentration. This effect could improve the performance of boric acid and deposition rate of nickel.
2. High shear stress resulting from high flow velocity of electrolyte at the electrode surface could separate adsorbed  $\text{H}_3\text{BO}_3$  or the complex formed between adsorbed  $\text{H}_3\text{BO}_3$  and nickel ions, causing more desorption from the electrode surface which could have a negative effect on boric acid performance and consequently, its ability to increase deposition current efficiency.

The balance of the above-mentioned effects during stirring leads to changes in surface coverage and could affect the performance of boric acid. Presented results indicate that increasing the rotation speed from 0 rpm to 900 rpm negatively impacted the ability of boric acid to increase deposition current efficiency. In fact, the contrary was observed where the addition of boric acid (0.49-0.65 M) to stirred sulfamate baths in the absence and presence of chloride ions lowered current efficiencies. As mentioned, this could be attributed to: (i) the shearing action of electrode rotation which could increase desorption of boric acid causing less boric acid presence at the electrode surface, and (ii) the lower pH of boric acid-containing electrolytes which means a higher proton concentration at the electrode surface.

Further evidence of the reduced interactions of boric acid at the electrode surface under stirred conditions could be gleaned from the decrease in Tafel slopes when

the rotation speed is increased from 0 to 900 rpm. Measured Tafel slopes in stirred baths which contain boric acid were found to be within range of the calculated Tafel slope (120 mV/decade) which has been used to corroborate the mechanism where nickel electrodeposition is limited by the direct adsorption of nickel hydrolytic or chloride complexes on the electrode surface as outlined in Equations 5.3 to 5.5. Tafel slopes obtained with electrode rotation in these experiments show good agreement with those obtained from literature (80-120 mV decade<sup>-1</sup>) in similarly stirred nickel sulfamate baths at 30-50 °C in the pH range 3-4 [61, 208]. The use of agitation seems to be particularly useful in sulfamate systems without boric acid where rotating the electrode at 900 rpm produced sound deposits with current efficiencies around 92%.

### 5.3 Summary of main findings

Polarisation, galvanostatic, and gravimetric measurements were employed to systematically investigate the influence of boric acid on the current efficiency and kinetics of nickel electrodeposition from sulfamate electrolytes at a 304 stainless steel disc electrode at different boric acid concentrations (0 to 0.81 M), temperatures (40-55 °C), and electrode rotation speeds (0-1600 rpm). It was found that the deposition of nickel from boric acid-free, unstirred baths at 40 °C is accompanied by high rates of hydrogen evolution, via either proton or water reduction, at low and high overpotentials (characterised by low current efficiencies), providing a narrow potential range over which deposits with high current efficiencies could be obtained. It was also found that all nickel deposits plated in these baths possessed high internal stresses characterised by many cracks. It was shown that increasing the solution temperature to 55 °C led to the production of nickel films with current efficiencies close to 100% and improved deposit appearances (i.e crack-free) at low current densities ( $\leq 20 \text{ mA cm}^{-2}$ ).

The addition of boric acid to unstirred electroforming electrolytes caused the deposition of flat and crack-free nickel films with current efficiencies close to 100% over a wide current/potential range. A decrease in overpotential could also be observed in the presence of boric acid which indicated higher deposition rates. It was concluded that boric acid suppressed hydrogen evolution which enabled low-internal-stress de-

posits; EDX analysis detected minimal amounts of impurities ( $< 1$  wt% O,  $< 3$  wt% N, and no S or B within detection limits) in the deposits indicating that the deposits were metallic. It is also concluded that the  $\text{Ni}^{2+}$  reduction reaction is facilitated in the presence of boric acid which led to increased deposition rates due to the suppression of side processes which block active sites. Increasing temperature in solutions containing boric acid shifted nickel deposition to less negative potentials but had a minimal effect on the current efficiency.

Still in unstirred baths, Tafel slopes and exchange current densities were determined in the absence and presence of boric acid at different temperatures. In most cases, the presence of boric acid gave rise to measured cathodic Tafel slopes above 140 mV/dec, compared to that of around 120 mV/dec for nickel sulfamate without boric acid. Ni exchange current densities were also lower in the absence of  $\text{H}_3\text{BO}_3$ . The high Tafel slopes measured in the presence of boric acid suggested that there was a surface resistance which provided an additional energetic barrier during nickel electrodeposition. Therefore, it was hypothesised that boric acid adsorbs on the electrode surface, preventing the adsorption of participating species in HER ( $\text{H}^+$  and/or  $\text{H}_2\text{O}$ ) while facilitating nickel electrodeposition.

Increase in electrode rotation speed from 0 rpm to 900 rpm in baths containing boric acid gave rise to lower deposition current efficiencies ( $\approx 90\%$ ), Tafel slopes (around 120 mV/dec), and Ni exchange current densities. Interestingly, current efficiencies for nickel deposition from stirred baths containing boric acid were lower than those for stirred baths lacking boric acid. It was also determined that stirred baths required a higher concentration of boric acid (0.81 M) than unstirred ones (0.49-0.65 M) to produce comparable current efficiencies. Therefore, it was concluded that agitation detrimentally affected the performance of boric acid by decreasing the adsorption of  $\text{H}_3\text{BO}_3$  on the electrode surface as a result of the electrolyte's high velocity flow.

# Chapter 6

## Effect of boric acid on the interfacial processes during nickel electrodeposition: An EQCM study

In the previous chapter, it has been demonstrated that the addition of boric acid to quiescent sulfamate electrolytes always led to the generation of flat, compact deposits with lower overpotential and current efficiencies close to 100% indicating that boric acid enhanced nickel electrodeposition and decreased the rate of hydrogen evolution. It is proposed that the modification of these surface reactions is due to the formation of complexes between  $\text{NiX}^+$  (where X is OH or Cl) and boric acid molecules, most probably adsorbed on the electrode surface, taking place at the initial stages of the formation of the bulk Ni deposit; this route manifests itself in the Tafel slope values exceeding the value (120 mV/decade) expected for the route where  $\text{NiX}^+$  is discharged via two consecutive single-electron transfer steps on an electrode surface which has no adsorbed species.

Using potentiodynamic experiments combined with an EQCM, Song et al [65] reported on the initial stages of nickel electrodeposition from a sulfate electrolyte at room temperature in the absence and presence of boric acid on a Pt-coated quartz crystal electrode. The findings demonstrated that, in the absence of boric acid,  $\text{Ni(OH)}_2$  was produced during the early stages of deposition, indicating the generation of  $\text{OH}^-$  at the start. An independent investigation using microsensor measurements also showed that the pH at the electrode surface increased to values that were markedly higher than that in the bulk immediately after the application of a current density of  $180 \text{ mA cm}^{-2}$  to electrodeposit nickel from a boric acid-free sulfamate electrolyte [68]. Song et al. [65] presumed that  $\text{Ni(OH)}_2$  does not form in sulfate electrolytes containing boric acid but they did not provide adequate explanation for the cause of this presumption. As stated earlier, it is hypothesised that boric acid adsorbs on the electrode surface to obstruct hydrogen evolution via proton or water reduction. This hypothesis has also been put

forward in previous nickel electrodeposition studies [61, 73–75] but the adsorption of boric acid on the electrode surface has not been experimentally confirmed in these studies.

The aim of this chapter is to combine potentiodynamic and QCM experiments to provide a dynamic description of the interface as a function of key variables: potential, boric acid, and substrate material in the absence and presence of nickel ions. First, EQCM experiments were conducted to verify that the current-potential and current efficiency results obtained at the stationary RDE shown in the previous chapter (section 5.1) were reproducible at the quartz crystal electrode. Furthermore, the effects of boric acid on the hydrogen evolution reaction and initial stages of nickel electrodeposition are studied on Ni, Au, Cu, and 304 SS, to investigate the different interactions between boric acid and metals and to understand the influence of the substrate material.

## 6.1 Response of the quartz crystal to mass changes on the electrode surface

Mass changes and thus frequency variations at the electrode surface could be caused by electrodeposition, adsorption, absorption, desorption, and oxidation processes. Therefore, to understand the results in this chapter and evaluate the interfacial processes during nickel electrodeposition, the frequency and mass changes caused by a single monolayer of potentially adsorbed compounds during nickel electrodeposition are computed in this section and summarised in Table 6.1.

The mass of a monolayer ( $\Delta m_{monolayer}$ , g) is evaluated using the formula:

$$\Delta m_{monolayer} = m_a \theta_{compound} G_{compound} A_{EQCM} \quad (6.1)$$

where  $m_a$  (=molar mass [ $\text{g mol}^{-1}$ ] / Avogadro constant [ $6.022 \times 10^{23} \text{ mol}^{-1}$ ]) represents the mass of an atom or molecule of the compound (g),  $\theta_{compound}$  is the surface coverage (0 to 1),  $G_{compound}$  is the atom or molecule packing density ( $\text{atoms cm}^{-2}$ ), and  $A_{EQCM}$  is the area of the quartz electrode ( $0.196 \text{ cm}^2$ ). To calculate the change in electrode mass owing to maximal surface coverage by an adsorbed monolayer,  $\theta_{compound}$

Table 6.1: Theoretical mass and frequency changes calculated for various processes expected to take place during nickel electrodeposition [EQCM surface area = 0.196 cm<sup>2</sup>].

Adsorbate/substrate	Mass per atom (g)	Atomic packing density G (atoms cm <sup>-2</sup> )	$\Delta m_{monolayer}$ (ng)	$\Delta f_{monolayer}$ (Hz)	$Q_{monolayer}$ (mC)
Ni (100)/304SS	$9.75 \times 10^{-23}$	$1.61 \times 10^{15}$	30.77	27.88	0.10
Ni (110)/304SS	$9.75 \times 10^{-23}$	$1.14 \times 10^{15}$	21.79	19.74	0.07
Ni (111)/304SS	$9.75 \times 10^{-23}$	$1.85 \times 10^{15}$	35.35	32.03	0.12
H/Ni-coated Au	$1.67 \times 10^{-24}$	$1.53 \times 10^{15}$	0.50	0.38	0.05
H <sub>3</sub> BO <sub>3</sub> /Ni-coated Au	$1.03 \times 10^{-22}$	$1.69 \times 10^{15}$	34.12	25.66	-
H <sub>2</sub> O/Ni-coated Au	$2.99 \times 10^{-23}$	$1.53 \times 10^{15}$	8.97	6.75	-
(NH <sub>2</sub> SO <sub>3</sub> ) <sup>-</sup> /Ni-coated Au	$1.60 \times 10^{-22}$	$1.43 \times 10^{15}$	44.80	33.69	-
OH <sup>-</sup> /Ni-coated Au	$2.82 \times 10^{-23}$	$1.53 \times 10^{15}$	8.46	6.36	-
NiO/Ni-coated Au	$1.24 \times 10^{-22}$	$1.53 \times 10^{15}$	37.19	27.97	0.10
NiO(OH)/Ni-coated Au	$1.52 \times 10^{-22}$	$1.53 \times 10^{15}$	45.58	34.28	0.10
Ni(OH) <sub>2</sub> /Ni-coated Au	$1.54 \times 10^{-22}$	$1.53 \times 10^{15}$	46.18	34.73	0.10
Ni→NiO/Ni-coated Au	$2.66 \times 10^{-23}$	$1.53 \times 10^{15}$	7.97	5.99	0.10
Ni→Ni(OH) <sub>2</sub> /Ni-coated Au	$5.65 \times 10^{-23}$	$1.53 \times 10^{15}$	16.94	12.74	0.10
Cu (100)/Au	$1.06 \times 10^{-22}$	$1.52 \times 10^{15}$	31.58	23.75	0.10
Cu (110)/Au	$1.06 \times 10^{-22}$	$1.08 \times 10^{15}$	22.44	16.87	0.07
Cu (111)/Au	$1.06 \times 10^{-22}$	$1.76 \times 10^{15}$	36.57	27.50	0.11

is assumed to be one. Frequency changes caused by the adsorption/desorption of a single monolayer ( $\Delta f_{monolayer}$ , Hz) are calculated as follows using the sensitivity coefficient of the substrate [For steel,  $C_f$  of 0.906 Hz ng<sup>-1</sup>; Au,  $C_f$  of 0.752 Hz ng<sup>-1</sup>]:

$$\Delta f_{monolayer} = C_f \Delta m_{monolayer} \quad (6.2)$$

The lattices of metallic Ni and Cu are face-centred cubic (FCC) structures with optimised lattice parameters,  $a$ , of 0.35295 and 0.36258 nm, respectively [246]. Thus, the atomic packing densities,  $G$  for fcc(100), fcc(110), and fcc(111) planes were calculated using the following formulas:

$$\text{For FCC}(100) : G = \frac{2}{a^2} \quad (6.3)$$

$$\text{For FCC}(110) : G = \frac{\sqrt{2}}{a^2} \quad (6.4)$$

$$\text{For FCC}(111) : G = \frac{4}{\sqrt{3}a^2} \quad (6.5)$$

where  $a$  is the optimised lattice parameter (cm).

It is reasonable to assume, based on experimental evidence [101, 117], that hydrogen evolves on nickel during nickel electrodeposition, whether it originates on a foreign or nickel substrate. Therefore, the average of the atomic packing densities for the three Ni FCC planes was used to calculate an average value for  $\Delta m_{monolayer}$  for small molecules such as H and OH. It is necessary to assume that full surface coverage cannot exceed one molecule/atom/anion for a single Ni atom when calculating  $\Delta m_{monolayer}$ . For larger molecules such as  $H_3BO_3$  and  $(NH_2SO_3)^-$ , the surface area of a single molecule was found by using the B-O (0.1365 nm) and S-O (0.149 nm) bond lengths as the radius of a circle [247, 248]. The inverse of this molecular area provided the molecular packing density.

Additionally, the amount of charge,  $Q_{monolayer}$ , required to form a monolayer was calculated from Faraday Equation 6.6:

$$Q_{monolayer} = \frac{\Delta m_{monolayer} n F}{M} \quad (6.6)$$

where  $Q_{monolayer}$  is the amount of charge passed to form a monolayer (C),  $\Delta m_{monolayer}$  is the mass of a monolayer (g),  $n$  is the number of electrons transferred in the reaction,  $F$  is Faraday constant (96485 C/mol), and  $M$  is the atomic mass/molar mass of the adsorbed species (g/mol).

Some observations could be made from the data in Table 6.1:

1. The frequency changes caused by the adsorption of a single monolayer of hydrogen and Ni FCC (110) are 0.38 and 19.74 Hz, respectively. The EQCM's detection accuracy for frequency change is 1 Hz and therefore, it is not expected that a hydrogen adlayer could be reliably detected but the formation of a nickel monolayer should be clearly detected once deposition begins.
2. The mass of an adlayer of hydroxyl ions ( $OH^-_{ads}$ ) is nearly the same as that of  $H_2O_{ads}$ . Notwithstanding, a full surface coverage by hydroxyl ions ( $OH^-_{ads}$ ) is improbable due to repulsive interactions between the negatively charged ions. However, a mixed  $H_2O_{ads}/OH^-_{ads}$  ad-layer with a mass nearly equal to that of a monolayer of solely  $H_2O_{ads}$  or  $OH^-_{ads}$  may provide full coverage.



3. The masses of adlayers of Ni(111) and  $\text{H}_3\text{BO}_3$  are the same. This indicates that adsorption of boric acid and the formation of a Ni monolayer would be indistinguishable during nickel electrodeposition, but they would be distinguished in terms of charge required to discharge them.
4. The masses of adlayers of  $\text{Ni}(\text{OH})_2$  and  $\text{NiO}(\text{OH})$  are the same and are at least 10 ng greater than that of Ni. Therefore, the formation of oxyhydroxides/hydroxides could be indicated by the measurement of a greater mass than that expected for metallic Ni for a certain amount of charge passed. However, the EQCM is unable to distinguish between  $\text{Ni}(\text{OH})_2$  and  $\text{NiO}(\text{OH})$ .

## 6.2 Effect of boric acid on nickel electrodeposition

An EQCM was used to study the effect of boric acid concentration in an electroforming bath on the nickel deposition rate and current efficiency at different temperatures by performing potentiodynamic measurements. As mentioned earlier, these experiments were performed to verify reproducibility of the results obtained at the stationary RDE shown in the previous chapter. In this way, subsequent results obtained the quartz crystal electrode could be related to those obtained at the larger RDE electrode.

### 6.2.1 Ni electrodeposition in the absence of boric acid

Figure 6.1 shows the measured current (solid black line) obtained from a Linear Sweep Voltammetry experiment performed from OCP ( $\approx -0.172$  V) to  $-1.2$  V in pure nickel sulfamate solution (Bath A) at  $45^\circ\text{C}$  on a 304 SS quartz crystal electrode. Figure 6.1 also shows the frequency change curve (dotted red line) obtained from the EQCM as a function of the potential scan measured concurrently with the Linear Sweep Voltammogram.

The overall observation from Figure 6.1 is that the frequency change ( $\Delta f$ ) decreases as the measured current density increases. This decrease in  $\Delta f$  corresponds to an increase in mass at the electrode surface. Since it is known that nickel electrode-

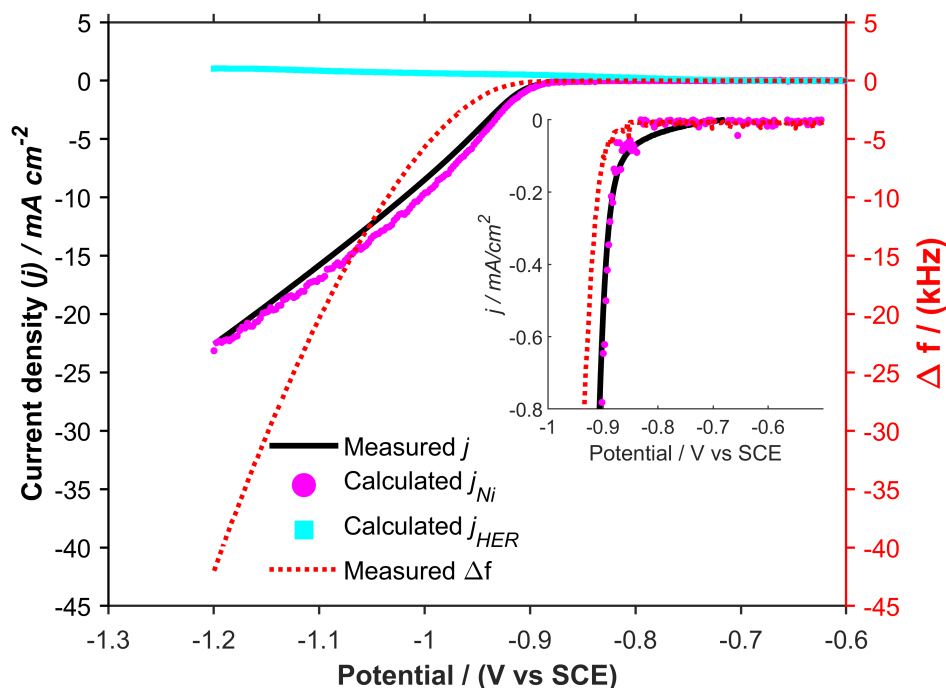


Figure 6.1: Polarisation scan performed on 304 stainless steel quartz crystal electrode in 1.78 M nickel sulfamate solution at 45 °C with scan rate 5 mV s<sup>-1</sup>, showing the measured current density, calculated current density for Ni deposition, calculated current density for HER, and frequency change. The Figure inset shows the effect of hydrogen evolution on the initial stage of nickel electrodeposition observed from the negative potential shift of frequency and calculated Ni current breakthrough compared to that of the measured current.

position is the only reduction reaction responsible for a mass change on the electrode surface, the frequency measurements were converted into a current density,  $j_{calc}$ , to characterise the rate of Ni electrodeposition onto the surface of the electrode. This was calculated using Equation 4.19 already given in Chapter 4. As stated in chapter 4, Sauerbrey Equation is only valid for frequency changes less than 2% of the resonant frequency in solution. Therefore, for 304SS crystals oscillating at 9.07 MHz, Equation 4.19 is only valid for  $\Delta f$  values up to 181.4 kHz. Values of  $\Delta f$  measured during nickel plating experiments were less than 100 kHz which meant that Equation 4.19 could be applied to all analysis.

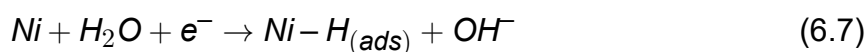
From this point, the current density,  $j_{calc}$ , is referred to as the calculated current density and is displayed in Figure 6.1 as magenta circles. As stated earlier, this

current density is directly related to the rate at which nickel is deposited onto the surface of the electrode. Therefore, the difference between the measured and calculated currents is due to side reactions which would present virtually no mass change on the electrode surface. Solutions were purged with nitrogen gas to remove dissolved oxygen prior to collecting the measurements. Therefore, it is assumed that the current density pertaining to the oxygen reduction reaction is negligible. The two main side reactions in this case would be the reduction of protons and water which constitute the hydrogen evolution reaction (HER). Calculated current densities were subtracted from the measured current densities to determine the HER current densities. HER current densities are plotted as cyan squares in Figure 6.1.

It can be observed from Figure 6.1 that the calculated current density started to increase with the measured current density at -0.90 V (see inset, Figure 6.1) indicating that the measured currents are responsible for a mass increase on the electrode surface which could be attributed to Ni adsorption or deposition. It is also observed that the measured and calculated currents are in good agreement for potential values up to -0.94 V. This indicates that Ni electrodeposition is the dominant reaction over this potential range.

At potentials more negative than -0.94 V, calculated current densities exceeded the measured current density which means the frequency/mass change is greater than that for a process in which nickel ions are reduced electrochemically to metallic Ni. This indicates that Ni is deposited with other products. The additional mass gain could contain a contribution from the incorporation of nickel hydroxide ( $\text{Ni}(\text{OH})_{2(s)}$ ) during the growth of the deposit due to hydrogen evolution in this potential region.

During the initial scan, the cathode surface was gradually covered by nickel, and the substrate changed from stainless steel to nickel. Water reduction on electrodeposited nickel (Equation 6.7) would lead to the formation of hydroxyl ions that could react with  $\text{Ni}^{2+}$  to precipitate nickel hydroxide on the electrode surface (Equation 6.8).



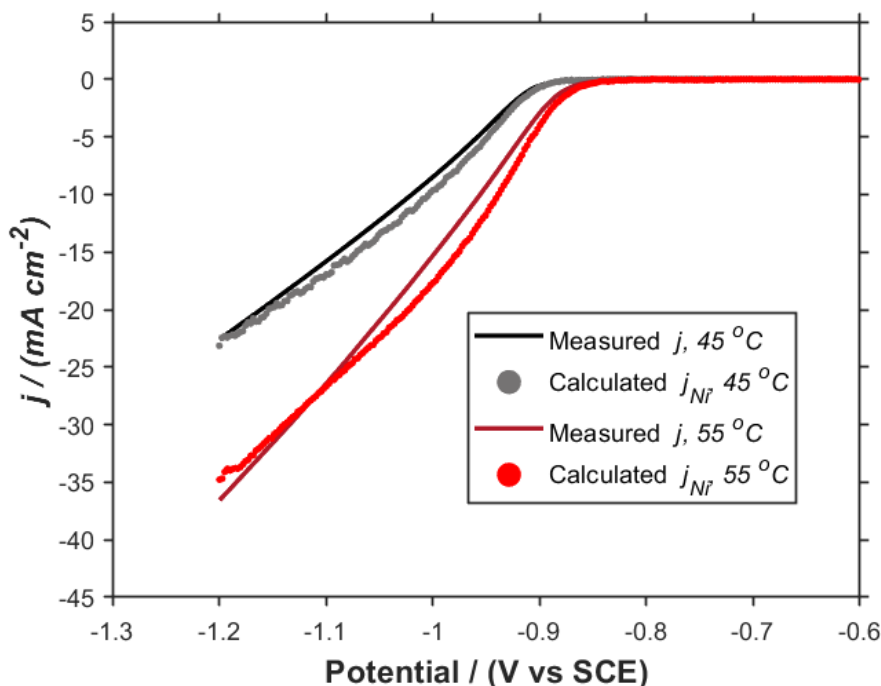


Figure 6.2: Polarisation scan performed on 304 stainless steel quartz crystal electrode in 1.78 M nickel sulfamate solution at 45 °C and 55 °C with scan rate 5 mV s<sup>-1</sup>.

Nickel electrodeposition from pure nickel sulfamate solution was also investigated at 55 °C and the results are shown in Figure 6.2. The measured and calculated polarisation scans are shifted to less negative potentials at 55 °C. This could be attributed to an increase in solution temperature increasing the charge transfer rate of both Ni<sup>2+</sup> electroreduction and HER. This is because an increase in temperature will usually increase the conductivity of the solution, the diffusivity of ions, and the rate of charge transfer which would lower the activation and concentration overpotentials of reactions.

At 55 °C and a potential of -0.85 V, calculated currents exceeded measured currents up to -1.09 V which could again be attributed to nickel hydroxide formation. It could also be observed that the potential at which the calculated current exceeded the measured current is less negative at 55 °C compared to that at 45 °C. This could indicate that an increase in temperature increases the kinetics for water reduction. This is because the appearance of hydroxyl ions responsible for the formation of Ni(OH)<sub>2</sub> is inseparable from water reduction. At potentials more negative than -1.09 V, calculated

current decreased below the measured current which might imply a suppression of nickel deposition by the adsorbed  $\text{Ni}(\text{OH})_{2(s)}$  layer or an increase in the rate of HER.

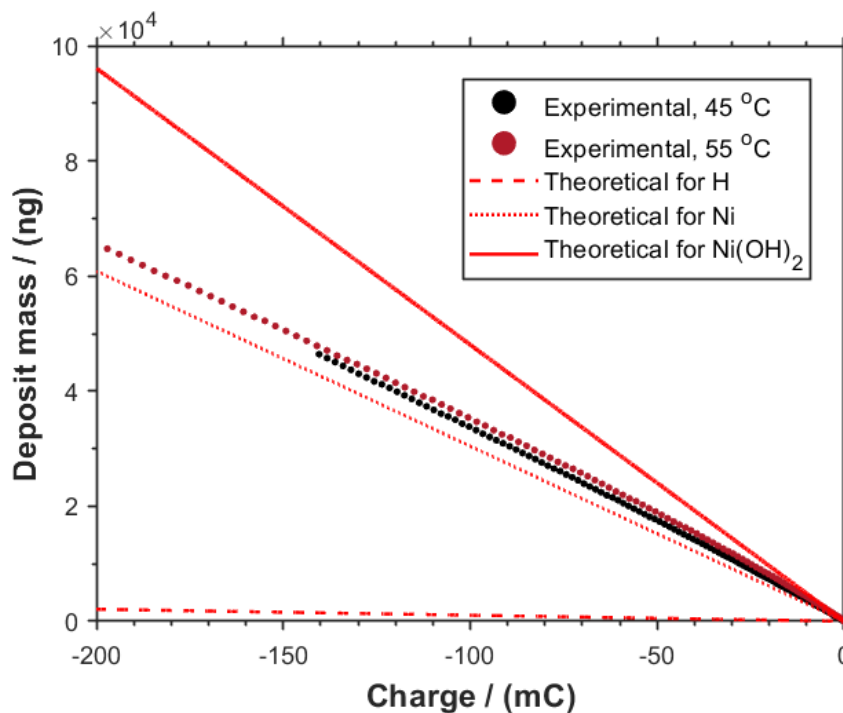


Figure 6.3: Charge vs mass change during Ni electrodeposition on 304SS quartz crystal electrode from 1.78 M nickel sulfamate solution at 45 °C and 55 °C.

To evaluate the reduced species in the electrochemical reaction, the frequency data was converted to mass changes and plotted against charge as shown in Figure 6.3. The charge was determined by integrating the measured currents in Figure 6.2 with respect to time. For comparison, Figure 6.3 also shows the theoretical lines of mass change vs. charge for hydrogen evolution, nickel deposition, and nickel hydroxide with slopes calculated using Faraday Equation:

$$\frac{\Delta m}{Q} = \frac{M}{zF} \quad (6.9)$$

where  $\Delta m$  is the mass change caused by the reaction (g),  $M$  is the Molecular weight (g/mol),  $Q$  is the charge passed (C),  $z$  is the number of electrons transferred in the reaction, and  $F$  is Faraday constant (96485 C/mol). Considering an ideal nickel ion reduction reaction involving 2 moles of electrons (Equation 6.10), the  $\Delta m/Q_{Ni}$  ratio must be 304.16 ng/mC (MW Ni = 58.6934 g/mol).



For hydrogen evolution,  $\Delta m/Q_H$  ratio corresponds to 10.45 ng/mC (MW H = 1.00784 g/mol) following Equation 2.12. Following the global reactions from Equations 2.13 and 6.8,  $\text{Ni}(\text{OH})_2$  formation corresponds to a  $\Delta m/Q_{\text{Ni}(\text{OH})_2}$  ratio of 480.43 ng/mC (MW  $\text{Ni}(\text{OH})_2 = 92.708$  g/mol).

It was observed from Figure 6.3 that the mass increased linearly with charge with a slope of 336.35 and 332.64 ng/mC at 45 and 55 °C, respectively, which is greater than the  $\Delta m/Q$  ratio for nickel deposition (304.16 ng/mC). To calculate the fraction of the deposit that consists of metallic nickel, an overall mass balance could be done as follows:

$$\Delta m_{\text{measured}} = \alpha \Delta m_{\text{Ni}} + (1 - \alpha) \Delta m_{\text{Ni}(\text{OH})_2(\text{ads})} \quad (6.11)$$

where  $\Delta m_{\text{measured}}$  is the total mass of the deposit measured during the experiment,  $\alpha$  is the fraction of the deposit consisting of metallic nickel,  $\Delta m_{\text{Ni}}$  is the mass change pertaining to metallic nickel, and  $\Delta m_{\text{Ni}(\text{OH})_2(\text{ads})}$  is the mass change pertaining to  $\text{Ni}(\text{OH})_2(\text{ads})$ . Dividing Equation 6.11 through by the total charge, Q:

$$\left[ \frac{\Delta m}{Q} \right]_{\text{measured}} = \alpha \frac{\Delta m_{\text{Ni}}}{Q} + (1 - \alpha) \frac{\Delta m_{\text{Ni}(\text{OH})_2(\text{ads})}}{Q} \quad (6.12)$$

$$\left[ \frac{\Delta m}{Q} \right]_{\text{measured}} = 304.16\alpha + 480.43(1 - \alpha) \quad (6.13)$$

Rearranging Equation 6.13 for  $\alpha$ ,

$$\alpha = \frac{\left[ \frac{\Delta m}{Q} \right]_{\text{measured}} - 480.43}{304.16 - 480.43} \quad (6.14)$$

The value for  $\alpha$  was calculated to be 0.81 and 0.84 at 45 and 55 °C, respectively. Therefore, in the absence of boric acid, about 15-20% of nickel hydroxide is deposited alongside nickel which is similar to the findings of other researchers in Watts-type [65] and chloride-type [227] baths.

In summary, a large amount of  $\text{OH}^-$  is generated in the solution in the vicinity of the electrode surface in the absence of boric acid. These  $\text{OH}^-$  combine with  $\text{Ni}^{2+}$  to form  $\text{Ni}(\text{OH})_2$ , decreasing the surface concentration of  $\text{Ni}^{2+}$  available to participate in the faradaic reaction. The appearance of  $\text{OH}^-$  on the cathode surface could only come from water reduction as it is the only cathode reaction which would generate  $\text{OH}^-$ . Therefore, it can be concluded that adsorbed  $\text{Ni}(\text{OH})_2$  decreases the conductivity of the electrode surface and impedes the deposition of nickel.

## 6.2.2 Ni electrodeposition in the presence of boric acid

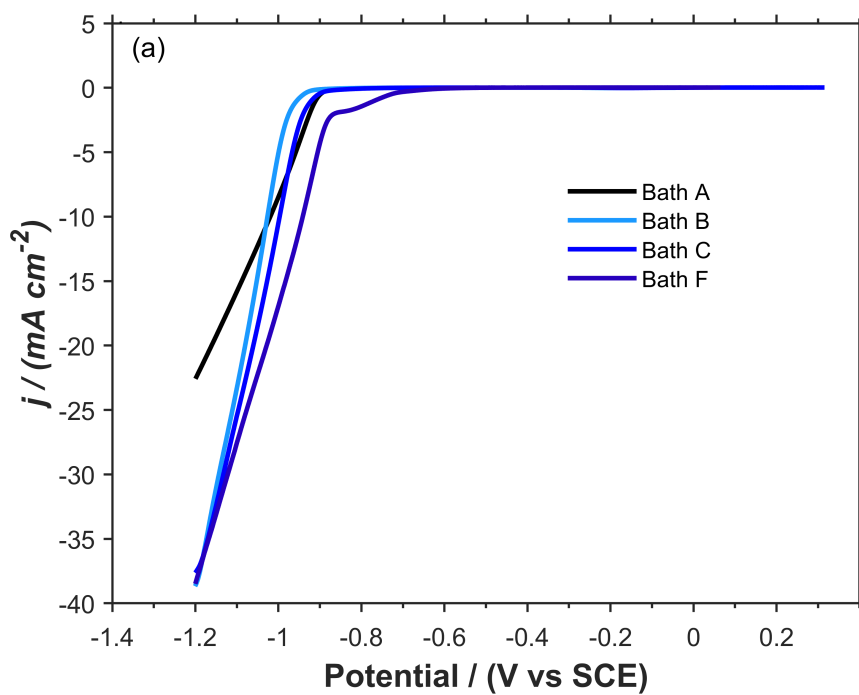
The LSVs and frequency changes recorded for nickel electrodeposition on 304SS quartz crystal electrode at 45 °C in nickel sulfamate solutions containing varying boric acid concentrations from 0 to 0.81 M are shown in Figures 6.4a and b, respectively.

The polarisation scans in Figure 6.4a show that the addition of increasing concentrations of  $\text{H}_3\text{BO}_3$  decreases the overpotential for nickel electrodeposition. The frequency scans measured in the same solutions also shift to less negative potentials as the concentration of boric acid in the bath is increased indicated an increase in the deposition rate which is in accordance with the increase in polarisation currents. These results also verify the findings in section 5.1.2.

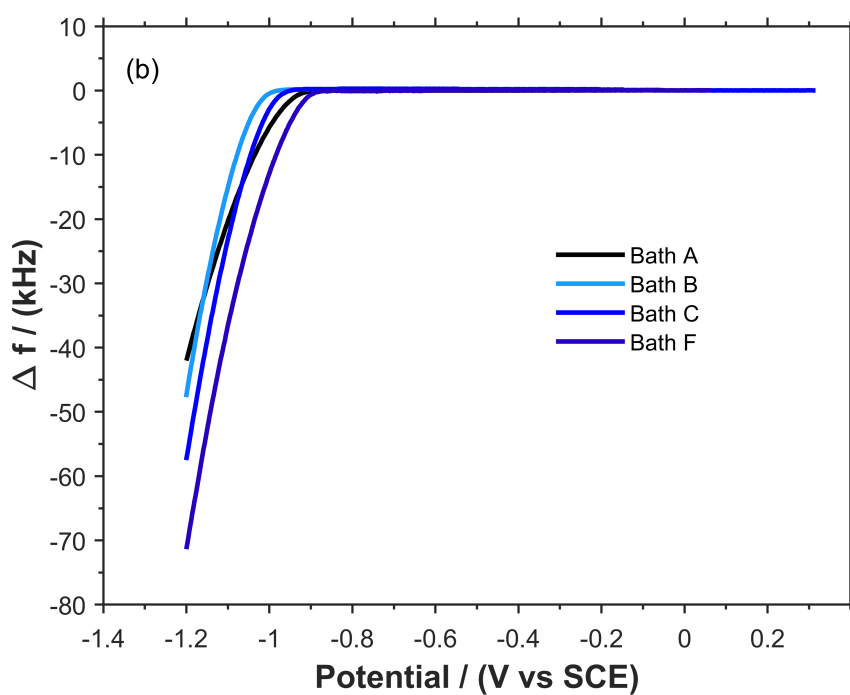
This finding was further investigated by determining current densities calculated from  $\Delta f$  measured in nickel sulfamate solutions with varying boric acid concentrations and comparing them against experimentally observed currents. For easy comparison, these calculated current densities were plotted as dotted lines alongside measured current densities (solid lines) from the potentiodynamic experiments as shown in Figure 6.5. It can be observed that, in all baths containing boric acid, the measured and calculated current densities were in good agreement which indicates that frequency changes of the electrode are mainly caused by the reduction of  $\text{Ni}^{2+}$  to Ni. This is in accordance with the RDE gravimetry results in section 5.1.2.

A second observation is that at potentials corresponding to zone B ( $-0.7 \text{ V} > U > -0.93 \text{ V}$ ) in the presence of 0.81 M  $\text{H}_3\text{BO}_3$ , there is a slow increase in measured current density to  $2.5 \text{ mA cm}^{-2}$ . However, there is no discernible increase in calculated current, so the current detected in Zone B could be attributed to the reduction of protons (Equation 2.12). HER was also observed during the early phases of nickel electrodeposition in solutions containing lower concentrations of boric acid, i.e. 0.49-0.65 M, albeit to a lesser level.

The addition of boric acid therefore appears to facilitate the relative reduction of  $\text{Ni}^{2+}$  while decreasing active sites available for the adsorption of  $\text{H}^+$  and  $\text{H}_2\text{O}$ . However, the addition of  $\text{H}_3\text{BO}_3$  decreases bulk solution pH which can affect  $\text{H}^+$  reduction



(a)



(b)

Figure 6.4: (a) Polarisation and (b) frequency scans for nickel electrodeposition in quiescent Bath A (●); Bath B (●); Bath C (●); and Bath F (●) at 45 °C; scan rate = 5 mV/s



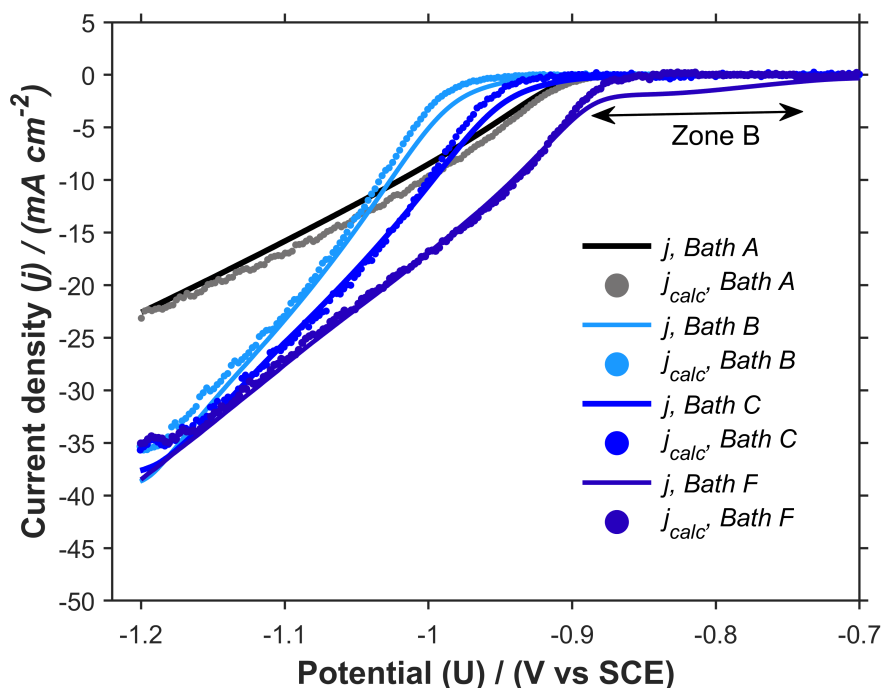


Figure 6.5: LSV of nickel electrodeposition in quiescent Bath A (●); Bath B (●); Bath C (●); and Bath F (●) at 45 °C, showing the measured current densities,  $j$  (solid lines) and calculated current densities,  $j_{calc}$  (circles)

during the early stages of nickel electrodeposition, i.e., between the current break-through potential and 200 mV following this potential. Hence, in the solution with the lowest bulk pH, i.e. nickel sulfamate containing 0.81 M  $H_3BO_3$  (Bath F),  $H^+$  reduction is the predominant reaction at the start of polarisation (Zone B, Figure 6.5).

Figure 6.6 shows the effect of varying boric acid concentration from 0 to 0.81 M on the measured and calculated polarisation scans at 55 °C. An increase in temperature from 45 to 55 °C has two main effects: (i) increases measured polarisation currents and (ii) calculated currents become lower than the measured values especially in the bath containing the highest concentration of boric acid (0.81 M). These results also verify the findings in the previous chapter (section 5.1.2.3).

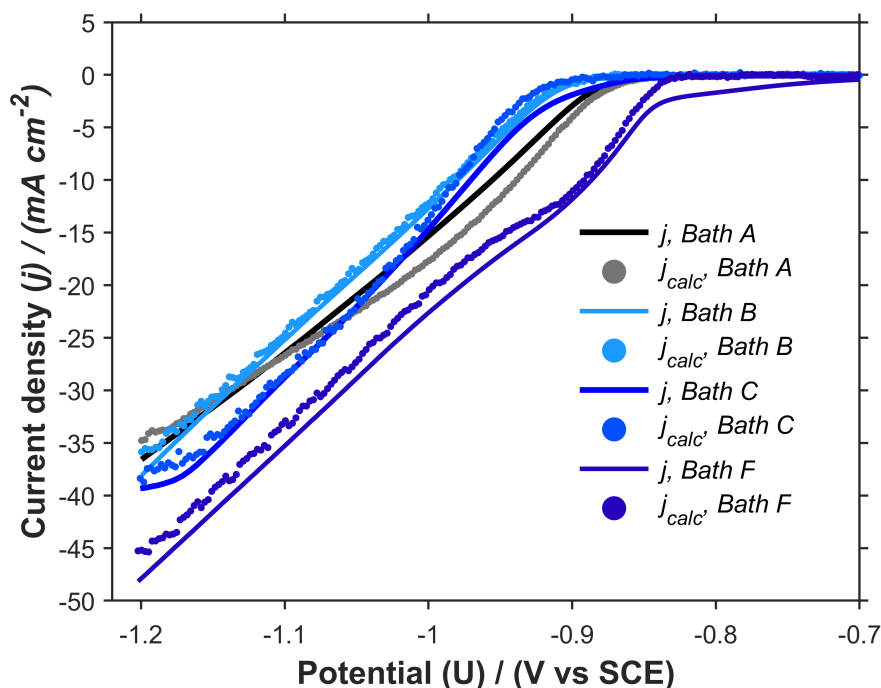


Figure 6.6: LSV of nickel electrodeposition in quiescent Bath A (●); Bath B (●); Bath C (●); and Bath F (●) at 55 °C, showing the measured current densities,  $j$  (solid lines) and calculated current densities,  $j_{calc}$  (circles)

### 6.2.3 Gravimetric analysis

Current efficiencies were also calculated from measured and calculated current densities shown in Figures 6.5 and 6.6 using Equation 6.15. The EQCM current efficiency data is given in Table 6.2.

$$EQCM \text{ current efficiency} = \frac{\text{calculated current density}}{\text{measured current density}} \quad (6.15)$$

The EQCM current efficiency data tabulated in Table 6.2 show that current efficiencies calculated in the absence of boric acid (Bath A) are often greater than 100% which has been attributed to the inclusion of nickel hydroxide from findings in section 6.2.1. An overall decrease in current efficiency is observed when boric acid is added to the sulfamate bath or the solution temperature is increased which could be attributed to a suppression of nickel hydroxide deposition or increased HER kinetics via  $H_2O$  reduction. In any instance, current efficiencies are greater than 87% which are comparable to the results obtained gravimetrically at the RDE.

Table 6.2: Current efficiencies and mass-charge slopes calculated from EQCM  $\Delta f$  signals measured in solutions studied, assuming all of the QCM  $\Delta f$  signal arises from the electrochemical deposition of Ni.

Baths	Current efficiency (%)				mass-charge slope (ng/mC)
	10 mA cm <sup>-2</sup>	20 mA cm <sup>-2</sup>	30 mA cm <sup>-2</sup>	40 mA cm <sup>-2</sup>	
Temperature: 45 °C and Rotation rate: 0 rpm					
A	114.0	105.2	-	-	-336.3
B	89.8	99.3	97.6	-	-281.8
C	98.7	104.1	101.8	-	-296.9
F	106.5	100.7	97.2	-	-288.8
Temperature: 55 °C and Rotation rate: 0 rpm					
A	127.2	109.8	99.4	-	-332.6
B	97.0	98.8	97.6	-	-294.6
C	87.7	101.2	98.3	-	-288.0
F	95.1	90.8	94.6	95.9	-277.1

Figures 6.7 a and b show mass against charge plots measured in Baths A, B, C, and F at 45 °C and 55 °C, respectively; evaluated slopes of the linear plots are outlined in Table 6.2. The mass-charge plots in all baths follow the straight line meant for Ni deposition at 100% current efficiency (red dotted line) - except for Bath A as mentioned earlier. It is also observed that the mass changes for all baths at 55 °C are greater indicating that the nickel deposition rate at 55 °C is faster which explains the higher polarisation currents observed in Figure 6.6. Although nickel deposition is the predominant reaction, gradients of the mass-charge plots ( $\Delta m/\Delta Q$  function) suggest that other reaction products, such as nickel hydroxide, are included in the deposits when boric acid is absent.

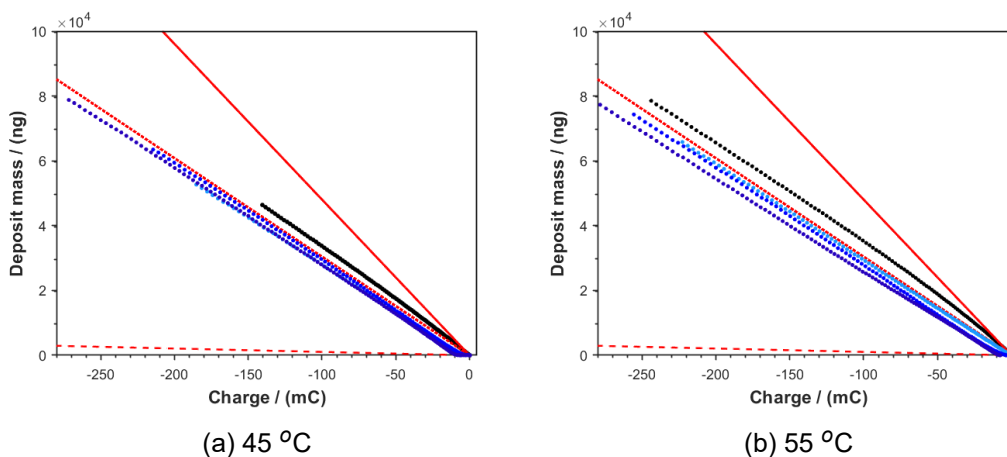


Figure 6.7: Effect of boric acid concentration: Charge vs mass change during Ni electrodeposition on a steel quartz crystal electrode in quiescent Bath A (●); Bath B (●); Bath C (●); and Bath F (●) at (a) 45 °C and (b) 55 °C. Theoretical plots for H (slope = -10.45 ng/mC), Ni (slope = -304.14 ng/mC), and Ni(OH)<sub>2</sub> (slope = -480.427 ng/mC) are given by the dashed, dotted, and solid red lines, respectively.

### 6.3 Hydrogen evolution reaction (HER) kinetics in the absence of nickel ions

Since boric acid appears to influence both Ni<sup>2+</sup> reduction and hydrogen evolution reactions (HER), it is important to obtain a better understanding of its effect on the initial stages of HER before proceeding to study the initial stages of nickel electrodeposition. In addition, researchers have used a variety of substrates to study nickel electrodeposition, and therefore, it is important to discern the differences between them. For this purpose, HER on 304SS, Au, Cu, and Ni-coated quartz crystal electrodes were studied.

#### 6.3.1 Study of HER kinetics on different substrates in the absence of boric acid

As mentioned, the hydrogen evolution reactions (HER) from protons and water are both heterogeneous electrochemical reactions and thus, strongly depend on the electrode

material. Figures 6.8 a and b show LSVs and corresponding massograms of 3.57 M potassium sulfamate (adjusted to pH 4) for all working electrodes studied. These are 304 stainless steel (SS), Au, Cu-coated, and Ni-coated quartz crystal electrodes.

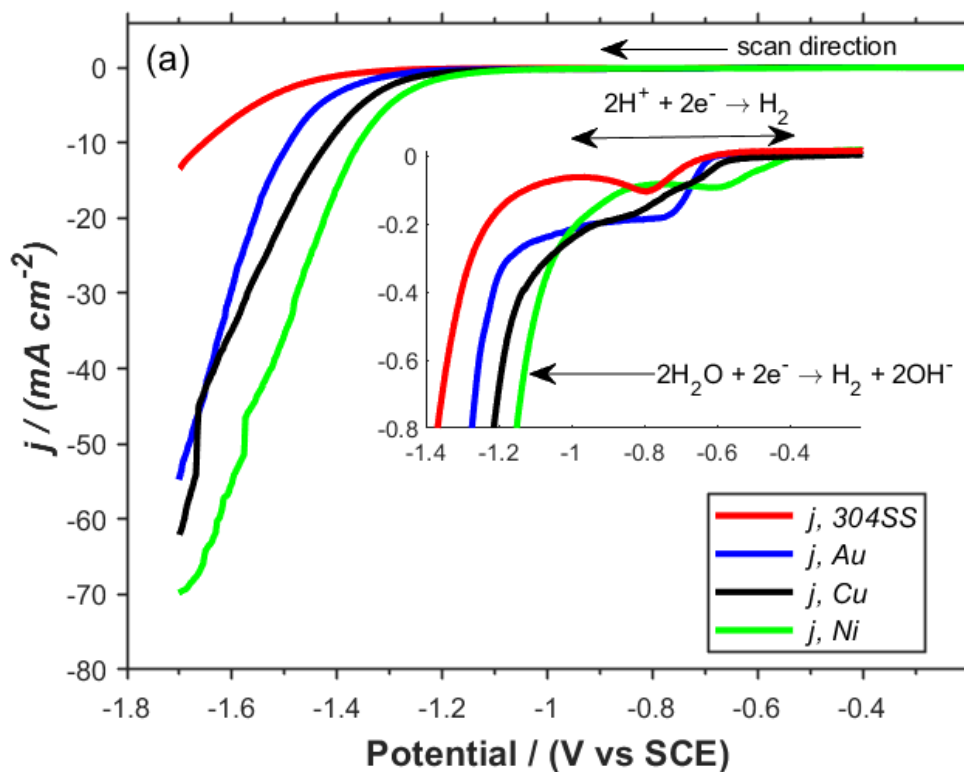
For a blank solution of 3.57 M potassium sulfamate, the cathodic current observed in Figure 6.8a is due to HER and the reduction reactions are given by Equations 2.12 and 2.13. Both reactions could change the pH near the cathode due to the consumption of protons or production of hydroxyl ions, respectively. The extent of this pH change depends on the applied current density, mass transport conditions, and dissociation equilibria in solution [74]. The equilibrium potential for proton reduction is -0.497 V (pH=4.0; T=45 °C), but there is no precise thermodynamic prediction of the electrode potential at which water reduction would occur. The transition from H<sup>+</sup> to H<sub>2</sub>O reduction is expected to be influenced mainly by the value of the interfacial pH.

The LSVs in Figure 6.8a reveal diffusion-limited waves in the potential range of -0.4 to -1.0 V, attributed to the reduction of free protons at pH 4.0 (inset, Figure 6.8a). The limiting current density of protons ( $j_{lim}$ ) in the HER could be calculated using the following equation:

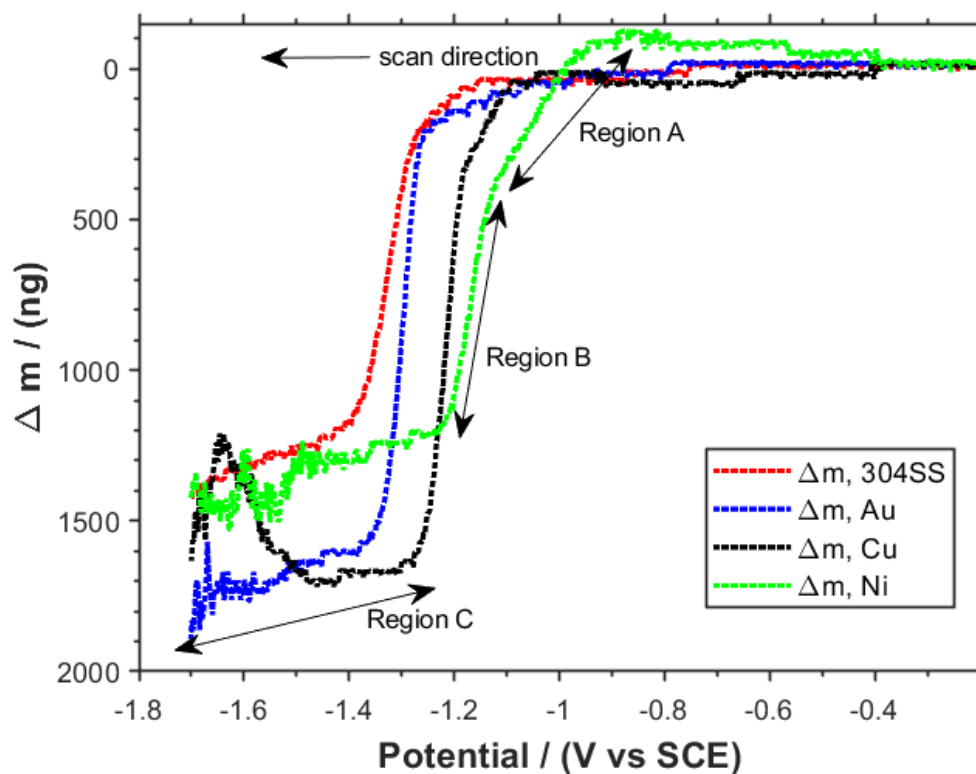
$$j_{lim} = -\frac{nFD_{H^+}C_{H^+}}{\delta} \quad (6.16)$$

where  $j_{lim}$  is the limiting current density (A/cm<sup>2</sup>),  $n$  the number of electrons transferred in the HER reaction ( $n=2$ ),  $F$  the Faraday constant (96485 C/mol),  $D_{H^+}$  the diffusion coefficient of H<sup>+</sup> ( $9.312 \times 10^{-5}$  cm<sup>2</sup>/s [74]),  $C_{H^+}$  is the concentration of H<sup>+</sup> ( $10^{-7}$  mol/cm<sup>3</sup>, pH=4), and  $\delta$  is the thickness of the diffusion layer (assuming  $10^{-2}$  cm for unstirred solution [249]).  $j_{lim}$  for proton reduction in a solution of pH 4.0 is evaluated to be -0.18 mA/cm<sup>2</sup> which is comparable to the current densities of the diffusion-limited waves in Figure 6.8a.

The proton reduction wave is followed by a rapid increase in cathodic current density at potentials more negative than -1.0 V which is associated with water reduction. For comparison, onset potentials for proton and water reduction on the different substrates were obtained from Figure 6.8a and are given in Table 6.3. For quantitative determination, the onset potentials were defined as the potentials at which the current exceeds a certain defined value, in this case, -0.008 and -0.4 mA cm<sup>-2</sup> were selected



(a)



(b)

Figure 6.8: a) Polarisation curves and (b) massograms for HER in 3.57 M potassium sulfamate without boric acid on different quartz crystal electrodes.

as the thresholds for proton and water reduction, respectively. The data, given in Table 6.3, obtained from the LSVs show that the overpotentials for proton and water reduction follows the order 304SS > Au > Cu > Ni. This suggests that hydrogen transfer steps from protons and water occur most readily on Ni. This is in agreement with work carried out by other researchers which often indicated that the exchange current density on Ni was highest among Au, Fe, and Cu [193, 195, 196]. Additionally, a chromium oxide film ( $\text{Cr}_2\text{O}_3$ ) forms spontaneously on the stainless steel surface [250] which could increase the activation energy for proton or water discharge.





In the corresponding massograms shown in Figure 6.8b, there are three clear separate regions where there is an increase in mass. These are annotated as "Region A", "Region B", and Region C" in the figure. The onset potentials and mass changes for each region are also summarised in Table 6.3. For all electrodes, the breakthrough for mass increase in Region A occurs at potentials between the onset potentials for proton and water reduction. The onset potentials of  $\Delta m$  on all substrates in Region A correspond to potentials in the LSVs where the current begins to increase again following the diffusion-limited waves. This suggests that the transition from proton to water reduction is mainly responsible for the slow increase in mass observed in Region A.

At potentials slightly more negative than the onset potentials for water reduction currents, the massograms for all electrodes are characterised by a sharp increase in mass in Region B. As mentioned earlier, the adsorption of protons on the electrode surface from water is not expected to cause visible change in mass on the electrode surface. However, water reduction (Equation 2.13) produces hydroxyl ions which increase the interfacial pH and could allow the spontaneous formation of metal oxides/hydroxides under the applied cathodic potentials.

Using EDS and EQCM measurements, researchers [251, 252] have previously reported the formation of oxides/hydroxides during HER on nickel in solutions of high pH, which are in agreement with the observations in these experiments. Micrographic examination of passive films on numerous metals show that they consist of two layers: an outer layer of hydroxide film on top of an oxide layer [253]. It is well established that the hydroxide forms first, followed by the formation of the oxide which grows into the metal [253].

Table 6.4 shows the equilibrium potential formulations for some reactions that lead to the formation of metal hydroxides and oxides on the substrate materials of interest. For better representation, a diagram of equilibrium potential against pH at 298 K is shown in Figure 6.9 which has been constructed based on the thermodynamic equilibrium of the reactions given in Table 6.4. This diagram clearly shows the sequence of reactions from the metal to the oxide layer. It is known that  $\text{Cr}_2\text{O}_3$  forms on austenitic stainless steel [250] and therefore, it was assumed that the oxide layer on

Table 6.4: Metal hydroxide and oxide formation reactions and their equilibrium potentials on the different EQCM substrate materials at 25 °C. Calculations are based on  $U^0$  values found in [136].

Substrate	Reactions	Equilibrium potential (V vs SCE)
304 SS	(1) $\text{Cr} + 3\text{H}_2\text{O} \leftrightarrow \text{Cr}(\text{OH})_3 + 3\text{H}^+ + 3\text{e}^-$	$-0.895 - 0.0591 \cdot \text{pH}$
	(2) $2\text{Cr} + 3\text{H}_2\text{O} \leftrightarrow \text{Cr}_2\text{O}_3 + 6\text{H}^+ + 6\text{e}^-$	$-0.82 - 0.0591 \cdot \text{pH}$
	(3) $\text{Cr}_2\text{O}_3 + \text{H}_2\text{O} \leftrightarrow 2\text{CrO}_2 + 2\text{H}^+ + 2\text{e}^-$	$0.819 - 0.0591 \cdot \text{pH}$
Ni	(4) $\text{Ni} + \text{H}_2\text{O} \leftrightarrow \text{Ni}(\text{OH})_2 + 2\text{H}^+ + 2\text{e}^-$	$-0.131 - 0.0591 \cdot \text{pH}$
	(5) $\text{Ni} + \text{H}_2\text{O} \leftrightarrow \text{NiO} + 2\text{H}^+ + 2\text{e}^-$	$-0.125 - 0.0591 \cdot \text{pH}$
Cu	(6) $2\text{Cu} + \text{H}_2\text{O} \leftrightarrow \text{Cu}_2\text{O} + 2\text{H}^+ + 2\text{e}^-$	$0.23 - 0.0591 \cdot \text{pH}$
	(7) $\text{Cu} + \text{H}_2\text{O} \leftrightarrow \text{CuO} + 2\text{H}^+ + 2\text{e}^-$	$0.329 - 0.0591 \cdot \text{pH}$
Au	(8) $\text{Au} + 3\text{H}_2\text{O} \leftrightarrow \text{Au}(\text{OH})_3 + 2\text{H}^+ + 2\text{e}^-$	$1.216 - 0.0591 \cdot \text{pH}$
	(9) $\text{Au} + 3\text{H}_2\text{O} \leftrightarrow \text{Au}_2\text{O}_3 + 6\text{H}^+ + 6\text{e}^-$	$1.27 - 0.0591 \cdot \text{pH}$

304 stainless steel increases or is transformed to a higher oxide. Hence, the mass increase observed in Regions A and B could be attributed to the formation of hydroxides or oxides in the metal.

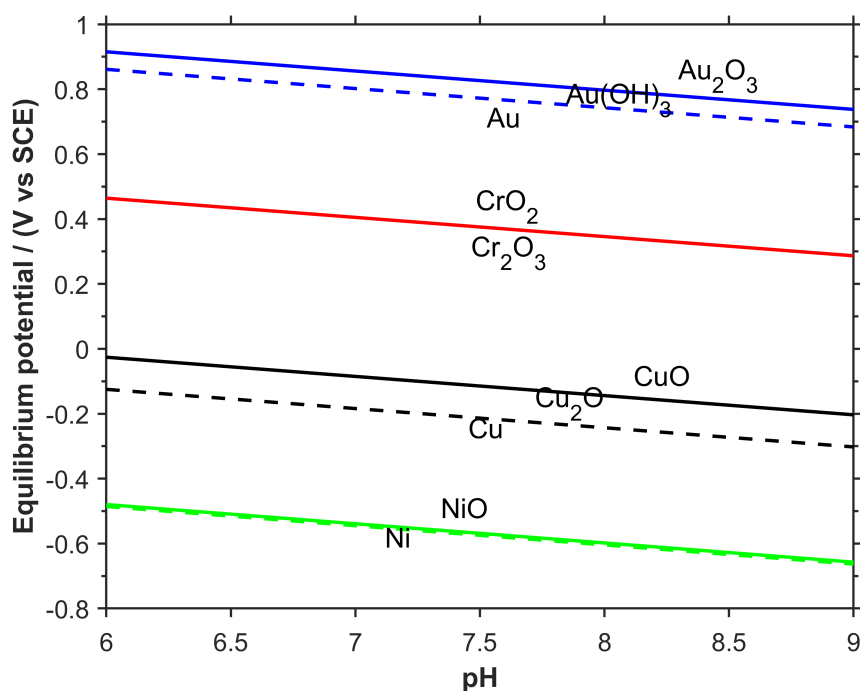


Figure 6.9: Potential-pH equilibrium diagram for Au, Cu, Ni, and  $\text{Cr}_2\text{O}_3$  (passive film on 304 stainless steel) in water (pH = 6-9) at 25 °C.

Region C in Figure 6.8b is characterised by a slow, noisy increase in mass observed after oxide/hydroxide formation. This part of the gravimetric scan corresponds to potentials of the polarisation curves (Figure 6.8a) where a strong increase in cathodic current (originating from the hydrogen evolution reaction via water reduction) is observed. At such high current densities, vigorous hydrogen evolution strongly disturbs the EQCM response due to the formation and discharge of hydrogen gas bubbles on the electrode surface. Similar frequency response in the HER region was also reported for Au electrodes [216].

To further investigate the detailed reaction kinetics and underlying mechanism of HER due to water discharge on the investigated quartz crystal electrodes, the corresponding Tafel plots for LSV curves in Figure 6.8a are shown in Figure 6.10.

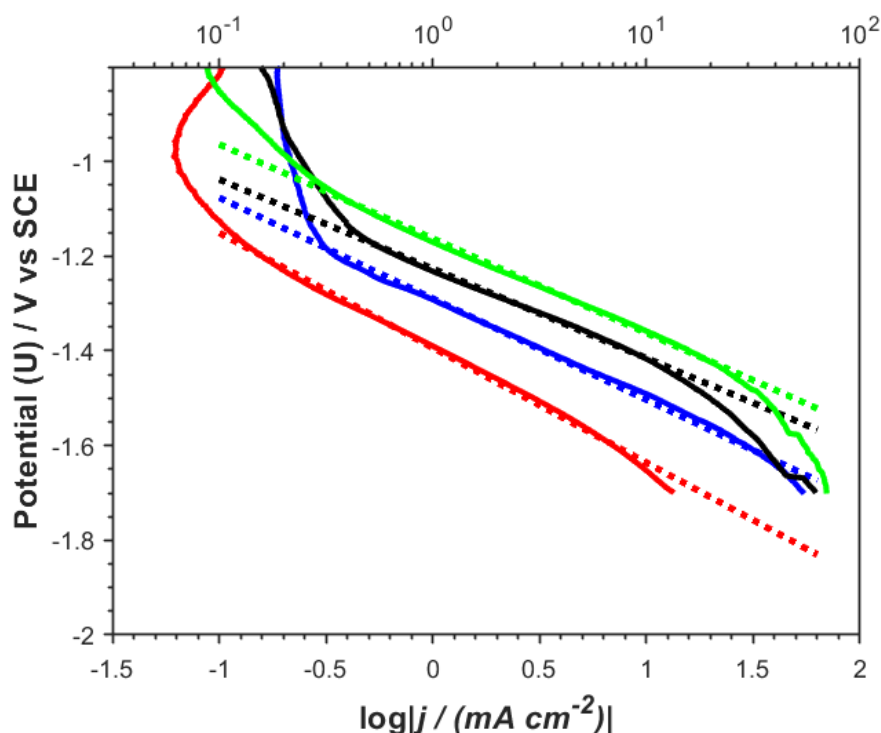


Figure 6.10: Tafel plots for HER in 3.57 M potassium sulfamate without boric acid on 304SS (Red), Au (blue), Cu (black), and Ni (green).

The linear regions of Tafel plots in the potential range ( $\geq 1.0$  V) where water reduction occurs and the mass increase was observed were fitted according to the Tafel formula:

$$\eta_s = U - U_{eq} = b \log|j| + a \quad (6.17)$$

where  $U$  is the applied potential (mV),  $U_{eq}$  the equilibrium potential (mV),  $\eta_s$  the surface

overpotential (mV),  $b$  the Tafel slope (mV/dec),  $j$  the current density ( $\text{mA}/\text{cm}^{-2}$ ), and  $a$  is a constant. Tafel slopes of 243, 213, 189, and 199 mV/dec were measured for 304SS, Au, Cu, and Ni quartz crystal electrodes, respectively. Such high Tafel slopes are uncommon for hydrogen evolution on metals free from adsorbed species [254]. However, these Tafel slopes have been observed on film-covered surfaces and in such instances, the slopes have been attributed to the presence of an oxide or hydroxide film on the electrode surface [249,252] which supports the findings from the gravimetric scans.

### 6.3.2 Study of HER kinetics in the presence of boric acid

The polarisation scan and EQCM massogram recorded on the 304 SS electrode in potassium sulfamate solution containing  $\text{H}_3\text{BO}_3$  is presented in Figure 6.11. The addition of boric acid to the solution had the effect of decreasing current densities measured prior to the mass transport limited region (inset, Figure 6.11) and increasing current densities measured in the post-mass transport control region. As mentioned in the previous section, current densities prior to the mass transport limited region, which occur over the potential range between -0.58 V and -0.78 V on 304SS in the absence of boric acid, are associated with  $\text{H}^+$  reduction, while water reduction occurs in the post-mass transport control region. Similar effects of boric acid on the measured current densities for  $\text{H}^+$  and water reduction have previously been reported in sodium sulfate on Cu [74] and on Pt [103], as well as in potassium sulfate on Co [71]. However, the causative reason for this observation has not been adequately explained.

The massogram measured in the presence of boric acid on 304SS (dotted blue line) imparts more information on processes occurring on the electrode surface. For clarification of these processes, Figure 6.11 has been annotated. When boric acid is added to the solution, it is observed that the massogram feature associated with oxide formation on the electrode surface disappears. Instead, the massogram obtained in the presence of  $\text{H}_3\text{BO}_3$  shows a region where there is an increase in mass beginning at -0.84 V ( $U_{ad}$ , Figure 6.11) indicative of adsorption on the electrode surface. Maximum adsorption occurred at approximately -1.14 V ( $U_{des}$ , Figure 6.11) where a

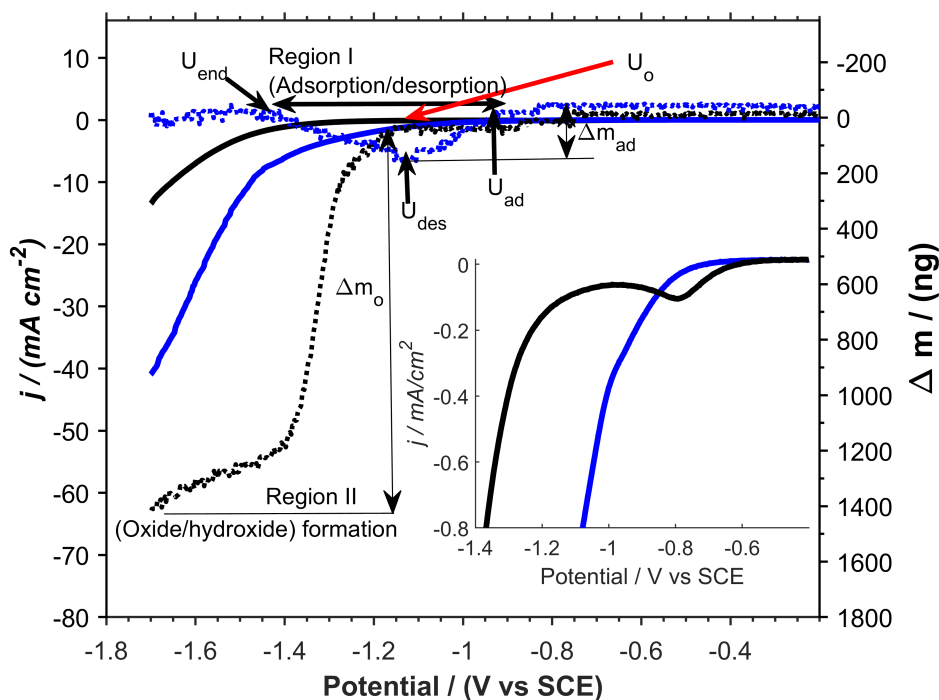


Figure 6.11: Polarisation scans measured in 3.57 M potassium sulfamate solution without (black) and with 0.65 M boric acid (blue) with a scan rate of 5 mV/s on 304SS showing the measured current (solid lines) and mass changes (dotted lines). The Figure inset shows the effect of boric acid on the diffusion limited peak associated with  $H^+$  reduction.

maximum mass change of 173.3 ng was observed. It should be noted that the measured current in this adsorption region is less than  $1.2 \text{ mA cm}^{-2}$ . Hence, adsorption proceeds without significant charge transfer. However, as the potential became more negative than  $-1.14 \text{ V}$ , the mass on the electrode surface decreased which may be indicative of desorption from the surface. This was accompanied by a slow increase in measured current density. Desorption lasts until  $-1.42 \text{ V}$  ( $U_{end}$ , Figure 6.11), at which point the mass decreases to zero with no further change in mass. At potentials following complete desorption, i.e. more negative than  $-1.42 \text{ V}$ , a faster increase in measured current density is observed.

The adsorption/desorption region annotated as "Region I" in Figure 6.11 was not observed in the absence of boric acid. Hence, the species adsorbing could be boric acid or a species associated with  $H_3BO_3$  (such as polyborates). It can also be deduced that this species adsorbs in the potential region corresponding to the early

stages of water reduction where oxides/hydroxides begin to form (inset, Figure 6.11). The absence of oxide/hydroxide formation in the presence of boric acid suggests that the adsorption of  $\text{H}_3\text{BO}_3$  or a  $\text{H}_3\text{BO}_3$ -related species obstructs water reduction.

It is not clear from the data in Figure 6.11 whether the adsorption of  $\text{H}_3\text{BO}_3$  is responsible for the decrease in current densities associated with  $\text{H}^+$  reduction, i.e., between -0.61 V and -0.85 V (inset, Figure 6.11) because discernible mass change was not observed in this potential region.

It is of interest to also investigate the adsorption of boric acid on the electroplated Ni as well as other substrates, such as Au and Cu, which have been employed by previous researchers in nickel electrodeposition studies from sulfamate electrolytes [68, 117, 118]. It has also been determined, in the previous section, that HER kinetics is more favourable on these substrates. Therefore, it was necessary to investigate whether the adsorption of  $\text{H}_3\text{BO}_3$  on these substrates was affected by the competitive adsorption of hydrogen.

Figure 6.12 shows the LSV and associated massograms obtained from 3.57 M potassium sulfamate with and without 0.65 M boric acid (pH adjusted to 4.0) on Au, Cu-coated, and Ni-coated quartz crystal electrodes. The data reveals some interesting aspects about the interaction of boric acid with Au, Cu, and Ni: (1) addition of  $\text{H}_3\text{BO}_3$  has little effect on the initial part of the measured polarisation scan which is associated with  $\text{H}^+$  reduction current densities but it shortens the length of the diffusion-limited plateau consequently leading to lower overpotentials for HER in the presence of boric acid, (2) compared to 304 stainless steel,  $\text{H}_3\text{BO}_3$  adsorption/desorption occurs at more negative potentials, (3) the amount of adsorbed boric acid on Au, Cu, and Ni was evaluated to be 168.7 ng, 132.1 ng, and 171.4 ng, respectively, and (4) after the desorption of  $\text{H}_3\text{BO}_3$ , a noisy increase in mass is observed which is similar to the trends observed in Region C of Figure 6.8b. Explanations for these observations are discussed in the forthcoming paragraphs

The first observation shows that the addition of boric acid to sulfamate solution decreases the overpotential for hydrogen evolution by affecting the potential region where hydrogen evolution transitions from proton to water reduction. This could

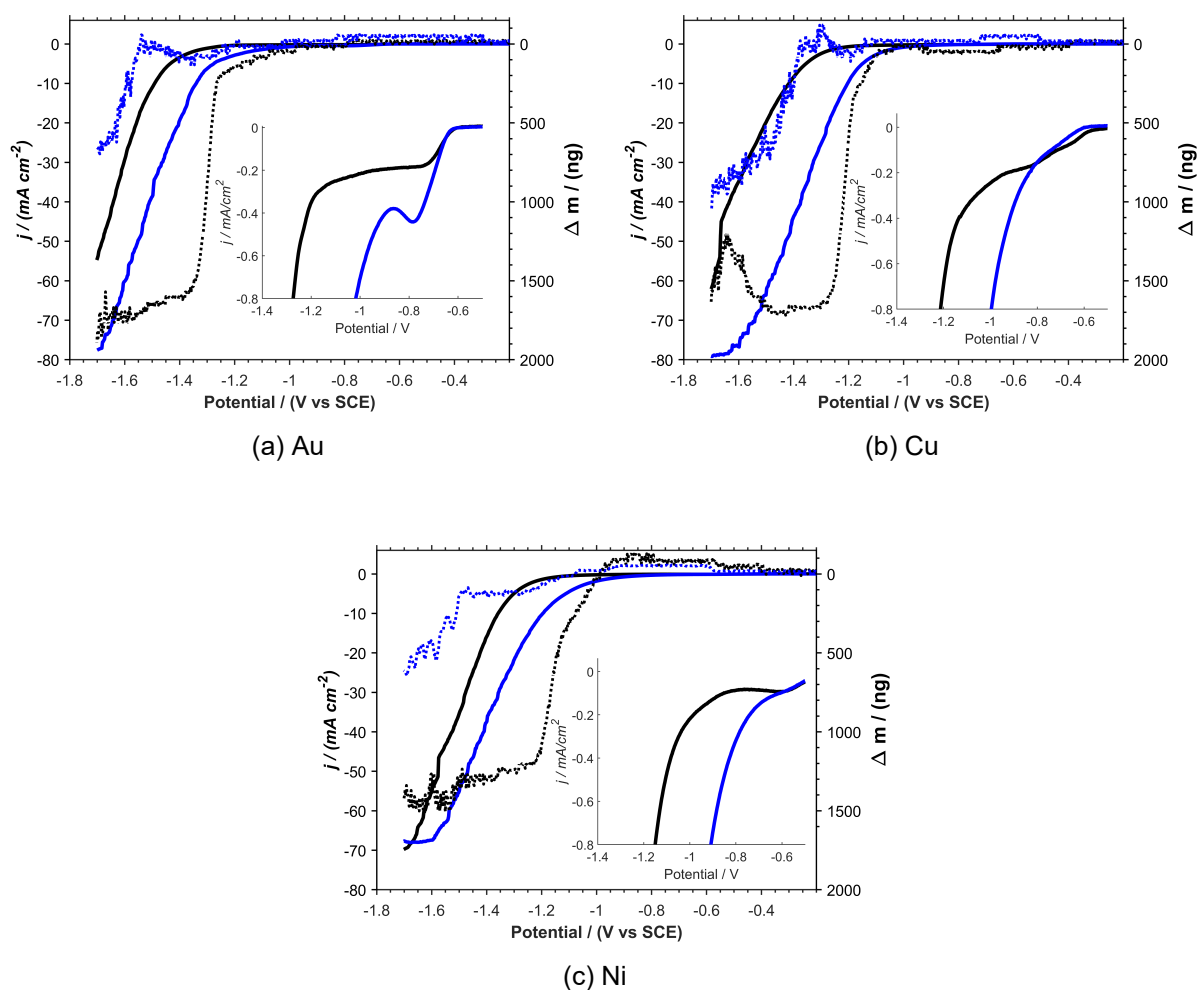
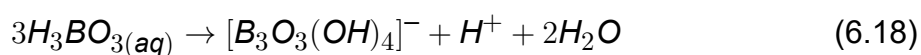


Figure 6.12: Polarisation scans measured in 3.57 M potassium sulfamate solution without (black) and with 0.65 M boric acid (blue) with a scan rate of 5 mV/s on (a) Au, (b) Cu, and (c) Ni showing the measured current (solid lines) and mass changes (broken lines). The Figure insets show the effect of boric acid on the diffusion limited region associated with  $H^+$  reduction.

be attributed to the obstruction of water discharge and continued HER from protons. Hydrogen evolution from  $H_2O$  requires a higher overpotential than that needed for  $H^+$  discharge because additional energy is required to overcome the energy barrier of breaking the HO-H bond. Previous studies have reported that the overpotential increases when the primary reactant in HER is switched from  $H^+$  to  $H_2O$  by increasing the electrolyte pH [252, 255]. Therefore, obstruction of water discharge by  $H_3BO_3$  ensures that protons continue to be the primary reactant for HER which require lower

overpotentials. Hence, these results do not support claims made by Horkans [103] that boric acid lowers the overpotential for water discharge as oxide/hydroxide formation (which result from water reduction) was obviated on the investigated substrates in the presence of boric acid. However, if water reduction is obstructed and HER continues only from  $H^+$  reduction which is under mass transfer, it is expected that the diffusion-limited current plateau will extend to more negative potentials in the presence of boric acid. However, this is the opposite effect in the presence of boric acid which suggests that there are an additional supply of protons that result from the addition of boric acid. This causes proton discharge to exceed the value of the diffusion-limited current plateau. It should be noted that before the experiments, the pH of the blank solutions with and without  $H_3BO_3$  were adjusted to pH 4.0 so they have the same proton concentration. Therefore, the extra protons that are produced in the presence of boric acid are supplied during and not before the experiment.

Rigsby et al. [71] have provided evidence from Raman spectroscopy of the possibility of formation of polyborates (primarily tetraborate) at pH 4, but the quantity formed was sufficiently small so as to make it unlikely that the dissociation of  $H_3BO_3$  to polyborates plays a significant role at pH 4. Titration experiments of 0.65 M  $H_3BO_3$  in water at pH 2.6 indicated that this solution started to provide buffering capacity at pH 5 [71]. Therefore, it is proposed that continued HER from protons in the presence of  $H_3BO_3$  is due to a two-fold effect: (i) the adsorption of the boric acid to obstruct water adsorption, and (ii) boric acid dissociation (via Equation 6.18) in the vicinity of the electrode surface which supplies additional protons for discharge; this reaction becomes possible due to a decrease in acidity during hydrogen evolution via proton reduction.



The second observation is suggestive of competitive adsorption between hydrogen and  $H_3BO_3$  on substrates with faster hydrogen evolution kinetics compared to 304 SS. The third aspect shows that boric acid adsorbs to various degrees on the different substrate materials in the order: 304 SS > Ni > Au > Cu. A proposed mechanism for the adsorption of boric acid on metal surfaces is schematically shown in Figure 6.13. It is proposed that boric acid could form two possible surface complexes. The monodentate and bidentate complexes adsorb in the planar configuration through co-



valent bonds with the oxygen atom. The mass of a monolayer of boric acid molecules is estimated to be 34.12 ng as given in Table 6.1. Hence, the total amount of boric acid adsorbed on the electrode surface (132.1-173.3 ng) corresponds to about 4-5 monolayers. The first monolayer is connected to subsequent monolayers through hydrogen bonds (H-O- - H).

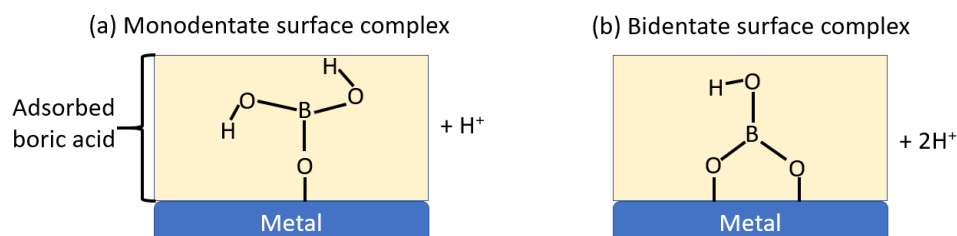


Figure 6.13: Proposed mechanism for the adsorption of boric acid on the metal substrate.

Figure 6.14 shows measured currents and mass changes for HER in the presence of  $\text{H}_3\text{BO}_3$  on the different materials to clearly explain the fourth aspect observed in the region of the gravimetric curves annotated as A in the figure. This region (A, Figure 6.14) is characterised by noisy mass changes which correspond to potentials where significant HER current densities ( $> 45 \text{ mA cm}^{-2}$ ) are measured in the polarisation scans. As mentioned earlier, this noisy increase in mass is caused by vigorous hydrogen evolution due to the attachment and detachment of gas bubbles. Notably, this region of the gravimetric curves observed for HER on Au, Cu, and Ni was absent for HER on 304 SS likely due to the relatively lower rate of HER observed on the latter material.

Figure 6.15 shows the mass vs charge plots measured for HER on 304SS, Au, Cu, and Ni in sulfamate baths with and without boric acid. The mass-charge plots for HER in sulfamate-only baths on all metal substrates initially follow the straight lines which correspond to the formation of their respective oxides/hydroxides. Passive films on nickel and stainless steel are reportedly around 5 nm thick [253], but alter in thickness with the environment. Based on the information in Figure 6.15, it is assumed that NiO (density= $6.67 \text{ g/cm}^3$ ) and  $\text{Cr}_2\text{O}_3$  (density= $5.22 \text{ g/cm}^3$ ) are the passive films formed on the Ni and 304 SS electrodes, respectively. The thickness,  $h$  (nm) of these

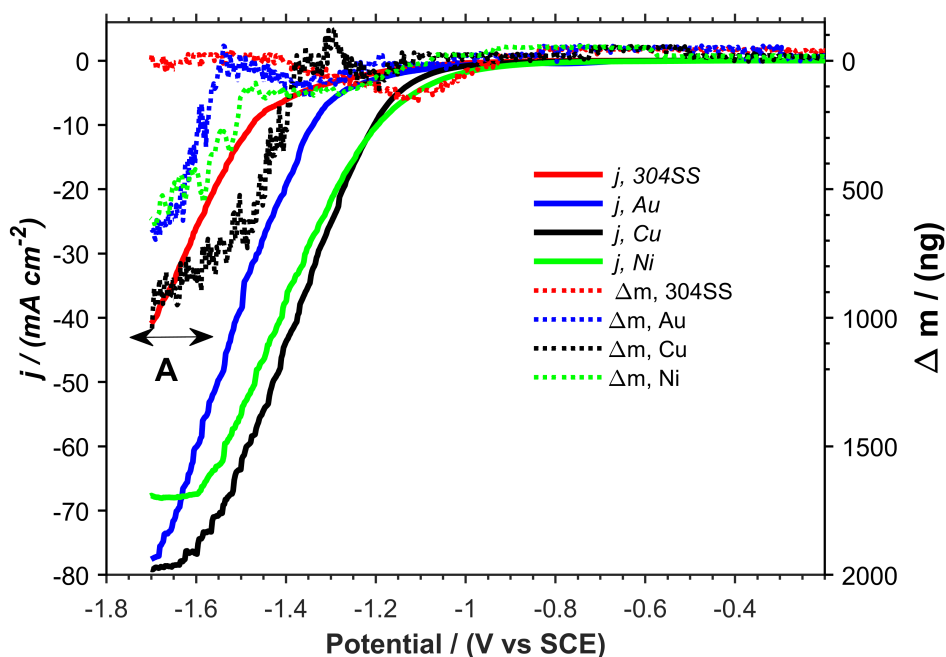


Figure 6.14: Polarisation scans measured in 3.57 M potassium sulfamate solution with 0.65 M boric acid with a scan rate of 5 mV/s on 304 SS (red), Au (blue), Cu (black), and Ni (green) showing the measured current (solid lines) and mass changes (broken lines).

passive films were estimated using Equation 6.19:

$$h = \frac{0.01\Delta m}{\rho A} \quad (6.19)$$

where  $h$  is the estimated thickness of the passive film (nm),  $\Delta m$  the measured mass of the passive film on Ni and 304 SS ( $\approx 1200$  ng),  $\rho$  the density of the passive film (g/cm), and  $A$  the EQCM area ( $0.196$  cm<sup>2</sup>). The passive films on Ni and 304 SS were estimated to be 9 nm and 12.7 nm, respectively.

Still in the same sulfamate-only bath, the slope is observed to decrease as the amount of charge passed is increased; this lower slope corresponds to Region C in Figure 6.8b which has been attributed to the region where vigorous hydrogen evolution occurs. When boric acid is added to sulfamate solutions, the slopes of the mass-charge plots for HER on all substrates are much lower than those expected for oxide/hydroxide formation indicating that boric acid blocks the formation of oxides/hydroxides on the electrode surface. As mentioned earlier, this is attributed to the adsorption of boric

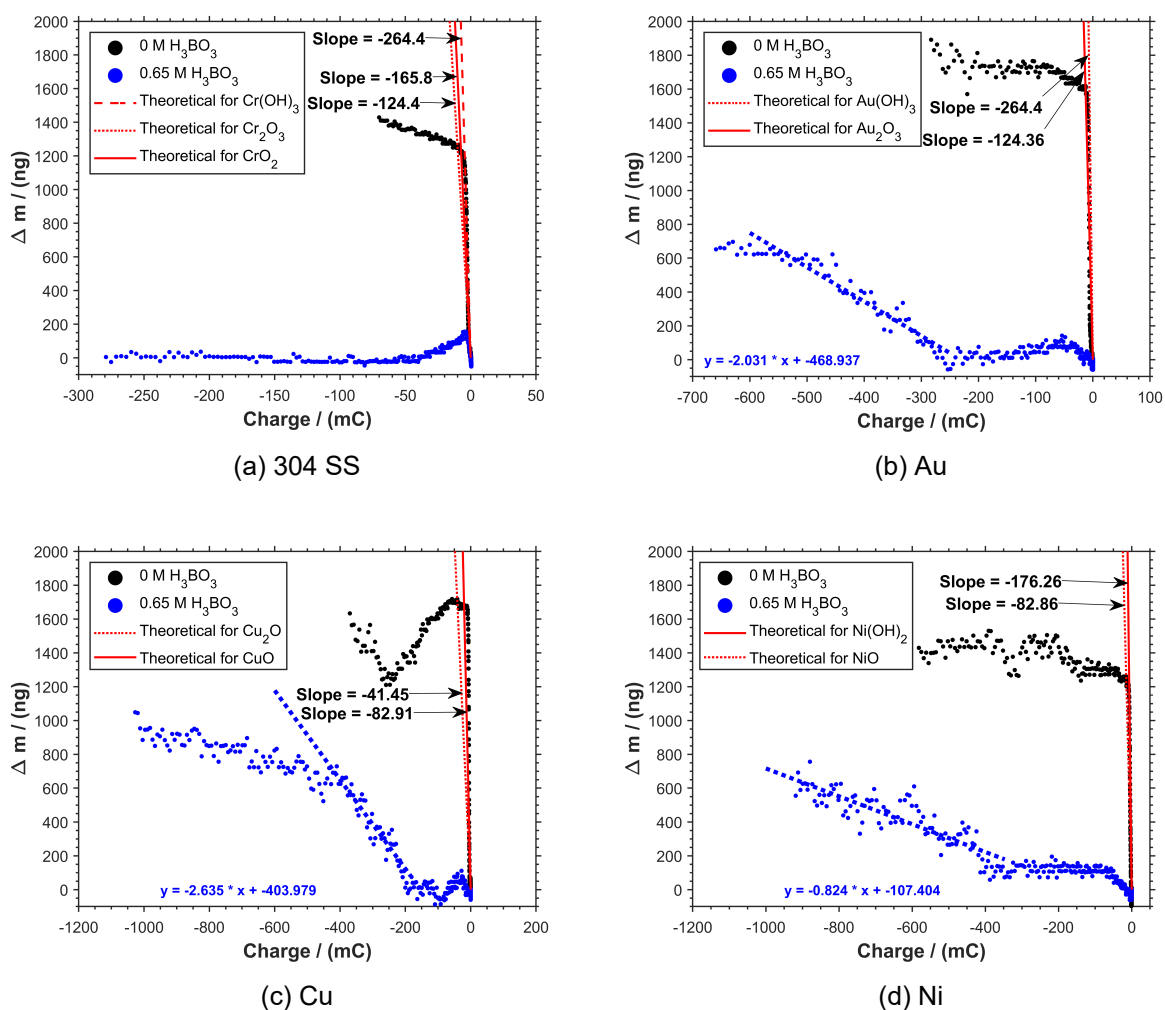


Figure 6.15: Mass vs charge plots during HER on different quartz crystal electrode materials in 3.57 M potassium sulfamate solution without (black) and with 0.65 M boric acid (blue) at 45 °C.

acid on the electrode surface which obstructs the reduction of water and prevents the formation of  $\text{OH}^-$  in the interfacial electrolyte.

## 6.4 Effect of boric acid on the initial stages of nickel deposition

It was shown in the preceding section that adding boric acid to potassium sulfamate electrolytes obstructs hydrogen evolution via water reduction and subsequent oxide/hydroxide production. However, changes to the electrode surface must be identified when  $\text{Ni}^{2+}$  are added to the electrolyte in order to comprehend how boric acid impacts the early

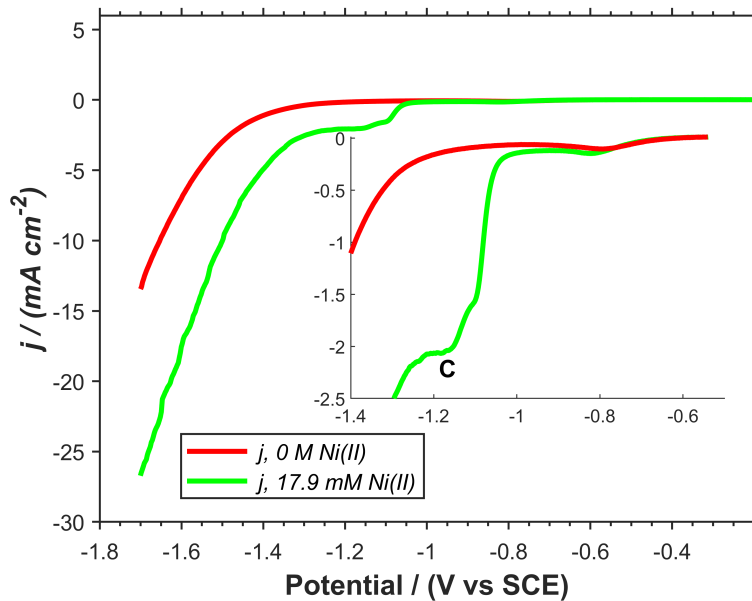
phases of nickel electrodeposition which up to now has not been reported in sulfamate electrolytes. The challenge for this study in electroforming solutions, typically composed of 1.785 M  $\text{Ni}^{2+}$  is the high deposition rates encountered. In order to decrease deposition rates and distinguish between Ni electrodeposition, hydrogen evolution, and oxide/hydroxide formation using EQCM measurements, a dilute electrolyte with a concentration of 17.85 mM  $\text{Ni}^{2+}$  was employed in the present experiments. To understand how modifications to the electrode surface might impact the interfacial reactions, nickel electrodeposition studies were performed on 304 SS, Au, and Cu electrodes.

#### 6.4.1 Nickel electrodeposition in the absence of boric acid

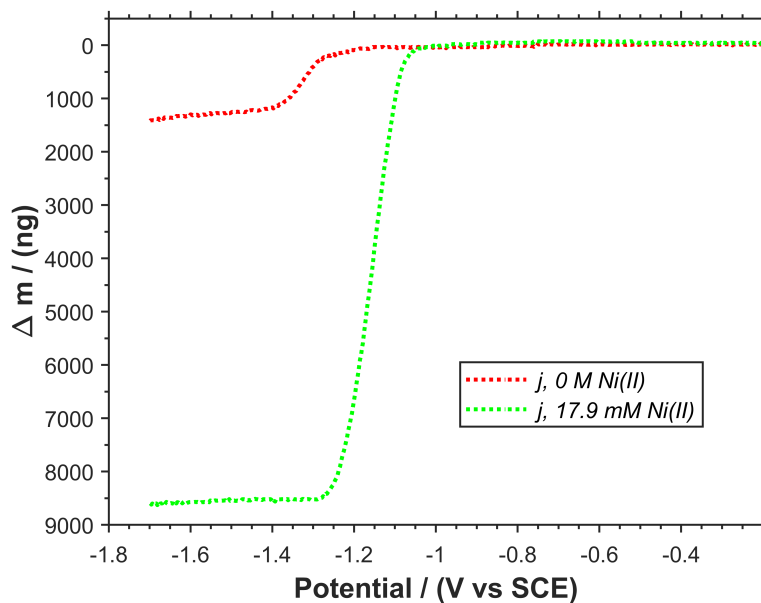
Figure 6.16 shows a comparison of the measured polarisation and  $\Delta m$  scans obtained on a 304 SS electrode in the blank electrolyte (3.5 M  $\text{KSO}_3\text{NH}_2$ ), without  $\text{Ni}^{2+}$  (red line) and with  $\text{Ni}^{2+}$  (green line) in solution. This figure was used to probe the potential region where nickel deposition competes with hydrogen evolution via proton and water reduction.

It is observed from the inset in Figure 6.16a that the polarisation curve measured in the presence of  $\text{Ni}^{2+}$  deviates from that measured in the  $\text{Ni}^{2+}$ -free electrolyte at about -1.03 V, indicating the onset potential for  $\text{Ni}^{2+}$  reduction since a mass change is recorded simultaneously. Interestingly, the massograms recorded in the absence and presence of  $\text{Ni}^{2+}$  show similar features, i.e a steep increase in mass which terminates in a plateau. This feature has been attributed to the formation of oxides/hydroxides on the electrode surface. Notably, the addition of  $\text{Ni}^{2+}$  to the bath leads to a sevenfold increase in the measured mass which could be attributed to (1) the deposition of nickel and/or (2) the continuous growth of the oxide film due to the precipitation of  $\text{Ni}(\text{OH})_2$  on the electrode surface (via Equation 6.8).

A current peak (C in the inset of Figure 6.16) is observed at -1.17 V for  $\text{Ni}^{2+}$ -containing electrolytes which indicates the point where  $\text{Ni}^{2+}$  reduction becomes limited by its diffusion from the bulk solution to the electrode surface. The cathodic current increases again at a potential more negative than -1.24 V while  $\Delta m$  attains a nearly



(a)



(b)

Figure 6.16: a) Polarisation scans and (b) massograms obtained in  $x$  M Ni(II) + 3.57 M potassium sulfamate (pH 4.0) systems at two different Ni(II) concentrations:  $x = 0$  (red line) and  $x = 17.9$  mM (green line) on 304SS quartz crystal electrode; scan rate =  $5 \text{ mV s}^{-1}$ . The inset is an amplification of the region corresponding to Ni deposition

constant value indicating that this second increase in current is due to hydrogen evolution via water reduction. Thus, the findings in Figure 6.16 imply that nickel deposition

is restricted to the potential regime of the cathodic wave labelled as C and that its rate is negligible at potentials more negative than this regime.

In order to understand the nickel deposition process corresponding to peak C, a  $j$ - $U$  curve was prepared from the  $\Delta m$ - $U$  response and compared with the  $j$ - $U$  curve obtained directly from LSV experiments. The results of this evaluation are shown in Figure 6.17.

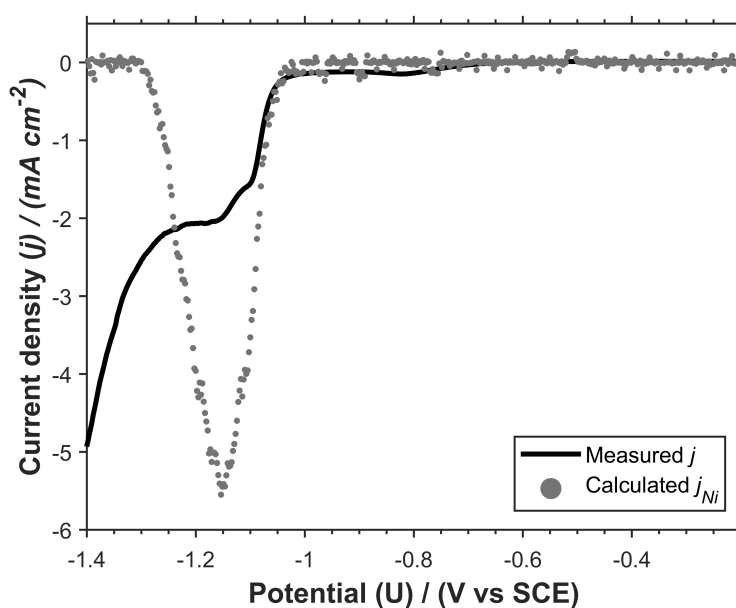


Figure 6.17: Comparison of measured  $j$ - $U$  curves from the LSV experiment and  $j$ - $U$  curves calculated from  $\Delta m$ - $U$  response in 17.9 mM Ni(II) + 3.57 M potassium sulfamate (pH 4.0) system on a 304 SS quartz crystal electrode ; scan rate =  $5 \text{ mV s}^{-1}$

For the potential region,  $-1.03 < U < -1.08$  where  $|j| < 1.08 \text{ mA cm}^{-2}$ , measured and calculated currents are in close agreement which suggests that nickel electrodeposition is the main electrode process with a current efficiency of close to 100%. For potentials more negative than  $-1.08 \text{ V}$  up to  $-1.24 \text{ V}$ , calculated currents from gravimetric data are much greater than the measured currents which suggests the deposition of Ni and  $\text{Ni(OH)}_2$  on the electrode surface. It is also observed that as the applied potential is made more negative than the potential where  $\text{Ni}^{2+}$  reduction becomes transport limited ( $-1.17 \text{ V}$ ), calculated currents decrease to  $0.003 \text{ mA cm}^{-2}$  at  $-1.3 \text{ V}$  which is coincident with the onset of water reduction. This decrease in calculated currents indicates the termination of Ni and  $\text{Ni(OH)}_2$  deposition which could be ascribed to (1)

obstruction of nickel electrodeposition by the  $\text{Ni}(\text{OH})_2$  layer and (2)  $\text{OH}^-$  generation outpacing the  $\text{Ni}^{2+}$  flux which results in the pH depletion layer extending into the solution, causing the precipitation of  $\text{Ni}(\text{OH})_2$  in the interfacial electrolyte as opposed to the electrode surface, as has been proposed by other researchers [256,257].

Further information about the increase in electrode mass during the initial stages of Ni deposition may be obtained from a plot of mass change vs charge ( $\Delta m$ -Q) for the potential regimes shown in Figure 6.17. This measured mass-charge plot is represented by the green curve in Figure 6.18.

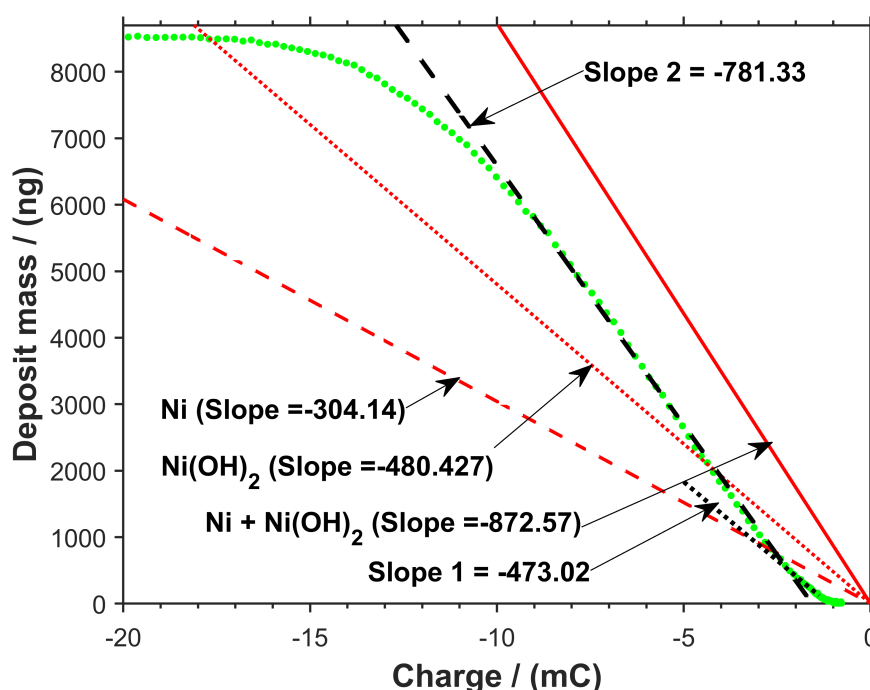


Figure 6.18: Mass change vs Charge ( $\Delta m$ -Q) during Ni electrodeposition in 17.9 mM Ni(II) + 3.57 M potassium sulfamate (pH 4.0) system on a 304 SS quartz crystal electrode. The black lines represent best fit lines. Theoretical plots for Ni (slope = -304.14 ng/mC),  $\text{Ni}(\text{OH})_2$  (slope = -480.427 ng/mC), and Ni +  $\text{Ni}(\text{OH})_2$  (slope = -872.57 ng/mC) are given by the dashed, dotted, and solid red lines, respectively.

Best fit lines were plotted over two linear regions of the mass-charge plot which correspond to the potential regimes of  $-1.03 \text{ V} < U < 1.08 \text{ V}$  (dotted black line) and  $-1.08 \text{ V} < U < 1.17 \text{ V}$  (dashed black line), respectively. The former potential region was attributed to the nickel electrodeposition since the measured and calculated currents showed good agreement. However, the mass-charge slope (dashed black

line, Figure 6.18) of this region was determined to be -473 ng/mC which is greater than the theoretical mass-charge slope expected for nickel electrodeposition (-304.14 ng/mC) but is close to the mass-charge slope expected for Ni(OH)<sub>2</sub> precipitation (-480.43 ng/mC) on the electrode surface. This indicates that the first few monolayers on 304 SS are predominantly composed of Ni(OH)<sub>2</sub> which suggests water reduction occurs prior to nickel electrodeposition. Studies on HER in alkaline media have shown that Ni/Ni(OH)<sub>2</sub> show higher rates of water reduction than bare Ni [258, 259]. Thus, the interaction of H<sub>2</sub>O and the first few layers of Ni(OH)<sub>2</sub> on 304 SS could lead to the generation of more OH<sup>-</sup> and consequently, the precipitation of more Ni(OH)<sub>2</sub>.

The second mass-charge linear region (dashed black line, Figure 6.18) is characterised by a comparatively steeper slope of -781 ng/mC which is much greater than theoretical slopes corresponding to Ni only (-304.14 ng/mC) or Ni(OH)<sub>2</sub> only (-480.43 ng/mC). This slope, however, is more comparable to the theoretical slope for Ni and Ni(OH)<sub>2</sub> (-872.57 ng/mC) which indicate that nickel is co-deposited with Ni(OH)<sub>2</sub>. It is also interesting to compare the slope of the second mass-charge region (-781 ng/mC) measured in 17.9 mM Ni(II) + 3.57 M potassium sulfamate to that measured in the solution containing 1.785 M Ni<sup>2+</sup> concentration (-336.3 ng/mC Table 6.2). According to thermodynamic predictions, the tendency for Ni(OH)<sub>2</sub> precipitation should rise with increase in Ni<sup>2+</sup> concentration [136]. However, a decrease in Ni<sup>2+</sup> concentration in these experiments results in a greater mass-charge slope which could be attributed to increased Ni(OH)<sub>2</sub> precipitated on the electrode surface. This could be explained by a decrease in the amount of Ni<sup>2+</sup> in the solution adjacent to the electrode surface which results in decreased adsorption of the nickel ion intermediate and therefore, decreases the competition with water molecules for active sites.

#### **6.4.2 Nickel electrodeposition in the presence of boric acid**

Figure 6.19 shows the effect of boric acid on the measured and calculated currents obtained in 17.9 mM Ni(II) + 3.57 M potassium sulfamate on 304 SS. Values of  $j_{Ni}$  are calculated from the EQCM gravimetric data shown in Figure 9.3 in Appendix D. The addition of boric acid to the electrolyte leads to two major changes: (1) there is a



continuous increase in the calculated currents as the applied potential is made more negative, and (2) calculated currents are much lower than the measured currents.

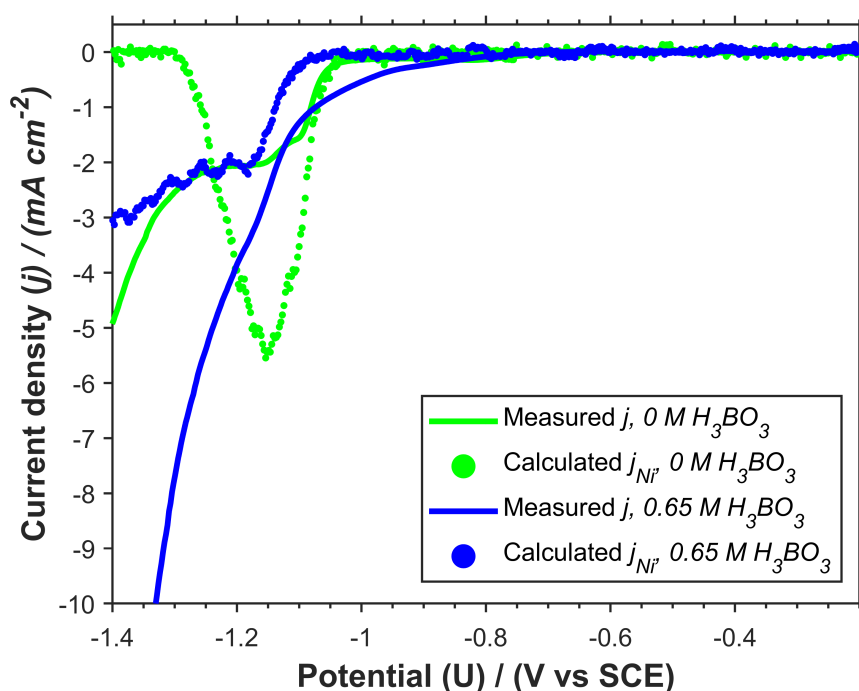


Figure 6.19: Comparison of measured  $j$ - $U$  curves from the LSV experiment and  $j$ - $U$  curves calculated from  $\Delta m$ - $U$  response in 17.9 mM Ni(II) + 3.57 M potassium sulfamate (pH 4.0) system on a 304 SS quartz crystal electrode with and without 0.65 M  $H_3BO_3$ ; scan rate =  $5 \text{ mV s}^{-1}$

The first aspect could be correlated to the absence of the mass plateau in the EQCM data measured in the presence of boric acid (Figure 9.3, Appendix D). Instead, mass increases continuously throughout the experiment. This shows that the addition of boric acid prevents the production of  $Ni(OH)_2$ . The differences between measured and calculated currents provide more support for this and indicate that nickel electrodeposition proceeds with proton reduction only. An increasing discrepancy between  $j$  and  $j_{Ni}$  is observed for potentials more negative than -1.19 V which could be attributed to the diffusion limitations of  $Ni^{2+}$ .

It could also be observed from Figure 6.19 that the onset of nickel deposition is shifted from -1.03 V to -1.1 V in the presence of boric acid. In order to better define the contribution of boric acid in nickel deposition on 304 SS, massograms obtained in the absence and presence of  $Ni^{2+}$  in boric acid-containing sulfamate solutions are

shown in Figure 6.20.

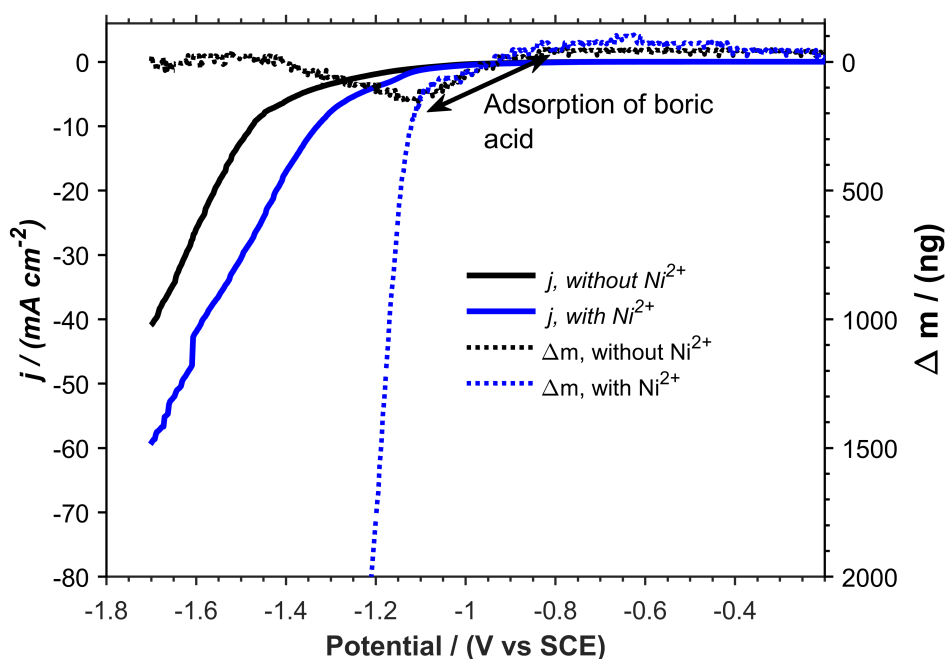


Figure 6.20: Polarisation scans measured in 3.57 M potassium sulfamate + 0.65 M boric acid solution without  $\text{Ni}^{2+}$  (black) and with  $\text{Ni}^{2+}$  (blue) with a scan rate of 5 mV/s on 304 SS showing the measured current (solid lines) and mass changes (broken lines).

The massogram measured in the presence of  $\text{Ni}^{2+}$  (dotted blue line, Figure 6.20) shows two clear regions where there is an increase in mass. The first region begins from -0.9 V and lasts until -1.1 V. In this region, the massogram is very well superimposed on that measured in the absence of  $\text{Ni}^{2+}$  (dotted black line, Figure 6.20) corresponding to the adsorption of 5 monolayers of boric acid as earlier discussed in section 6.3.2. Still in the same  $\text{Ni}^{2+}$ -containing solution, the second region is characterised by a steep increase in mass at potentials more negative than -1.1 V which could be attributed to nickel electrodeposition, evident from the monotonic increase in the current calculated from the gravimetric data (cf. Figure 6.20). These results indicate that boric acid adsorbs on the electrode surface to suppress water reduction while delaying the onset of nickel electrodeposition and hence, shifting it to more negative overpotentials due to the additional energetic barrier of the adlayer. This implies that nickel electrodeposition occurs over a layer of adsorbed boric acid molecules support-

ing the Tafel slope findings measured in quiescent boric acid-containing electrolytes in chapter 5. Here, it was proposed that higher Tafel slopes were measured in boric acid-containing electrolytes because boric acid species were adsorbed on the cathode surface.

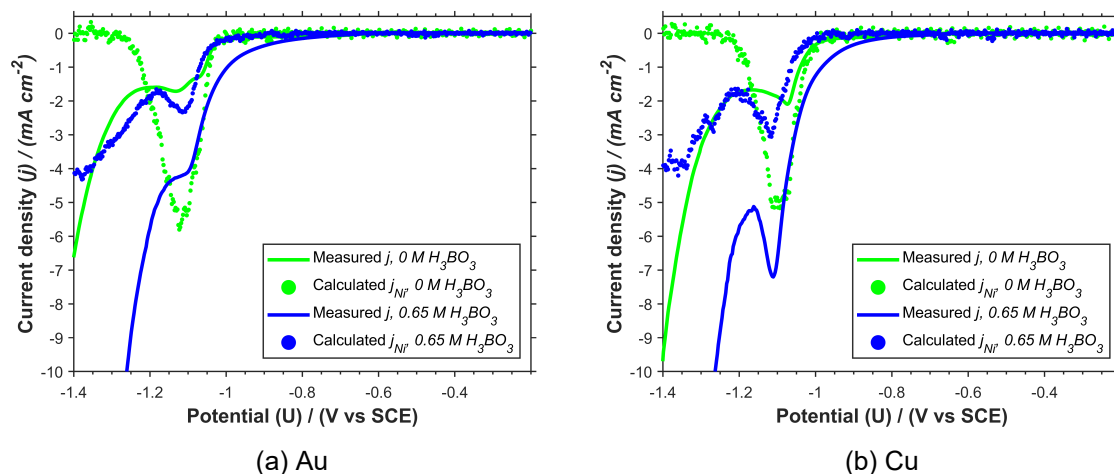


Figure 6.21: Comparison of measured  $j$ - $U$  curves from the LSV experiment and  $j$ - $U$  curves calculated from  $\Delta m$ - $U$  response in 17.9 mM Ni(II) + 3.57 M potassium sulfamate (pH 4.0) system on (a) Au and (b) Cu quartz crystal electrodes with and without 0.65 M  $H_3BO_3$ ; scan rate =  $5 \text{ mV s}^{-1}$

The adsorption of boric acid during nickel electrodeposition was also investigated on Au and Cu. Measured currents and currents calculated from EQCM gravimetric data for the initial stages of nickel deposition on Au and Cu substrates in  $Ni^{2+}$ -containing solutions with and without boric acid are compared in Figure 6.21. Similar to those on 304 SS, the results on Au and Cu show that in the absence of boric acid, Ni is deposited with  $Ni(OH)_2$ , as is seen from the significantly higher values of calculated current compared to measured current. The lower calculated currents obtained in the presence of boric acid show that boric acid appears to prevent the formation of  $Ni(OH)_2$ .

It is also found from the calculated currents that the addition of boric acid has a minimal influence on the onset potentials for nickel deposition which suggested that there is no significant boric acid adsorption prior to nickel deposition on Au and Cu electrodes. This results in  $Ni^{2+}$  reduction occurring at less negative potentials on Au

and Cu as compared to that observed on 304 SS. To determine the contribution of boric acid on Au and Cu, Figure 6.22 shows measured currents and EQCM mass changes measured on Au and Cu in boric acid -containing solutions with and without  $\text{Ni}^{2+}$ .

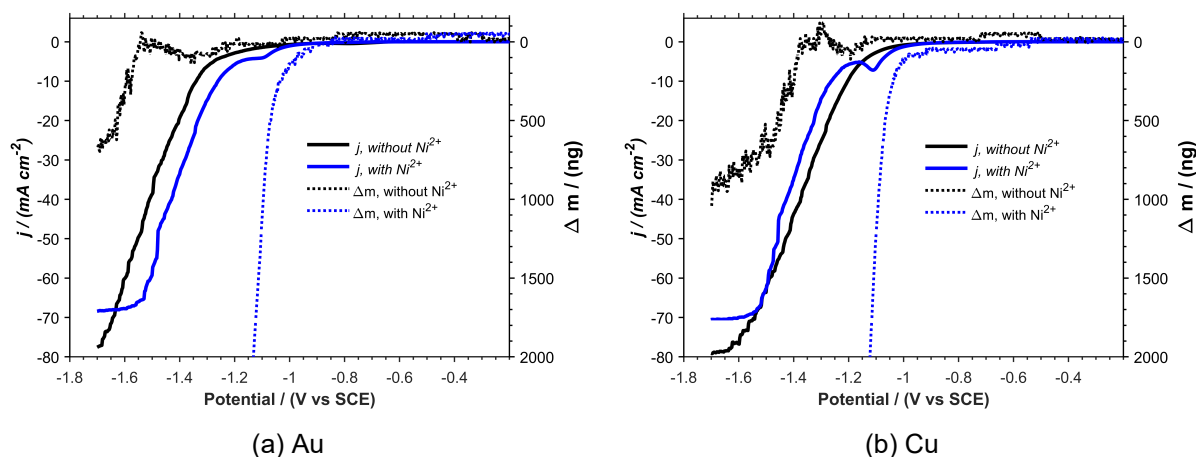


Figure 6.22: Polarisation scans measured in 3.57 M potassium sulfamate + 0.65 M boric acid solution without  $\text{Ni}^{2+}$  (black) and with  $\text{Ni}^{2+}$  (blue) at a scan rate of 5 mV/s on (a) Au and (b) Cu showing the measured current (solid lines) and mass changes (broken lines).

As was already established, compared to 304 SS, boric acid adsorbs at more negative potentials ( $> -1.1$  V) on Au and Cu in the absence of  $\text{Ni}^{2+}$ . Prior to the calculated Ni current breakthrough at  $-1.0$  V on Au and Cu (cf. Figure 6.21), there is a region of mass change ( $\approx 109$  ng) when a small amount of  $\text{Ni}^{2+}$  is added to the electrolyte according to Figure 6.22. This mass change is smaller than that observed on 304 SS ( $\approx 173$  ng) which indicates a decrease in boric adsorption on Au and Cu electrodes and explains a shift in nickel deposition to less negative potentials on these electrodes.

Table 6.5 summarises changes in current efficiency (i.e.  $j_{\text{Ni}}/j$ ) with current density obtained from the calculated and measured currents on 304 SS, Au, and Cu in the presence of boric acid shown in Figure 6.19 and 6.21. The results indicate that on all substrates, current efficiency decreases as the measured current density increases presumably due to mass transport limitations of  $\text{Ni}^{2+}$  to the electrode surface. In the presence of boric acid,  $\text{Ni}^{2+}$  reduction current efficiencies obtained on 304 SS in the presence of 1.79 M  $\text{Ni}^{2+}$ , which are  $\geq 98.7\%$  (Table 6.2), are significantly greater than

those obtained on the same substrate in the presence of 17.85 mM Ni<sup>2+</sup> (Table 6.5) which are  $\leq 26.5\%$ . These results show that the current efficiency is dependent on the concentration of Ni<sup>2+</sup>.

Table 6.5: Current efficiencies (%) calculated from EQCM  $\Delta f$  signal measured on different substrates in solutions containing 3.57 M potassium sulfamate, 0.65 M boric acid, and 17.85 mM Ni<sup>2+</sup> at 45 °C, assuming all of the QCM  $\Delta f$  signal arises from the electrochemical deposition of Ni.

Substrate material	Current density (mA/cm <sup>2</sup> )				
	-10	-20	-30	-40	-50
304 SS	26.53	16.59	12.19	9.06	7.21
Au	30.52	19.19	10.43	10.96	6.91
Cu	24.4	16.72	12.96	9.89	4.56

Figure 6.23 shows the plots of mass change vs charge in the presence and absence of boric acid. In the presence of boric acid, the  $\Delta m$ -Q plot consists of three linear regions. It can be observed that the slope of the first linear region of the mass-charge plot measured in the presence of boric acid is much lower than those corresponding to theoretical slopes for Ni and Ni(OH)<sub>2</sub> deposition. In addition, the slope decreases as the cathodic charge increases (or the potential becomes more negative). This observation indicates that as the potential becomes more negative, increasing proportions of the charge are consumed by hydrogen evolution via proton reduction in agreement with the current efficiency findings in Table 6.5. The results also indicate that nickel hydroxide is not formed during nickel electrodeposition in the presence of boric acid.

## 6.5 Summary of main results

The Electrochemical Quartz Crystal Microbalance (EQCM) was used to further investigate the interplay between nickel deposition, proton reduction, water reduction, and hydroxide formation with a focus on gaining further insight into the function of boric acid at the interface. The EQCM could measure mass-related frequency changes down to

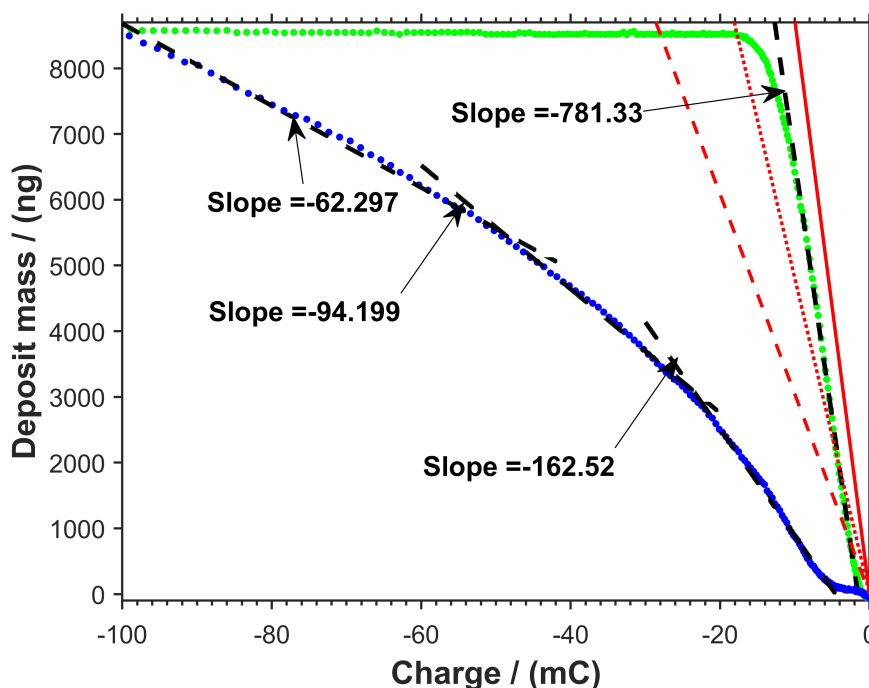


Figure 6.23: Mass change vs Charge ( $\Delta m$ -Q) during Ni electrodeposition in 17.9 mM Ni(II) + 3.57 M potassium sulfamate (pH 4.0) system without (green) and with (blue) 0.65 M  $H_3BO_3$  on a 304 SS quartz crystal electrode. Best fit lines are represented by the black dashed lines. Theoretical plots for Ni (slope = -304.14 ng/mC),  $Ni(OH)_2$  (slope = -480.427 ng/mC), and Ni +  $Ni(OH)_2$  (slope = -872.57 ng/mC) are given by the dashed, dotted, and solid red lines, respectively.

0.1 ng which make it a powerful tool to distinguish interfacial reactions based on the amount of charge passed.

First, polarisation experiments were performed in nickel sulfamate solutions (containing 1.78 M  $Ni^{2+}$ ) with varying concentrations of  $H_3BO_3$  to verify that the results obtained at the 304 SS disc electrode could be reproduced at a quartz crystal electrode. The results indicated that the current efficiencies measured from the EQCM were comparable to those obtained by gravimetry of the 304 SS disc electrode. The slopes of mass-charge plots obtained from frequency changes of the EQCM indicated that nickel electrodeposited during potentiodynamic experiments in the absence of boric acid consisted of 15-20%  $Ni(OH)_2$ . In the presence of boric acid, mass-charge slopes close to the value predicted for nickel deposition were obtained which suggested that most of the charge was consumed in nickel electrodeposition and  $Ni(OH)_2$  was not produced. It

was also observed from these experiments that an increase in boric acid concentration led to an increase in the nickel deposition rate which corroborated findings at the larger disc electrode. The causative reason for this observation was further investigated by conducting experiments in the blank electrolyte.

Polarisation experiments were performed in 3.57 M  $\text{KSO}_3\text{NH}_2$  in order to eliminate nickel deposition and investigate the effect of boric acid on the side reactions (proton and water reduction) taking place on bare electrode surfaces (304SS, Au, and Cu) and the electrodeposited nickel film. The massogram measured in the absence of boric acid revealed the formation of metal hydroxides and oxides at potentials corresponding to the onset potential of water reduction. This was corroborated by the high Tafel slopes measured for water reduction on these substrates. The formation of these hydroxides and oxides was not observed in the presence of boric acid. Instead, the massograms measured in the presence of boric acid revealed an important increase in mass (adsorption) and subsequent decrease in mass (desorption) beginning at potentials corresponding to the onset of water reduction which was interpreted as the adsorption and desorption of boric acid or a boric acid-related species. Therefore, it was concluded that the adsorption of this species prevented access of water to the electrode surface. This meant that the production of  $\text{OH}^-$  was minimised and oxide/hydroxide formation was obviated. The results also indicated that boric acid adsorbed more on 304 SS and Ni compared to Au and Cu; 4-5 monolayers of boric acid were adsorbed in any case.

The adsorption of boric acid during nickel electrodeposition was investigated by performing potentiodynamic experiments in sulfamate electrolytes containing small concentrations of  $\text{Ni}^{2+}$  (17.85 mM). The results reveal that nickel deposition in the absence of boric acid proceeds after the onset of  $\text{H}_2\text{O}$  reduction. Consequently,  $\text{Ni}(\text{OH})_2$  was codeposited with nickel in the first few monolayers on the electrode surface during nickel electrodeposition in the absence of boric acid. In the presence of boric acid, the formation of  $\text{Ni}(\text{OH})_2$  was obviated and nickel electrodeposition proceeded with hydrogen evolution from proton reduction. By comparing the massogram measured in the absence and presence of  $\text{Ni}^{2+}$ , it could be observed that boric acid adsorbed on the 304 SS electrode surface prior to nickel electrodeposition. This occurred to a

lesser extent on Au and Cu electrodes presumably due to increased competitiveness between  $\text{H}_3\text{BO}_3$  and H adsorption on Au and Cu which have more favourable HER kinetics. Therefore, it was concluded that boric acid adsorbed on the electrode surface prior to nickel electrodeposition to prevent water reduction and the formation of nickel hydroxide which could inhibit  $\text{Ni}^{2+}$  reduction. Therefore, the reduction of  $\text{Ni}^{2+}$  was facilitated in the presence of boric acid. A schematic of the action of boric acid during nickel electrodeposition is provided in Figure 6.24.

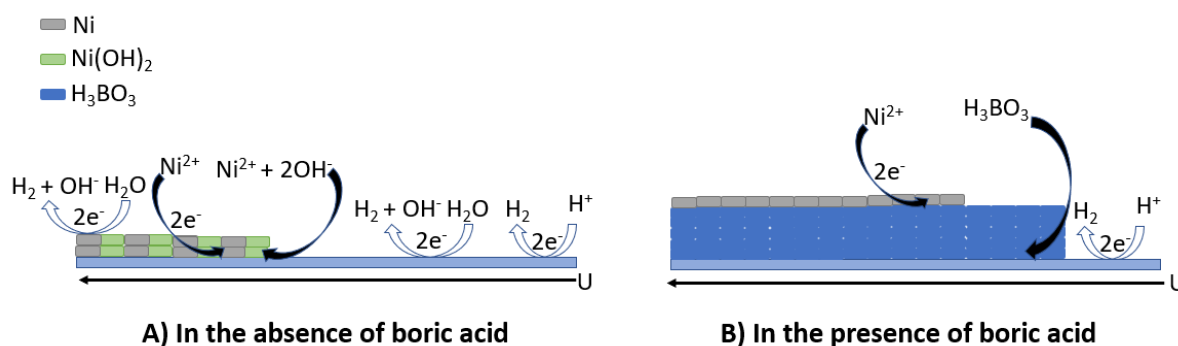


Figure 6.24: Schematic of proposed mechanism for the action of boric acid during nickel electrodeposition as a function increasing cathode potential depicted by the direction of the arrow.

Overall, the results indicate that the current efficiency of nickel electrodeposition decreased when the concentration of  $\text{Ni}^{2+}$  in the bath was lowered which suggested that the presence of  $\text{Ni}^{2+}$  decreased the rate of hydrogen evolution via proton reduction. Therefore, the overall suppression of proton and water reduction during nickel electroforming in the presence of boric acid is due to the synergistic adsorption of both boric acid and nickel ions.



# Chapter 7

## Characterisation of anode materials for nickel electroforming

Anodes are an essential part of the electroforming process but have received limited attention. Most of the significant work done to characterise anodes in sulfamate solutions appeared between the 1960s and 1990s [125, 127–129, 135, 173]. Currently, the electroforming process employs new soluble nickel anodes with distinct forms and compositions. Ideally, a nickel anode should dissolve in an active state (i.e., at low overpotentials close to the reversible potential of  $\text{Ni}^{2+}/\text{Ni}$ ) with 100% current efficiency so as to maintain the concentration of  $\text{Ni}^{2+}$  in the electrolyte and avoid side reactions that could alter the electrolyte composition [55, 138, 260]. In reality, several anodes have been found to passivate and dissolve with high overpotentials [50, 130, 180, 181]. Under these conditions, several other reactions have been demonstrated to occur [125, 127–129, 173]. Importantly, products generated from the oxidation of sulfamate ions influence deposit characteristics [125, 127, 128, 181, 261]. Although these substances have some beneficial effects on electrodeposited nickel (such as decreasing internal stress and improving brightness and hardness), they are introduced into the electrolyte in an unregulated manner, and their chemical nature is not well understood.

To answer the scientific questions discussed in section 4.3, a characterisation study of a number of commercially available anode materials is presented in this chapter. Initial studies will identify active, passive, and transpassive regions, establish their basic dissolution characteristics, and determine anode current efficiencies using polarisation and chronopotentiometry measurements. A second set of studies assessed conditions that lead to the formation of sulfamate decomposition products at various anodes. Finally, the influence of these products on the deposition process was demonstrated by collecting cathodic polarisation curves and current efficiencies after the build-up of these products in the electrolyte. It is anticipated that the findings

presented in this chapter will assist commercial electroformers in selecting appropriate anodes and conditions for a range of applications.

Compared with the use of soluble nickel anodes, the application of insoluble anodes to electroforming is on a much smaller scale, mostly in laboratory environments [132,133]. Even so, insoluble anodes offer some technical benefits in specialised uses, such as, the production of complex- and hollow-shaped electroforms with a uniform thickness distribution [126,221]. Therefore, investigations were conducted to compare the performance of soluble anodes with that of insoluble platinum.

## **7.1 Polarisation behaviour of different anode materials in nickel sulfamate solution**

Linear Sweep Voltammetry (LSV) was applied to determine the electrochemical behaviour of several commercially available nickel anodes using a scan rate of 5 mV/s. Three low-sulfur nickel anodes (plating chips, Goodfellow Ni rod, and P-pellets) and three sulfur-activated nickel anodes (S-rounds, S-pellets, and D-crowns) were investigated. These experiments are useful in identifying current density ranges of active and transpassive dissolution for the different anodes. Polarisation plots of the nickel anode samples in 1.785 M  $\text{Ni}(\text{SO}_3\text{NH}_2)_2$  and 0.65 M  $\text{H}_3\text{BO}_3$  are presented in Figure 7.1. Given that the performance of soluble anodes is compared with that of insoluble platinum in later parts of this chapter, the polarisation curve for a Pt wire in the same solution is also shown in Figure 7.1.

Three characteristic regions could be identified from the polarisation plots of commercial nickel anodes shown in Figure 7.1. These distinctive regions and their distinguishing features are summarised as follows:

1. active dissolution - an increase in current density which begins around -0.3 V close to the equilibrium potential of Ni (-0.469 V vs SCE) and lasts till peak  $A_2$  (defined as the critical current density,  $j_p$ );
2. passivation - a decrease in current density after peak  $A_2$  and very low current

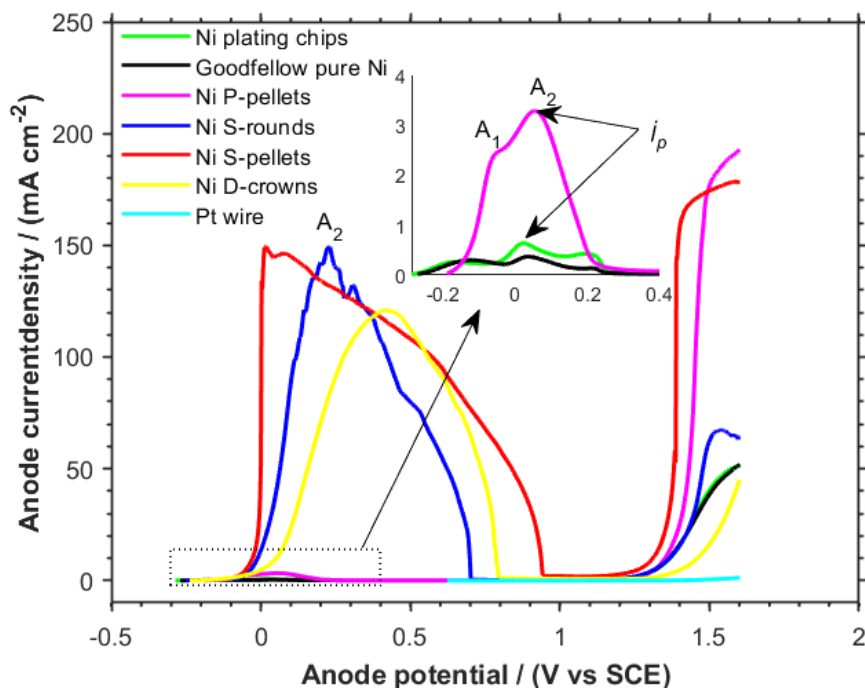


Figure 7.1: Polarisation plots for various types of anode materials at a scan rate of  $5 \text{ mV s}^{-1}$  illustrating active, transpassive, and passive regions. The electrolyte comprised of  $1.785 \text{ M Ni}(\text{SO}_3\text{NH}_2)_2 \cdot 4\text{H}_2\text{O}$  and  $0.65 \text{ M H}_3\text{BO}_3$ . The inset shows the active/passive region in detail.

densities of about  $0.07 \text{ mA/cm}^2$  thereafter; and

3. transpassive dissolution - a renewed increase in current density around  $1.3 \text{ V}$ .

These characteristic regions have also been identified by other researchers [50, 180] who measured potentiodynamic polarisation plots of nickel in nickel sulfamate solutions; their results have been shown in Figures 2.8 and 2.9 in chapter 2 of this thesis. It is noted that the common characteristics shared by nickel polarisation plots were absent in that of the Pt wire. In fact, no observable current density increase was found on Pt within the scan range applied, i.e., from OCP to  $1.6 \text{ V}$ . This means that current densities passed for electroforming can only be supported by a Pt anode at potentials more noble than  $1.6 \text{ V}$ .

Although all three characteristic regions mentioned above are present in the polarisation scans of the soluble anode materials shown in Figure 7.1, the current density ranges for active and transpassive dissolution are very different for low-sulfur and

sulfur-activated nickel materials. It should be mentioned that the maximum current densities of active dissolution, defined as the critical current densities ( $j_p$ ), were reproducible within 55% ( $\pm 0.5 \text{ mA/cm}^2$ ) for plating chips/Goodfellow Ni discs, 10% ( $\pm 0.3 \text{ mA/cm}^2$ ) for P-pellets, 25% ( $\pm 37 \text{ mA/cm}^2$ ) for S-pellets, and 6% ( $\pm 7 \text{ mA/cm}^2$ ) for S-rounds/D-crowns based on at least three repeat measurements. Nevertheless, the polarisation plots of sulfur-activated nickel anodes show  $j_p$  values about 2 orders of magnitude greater than those of low-sulfur nickel anodes, within error. The voltammograms of S-pellets, S-Rounds, and D-crowns, which are all sulfur-activated nickel anodes, show a wide active state which supports current densities above  $100 \text{ mA/cm}^2$  before undergoing passivation whereas the critical current densities for low-sulfur nickel anodes do not exceed  $4 \text{ mA cm}^{-2}$ , within error. Good agreement is observed between these results and earlier findings on sulfur-activated and low-sulfur nickel anodes in nickel sulfamate baths by other researchers [50, 130, 180].

Active dissolution of nickel is attributed to the direct passage of Ni atoms into the electrolyte in the form of  $\text{NiOH}^+$ ; the overall reaction is represented as follows [149]:



It has been proposed in literature [159, 161, 162] that sufficiently high concentrations of  $\text{NiOH}^+$  in the vicinity of the electrode surface could precipitate a layer of  $\text{Ni(OH)}_2$  on the anode surface according to Equation 7.2. It has been demonstrated using chronoellipsometric experiments, described in chapter 2, that this  $\text{Ni(OH)}_2$  film does not render the anode surface passive due to its porous and electronic insulating nature [159]. This is because the onset of this film formation is not accompanied by a decrease in dissolution current but a decrease in the gradient of the current-potential line. Based on these observations made by other researchers [159, 161, 162], the inflection point at  $A_1$ , observed in the voltammograms of low-sulfur anodes, prior to the critical current density at peak  $A_2$  could indicate the formation of this  $\text{Ni(OH)}_2$  layer.



Passivation occurs when the pre-passive  $\text{Ni(OH)}_2$  film is converted to an electronic conducting layer which consists mainly of NiO [159]. Researchers [159] demonstrated using steady-state current-potential and ellipsometric measurements that the

formation of this passive film is accompanied by a sharp decrease in current. The results presented in Figure 7.1 agree with those found by these researchers [159] which suggests the formation of NiO during the dissolution of the nickel anodes which renders the anode surface passive.

It has been determined that sulfur-activated nickel is able to dissolve at high current densities before passivating because of the nickel sulfide ( $\text{Ni}_3\text{S}_2$ ) layer formed on the anode surface [176], which has been confirmed using X-ray Photoelectron Spectroscopy [177, 178]. The  $\text{Ni}_3\text{S}_2$  layer is proposed to prevent the adsorption of  $\text{OH}^-$  required for the formation of  $\text{Ni}(\text{OH})_2$  while allowing nickel to pass into the electrolyte from the layer leaving a sulfide with a lower nickel content [179]. Therefore, the major differences between the polarisation plots for low-sulfur and sulfur-activated nickel anodes could be attributed to sulfur impurities.

At potentials more anodic than 1.3 V, the passive film breaks down and transpassive dissolution commences indicated by the renewed increase in current density. The mechanisms by which the passive layer breaks down has been extensively studied by Marcus et al. [165]. Thinning at the oxide/electrolyte interface due to enhanced dissolution at oxide grain boundaries, creation of vacancies and particle growth at the metal/oxide interface are some breakdown mechanisms of the oxide layer suggested by Marcus et al. [165].

S-rounds and D-crowns, two electrorefined materials, exhibit some resemblances in their polarisation plots; any discrepancies could be attributed to different chemical compositions and microstructures. The polarisation plot of the S-pellet made using the carbonyl method, also differs from that of the S-round, which could be a result of the different manufacturing processes used and the associated compositional and microstructural variations. Similar to this, discrepancies among low-sulfur nickel anodes — all made using the carbonyl process — could be the result of similar variations.

In summary, the results in Figure 7.1 indicate that the use of sulfur-activated nickel can support higher current densities at low potentials when compared to low-sulfur nickel anodes. This means, for a particular applied current density, the use of

sulfur-activated nickel anodes could provide a lower cell voltage during electroforming and reduce energy requirements of the process.

Electroforming solutions typically contain a small amount of nickel chloride hexahydrate ( $\approx 0.021$  M) to improve the dissolution rate of the nickel anode while maintaining low internal stress in the deposits. Additionally, the electrolyte in the electroforming process would be pumped into the tank effectively creating agitated conditions to allow for sufficient electrolyte circulation [122]. Therefore, it is of interest to study how these nickel anode materials will perform in the presence of chloride ions and agitation.

## **7.2 Polarisation behaviour of pure nickel anodes in nickel sulfate solution**

### **7.2.1 Effect of electrode rotation speed**

Figure 7.2 shows the effect of electrode rotation speed on the electrochemical behaviour of Ni plating chips in 1.785 M  $\text{Ni}(\text{SO}_3\text{NH}_2)_2$  and 0.65 M  $\text{H}_3\text{BO}_3$ . This study was only possible for disc-shaped geometries, such as the plating chips, that could be fitted into the RDE holder to provide controlled hydrodynamic conditions at the anode. The results indicate that an increase in electrode rotation speed increased the current densities both in the active and transpassive regions. Its impact on the active state of nickel dissolution is more significant and can be attributed to an increase in the rate of  $\text{NiOH}^+$  diffusion from the electrode surface to the bulk solution which prevents the build-up of  $\text{NiOH}^+$  at the electrode-electrolyte interface that would lead to the formation of the pre-passive film,  $\text{Ni}(\text{OH})_2$  [161]. This is important to electroforming because it shows that agitation extends the current density region over which the anode could dissolve uniformly. The anode dissolves unevenly at current densities above the critical current density (i.e. in the transpassive region), undercutting grains and producing nickel fines. This uneven dissolution also increases the need for anode bag maintenance and could increase the deposit's roughness, if fines are present in solution

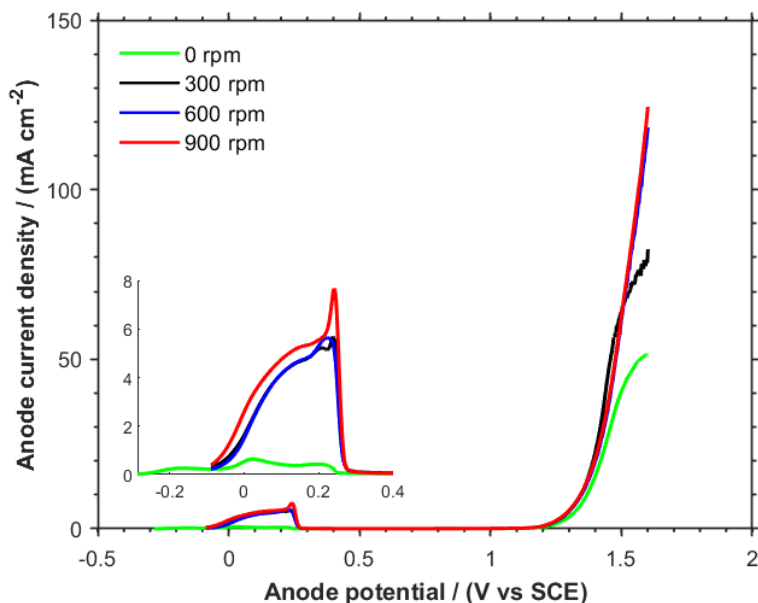


Figure 7.2: Influence of electrode rotation speed on the polarisation plots for a low-sulfur nickel anode material (plating chip) at a scan rate of  $5 \text{ mV s}^{-1}$ . The base electrolyte comprised of  $1.785 \text{ M Ni}(\text{SO}_3\text{NH}_2)_2 \cdot 4\text{H}_2\text{O}$  and  $0.65 \text{ M H}_3\text{BO}_3$ . The inset shows the active/passive region in detail.

[126]. The main point to be emphasised here is that solution agitation promotes the dissolution of low-sulfur anodes in the active region where they can dissolve uniformly.

## 7.2.2 Effect of chloride ions

Figure 7.3 shows the voltammograms of low-sulfur nickel anodes measured in nickel sulfamate solution in the absence (solid lines) and presence (broken lines) of  $0.021 \text{ M Cl}^-$ . In the presence of  $\text{Cl}^-$ , the polarisation plots of the anodes maintain active, passive, and transpassive regions. Similar to other studies [50, 130], the addition of a low concentration of  $\text{Cl}^-$  (such as  $0.021 \text{ M}$ ) slightly improved the dissolution characteristics of low-sulfur anode materials by shifting the oxidation potentials in a less positive direction but did little to extend the current density region over which active dissolution occurred.

Interestingly, the presence of  $0.021 \text{ M Cl}^-$  in nickel sulfamate solution had little effect on the onset potential of transpassive dissolution, but this is not the case

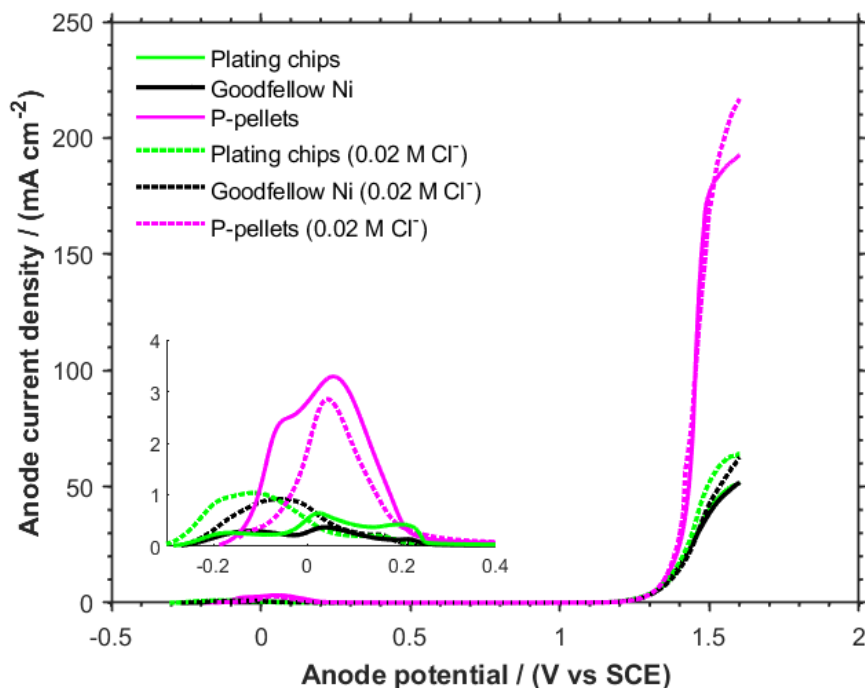


Figure 7.3: Influence of chloride ions on the polarisation plots for low-sulfur nickel anode materials at a scan rate of  $5 \text{ mV s}^{-1}$ . The base electrolyte comprised of  $1.785 \text{ M Ni}(\text{SO}_3\text{NH}_2)_2 \cdot 4\text{H}_2\text{O}$  and  $0.65 \text{ M H}_3\text{BO}_3$  with and without  $0.021 \text{ M NiCl}_2 \cdot 6\text{H}_2\text{O}$ . The inset shows the active/passive region in detail.

for sulfate electrolytes. A lower breakdown potential was observed for a P-pellet in a sulfate system containing the same concentration of  $\text{Cl}^-$  as the nickel sulfamate bath; the results are shown in Figure 7.4.

Changing the anionic species from sulfamate to sulfate influenced the behaviour of Ni both in the active and passive regions as shown in Figure 7.4. In the sulfate bath, the P-pellet exhibits an active dissolution region between 0 and 0.3 V which can only sustain current densities  $< 2 \text{ mA cm}^{-2}$ . In contrast to the sulfamate system, the active region of the P-pellet in nickel sulfate is almost immediately followed by a sharp increase in current density at about 0.5 V. These results are in agreement with those reported for nickel in a Watts bath [50, 262]. As mentioned earlier, a porous  $\text{Ni}(\text{OH})_2$  film is generated during the dissolution of nickel which does not passivate the electrode surface. It is only the conversion of this  $\text{Ni}(\text{OH})_2$  film to a fully stable layer of electronically conducting NiO that would result in full passivation of the anode surface [159]. The results in Figure 7.4 suggests that the stability of the passive film formed



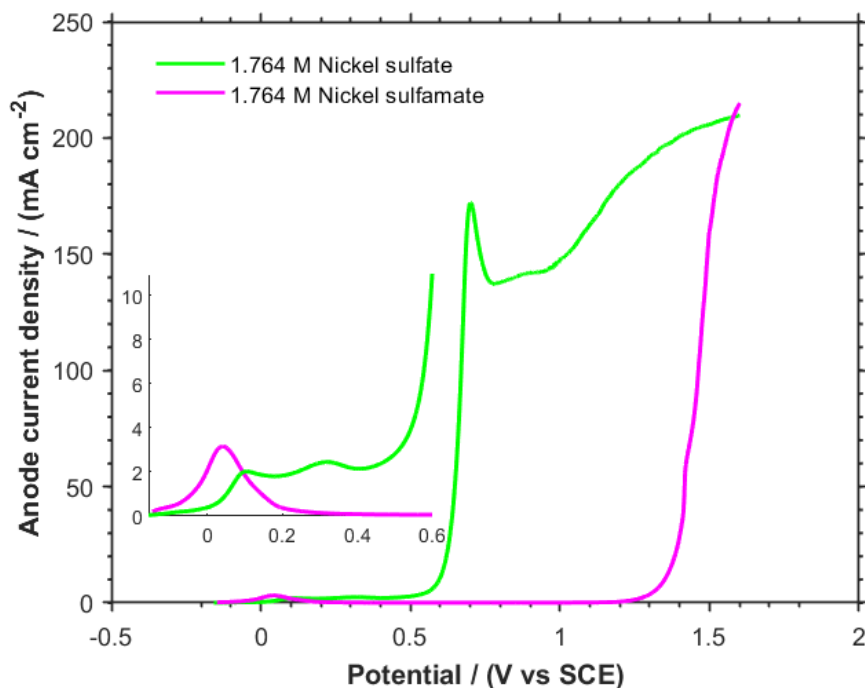


Figure 7.4: Polarisation plots for the nickel P-pellet in sulfamate and sulfate based solutions containing 0.65 M  $\text{H}_3\text{BO}_3$  and 0.021 M  $\text{NiCl}_2 \cdot 6\text{H}_2\text{O}$ . The inset shows the active/passive region in detail.

on a low-sulfur nickel anode during its active dissolution is lower in sulfate-based solutions compared to sulfamate-based electrolytes. Therefore, chloride ions are more effective at inducing breakdown of the less stable passive film at lower potentials in nickel sulfate solution.

The passivation issue of low-sulfur nickel anodes in sulfate electrolytes used for electrodeposition has been countered by utilising high levels of chloride ions (0.25 M), as opposed to sulfamate baths (<0.028 M) [24]. This strategy is not practical in sulfamate systems as chloride ions could increase tensile stress of deposits [125, 173, 175]. Additionally, although low-sulfur nickel dissolves at lower potentials in Watts-type baths, it does so non-uniformly, i.e., through pits producing residue in the process [262].

## 7.3 Polarisation behaviour of sulfur-depolarised nickel anodes in nickel sulfamate solution

### 7.3.1 Effect of rotation speed

Results in Figure 7.1 have shown that sulfur-activated nickel materials can dissolve with high critical current densities between 120 and 150 mA/cm<sup>2</sup> in the active region without stirring of the solution. An investigation was carried out to determine how solution agitation will affect the dissolution characteristics of sulfur-activated nickel. D-crowns, which showed the lowest critical current density in quiescent sulfamate electrolytes, were selected for this study.

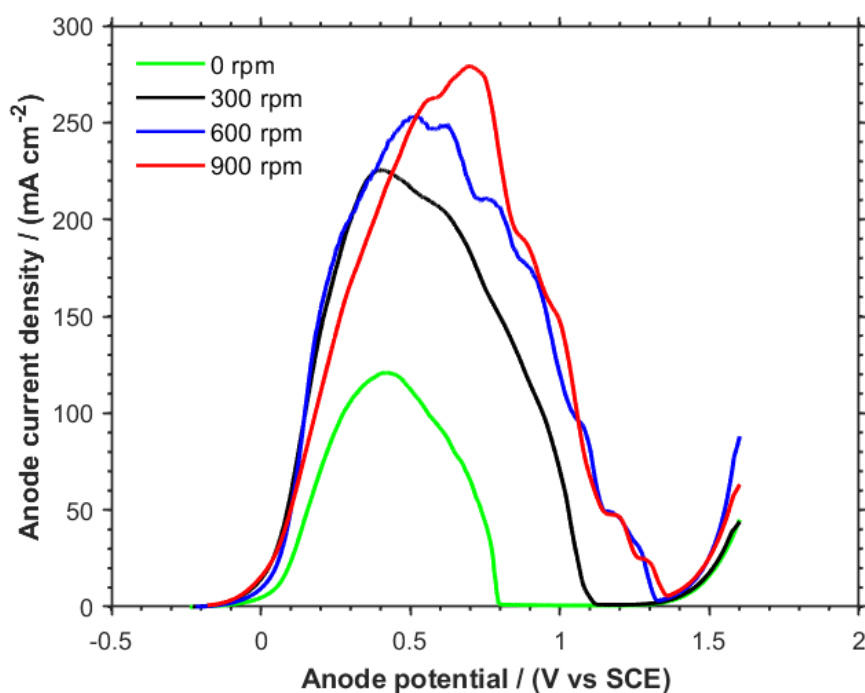


Figure 7.5: Influence of electrode rotation speed on the polarisation plots for a sulfur-depolarised nickel anode material (D-crowns) at a scan rate of 5 mV s<sup>-1</sup>. The base electrolyte comprised of 1.785 M Ni(SO<sub>3</sub>NH<sub>2</sub>)<sub>2</sub>·4H<sub>2</sub>O and 0.65 M H<sub>3</sub>BO<sub>3</sub>.

Figure 7.5 shows the effect of electrode rotation speed on the polarisation plots of Ni D-crowns. Increase in rotation speed significantly extended the current density and potential range over which active dissolution of Ni D-crowns occurred, as

was also observed with low-sulfur plating chips in Figure 7.2.

Although results in Figure 7.5 indicate that sulfur-activated Ni could sustain current densities greater than  $120 \text{ mA/cm}^2$  in the active region by stirring the solution, this is of little importance to electroforming because these dissolution rates are equivalent to cathode current densities  $> 220 \text{ mA/cm}^2$  for an anode-to-cathode area ratio of 2:1 typically used in plating baths [125, 135]. These cathode current densities are well above practical electroforming conditions ( $5\text{-}50 \text{ mA cm}^{-2}$ ) [24]. Therefore, the advantages of agitation on the current density range in the active region of sulfur-activated nickel could be viewed as minimal in electroforming.

It is also apparent that Ni D-crowns are more active in stirred solutions than unstirred ones, i.e., equivalent current densities in the active region can be obtained at lower potentials in stirred solutions. However, in the region of the polarisation plot corresponding to practical dissolution rates anticipated in electroforming ( $\leq 25 \text{ mA/cm}^2$ ), the differences between the dissolution potentials of D-crowns in stirred and unstirred solutions are small. Therefore, it is reasonable to conclude that sulfur-activated nickel is no less active in unstirred solutions than it is in stirred ones during nickel electroforming.

### 7.3.2 Effect of chloride ions

Figure 7.6 shows the polarisation plots of sulfur-activated nickel in the presence and absence of chloride ions. The findings demonstrate that regardless of the presence of  $\text{Cl}^-$ , all sulfur-activated nickel anodes are capable of supporting high current densities in the active region. Nevertheless, the presence of chloride ions enhances the sulfur-activated anode's capacity to dissolve at higher rates. However, the region of the polarisation plots where chloride ions have a significant impact does not correspond to practical dissolution current densities. Thus, much like solution agitation, one could view the advantages of chloride ions as minimal in the dissolution of sulfur-activated nickel.

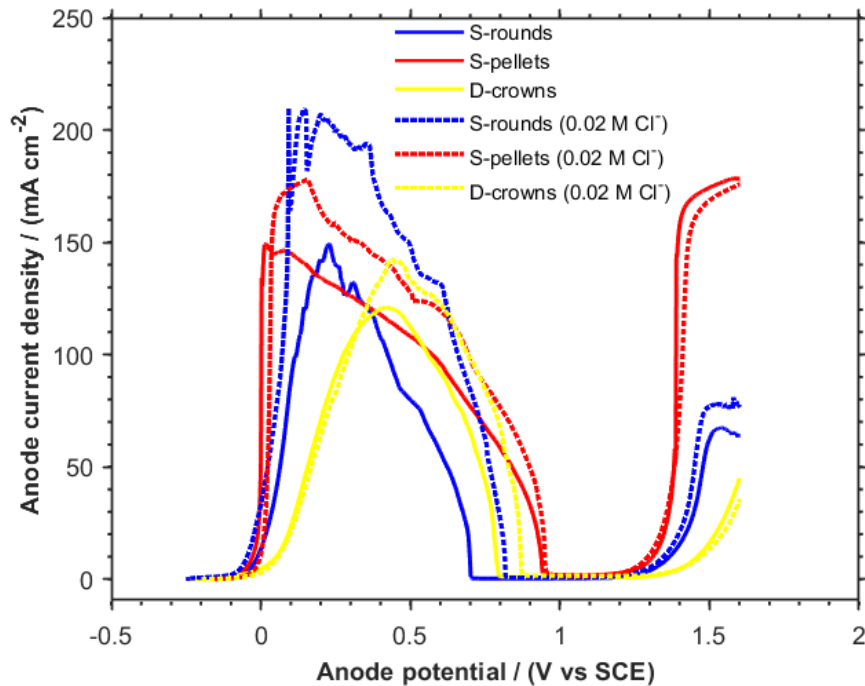


Figure 7.6: Influence of chloride ions on the polarisation plots for sulfur-depolarised nickel anode materials at a scan rate of  $5 \text{ mV s}^{-1}$ . The base electrolyte comprised of  $1.785 \text{ M Ni}(\text{SO}_3\text{NH}_2)_2 \cdot 4\text{H}_2\text{O}$  and  $0.65 \text{ M H}_3\text{BO}_3$  with and without  $0.021 \text{ M NiCl}_2 \cdot 6\text{H}_2\text{O}$ .

#### 7.4 Concluding remarks on the polarisation behaviour of nickel anodes

The polarisation curves of nickel materials show three characteristic regions (active, passive, and transpassive). The active and transpassive regions correspond to the dissolution of the metal. One of the pertinent questions in this thesis is: "Does dissolution of the anode occur in the active or transpassive region?" Critical current densities ( $j_p$ ) collected from the polarisation curves could help to answer this question as it is known that [263]:

1. At applied anode current densities ( $j$ )  $< j_p$ , dissolution will occur in the active region (i.e at low potentials).
2. At  $j > j_p$ , dissolution will transition from the active to the transpassive region which occurs at higher potentials; the transition time will depend on the current density

and is expected to decrease as the current density increases.

For an anode-to-cathode surface area ratio of 2:1 which is applied in electroforming [125, 135], practical anode current densities could be anticipated to range from 2.5 to 25 mA cm<sup>-2</sup> in correspondence to electroforming current densities of 5-50 mA cm<sup>-2</sup> [24]. The results shown in Figures 7.3 and 7.6 indicate that the critical current densities for low-sulfur and sulfur-activated nickel anodes are <3 mA/cm<sup>2</sup> and >130 mA/cm<sup>2</sup>, respectively, in typical chloride-containing electroforming solutions. According to the comments made above, these results suggest that, if low-sulfur anodes are to be employed at reasonable electroforming current densities (i.e. >10 mA/cm<sup>2</sup>), they are likely to be undergoing transpassive rather than active dissolution. In contrast, sulfur-activated nickel will likely only dissolve in the active region during electroforming.

Results in this chapter have shown that the critical current densities of nickel anodes are influenced by solution stirring, and the nature and concentration of the electrolyte anions. Critical current densities are also reportedly affected by the scan rate [50]. Therefore, the critical current density measured under potentiodynamic conditions is not often well defined and cannot solely serve as a diagnostic for the dissolution region of the nickel anodes. To confirm the dissolution characteristics of the various types of nickel materials and answer the question posed above, measurements of the anode potential during dissolution is needed, which are explored in the forthcoming section.

## **7.5 Dissolution potential and current efficiency of nickel anodes**

### **7.5.1 Dissolution potential**

Chronopotentiometry experiments were conducted using constant anode current densities ranging from 1.7 to 8.6 mA/cm<sup>2</sup>. This current density range was purposely selected to include the active region for low-sulfur nickel pellets. As mentioned, the aim of these experiments was to confirm dissolution characteristics of low-sulfur and sulfur-activated nickel materials. Due to their lack of characterisation in the literature, carbonyl nickel pellets were selected for these studies.

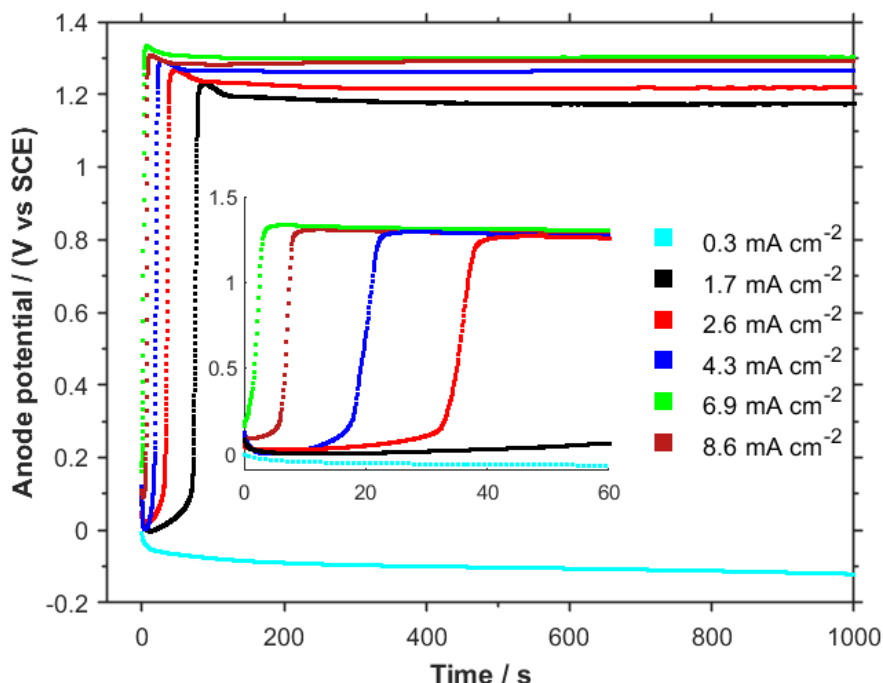


Figure 7.7: Time dependence of the anode potential when various current densities are applied to a P-pellet anode. The zoomed inset shows the time it takes for the anode potential to transition from the active to the transpassive region. The base electrolyte comprised of 1.785 M  $\text{Ni}(\text{SO}_3\text{NH}_2)_2 \cdot 4\text{H}_2\text{O}$ , 0.021 M  $\text{NiCl}_2 \cdot 6\text{H}_2\text{O}$ , and 0.65 M  $\text{H}_3\text{BO}_3$ .

Figure 7.7 shows plots of potential against time recorded for the dissolution of a Ni P-pellet anode at various anode current densities. Careful inspection of these plots (see inset of Figure 7.7) shows a distinct arrest in potential at very low values around 0 V at the beginning of the measurement. This potential falls within the active region of the polarisation plots of Ni P-pellets (c.f. Figure 7.3) which suggests that the anode initially dissolves in the active region. For a current density of 1.7–8.6  $\text{mA cm}^{-2}$ , the anode potential increases sharply after a certain duration to stable values above 1.2 V which lie within the transpassive region (c.f. Figure 7.3). This potential transition indicates a shift from active to transpassive dissolution for the P-pellets which apparently occurs within a relatively short transition time in the order of seconds; this transition time decreases as the applied current density increases. Based on literature which report similar characteristics in the potential transients of Ni dissolution [264], the transition could be ascribed to passivity breakdown and subsequent dissolution through pits in order to maintain the desired current density. Thus, the chronopotentiometric

measurements confirm that low-sulfur nickel pellets will dissolve in the transpassive region during electroforming. These findings are in good agreement with earlier electrochemical studies [50, 130] that demonstrate that low-sulfur nickel materials typically undergo transpassive dissolution at a relatively high potential in nickel sulfamate electrolytes. These materials would require very low current densities (such as  $0.3 \text{ mA cm}^{-2}$ ) to ensure active dissolution.

Some anomalies are noted for the P-pellet's potential transients obtained under applied an current density of  $1.72\text{-}2.58 \text{ mA cm}^{-2}$  which fall below the apparent critical current density ( $2.85 \text{ mA cm}^{-2}$ ) of its polarisation plot shown in Figure 7.3; while the polarisation plot suggests that the Ni anode should dissolve in the active region under these conditions, the chronopotentiometric transients indicate otherwise. It should be mentioned that the standard deviation of the critical current density of the P-pellet is  $\pm 41\%$  ( $\pm 1.16 \text{ mA cm}^{-2}$ ). These deviations in the dissolution characteristics of different P-pellets could be attributed to the changing composition of the lamellar structures of individual pellets due to varying temperatures and  $\text{Ni(CO)}_4$  partial pressures within decomposition chambers of the carbonyl process [262].

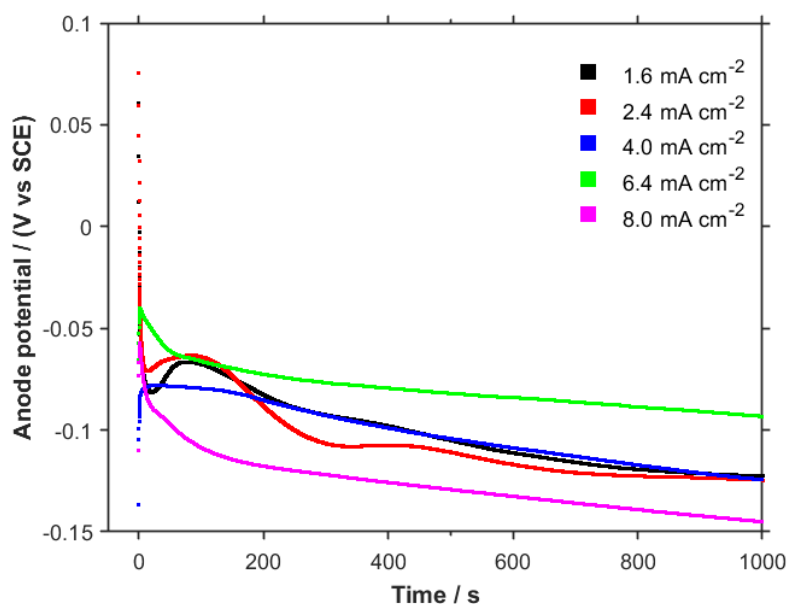


Figure 7.8: Time dependence of the anode potential when various current densities are applied to an S-pellet. The base electrolyte comprised of  $1.785 \text{ M Ni(SO}_3\text{NH}_2)_2 \cdot 4\text{H}_2\text{O}$ ,  $0.021 \text{ M NiCl}_2 \cdot 6\text{H}_2\text{O}$  and  $0.65 \text{ M H}_3\text{BO}_3$ . Dissolution occurred in the active region.

The potential transients measured for the dissolution of Ni S-pellets under different current densities are shown in Figure 7.8. The results indicate that they typically dissolve at potentials more negative than -0.05 V which lie in the active region of their polarisation plot shown in Figure 7.6. This behaviour is expected because the applied current densities ( $1.6\text{-}8\text{ mA cm}^{-2}$ ) are much lower than the critical current density ( $180\text{ mA cm}^{-2}$ ) of the S-pellets. These results are in agreement with earlier studies which demonstrated that sulfur-activated nickel materials typically dissolve in the active region at a relatively low potential in nickel sulfamate solution [50, 181].

### 7.5.2 Anode current efficiencies

The high oxidation potentials exhibited by low-sulfur nickel during transpassive dissolution could drive other reactions such as the oxidation of water and sulfamate ions, which lower anode current efficiency. The equilibrium potential of water oxidation under the temperature (318 K) and pH (3.26) conditions of the electroforming bath is 0.78 V which falls below the dissolution potentials of the Ni P-pellet shown in Figure 7.7. This suggests that oxygen evolution is likely to occur during dissolution of low-sulfur Ni pellets. Although there is no thermodynamic data for sulfamate ion oxidation, it could be gleaned from potentiostatic and galvanostatic experiments in literature that it occurs at potentials close to those of water oxidation [127, 130, 135]. These side reactions could create unstable conditions in the process including unwanted pH changes and the production of chemicals that could impact deposit characteristics [55, 138, 260]. As a result, a key determining factor for the stability of the electroforming solution is the anode current efficiency.

Anode efficiencies for the dissolution of Ni P-pellets and S-pellets were evaluated from weight loss measurements following chronopotentiometry experiments; the results are summarised in Table 7.1. As clearly observed in the table, the dissolution of sulfur-activated nickel, which occurs in the active region, proceeds with current efficiencies of 94-106%. To ensure a current efficiency of 100% during the dissolution of low-sulfur nickel in the transpassive region would require low current densities of  $1.7\text{-}2.6\text{ mA cm}^{-2}$ . Higher current densities of  $4.3\text{-}8.6\text{ mA/cm}^2$  which increased anode



potentials led to efficiencies of the order 79-93%.

Table 7.1: Summary of anodic current efficiencies for dissolution of two types of nickel anodes. Total charge passed was 43.77 C.

<b>P-pellet anode</b>		<b>S-pellet anode</b>	
<b>Current density (mA cm<sup>-2</sup>)</b>	<b>Current efficiency (%)</b>	<b>Current density (mA cm<sup>-2</sup>)</b>	<b>Current efficiency (%)</b>
1.72	103.6	1.60	105.9
2.58	100.7	2.41	101.2
4.30	93.4	4.01	101.9
6.89	78.7	6.42	94.4
8.61	84.2	8.02	98.4

The findings from Table 7.1 suggest that relatively high anode potentials (i.e. >1.2 V) would lead to lower dissolution current efficiencies, especially in the case of low-sulfur nickel. To confirm this hypothesis, anode current efficiencies measured from potentiostatic experiments conducted at potentials in the active and transpassive regions of the polarisation plots were compared. The measured values, which are summarised in Table 7.2, clearly indicated that low-sulfur and sulfur-activated nickel dissolved with higher current efficiencies in the active region compared to the transpassive region. These results confirm that other reactions occur during transpassive dissolution.

In certain cases in Tables 7.1 and 7.2, anode current efficiencies above 100% are observed which exceed the error ( $\pm 0.8\%$ ), indicating that the experimental mass loss is greater than that expected based on the charge passed. This is especially observed when sulfur-activated nickel pellets are employed. This "anomalous dissolution" has occasionally been encountered in anodic dissolution literature [125,265,266]. One possible explanation for this effect is anode disintegration where metallic fines are detached from the electrode in an essentially non-electrochemical process due to metal undercutting. Such metallic residues have been reported for anodes dissolved in nickel electrolytes [147, 222, 262, 265].

To conclude, polarisation and chronopotentiometric data confirmed that sulfur-

Table 7.2: Summary of anodic current efficiencies for dissolution of two types of nickel anodes at various anode potentials selected from the active and transpassive regions. Total charge passed was 43.77 C

Dissolution region	P-pellet anode		S-pellet anode	
	Potential	Current efficiency	Potential	Current efficiency
	(V)	(%)	(V)	(%)
Active	-0.01	96.7	-0.08	113.7
	0.00	104.5		
Transpassive	+1.20	89.9	+1.19	103.4
	+1.25	92.9		

activated and low-sulfur nickel pellets will dissolve in the active and transpassive regions, respectively, in the electroforming bath. A study of current efficiencies from galvanostatic and potentiostatic experiments showed values close to 100% for the dissolution of both low-sulfur and sulfur-activated nickel in the active region. In contrast, for transpassive dissolution of low-sulfur anodes, current efficiencies were typically of the order of 79-100% depending on the current density.

It is possible to employ low-sulfur anodes in sulfamate solutions, but there are some issues that must be taken into consideration. Firstly, the anode potential will be significantly higher than that for sulfur-activated Ni anodes which would lead to a substantial increase in cell potential and therefore energy consumption. Prior research [134, 144] has demonstrated that sulfur-activated anodes can reduce energy consumption by 5-30%, depending on the current density and other process conditions. Secondly, side reactions occur during transpassive dissolution, such as, water and sulfamate oxidation [125, 127–130]. These cause additional uncertainties in the process [55, 138, 260], the most important of which is the production of sulfamate decomposition products from sulfamate oxidation which can perturb the electroforming process [125, 128, 130].

## 7.6 Anodic oxidation products in nickel sulfamate solution

The relatively high dissolution potential and low current efficiency of low-sulfur nickel in sulfamate electrolytes prompted an investigation to detect decomposition products formed from oxidation of sulfamate ions at the anode. These products typically give rise to broad absorption bands in the UV-Vis spectra of sulfamate electrolytes at a wavelength of about 245 nm [127–130]. An example of such a UV-Vis spectra is shown in the Figure 7.9 measured by Nakano et al. [130] for decomposition products formed after electrolysis with low-sulfur nickel and Pt anodes at various anode current densities. Each UV spectrum was evaluated from the difference of the electrolyte absorbance before and after electrolysis. Although other studies have reported the presence of sulfamate decomposition products in electrolysed sulfamate baths with insoluble anodes by UV-Vis analysis [127–129], this [130] is one of only two studies [128, 130] that have done so in sulfamate electrolytes containing nickel ions and with a Ni anode which is more applicable to electroforming.

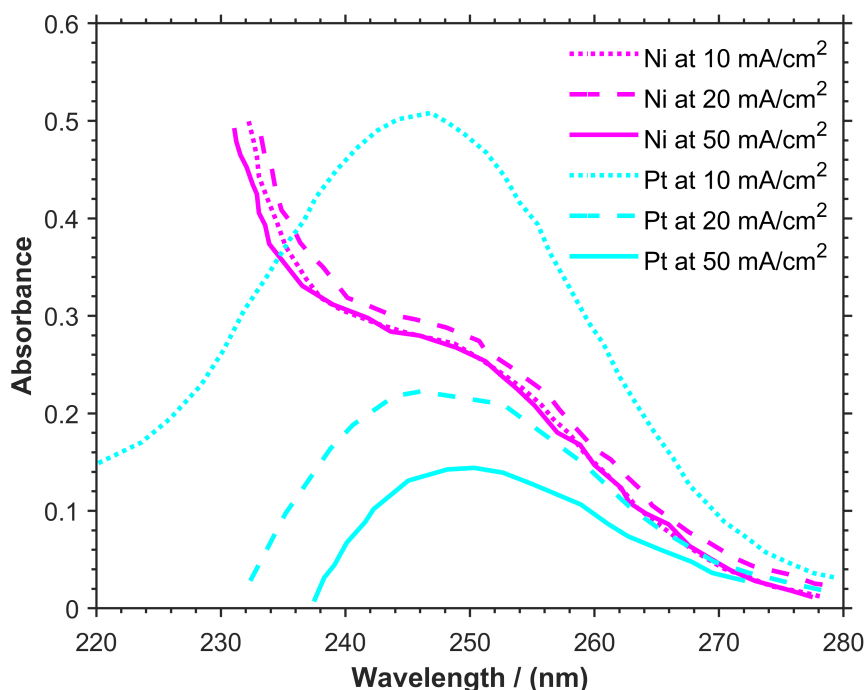


Figure 7.9: UV absorption spectra of the solutions electrolysed at various anode current densities for Pt and Ni electrodes. The base electrolyte comprised of 1 M  $\text{Ni}(\text{SO}_3\text{NH}_2)_2 \cdot 4\text{H}_2\text{O}$  only at pH 4 and 50 °C. Adapted from [130]

The following observations can be made from Figure 7.9 for current densities of 10-50 mA cm<sup>-2</sup>:

1. The newly generated products at a Pt electrode gave rise to absorbance peaks around 245 nm in agreement with previous studies [127–129],
2. The newly generated products at a Ni electrode gave rise to an absorbance "shoulder" rather than a peak which suggests that the products generated from sulfamate oxidation at the Ni electrode might differ from those generated at a Pt electrode.
3. The absorbance (concentration) of the product generated at a Pt electrode decreased as the anode current density was increased whereas that of the species formed at the Ni electrode changed little with increase in current density.

From the data reported by Nakano et al. [130], it is clear that the nature of the sulfamate decomposition product at a Ni electrode is largely unresolved and requires further investigation because it does not show similar spectra to those previously reported for products formed at an insoluble anode which have been extensively studied [127–129]. Therefore, before considering how sulfamate decomposition products affect the deposition reaction, the following inquiries were addressed: (i) What conditions lead to the formation of sulfamate decomposition products? and (ii) Are products formed at a Ni electrode different from those formed at a Pt electrode? The inquiries were investigated under conditions which are representative of actual electroforming processes, which have a more complex bath chemistry compared to those used in earlier studies [127–130]. Additionally, a platinum wire was used to represent an insoluble anode and was used as a baseline for comparison because there is more information on the nature of the decomposition products formed at inert anodes (i.e. Pt or C).

### **7.6.1 Effect of isolation of the anode**

Products formed from sulfamate ion oxidation at the anode are investigated by using UV-Vis analysis to monitor chemical changes in the electrolyte. Since the purpose of

this section is to study the formation of sulfamate decomposition products under conditions which are representative of actual electroforming processes where the cathode and anode are not separated, an initial study was carried out to confirm that any changes in the electrolyte chemistry, observed from the UV-Vis spectra, were indeed caused by the anodic reaction.

A Ni P-pellet was dissolved in nickel sulfamate solution at  $25 \text{ mA cm}^{-2}$  by passing different quantities of charge (250 and 500 C). This current density was selected because it lies within the current density range where decomposition products were formed at a Ni electrode, as reported by Nakano et al. [130]. In some cases, a porous fritted glass tube was used to separate the anode from the cathode and to prevent mixing of the anolyte with the solution in the cathode compartment. The UV-Vis absorption spectra of the catholyte was taken before and after electrolysis and the results are shown in Figure 7.10.

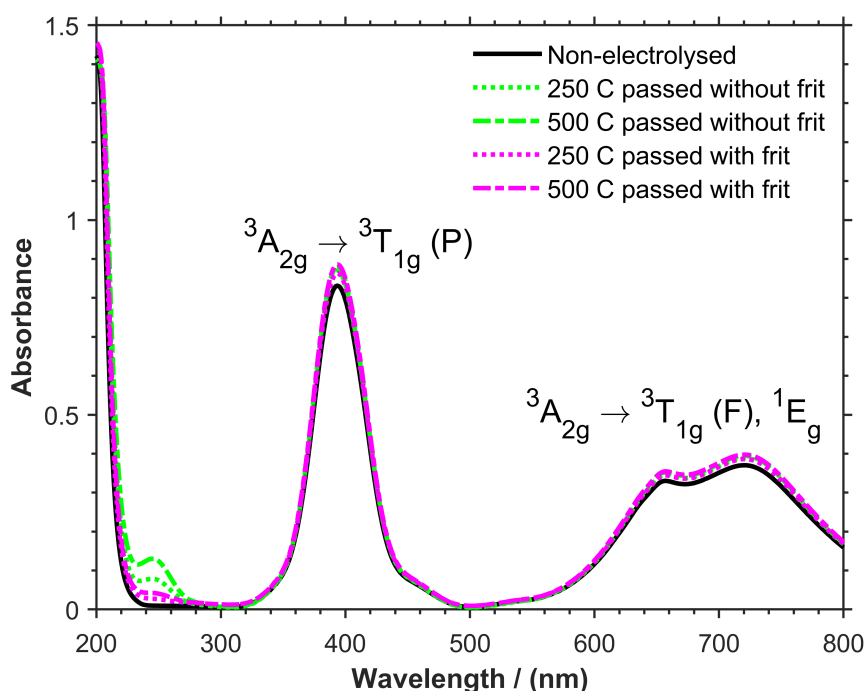


Figure 7.10: The UV-Vis spectra for catholyte samples electrolysed with a P-pellet anode placed within a fritted tube before and after charges of 250 C and 500 C were passed at an anodic current density of  $25 \text{ mA cm}^{-2}$ .

Understanding the UV-Vis spectra of the non-electrolysed sample is crucial before turning to the spectra of the electrolysed samples. The UV-Vis spectrum of a

fresh (non-electrolysed) nickel sulfamate sample (black line, Figure 7.10) shows two major absorption bands in the 300-800 nm range which predominantly correspond to uncomplexed  $\text{Ni}^{2+}$ ; identical spectra have also been measured in several types of aqueous nickel solutions [267]. As a first row transition metal, the electronic absorption spectra of  $\text{Ni}^{2+}$  can be readily interpreted using ligand field theory [268]. Six water ligands are present in the first coordination shell of aqueous  $\text{Ni}^{2+}$ , i.e.,  $[\text{Ni}(\text{H}_2\text{O})_6]^{2+}$ , which has a  $3d^8$  valence configuration and an octahedral structure. The ground state ( ${}^3A_{2g}$ ) has unpaired, spin-aligned valence electrons in two singly occupied  $e_g$  orbitals, while the three highest occupied orbitals all have  $t_{2g}$  symmetry. However, even little octahedral geometry deviations have a significant impact on these orbitals [269]. Therefore, the ground state ( ${}^3A_{2g}$ ) of  $\text{Ni}^{2+}$  in an octahedral field will have three major spin-allowed transitions [270]: (1)  ${}^3A_{2g}$  to  ${}^3T_{2g}$  transition located at about 1100 nm (not recorded); (2)  ${}^3A_{2g}$  to  ${}^3T_{1g}$  transition in the 800-520 nm range; and (3)  ${}^3A_{2g}$  to  ${}^3T_{1g}$  (P) transition in the 500-320 nm range. These transition bands have been marked in Figure 7.10. The absorption band in the 800-520 nm range is split with a peak at 722 nm and a shoulder at 658 nm. This is because the spin-orbit coupling mixes with the  ${}^3T_{1g}(F)$  and  ${}^1E_g$  states. It is unclear what the source is for the continuous absorbance band around 215 nm as these have not been allocated any specific electronic transition in the literature [267].

The UV-Vis spectra of electrolysed samples in Figure 7.10 maintain the absorption bands at 400 nm, 640 nm, and 730 nm with slightly higher absorbances compared to those of the fresh sample. According to the Beer-Lambert Law [224], spectral absorbance is directly proportional to concentration. Therefore, it follows that the increase in absorbance at 400 nm, 640 nm, and 730 nm reflects an increase in  $\text{Ni}^{2+}$  concentration after electrolysis. This finding could be attributed to water evaporation which occurs during electrolysis at 45 °C.

In addition to the absorbance bands at 400 nm, 640 nm, and 730 nm, the spectrum of a catholyte sample electrolysed without isolating the anode showed a clear absorbance peak at 245 nm which significantly increased when more charge was passed. This peak could be assigned to new species formed during electrolysis. When the anode was separated, the spectrum of the electrolysed sample showed a

very weak absorbance band at 245 nm irrespective of the amount of charge passed.

The observations mentioned above could be rationalised by considering that processes at the anode generate products that linger in the catholyte and display an absorbance peak at 245 nm in the UV-Vis spectra of electrolysed catholyte samples. When these products are prevented from mixing with the catholyte by using separate anode and cathode compartments, this peak nearly disappears. The faint absorbance band at 245 nm observed when separate anode and cathode compartments are used could be attributed to some anolyte leakage into the catholyte through the frit. Hence, these findings confirm that the species responsible for the peak at 245 nm is generated in an anodic process.

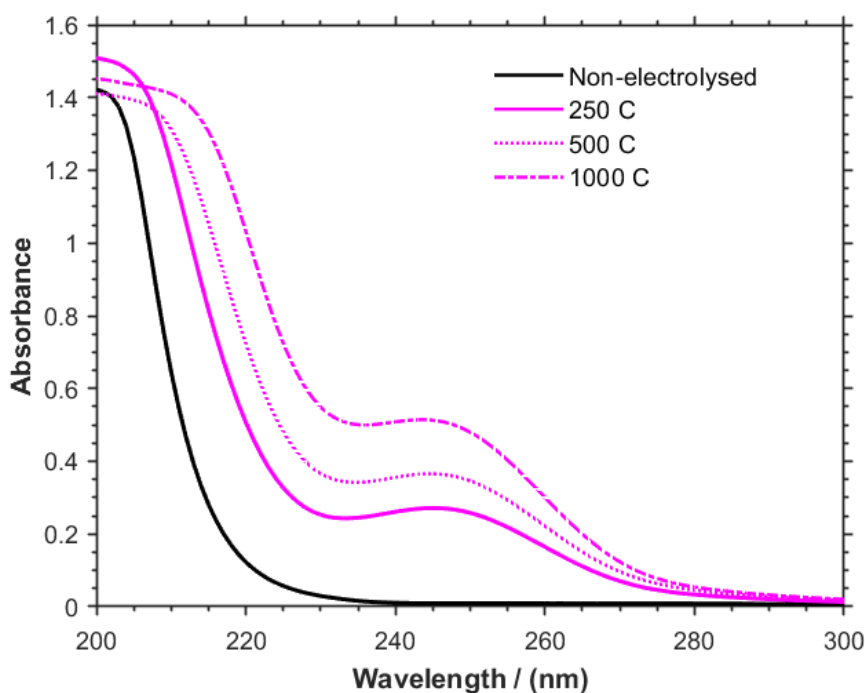


Figure 7.11: The UV-Vis spectra for the P-pellet before and after charges of 250, 500, and 1000 C were passed at an anode current density of  $25 \text{ mA cm}^{-2}$ .

Figure 7.11 shows the UV-Vis spectra of nickel sulfamate in the 200-300 nm range after galvanostatic dissolution with a P-pellet anode at a fixed current density of  $25 \text{ mA/cm}^2$  for varying amounts of charge that were passed. These experiments were performed in a smaller undivided cell. The results indicate that the absorbance peak at 245 nm increases as the charge increases. Based on Faraday's Law which indicates

that the mass of an electrochemically produced substance is directly proportional to the charge passed, the correlation between the absorbance and the amount of charge passed clearly signifies an electrochemical origin for the new species generated at the low-sulfur Ni anode.

The UV-Vis spectrum for the electrolysis product of a Ni P-pellet obtained in these experiments was more similar to that of the Pt electrode than it was to that of Ni electrode obtained by Nakano et al. [130] under similar conditions, as shown in Figure 7.12. Similar UV-Vis spectra to those obtained from these experiments (Figures 7.10 and 7.11) have also been measured by earlier researchers in sulfamate-based solutions electrolysed with Pt [127–129] and passive nickel [128, 261] anodes. This suggests that similar electrolysis products could be produced at low-sulfur Ni and Pt electrodes.

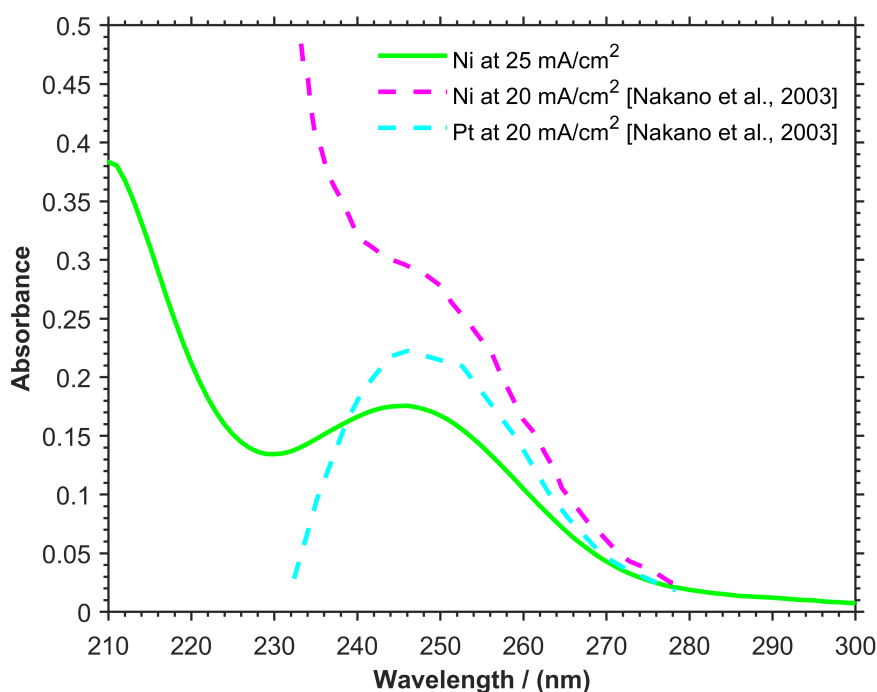


Figure 7.12: UV-spectra of the electrolysis product(s) obtained at a Ni P-pellet after 0.6 Ah/L compared to those obtained by Nakano et al. [130] after 0.5 Ah/L

The assignment of the 245nm peak shown in Figures 7.10 to 7.12 is contentious, and has been attributed to the absorption of sulfonated species based on the results of infrared spectroscopy and differential pulse polarography [127–129]. Although, many scientists acknowledge this species is typically generated from anodes



with sufficiently high potentials to oxidise sulfamate ions, the identity of the species remains a subject of debate. Because the majority of studies [127–129] concentrated on identifying the oxidation products of sulfamate ions, Ni(II)-free sulfamate baths with inert anodes were employed to prevent interference from nickel ions. While these studies were useful in elucidating the pathway for the decomposition of sulfamate ions and identifying a plethora oxidation products, the conditions used were not typical of the nickel electroforming process, which employ soluble anodes and a more complex bath chemistry. Therefore, experiments were carried out to identify conditions that lead to the production of these anode products during nickel electroforming.

## 7.6.2 Effect of anode material and current density

The findings so far have confirmed that the electrolysis product, that typically gave rise to a UV-Vis peak at 245 nm, is produced from the anode in an electrochemical reaction which is most likely the oxidation of sulfamate ions. Further experiments were performed to investigate the impact of the anode material and current density on the formation of sulfamate decomposition products. The aim of these experiments was to identify conditions the led to their formation. Three different anode materials were used: sulfur-activated Ni (S-pellet), low-sulfur Ni (P-pellet), and Pt wire. A fresh nickel sulfamate sample was electrolysed in a small undivided cell (with 60 ml electrolyte volume) by applying a constant anode current density of 5-25 mA/cm<sup>2</sup> and passing a charge of 500 C. To provide references for discussing the results, anode potentials and current efficiencies measured from the experiments are summarised in Table 7.3.

Table 7.3: Summary of anodic/cathodic current efficiencies (CE) and anode potentials for the dissolution of two types of nickel anodes and the platinum anode at various anode current densities. Total charge passed was 500 C. For the S-pellet and P-pellet, dissolution occurred in the active and transpassive regions, respectively.

Anode current density (mA cm <sup>-2</sup> )	S-pellet			P-pellet			Pt		
	Anode potential (V)	Anode CE (%)	Cathode CE (%)	Anode potential (V)	Anode CE (%)	Cathode CE (%)	Anode potential (V)	Anode CE (%)	Cathode CE (%)
5	-0.04 ± 0.02	98.0	98.4	1.20 ± 0.16	82.3	95.44	1.99 ± 0.04	-	87.1
10	-0.05 ± 0.01	99.6	98.5	1.44 ± 0.01	64.1	95.9	2.05 ± 0.05	-	91.5
25	-0.01 ± 0.01	97.4	99.3	1.42 ± 0.01	49.3	95.9	2.11 ± 0.05	-	93.9

Figure 7.13 shows the spectra of nickel sulfamate samples before and after electrolysis with an S-pellet anode at applied current densities of 5 and 25 mA/cm<sup>2</sup>. The absorption spectra of the electrolysed samples in the wavelength region below 300 nm are virtually identical to that of a non-electrolysed sample signifying the absence of the sulfamate decomposition product. Typically, the anode potential did not exceed -0.06 V vs SCE for these current densities and current efficiencies measured were 97.4-99.6% (Table 7.3). This implied that the low dissolution potential of the S-pellet was not sufficient enough to oxidise sulfamate ions. This is in good agreement with prior studies [130] which found that samples electrolysed with the S-pellet did not give the peak for potentials below 0.2 V vs SCE.

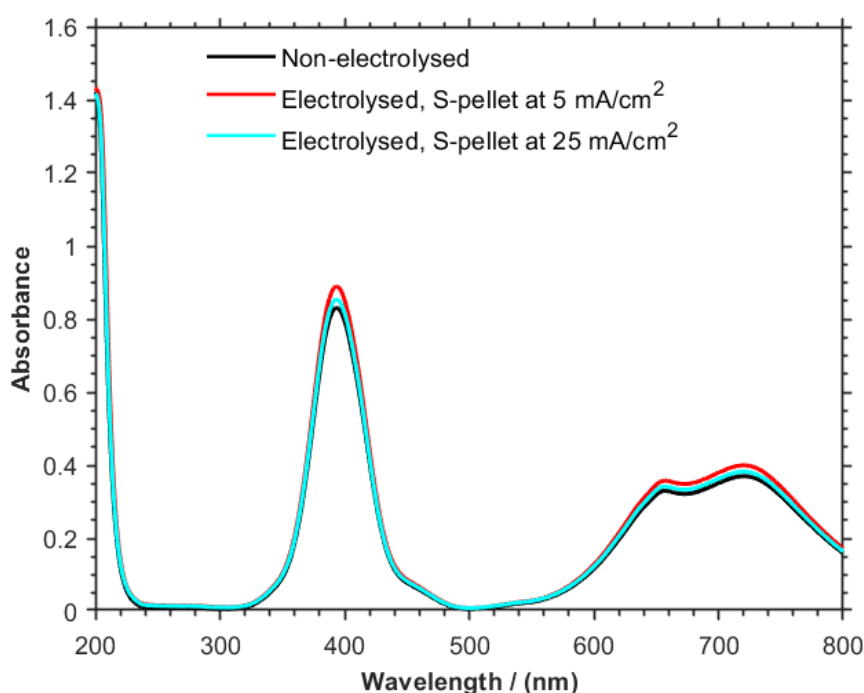


Figure 7.13: The UV-Vis spectra for the S-pellet before and after an anodic charge of 500 C was passed at current densities of 5, 10, and 25 mA cm<sup>-2</sup>.

In contrast, Figure 7.14 shows the spectra of nickel sulfamate samples before and after electrolysis with (a) a P-pellet and (b) a Pt wire where the 245 nm peak pertaining to the sulfamate decomposition product was visible at all applied current densities. In this instance, anode potential of the P-pellet and Pt attain values of the order of 1.25-1.4 V and 2.0-2.5 V (Table 7.3), respectively, which are sufficient enough to oxidise sulfamate ions [130].

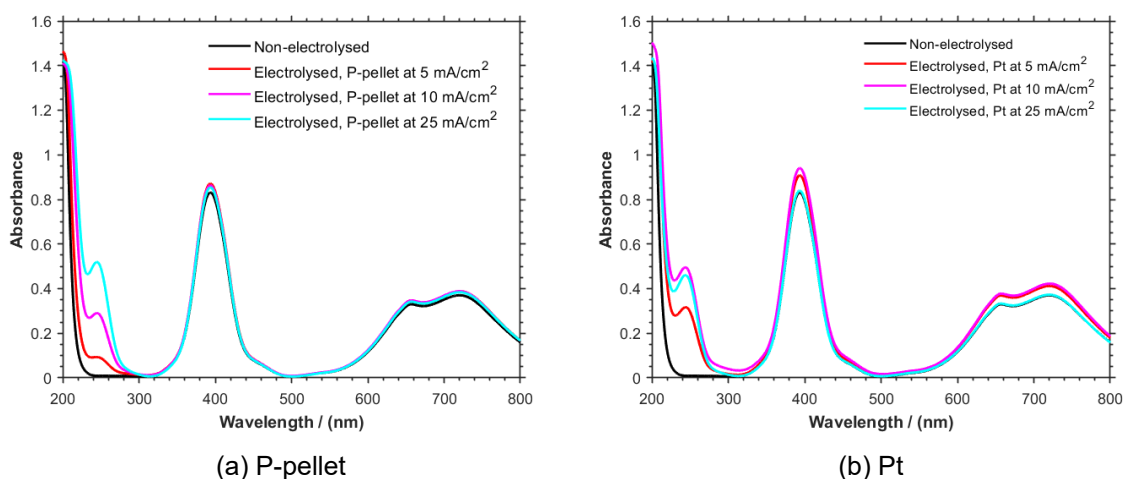


Figure 7.14: The UV-Vis spectra for a solution employing a P-pellet (a) and a Pt (b) before and after an anodic charge of 500 C was passed at current densities of 5, 10, and 25 mA cm<sup>-2</sup>.

As the current density is raised from 5 to 25 mA/cm<sup>2</sup>, it is clear from Figure 7.14a that the absorbance of the 245 nm peak increases which indicates an increase in the concentration of the decomposition product formed at the P-pellet, according to Beer-Lambert's law [224]. This can be correlated to the decrease in anode current efficiency values from 82.3 to 49.3% (Table 7.3) which could be attributed to an increase in the anode potential caused by a rise in current density.

Figure 7.14b also demonstrated that as the anode current density was increased from 5 to 10 mA/cm<sup>2</sup>, the absorbance at 245 nm, which corresponds to the concentration of the anodized product at a Pt wire, increased. The absorbance did, however, slightly decrease when the current density was increased from 10 to 25 mA/cm<sup>2</sup>. This agrees with the findings by Nakano et al [130] who identified that applying higher current densities could decrease the concentration of Pt product absorbing at 245 nm (Figure 7.9). This phenomenon could be explained by the decomposition of sulfamate ions to produce other products alongside the species absorbing at 245 nm. The increase in potential could make competing reactions from sulfamate ions more energetically possible and thereby, decrease the yield of the product absorbing at 245 nm [127, 129, 135].

Comparing Figures 7.14 a and b, it is observed that the concentration of the

oxidation product generated at a Pt electrode is greater than that generated at a Ni electrode for anode current densities between 5 and 10 mA/cm<sup>2</sup>. The higher rates of sulfamate ion oxidation on Pt compared to soluble Ni anodes could be explained by the higher operating potentials of Pt which enable electrochemical reactions that could not take place on nickel.

Conclusions from this section could be summarised as follows: (i) the use of sulfur-activated anodes are mandatory if the formation of sulfamate decomposition products is to be avoided under typical electroforming conditions, and (ii) if low-sulfur or inert anodes are used, sulfamate oxidation will invariably occur, but this may not in itself be an issue depending on the application. Some of the reported effects of this decomposition product on deposit characteristics could be regarded as favourable [125, 128, 130, 181], such as the production of deposits with decreased residual stress, enhanced lustre, finer grain sizes, and increased hardness. There was one caveat, however: the deposits frequently possess higher sulfur contents which could make their use undesirable for aerospace electroforming applications where sulphur embrittlement at high temperatures would result [49]. Nevertheless, anodes that could oxidise sulfamate ions have been reported advantageous for use in a specific procedure for electrodepositing Ni layers for semiconductor packages since acceptable deposition only took place when such anodes were used [261]. Low sulphur anodes are therefore recommended in situations where sulfamate breakdown products are desired for nickel electrodeposition. One could argue that using this product created "in situ" to obtain specific deposit features is preferable to manually adding bath additives, which deplete over time and must be replenished to maintain bath composition and deposit quality [271, 272]. Additionally, sulfur-activated nickel produce more anode residues than low-sulfur nickel and, may require regular cleaning and activation to maintain a low anode potential [144, 264]. Industrial best practice may therefore favour low-sulfur materials in many instances.

### 7.6.3 Nature of the sulfamate decomposition product

The specific identities of sulfamate oxidation products at Pt and Ni electrodes remain unclear. However, with the results from UV-Vis analysis [127, 128], mass and IR spectroscopic analysis [128, 129], and gas chromatography (GC) analysis [135], a combination of series and parallel reactions involved in the sulfamate oxidation process have been proposed in literature and are summarised in Figure 7.15. These reactions are discussed in the forthcoming paragraphs using Figure 7.15 as a reference.

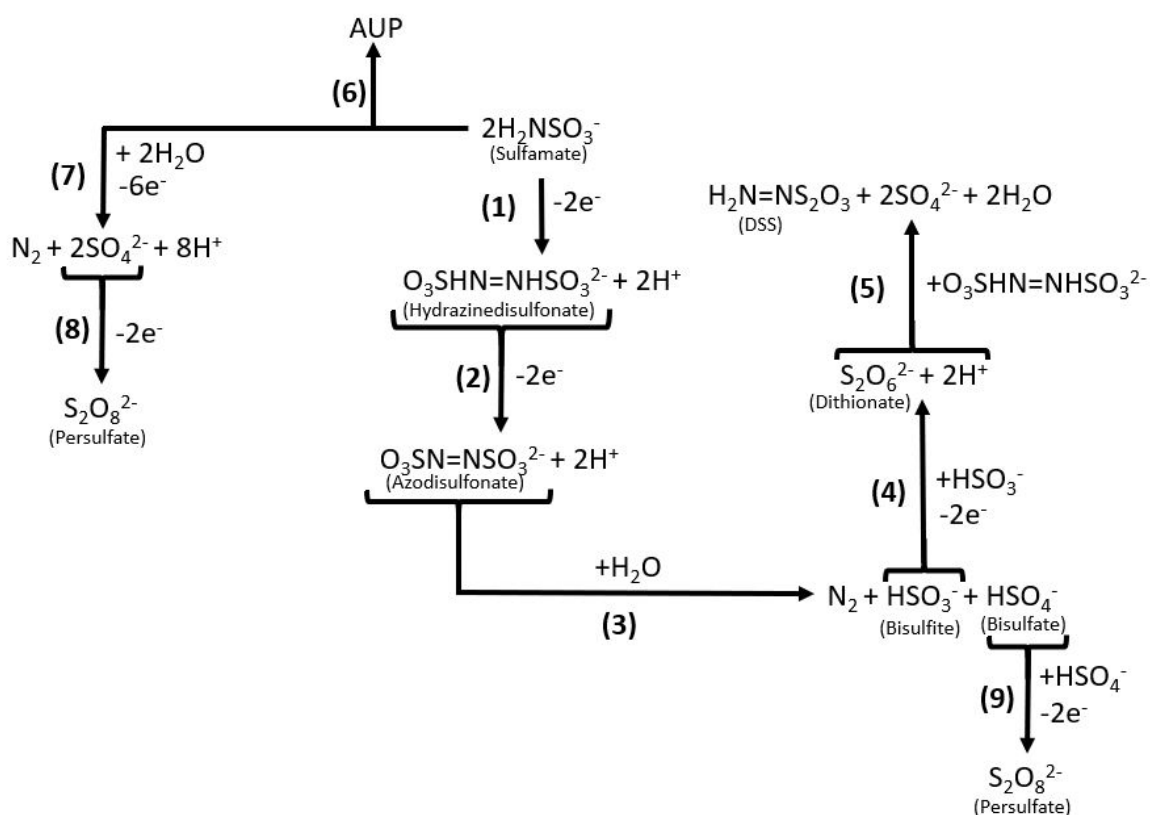


Figure 7.15: Diagram of electrochemical processes involved in oxidation of sulfamate ions at Pt and low-sulfur Ni anodes.

Greene [127] suggested that the oxidation of sulfamate ions initially proceeds according to reaction 1 (Figure 7.15) through the formation of hydrazinedisulfonate (HDS), based on UV analysis of nickel sulfamate electrolysed with inert Pt and C anodes. However, HDS is only formed as an intermediate and is readily oxidised to azodisulfonate (ADS) via reaction 2. ADS was found to produce a characteristic peak at 245 nm in the UV spectra. Gas chromatography was used by Novikov et al. [135] to

examine the oxidation of sulfamate ions at a pure nickel anode. It was proposed that the initial decrease in anode current efficiency from 100% at potentials greater than +1.06 V vs SCE was solely due to the oxidation of sulfamate ions to ADS via reactions 1 and 2 because no gas ( $O_2$  or  $N_2$ ) had been detected.

Azodisulfonate is unstable and can hydrolyse to produce nitrogen gas, bisulfite ions, and bisulfate ions via reaction 3 [127]. At sufficiently high anode potentials (or current densities), it is also suggested that sulfamate ions are oxidised to form nitrogen gas and sulfate ions via reaction 7 [127]. The sulfate ions produced could also be further oxidised to persulfate ions via reaction 8 [127]. Novikov et al. [135] detected nitrogen gas by GC at potentials above +1.36 V vs SCE. They also found that the rate of production of nitrogen gas increased as the anode potential was made more positive which support the proposition made by Greene [127]. Therefore, the steady-state concentration of ADS in solution depends on the relative rates of reactions 1, 2, 3, and 7 (at high polarisations). According to Greene [127], the amount of ADS in electrolysed nickel sulfamate solutions ranges between 0.5 and 5 mM, depending on the circumstances of the experiment.

A follow-up study by Jiazhu et al. [128] confirmed products from the mechanism proposed by Greene [127] but identified an additional sulfamate decomposition product denoted as AUP (reaction 6), a hitherto unknown substance. Similar to ADS, AUP also produced a UV peak at 245 nm and decreased deposit stress. The researchers also discovered the presence of dithionate ions, which could result from reaction 4 [128].

Zhang and Park [129] discovered an unidentified species that continued to exhibit a UV absorption band at 245 nm even after the elimination of ADS, HDS, dithionate, and sulfite. By using mass spectrometry, this species was tentatively identified as diimide S-sulfonate (DSS). It was suggested that reaction 5 produced DSS from dithionate ions and HDS [129].

Despite being discovered using chemical analysis and IR spectroscopy [128, 129], dithionate ions and sulfate ions do not show significant UV absorption. As a result, UV-Vis spectroscopy cannot characterize them. Contrarily, persulfate ions and

sulfite ions both display a continuous increase in absorption below 350 nm, illustrated in Figure 7.16, which is in good agreement with observations made by Greene [127].

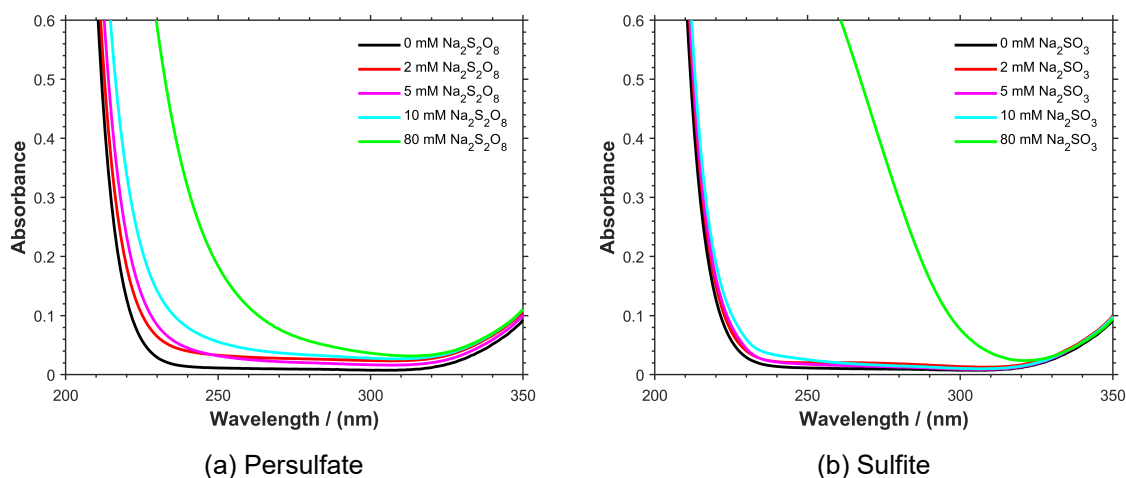


Figure 7.16: UV-vis spectra of a non-electrolysed nickel sulfamate bath with different concentrations of (a) persulfate ions and (b) sulfite ions.

There is some evidence of the production of sulfite or persulfate ions at Pt and low-sulfur Ni anodes from Figure 7.17 as well as Figure 7.11 where the continuous absorbance at 230 nm increases with charge. Additionally, this can only be seen when the peak corresponding to ADS is visible. These results are in line with the sulfamate oxidation reaction process shown in Figure 7.15 which indicates that ADS could result in the production of bisulfite (or sulfite) ions and persulfate ions via reactions 3 and 9, respectively.

Reaction 8 (Figure 7.15) could also produce persulfate ions. However, potentials more positive than the equilibrium potential of +1.75 V versus SCE (standard electrode potential,  $U^0 = 2.0$  V [273]) are needed to produce persulfate ions from sulfamate or bisulfate ions. Low-sulphur nickel electrodes did not attain potentials greater than 1.5 V even with the application of a high current density of 25 mA/cm<sup>2</sup> as shown in Figure 7.18. The formation of persulfate ions at the Ni anode is therefore improbable, and the continuous absorbance at 230 nm is most likely due to the formation of bisulfite ions. In contrast, Pt potentials frequently exceeded 2.0 V vs SCE (Figure 7.18 and Table 7.3), and it is possible that persulfate ions were generated in addition to bisulfite ions under these conditions.

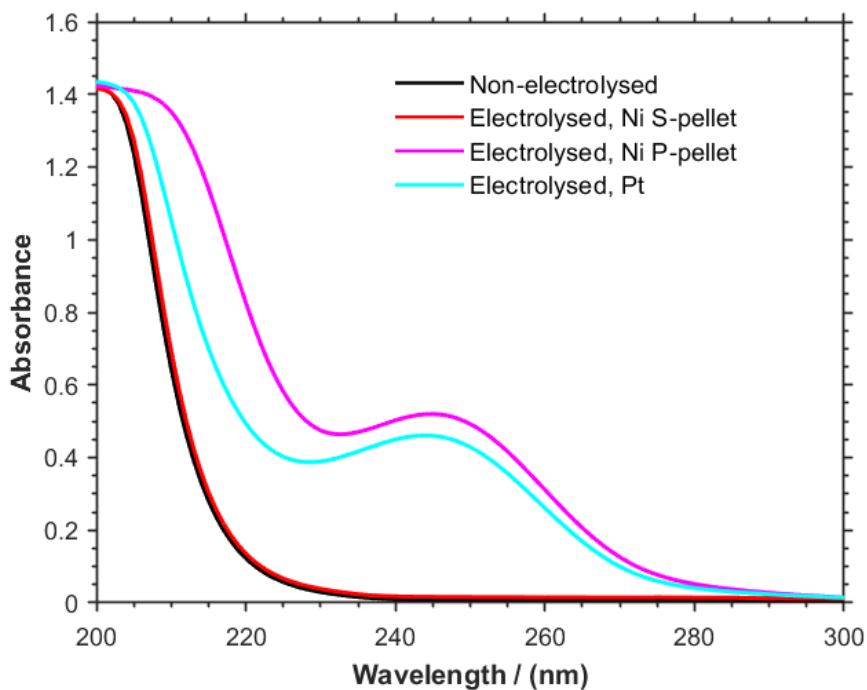


Figure 7.17: The UV-Vis spectra for various anode materials before and after a charge of 500 C was passed at an anode current density of  $25 \text{ mA cm}^{-2}$ .

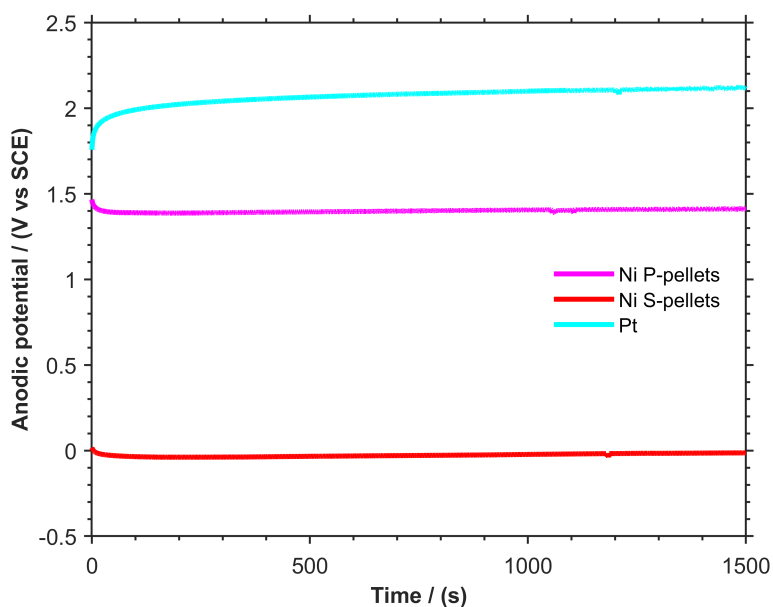


Figure 7.18: Anode potential as a function of time at nickel and Pt anodes for an anode current density of  $25 \text{ mA cm}^{-2}$ . The Ni P-pellet shows a transition from active to transpassive dissolution after 10 seconds.



In summary, researchers [127–129] have identified three sulfamate decomposition products (azodisulfonate (ADS), diimide S-sulfonate (DSS), and AUP) that could give rise to a UV peak at 245 nm. The presence of this peak could be correlated to reduced stress levels in nickel deposits [125, 128, 173, 181]. Klingenmaier [125] reported that the oxidation product at a Pt electrode changed the deposits from tensilely stressed to compressively stressed ones with extremely high levels of sulfur (0.026 wt%). This will cause the deposit to become brittle and deteriorate on heating to 240 °C [55]. As mentioned earlier, Greene [127] determined the product of the anodic reaction at a Pt electrode to be azodisulfonate. Therefore, the production of ADS at a nickel anode is not ideal for the production of electroforms that are used in high temperature applications, such as in the aerospace industry.

While the precise identification of the decomposition products was not the focus of investigations in this chapter, it was important to ascertain whether ADS is formed at low-sulfur nickel anodes because this will influence their use in electroforming for specific applications where a negligible sulfur content is mandatory.

Watson [181] claimed that the substance produced at the Pt electrode increases the sulfur content of the deposits while that produced at the nickel electrode does not. This led to the argument that different substances were produced at Pt and Ni electrodes. However, data to substantiate these claims is limited. Klingenmaier [125] demonstrated that nickel deposits plated from sulfamate baths at a cathode current density of 81 mA/cm<sup>2</sup> using depolarised nickel anodes had significantly less sulfur compared to those from solutions electrolysed using a platinised titanium anode. However, this in itself cannot be considered conclusive because the dissolution current efficiencies were found to be above 99% and one could argue that much lower quantities of the decomposition product were generated at the Ni electrode compared to the inert electrode. The production of ADS at a Ni electrode is therefore uncertain.

The UV-Vis spectra of the sulfamate decomposition products produced at Pt and low-sulfur nickel anodes in this chapter are compared to that of azodisulfonate measured by Greene [127] in Figure 7.19. To enable comparison of the spectral peak shapes and positions, the absorbance of each spectral ( $A_i$ ) at a given wavelength has been rescaled based on the maximal value of the peak,  $A_{max}$ , and minimal value below

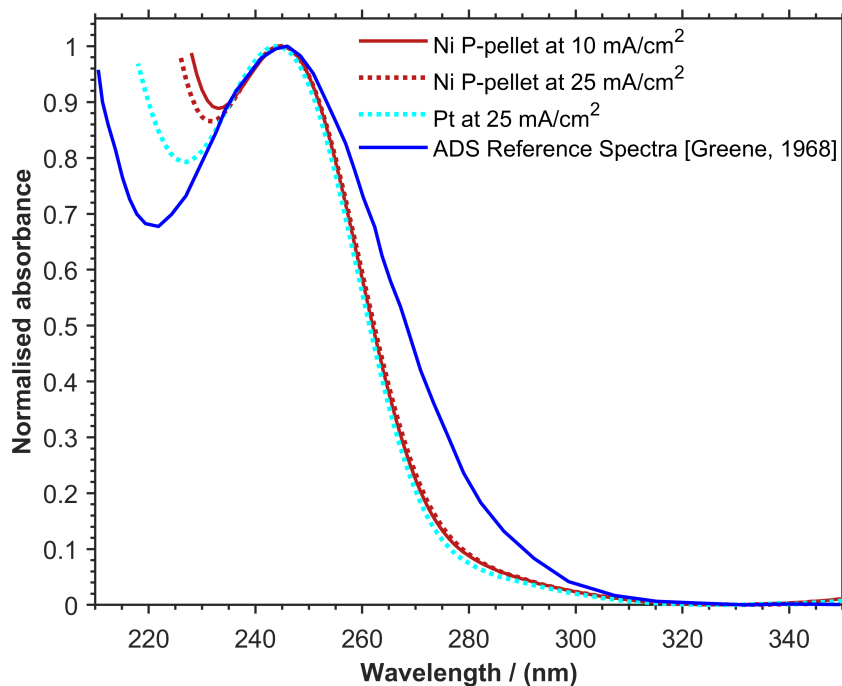


Figure 7.19: Comparison of the UV-Vis reference spectrum of azodisulfonate [127] with UV absorption peaks observed in different experiments employing low-sulfur (P-pellets) and Pt anodes. The spectra have been corrected to the non-electrolysed nickel sulfamate electrolyte.

the peak,  $A_{min}$ , using Equation 7.3 where  $y_i$  is the normalised absorbance.

$$y_i = \frac{A_i - A_{min}}{A_{max} - A_{min}} \quad (7.3)$$

There is strong indication from Figure 7.19 that ADS could be one of the end products of sulfamate oxidation at Pt and low-sulfur nickel anodes in this thesis which is based on the good agreement between the peak positions and shapes of the ADS and sulfamate decomposition product spectra. This, however, cannot be regarded as conclusive because AUP and DSS which have also been noted to create UV peaks at 245 cannot be disregarded.

It has been reported by researchers [127–129, 173] that compared to other oxidation products that give rise to UV peaks at 245 nm, ADS is only partially stable and can hydrolyse in water via Equation 7.4 when the solution is allowed to stand for several

days or when the solution is heated and stirred at 65 °C for an hour. Therefore, to provide further support for the assignment in Figure 7.19, experiments were carried out to investigate the thermal stability of the sulfamate decomposition products generated at low-sulfur Ni (P-pellet) and Pt anodes; a fixed anode current density of 25 mA/cm<sup>2</sup> was applied because this led to the production of comparable concentrations of the anode products as shown in Figure 7.17. The electrolysed solutions were heated and stirred at 67 °C for 25 hours to assess changes in the absorbance of the 245 nm peak.

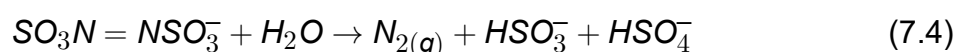


Figure 7.20 shows the spectra changes as a function of heating time for two solutions, (a) one electrolysed with a P-pellet and (b) one electrolysed with a Pt wire. Contrary to the spectra below 300 nm, the spectra above 300 nm exhibited little change over the heating duration. The spectra of both electrolysed solutions showed the characteristic peak at 245 nm (solid red line, Figures 7.20 a and b) at time, t = 0 min, i.e. prior to heating at 67 °C. This peak has been assigned to the sulfamate decomposition product. The absorbance of this 245 nm peak in both solutions progressively decreased over the course of heating at 67 °C indicating a decrease in the concentration of the decomposition species.

The results in Figure 7.20 a and b demonstrate that the species produced at the P-pellet and Pt anodes was decomposed by heating and stirring at 67 °C which strongly suggests that ADS is generated at the P-pellet and Pt electrodes as per reports in literature [127]. It appears that in the solution that was electrolysed with a Pt electrode, the rate of hydrolysis of the anode species was considerably faster. Figure 7.20 illustrates this observation more quantitatively by plotting normalised 245 nm absorbances in both solutions against the heating duration. The following Equation was used to normalise the absorbances:

$$y_i = \frac{x_i - x_{min}}{x_{max} - x_{min}} \quad (7.5)$$

where  $y_i$  represents the normalised value,  $x_i$  the absorbance at a given time,  $x_{max}$  and  $x_{min}$  the absorbance values for t = 0 min and t = 1500 min, respectively.

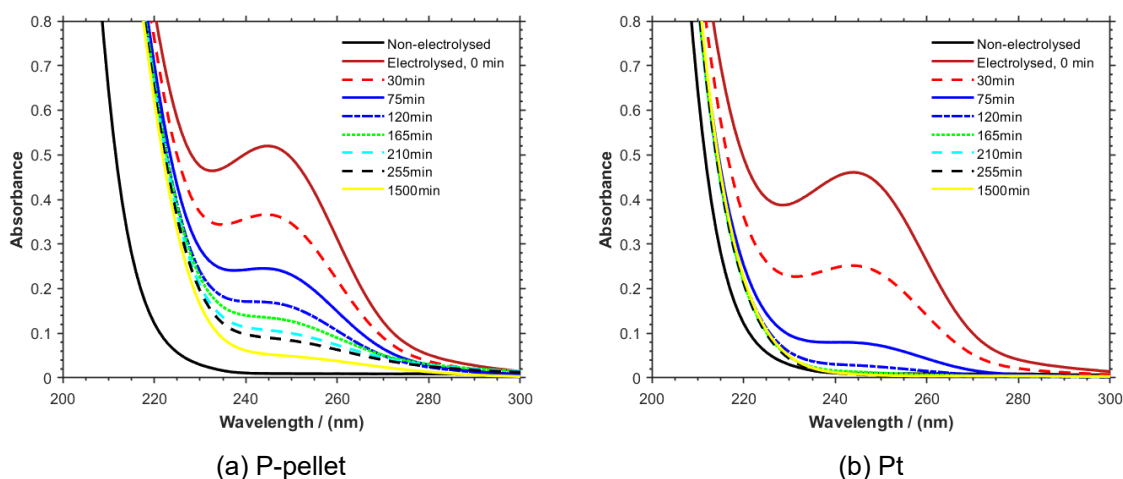


Figure 7.20: Spectra changes as a function of heating time at 67 °C for solutions electrolysed employing P-pellet (a) and Pt (b) anodes. During electrolysis, the anodes were maintained at 25 mA cm<sup>-2</sup> while a total charge of 500 C was passed.

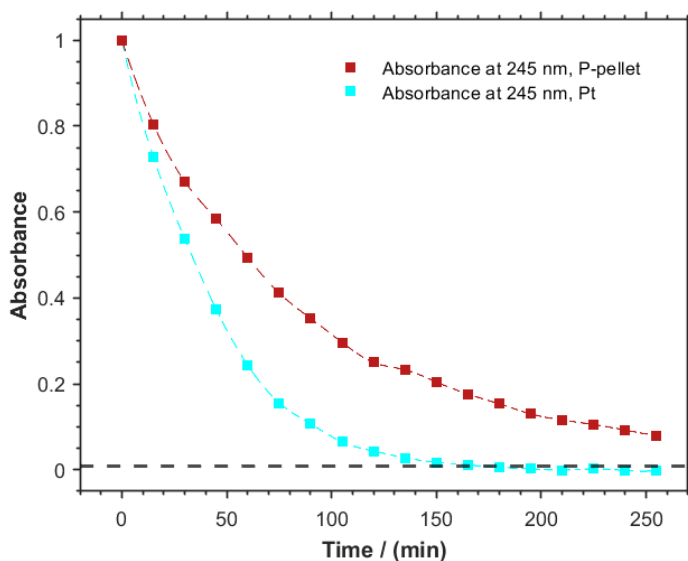


Figure 7.21: The decay in the absorbance of the UV-Vis peak at 245 nm for solutions electrolysed employing P-pellet (red) and Pt (cyan) anodes during heating at 67 °C. The broken black line shows the absorbance at 245 nm of a non-electrolysed sample.

After an hour of heating, the solution electrolysed with a Pt anode had a residual oxidation product proportion of 24% in comparison to 50% noted for the solution that was electrolysed with a low-sulfur Ni pellet (Figure 7.20). It should also be noted that after 150 minutes of heating, the absorbance of the solution electrolysed with a Pt

anode had dropped to a level comparable to that of a non-electrolyzed sample (black broken line, Figure 7.20), which suggested the complete removal of the species absorbing at 245 nm. In contrast, there remains some residual proportion ( $\approx 8\%$ ) of the oxidation species produced at the P-pellet anode, even after a heating duration of 25 hours which could suggest that other substances are produced at low-sulfur nickel and absorb at 245 nm along with ADS.

To quantitatively compare the rates of hydrolysis of the oxidation products generated at low-sulfur Ni and Pt anodes, kinetic parameters for the hydrolysis reaction were compared. The rate law for ADS (assuming this is generated at both soluble and insoluble anodes) hydrolysis by reaction 7.4 is represented by Equation 7.6:

$$v = \frac{[ADS]}{dt} = -k[H_2O]^a[ADS]^b \quad (7.6)$$

where  $v$  is the rate of conversion of ADS ( $\text{mol L}^{-1} \text{min}^{-1}$ ),  $[ADS]$  and  $[H_2O]$  are the concentrations of ADS and water, respectively ( $\text{mol L}^{-1}$ ),  $k$  is the rate constant ( $\text{mol}^{1-a-b} \text{L}^{a+b-1} \text{min}^{-1}$ ), and  $a$  and  $b$  represent the order of the reaction with respect to water and ADS, respectively. Since an excess amount of water is present in the electrolysed solutions and the reaction vessel was sealed to prevent water loss, changes in  $[H_2O]$  could be considered insignificant to the reaction so that  $k[H_2O]^a$  constitutes a new rate constant defined as the apparent rate constant,  $k_{app}$  ( $\text{mol}^{1-b} \text{L}^{b-1} \text{min}^{-1}$ ). The new rate law for ADS hydrolysis can be expressed as:

$$v = \frac{[ADS]}{dt} = -k_{app}[ADS]^b \quad (7.7)$$

The kinetics of ADS hydrolysis was profiled by first assuming a pseudo-first-order model associated with the integrated rate law expressed in Equation 7.8 where the order of the reaction with respect to ADS is 1. The concentration of ADS at the beginning of each hydrolysis experiment and at any time,  $t$ , thereafter are denoted as  $[ADS]_0$  and  $[ADS]_t$ , respectively.

$$\frac{[ADS]_t}{[ADS]_0} = \exp(-k_{app}t) \quad (7.8)$$

According to the Beer-Lambert Law, the spectral absorbance is directly proportional to concentration. Therefore, the absorbance of ADS in the electrolysed solutions at the beginning of the hydrolysis reaction and at any time,  $t$ , thereafter, denoted

by  $A_0$  and  $A_t$ , respectively, were related to  $[ADS]_0$  and  $[ADS]_t$ , respectively, in accordance with Equation 7.9 which could then be substituted in Equation 7.8 to give Equations 7.10 and 7.11.

$$\frac{A_t}{A_0} = \frac{[ADS]_t}{[ADS]_0} \quad (7.9)$$

$$\frac{A_t}{A_0} = \exp(-k_{app}t) \quad (7.10)$$

$$\ln\left(\frac{A_t}{A_0}\right) = -k_{app}t \quad (7.11)$$

Plots of  $\ln\left(\frac{A_t}{A_0}\right)$  against time in accordance with Equation 7.11 are shown in Figure 7.22 which gave straight lines for the products generated at low-sulfur Ni and Pt anodes. This corroborates the initial hypothesis of a pseudo-first-order reaction. Therefore, the hydrolysis of sulfamate decomposition products generated at low-sulfur Ni and Pt anodes exhibit first order kinetics.

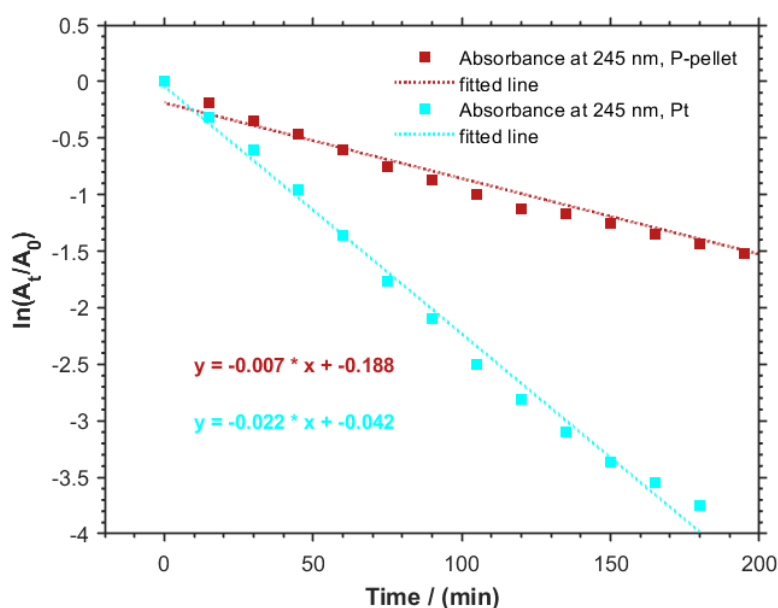


Figure 7.22: Kinetic plots of  $\ln\left(\frac{A_t}{A_0}\right)$  against heating time for ADS hydrolysis in solutions electrolysed with P-pellet and Pt anodes.

Kinetic parameters ( $k_{app}$  and half-life time,  $t_{0.5}$ ) for the hydrolysis reaction involving the oxidation products of the Ni and Pt electrodes could then be determined from the straight line equations shown in Figure 7.22; the values are summarised in

Table 7.4: Kinetic parameters of the hydrolysis reaction involving sulfamate oxidation products generated at different anodes.

	<b>Pt anode</b>	<b>P-pellet</b>
Apparent rate constant, $k_{app}$	0.007 min <sup>-1</sup>	0.022 min <sup>-1</sup>
half-life time, $t_{0.5}$	99 minutes	32 minutes

Table 7.4. It is noted from Table 7.4 that the kinetics of the hydrolysis reaction are different for the oxidation products at the Ni and Pt electrodes which could be attributed to the lower pH measured for the solution electrolysed with the Pt anode compared to that electrolysed with a Ni anode; a low pH favors the hydrolysis of ADS [127].

In conclusion, there are strong indications from the results in this section that, similar to the Pt electrode, ADS is the major sulfamate oxidation product at low-sulfur nickel materials. Additionally, the residual proportion of nickel's oxidation product even after 25 hours of heating suggests that smaller quantities of more thermally stable substances are produced alongside ADS during the oxidation of sulfamate ions at a low-sulfur nickel anode which corroborate the results reported in [127–129].

## **7.7 Impact of the anode process on the electroforming process from sulfamate baths**

As noted earlier, the anode current efficiency is a key determinant of the stability of the electroforming process. Current efficiencies for galvanostatic and potentiostatic dissolution of low-sulfur nickel in nickel sulfamate solution have indicated values less than 100% and the presence of decomposition products in solution resulting from sulfamate ion oxidation has been confirmed. The quality of electroformed nickel deposits in nickel electroforming baths has been known to be significantly impacted by the anodic breakdown products of sulfamate ions [125, 173]. This indicates that the sulfamate decomposition products interact with the cathode surface and may affect the electrochemical aspects (electrode polarisation and current efficiency) of electrodeposition. However, clear information on the influence of the oxidation product build-up on the

electrodeposition behaviour and current efficiency is limited. Therefore, investigations were conducted to study the effects of the anode material on the current efficiency of nickel electrodeposited from an electroforming bath in a broad range of bath ages (Ah/L). Prior to this, a set of experiments were carried out to confirm that the anode oxidation product interacted with the cathode surface by studying its effects on the cathode polarisation curves. It is expected that inquiries along these lines will provide more information about the effects of sulfamate decomposition products on the electrodeposition process and in such a manner, differences in the electrochemical aspects of the electrolyte may be better understood when different anodes are employed.

### **7.7.1 Electrodeposition behaviour of nickel**

As mentioned earlier, an investigation was conducted to confirm that the sulfamate decomposition product interacted with the cathode by measuring cathodic polarisation curves in the absence and presence of the product. The decomposition product was introduced into the electrolyte by dissolving a Ni P-pellet anode at  $25 \text{ mA/cm}^2$  with increasing amounts of charge to increase the concentration of the decomposition product. The change in cathode polarisation as a function of the concentration of the decomposition product is shown in Figure 7.23.

The results in Figure 7.23 indicate that the sulfamate decomposition product decreased the cathode overpotential for nickel electrodeposition at current densities below  $100 \text{ mA/cm}^2$ , i.e., equivalent current densities were achieved at less negative potentials. Above  $100 \text{ mA/cm}^2$ , the anode product polarised nickel electrodeposition, i.e., increased the cathode overpotential. The magnitude of the depolarising and polarising effects increased with an increase in amount of charge passed using the P-pellet which is directly proportional to the concentration of the sulfamate decomposition product in solution.

Based on the discussion in section 7.6.3, the sulfamate decomposition product is expected to be a S-containing compound and therefore shows a similar behaviour to other S-based additives in nickel electrodeposition studies [274]. Thiourea



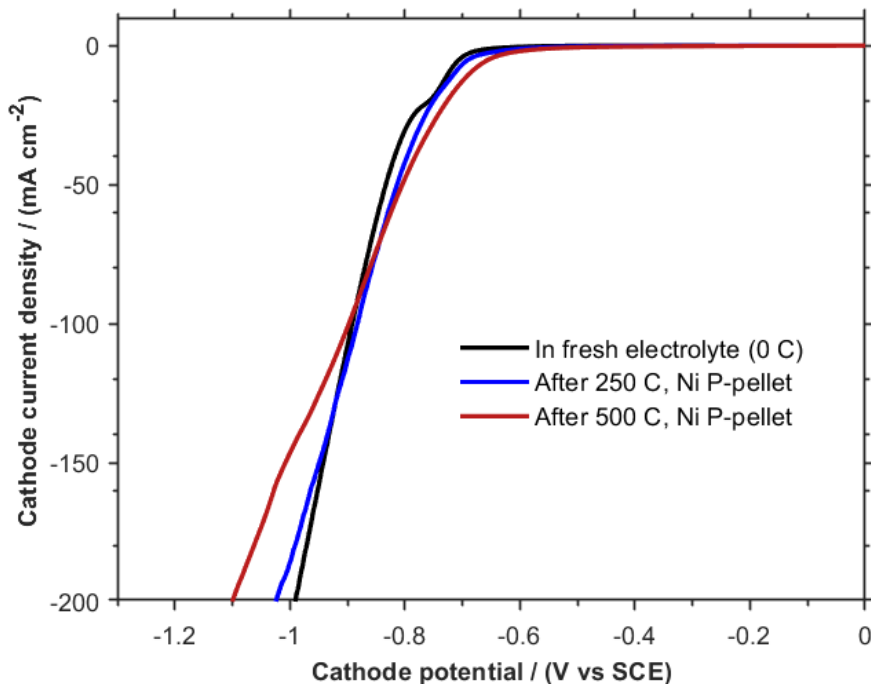


Figure 7.23: Polarisation plot (scan rate =  $5 \text{ mV s}^{-1}$ ) for the deposition of nickel at a stainless steel cathode from a base sulfamate electrolyte showing the influence of the amount of sulfamate decomposition product (represented as 0, 250 or 500 C of charge passed) on the cathodic process.

( $\text{H}_2\text{NCSNH}_2$ ) and bis(3-sulfopropyl) disulfide, sodium salt (SPS,  $\text{Na}_2^+[\text{SO}_3^-(\text{CH}_2)_3\text{S}]_2$ ) which are also S-based compounds have been reported to show a similar transition from depolarising behaviour at low overpotentials to polarising behaviour at high overpotentials during nickel electrodeposition [274]. Nakano et al. [130] also examined the partial current densities of nickel electrodeposition in the absence and presence of the decomposition product from a Pt anode. Although their data showed a wide spread of values, it could be discerned that the decomposition product increased the partial current densities between 1 to  $100 \text{ mA/cm}^2$ , which support the results in Figure 7.23. In conclusion, perturbations to the cathode process are anticipated to occur when low-sulfur nickel and Pt anodes are employed due to the generation of sulfamate decomposition products. This could introduce some instabilities in the process which will be explored in the forthcoming section.

## 7.7.2 Current efficiency of nickel electrodeposition

An investigation was performed to examine the role of the anode material on the current efficiency of nickel electrodeposition, and the stability of this parameter during extended usage of the bath (up to  $\approx 5$  Ah/L). Galvanostatic deposition of Ni onto 304 stainless steel rotating at 450 rpm was carried out at a constant current density of 40 mA/cm<sup>2</sup> in an electrolyte containing 1.764 M nickel sulfamate, 0.65 M boric acid, and 0.021 M nickel chloride using three different anode materials: low-sulfur Ni P-pellet, sulfur-activated Ni S-pellet, and platinum. Figure 7.24 shows the dependence of the electrodeposition current efficiency on the bath age, which was estimated by the ratio of the amount of charge that was passed per unit volume of the electrolyte. Note that this data is for deposition in a cell where the anode and cathode were not separated

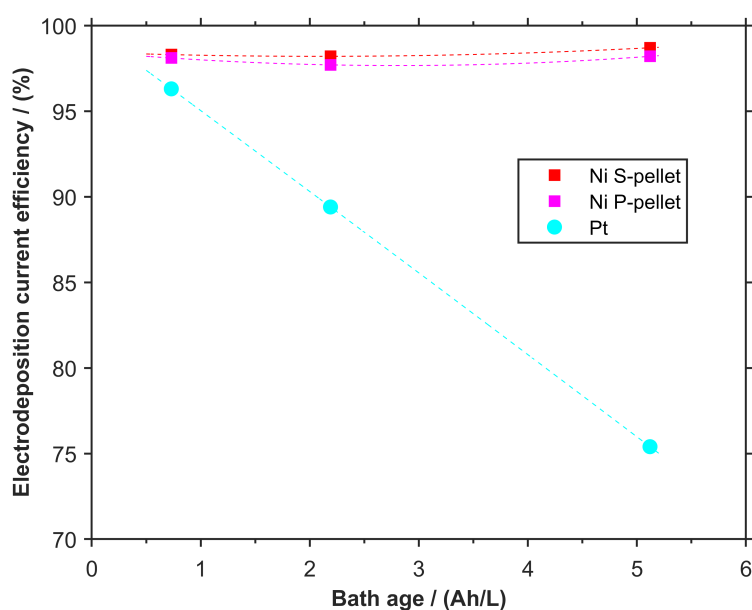


Figure 7.24: Effect of anode material on the current efficiency of nickel electrodeposition as a function of bath age (charge per unit volume (Ah/L)). A constant cathode current density of 40 mA cm<sup>-2</sup> was applied for electrolysis in an undivided cell

It can be observed from Figure 7.24 that the current efficiencies of Ni electrodeposition from electrolytes with soluble nickel anodes were fairly constant around  $98.2 \pm 0.3\%$  during prolonged electrolysis up to 5.12 Ah/L. In contrast, when a platinum anode was used, a lower cathode current efficiency (96.3%) was obtained for a bath age of less than 1 Ah/L. Increasing the age of solutions with a Pt anode up to 5.12 Ah/L

led to a further decrease in the cathode current efficiency to 75.4%. Therefore, it can be concluded that sulfur-activated and low-sulfur Ni anodes permitted longer usage of the bath than a Pt anode.

Sulfur-activated and low-sulfur Ni pellets dissolved in the active and transition regions, with corresponding potentials of about 0.1 V and 1.1 V versus SCE, respectively, during electrolysis up to 5.12 Ah/L. In contrast, the Pt anode required a higher oxidation potential of +2.5 V to supply the charge required at the cathode. These results agree with findings discussed in section 7.6.2. The dissolution current efficiencies of sulfur-activated and low-sulfur Ni pellets were measured to be  $96 \pm 2\%$  and 81-94%, respectively. The UV-Vis spectra after a bath age of 5.12 Ah/L, which is shown in Figure 7.25, indicated that sulfamate decomposition products were present in comparable quantities in solutions electrolysed with low-sulfur and Pt anodes but were absent in those electrolysed with an S-pellet which is also in agreement with findings discussed in section 7.6.2.

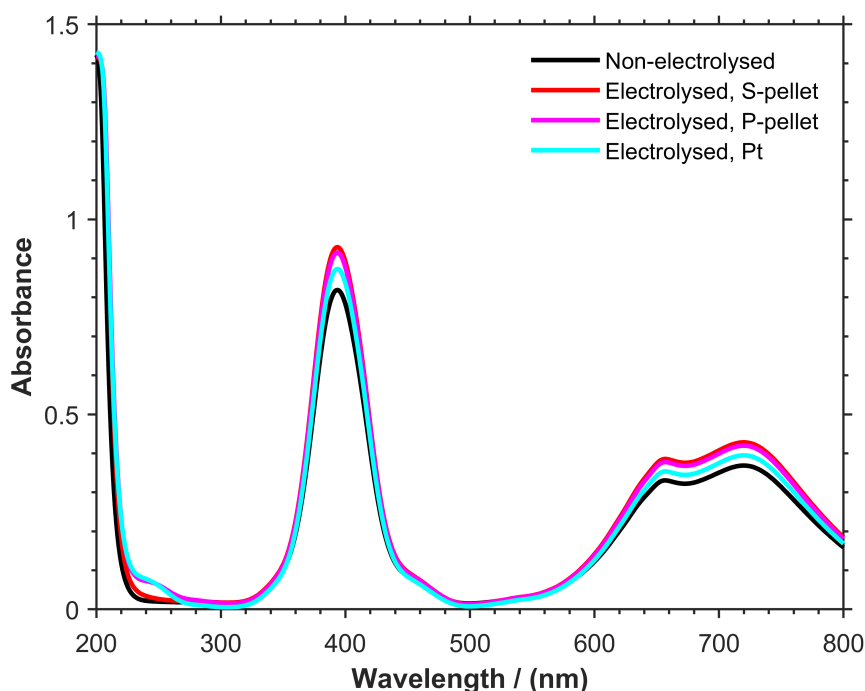


Figure 7.25: The UV-Vis spectra for non-electrolysed and aged (5.12 Ah/L) nickel sulfamate solutions. Electrolysis was performed with different anode materials by applying a constant cathode current density of  $40 \text{ mA/cm}^2$ .

The observed results in Figure 7.24 suggest that sulfamate decomposition

products produced have a marginal effect on the current efficiency of electrodeposition. The lower cathode current efficiencies encountered when Pt anodes are used could be attributed to the significant decrease in bulk pH of the bath that was measured during prolonged electrolysis. The bulk pH of the bath electrolysed with a Pt anode decreased by 1.83 units whereas the pH of baths electrolysed with soluble nickel anodes decreased by <0.5 units. The significant decrease in pH values could be caused by decrease in the concentration of  $\text{Ni}^{2+}$  and water decomposition at the Pt anode which has been reported in literature [55].

Therefore, the electroforming process is unstable when insoluble anodes are used unless they are isolated which is not practical in actual industrial plating. Soluble anodes should be employed to maintain a stable pH and constancy of the deposition current efficiency during long-term electrolysis.

Similar cathode current efficiencies were obtained with sulfur-activated and low-sulfur nickel anodes which suggested that the sulfamate decomposition products generated at the latter anode did not affect the current efficiency of electrodeposition. Therefore, sulfur impurities [125, 130] that have been reported in literature are likely incorporated through a physical adsorption process rather than an electrochemical process involving the decomposition products.

## 7.8 Summary of main findings

The aim of chapter 7 was to characterise several commercially available nickel anodes routinely employed in nickel sulfamate baths for the electroforming process. It was found that the composition of the soluble anodes could clearly be related to their electrochemical behaviour and their effect on sulfamate ion oxidation. Based on their composition, the soluble nickel anodes could be grouped into two categories: sulfur-activated anodes (which contained  $\approx 0.025$  wt%) and low-sulfur anodes (which contained <0.01 wt%).

Initial electrochemical studies indicated that sulfur-activated nickel anodes could sustain anode current densities greater than  $100 \text{ mA/cm}^{-2}$  in the active region,

i.e. at low potentials  $< 0$  V vs SCE, even in the absence of chloride ions or solution agitation. Such low potentials allowed sulfur-activated nickel to always operate at anode current efficiencies close to 100% which make them ideally suited for electroforming.

On the other hand, low-sulfur nickel anodes could only sustain current densities  $< 3$  mA/cm<sup>2</sup> in the active region before passivating and dissolving at higher potentials in the transpassive region. In practical terms, current densities applied for electroforming will cause the anode potential of low-sulfur nickel to transition from low potentials to high potentials ( $> 1.2$  V) within seconds of the experiment. The dissolution current efficiencies for low-sulfur nickel were always lower than for sulfur-activated nickel anodes since they operate at significantly higher potentials and therefore electrochemical reactions, such as water and sulfamate ion oxidation, that cannot take place on sulfur-activated nickel could now happen.

UV-Vis spectroscopy was used to investigate the presence of sulfamate breakdown products produced during the oxidation of sulfamate ions at various anode materials. A prominent UV absorption peak at 245 nm revealed the presence of compounds generated during electrolysis, and it was established that anodic electrochemical processes were responsible for their production. It was found that these oxidation products were generated at low-sulfur nickel and Pt anodes but not at sulfur-activated nickel anodes. This is most likely because sulfur-activated nickel operates at low potentials ( $< 0$  V vs SCE) while low-sulfur nickel and Pt anodes operate at significantly higher potentials of about 1.4 V and 2.0 V, respectively. Since Pt anodes function at higher potentials ( $> 2.0$  V vs SCE), their rates of sulfamate breakdown product formation are often much higher than those of low-sulfur nickel anodes. It was found that as the current density of the low-sulfur nickel anode increased from 5 to 25 mA/cm<sup>2</sup>, the rate of production of these sulfamate breakdown products also increased.

While a number of sulfonated species have been proposed in literature as the oxidation product, azodisulfonate was found to be the major oxidation product at low-sulfur nickel and Pt anodes. This was concluded from similarities in the spectra of the sulfamate oxidation product and that of ADS obtained from the literature, as well as the known thermal degradability of ADS which was found to be the case for the oxidation product at low-sulfur nickel and Pt anodes. Some evidence of the formation

of bisulfite and persulfate ions could also be deduced from the UV-Vis spectra. Based on the present results, the formation of persulfate ions at low-sulfur nickel anodes is improbable because they do not reach potentials that oxidise sulfate ions.

Sulfamate decomposition products formed at low-sulfur nickel anodes have been found to influence cathodic polarisation but had a marginal effect on the current efficiency of nickel electrodeposition. Nonetheless, these products have been reported to have significant effects on deposit characteristics. For example, ADS has been demonstrated to decrease stress in deposits but lead to high levels of sulfur. This could limit the use of low-sulfur nickel anodes for certain applications in nickel electroforming. If they must be employed, increasing the anode area used in the electroforming process could decrease the quantities of these decomposition products in the electrolyte and thereby, their effects on the deposit.

# Chapter 8

## Conclusions and Future Work

### 8.1 Conclusions

The main aim of this research project was to study the effect of boric acid and anode materials on the current efficiency and kinetics of nickel deposition and dissolution in electroforming (sulfamate) electrolytes. The designed experiments were carried out systematically according to the research plan. Key findings from this research are summarised in the forthcoming paragraphs.

Regarding the role of boric acid (Chapter 5), it was found that sulfamate electrolytes composed of boric acid (0.49-0.81 M) formed highly efficient solutions for the electroforming of low-stressed nickel on 304 SS disks with cathodic current efficiencies approaching 100% over a wide range of solution temperature from 40 to 55 °C. EDS confirmed that deposits were mainly composed of metallic Ni. The addition of boric acid was beneficial for deposition rates, current efficiency, and deposit appearance. Nickel ion reduction from baths without boric acid displayed low current efficiency and deposits with cracks. Increases in electrolyte temperature and cathode rotation speed were found to improve deposit quality and current efficiency in baths without boric acid. However, a decrease in current efficiency was measured when baths containing boric acid were stirred indicating that agitation was detrimental to the action of boric acid.

Systematic investigation of the influence of deposition conditions on kinetic parameters consistently revealed high cathodic Tafel slopes ( $>120$  mV/dec) for  $\text{Ni}^{2+}$  reduction in unstirred baths containing boric acid which was believed to mean that boric acid participated in the electrodeposition mechanism of Ni by adsorbing on the electrode surface. An increase in cathode rotation speed decreased cathodic Tafel slopes to values around 120 mV/dec in these unstirred baths which was believed to

indicate a decrease in adsorbed boric acid due to increased turbulent flow of the electrolyte. It could be discerned that addition of boric acid increased Ni exchange current densities at 40 °C indicating an increase in Ni deposition rates which suggested that the decrease in hydrogen evolution in the presence of boric acid resulted from the synergistic adsorption of boric acid and nickel ions.

The effect of boric acid on current efficiency and nickel deposition rates were found to be reproducible at a 304 SS quartz crystal resonator employed in EQCM investigations. The combination of QCM and LSV measurements in potassium sulfamate solutions (pH=4) has shown that a steep increase in mass is observed on 304SS, Ni, Au, and Cu electrode surfaces at the potentials corresponding to the onset of water reduction in the cathodic scan. This mass increase was attributed to the formation of oxides/hydroxides following the reduction of water but the detailed mechanism is unknown. The formation of oxides/hydroxides in the absence of boric acid was supported by high Tafel slope measurements corresponding to those typically measured on hydroxide covered surfaces in literature. When boric acid is present in solution, the rapid accumulation of mass due to oxide formation is retarded and displaced to more cathodic potentials. Instead, a small mass increase is observed in the scan at potentials prior to significant HER which was attributed to the adsorption of boric acid (or a related species). This is followed by a mass decrease at potentials where significant HER begins to occur which was attributed to the desorption of boric acid. It was concluded that the adsorbed layer of boric acid blocks the adsorption of water, thereby preventing the formation of hydroxyl ions. EQCM studies quantify the amount of adsorbed boric acid molecules as being in the range of 4-5 monolayers on all investigated substrates.

QCM and LSV measurements were also performed from potassium sulfamate electrolytes containing small amounts of Ni<sup>2+</sup> to study the effect of boric adsorption on nickel electrodeposition. In the absence of boric acid, nickel was electrodeposited with Ni(OH)<sub>2</sub>. The formation of Ni(OH)<sub>2</sub> was inhibited when boric acid was added to the electrolyte. This led to the conclusion that HER occurs via proton and water reduction in the presence and absence of boric acid, respectively. Some evidence of boric acid adsorption prior to nickel electrodeposition could be gleaned from scans measured on 304 SS. A mechanism for nickel electrodeposition in the absence and presence of boric



acid was proposed.

Lastly, the dissolution potential and current efficiency of low sulfur (<0.0002 wt%) and sulfur-activated (>0.02 wt%) carbonyl nickel anodes were assessed in a nickel electroforming bath. Polarisation and chronopotentiometric measurements confirm that low sulfur nickel anodes could only support significant anode current densities (> 1.72 mA/cm<sup>2</sup>) in the transpassive region where they dissolved with current efficiencies  $\leq$  100%. On the other hand, sulfur-activated nickel anodes dissolved in the active region where they could sustain current densities in excess of 100 mA/cm<sup>2</sup> and typically dissolved with current efficiencies close to 100%. The low dissolution current efficiency measurements of low-sulfur nickel prompted an investigation into sulfamate oxidation at these anodes and a Pt electrode using UV-Vis spectroscopy to detect its products. Sulfamate oxidation products were not detected when a sulfur-depolarised anode was used as the anode potential was not sufficiently high enough to oxidise sulfamate ions. In contrast, low sulfur Ni and Pt anodes attained high potentials which produced detectable amounts of sulfamate oxidation products which gave a distinct peak at 245 nm in the UV-Vis spectra of electrolysed samples. The products produced at the low sulfur anode were demonstrated to affect cathode polarisation curves but had little effect on cathode current efficiency. The results also indicated that azodisulfonate is the principal oxidation product generated at low sulfur Ni and Pt anodes on the basis of the thermal instability of the product. It could also be discerned from the spectral characteristics that bisulfite or persulfate ions were formed at these anodes.

## 8.2 Suggestions for Future Work

- Studies have indicated that nickel deposits plated from Watts and sulfamate baths display tensile and compressive stresses, respectively. The reason for lower stressed deposits from sulfamate baths has never been clearly elucidated to this day. The present results indicate that nickel deposits plated from sulfamate baths are doped with small amounts of nitrogen (about 2 wt%) which has not been previously reported. It would be beneficial to investigate the implications of this impurity on the internal stress which could lead to better understanding of the

differences in the nickel electrodeposition mechanisms in Watts and sulfamate electrolytes.

- The EQCM results have shown that when boric acid is present in solution, there is a certain increase in mass followed an equivalent mass decrease on the electrode surface. It would be desirable to correlate this to the concentration of boric acid in solution and plating rates of Ni.
- It is recommended that the EQCM measurements reported here be augmented with other tests such as electrochemical impedance spectroscopy to identify the dynamics of the various processes that occur, particularly the adsorption and desorption of boric acid and its dependence on potential.

## References

- [1] L Zhu, N Li, and PRN Childs. Light-weighting in aerospace component and system design. *Propulsion and Power Research*, 7(2):103–119, 2018.
- [2] David S Lee, DW Fahey, Agnieszka Skowron, MR Allen, Ulrike Burkhardt, Q Chen, SJ Doherty, S Freeman, PM Forster, J Fuglestvedt, et al. The contribution of global aviation to anthropogenic climate forcing for 2000 to 2018. *Atmospheric Environment*, 244:117834, 2021.
- [3] LQ Maurice and DS Lee. Assessing current scientific knowledge, uncertainties and gaps in quantifying climate change, noise and air quality aviation impacts. *Washington DC and Manchester: US Federal Aviation Administration and Manchester Metropolitan University*, 2009.
- [4] Matthew Marino, Roberto Sabatini, et al. Advanced lightweight aircraft design configurations for green operations. In *Practical Responses to Climate Change Conference 2014*, page 207. Engineers Australia, 2014.
- [5] Mohammad Sakhawat Hussain. Electroforming a process for macro/nano manufacturing. *International Journal of Nanomanufacturing*, 6(1-4):324–333, 2010.
- [6] Ron Parkinson. Electroforming: a unique metal fabrication process. *AIFM Galvano Tecnica e Nuove Finiture(Italy)*, 9(3):140–142, 1999.
- [7] A Jung, M Weinmann, and H Natter. Electroforming and electrodeposition on complex 3d geometries: special requirements and new methods. *Handbook of Nanoelectrochemistry*. Springer, Cham. [https://doi.org/10.1007/978-3-319-15207-3\\_46-1](https://doi.org/10.1007/978-3-319-15207-3_46-1), 2015.
- [8] JA McGeough, MC Leu, KP Rajurkar, AKM De Silva, and Q Liu. Electroforming process and application to micro/macro manufacturing. *CIRP Annals*, 50(2):499–514, 2001.

- [9] P Hernández, D Campos, P Socorro, A Benítez, F Ortega, N Díaz, and Ma D Marrero. Electroforming applied to manufacturing of microcomponents. *Procedia engineering*, 132:655–662, 2015.
- [10] Michael J Sole. Electroforming: methods, materials, and merchandise. *Jom*, 46(6):29–35, 1994.
- [11] Robert D Hilty and Lawrence J Masur. On the formation of lightweight nanocrystalline aluminum alloys by electrodeposition. *JOM*, 69(12):2621–2625, 2017.
- [12] Robert Hilty. High-strength electroformed nanostructured aluminum for lightweight automotive applications. Technical report, Xtallic Corporation, Marlborough, MA (United States), 2018.
- [13] Jian-Ming Yang, Dong-Hyun Kim, Di Zhu, and Kun Wang. Improvement of deposition uniformity in alloy electroforming for revolving parts. *International Journal of Machine Tools and Manufacture*, 48(3-4):329–337, 2008.
- [14] Wen-Ching Tsai, Chi-Chao Wan, and Yung-Yun Wang. Frequency effect of pulse plating on the uniformity of copper deposition in plated through holes. *Journal of the Electrochemical Society*, 150(5):C267, 2003.
- [15] Yong-Jun Tan and Kim Yong Lim. Understanding and improving the uniformity of electrodeposition. *Surface and Coatings Technology*, 167(2-3):255–262, 2003.
- [16] Bo Yang and Ming C Leu. Rapid production of engineering tools and hollow bodies by integration of electroforming and solid freeform fabrication, June 25 2002. US Patent 6,409,902.
- [17] S John, V Ananth, and T Vasudevan. Improving the deposit distribution during electroforming of complicated shapes. *Bulletin of electrochemistry*, 15(5-6):202–204, 1999.
- [18] Yong Choi. Ultrasonic agitation-floating classification of nano-sized ba–mg ferrites particles formed by using self-propagating high temperature synthesis and fabrication of nickel-ferrites thin sheet by pulse-electroforming. *Journal of nanoscience and nanotechnology*, 13(1):607–610, 2013.

- [19] Jong-Min Lee, John T Hachman, James J Kelly, and Alan C West. Improvement of current distribution uniformity on substrates for microelectromechanical systems. *Journal of Micro/Nanolithography, MEMS, and MOEMS*, 3(1):146–151, 2004.
- [20] Bing-yan Jiang, Can Weng, Ming-yong Zhou, Hui Lv, and Dietmar Drummer. Improvement of thickness deposition uniformity in nickel electroforming for micro mold inserts. *Journal of Central South University*, 23(10):2536–2541, 2016.
- [21] RJ Kendrick. High-speed nickel plating from sulphamate solutions. *Transactions of the IMF*, 42(1):235–245, 1964.
- [22] Peter Torben Tang, Peter Leisner, and Per Møller. Improvements of nickel deposit characteristics by pulse plating. In *SUR/FIN Manufacturing and Technology Conference 1993*. AESF, 1993.
- [23] HM Wu, HJ Shy, and C-H Huang. Internal stress control of electroformed nickel–iron alloys. *SUR/FIN'92.*, 1:629–642, 1992.
- [24] Sudipta Roy and Eleni Andreou. Electroforming in the industry 4.0 era. *Current Opinion in Electrochemistry*, 20:108–115, 2020.
- [25] Berl Stein. A practical guide to understanding, measuring and controlling stress in electroformed metals. In *Proc. of AESF Electroforming Symposium, Las Vegas*, 1996.
- [26] George A Di Bari. Electrodeposition of nickel. *Modern electroplating*, 5:79–114, 2000.
- [27] E Gnass. Electroforming with dispersed particles. *Eight Ulmer Gespräch-Galvanoformung, Eugen G. Leuze, Saulgau*, page 75, 1986.
- [28] A.J. Tuck Company. Advantages of electroforming. <https://www.ajtuckco.com/advantages-of-electroforming/>. Accessed: 2021-05-05.
- [29] Mario Monzo´n, Pedro M Herna´ndez, Antonio N Beni´tez, Mari´a D Marrero, Mari´a A A´lvarez, and Mark Kearns. An innovative electroforming process for oil

- heated rotational moulding tools. In *Engineering Systems Design and Analysis*, volume 48357, pages 185–191, 2008.
- [30] Ron Parkinson. Nickel plating and electroforming: Essential industries for today and the future. *NiDI Technical Series N°*, 2001.
- [31] DP Davies and SL Jenkins. Mechanical and metallurgical characterisation of electroformed nickel for helicopter erosion shield applications. *Materials Science and Engineering: A*, 607:341–350, 2014.
- [32] Adrián Uriondo, Manuel Esperon-Miguez, and Suresh Perinpanayagam. The present and future of additive manufacturing in the aerospace sector: A review of important aspects. *Proceedings of the Institution of Mechanical Engineers, Part G: Journal of Aerospace Engineering*, 229(11):2132–2147, 2015.
- [33] VA Tracey. Production of porous nickel for alkaline-battery and fuel-cell electrodes: Practical and economic considerations. *Powder Metallurgy*, 8(16):241–255, 1965.
- [34] Robert Kay and Marc Desmulliez. A review of stencil printing for microelectronic packaging. *Soldering & Surface Mount Technology*, 2012.
- [35] Shuo-Jen Lee, Yu-Pang Chen, and Ching-Han Huang. Electroforming of metallic bipolar plates with micro-featured flow field. *Journal of Power Sources*, 145(2):369–375, 2005.
- [36] Abolfazl Zolfaghari, Lin Zhang, Wenchen Zhou, and Y Yi Allen. Replication of plastic microlens arrays using electroforming and precision compression molding. *Microelectronic Engineering*, 239:111529, 2021.
- [37] WJ Hungerford, JW Larmer, and M Levinsohn. Ellipsoidal optical reflectors reproduced by electroforming. Technical report, 1964.
- [38] Massimiliano Rossi, Giuseppe Borghi, Iain A Neil, Giuseppe Valsecchi, Paolo Zago, and Fabio Emilio Zocchi. Electroformed off-axis toroidal aspheric three-mirror anastigmat multispectral imaging system. *Optical Engineering*, 53(3):031308, 2014.

- [39] Giovanni Pareschi, Oberto Citterio, Mauro Ghigo, Francesco Mazzoleni, A Mengali, and Carlo Misiano. Nickel-replicated multilayer optics for soft and hard x-ray telescopes. In *X-Ray Optics, Instruments, and Missions III*, volume 4012, pages 284–293. International Society for Optics and Photonics, 2000.
- [40] Michael Holz. Astrabismatic spectacles: a medical application for binary optics. In *Miniature and Micro-Optics: Fabrication and System Applications II*, volume 1751, pages 96–105. International Society for Optics and Photonics, 1993.
- [41] NS Qu, WH Qian, WZ Cai, ZH Xing, ZW Zhu, and YB Zeng. Fabrication of microprism mould by electroforming with high electrolyte flowrate. *Transactions of the IMF*, 91(4):221–224, 2013.
- [42] Honggang Zhang, Nan Zhang, Michael Gilchrist, and Fengzhou Fang. Advances in precision micro/nano-electroforming: a state-of-the-art review. *Journal of Micromechanics and Microengineering*, 30(10):103002, 2020.
- [43] Mohamed Gad-el Hak. *The MEMS handbook*. CRC press, 2001.
- [44] J Matovic. Application of ni electroplating techniques towards stress-free microelectromechanical system-based sensors and actuators. *Proceedings of the Institution of Mechanical Engineers, Part C: Journal of Mechanical Engineering Science*, 220(11):1645–1654, 2006.
- [45] Jian Liu, Hany Hassanin, Zhenyu Ni, Yi Yang, Gang Yang, and Kyle Jiang. Production of high-precision micro metallic components by electroforming process. *Materials and Manufacturing Processes*, 32(12):1325–1330, 2017.
- [46] Yuliy D Gamburg and Giovanni Zangari. *Theory and practice of metal electrodeposition*. Springer Science & Business Media, 2011.
- [47] Thomas F Fuller and John N Harb. *Electrochemical engineering*. John Wiley & Sons, 2018.
- [48] Wolfgang EG Hansal, Sudipta Roy, Peter Leisner, Todd Green, and Andreas Reichenbach. *Pulse plating*. 2012.
- [49] S Alec Watson. A tale of two billion. *Transactions of the IMF*, 77(1):10–15, 1999.

- [50] AC Hart, WR Wearmouth, and AC Warner. The anodic behaviour of nickel in nickel sulphamate electroplating solutions. *Transactions of the IMF*, 54(1):56–60, 1976.
- [51] L Cambi and R Piontelli. Sulphamate solutions for the electrodeposition of metals. *Rend. Inst. Lombardo Sci*, 72:128–138, 1938.
- [52] Richard C Barrett. Nickel plating from the sulfamate bath. *Plating*, 41:1027–1032, 1954.
- [53] DA Fanner and RAF Hammond. The properties of nickel electrodeposited from a sulphamate bath. *Transactions of the IMF*, 36(1):32–42, 1959.
- [54] M Halmdienst, WEG Hansal, G Kaltenhauser, and W Kautek. Pulse plating of nickel: influence of electrochemical parameters and composition of electrolyte. *Transactions of the IMF*, 85(1):22–26, 2007.
- [55] NV Mandich and DW Baudrand. Troubleshooting electroplating installations: nickel sulfamate plating systems. *Plating and surface finishing*, 89(9):68–76, 2002.
- [56] VI Maksin and OZ Standritchuk. Solubility diagrams of the systems nickel sulfamate-water and cobalt sulfamate-water. *Russian Journal of Applied Chemistry*, 80(7):1048–1054, 2007.
- [57] International Agency for Research on Cancer et al. Chromium, nickel and welding. *IARC monographs on the evaluation of carcinogenic risks to humans*, 49, 1990.
- [58] CM Whittington, WY Lo, and MY Yau. High speed nickel sulphamate plating of connector strip. *Transactions of the IMF*, 94(3):146–151, 2016.
- [59] S Sugiyama, Y Zhang, H Ueno, M Hosaka, T Fujimoto, R Maeda, and T Tanaka. A compact sr beamline for fabrication of high aspect ratio mems microparts. In *MHS'96 Proceedings of the Seventh International Symposium on Micro Machine and Human Science*, pages 79–84. IEEE, 1996.



- [60] Joseph Anthony McGeough. *Electroforming*, pages 443–446. Springer Berlin Heidelberg, Berlin, Heidelberg, 2014.
- [61] Antonello Vincenzo and Pietro Luigi Cavallotti. Structure and electrokinetic study of nickel electrodeposition. *Russian Journal of Electrochemistry*, 44(6):716–727, 2008.
- [62] I Epelboin and R Wiart. Mechanism of the electrocrystallization of nickel and cobalt in acidic solution. *Journal of the Electrochemical Society*, 118(10):1577, 1971.
- [63] A Saraby-Reintjes and M Fleischmann. Kinetics of electrodeposition of nickel from watts baths. *Electrochimica Acta*, 29(4):557–566, 1984.
- [64] James P Hoare. On the role of boric acid in the watts bath. *Journal of the Electrochemical Society*, 133(12):2491, 1986.
- [65] Ki-Deok Song, Kwang Bum Kim, Seong Ho Han, and Hong Ke Lee. A study on effect of hydrogen reduction reaction on the initial stage of ni electrodeposition using eqcm. *Electrochemistry communications*, 5(6):460–466, 2003.
- [66] BV Tilak, AS Gendron, and MA Mosoiu. Borate buffer equilibria in nickel refining electrolytes. *Journal of Applied Electrochemistry*, 7(6):495–500, 1977.
- [67] J Ji, WC Cooper, DB Dreisinger, and E Peters. Surface ph measurements during nickel electrodeposition. *Journal of Applied electrochemistry*, 25(7):642–650, 1995.
- [68] Y Tsuru, M Nomura, and FR Foulkes. Effects of boric acid on hydrogen evolution and internal stress in films deposited from a nickel sulfamate bath. *Journal of Applied Electrochemistry*, 32(6):629–634, 2002.
- [69] Shailesh Gadad and Thomas M Harris. Oxygen incorporation during the electrodeposition of ni, fe, and ni-fe alloys. *Journal of the Electrochemical Society*, 145(11):3699, 1998.
- [70] CQ Cui and Jim Y Lee. Nickel deposition from unbuffered neutral chloride solutions in the presence of oxygen. *Electrochimica Acta*, 40(11):1653–1662, 1995.

- [71] Matthew A Rigsby, Tighe A Spurlin, and Jonathan D Reid. The multi-functional role of boric acid in cobalt electrodeposition and superfill. *Journal of The Electrochemical Society*, 167(11):112507, 2020.
- [72] Anais Graff, Etienne Barrez, Philippe Baranek, Martin Bachet, and Pascale Bénézeth. Complexation of nickel ions by boric acid or (poly) borates. *Journal of solution chemistry*, 46(1):25–43, 2017.
- [73] K-M Yin and B-T Lin. Effects of boric acid on the electrodeposition of iron, nickel and iron-nickel. *Surface and Coatings Technology*, 78(1-3):205–210, 1996.
- [74] N Zech and D Landolt. The influence of boric acid and sulfate ions on the hydrogen formation in ni–fe plating electrolytes. *Electrochimica acta*, 45(21):3461–3471, 2000.
- [75] Christopher Karwas and Tadeusz Hepel. Influence of boric acid on electrodeposition and stripping of ni-zn alloys. *Journal of the Electrochemical Society*, 135(4):839, 1988.
- [76] Sung Kyoung Kim, Sang Bok Lee, et al. Role of boric acid in nickel nanotube electrodeposition: a surface-directed growth mechanism. *Chemical Communications*, 50(5):527–529, 2014.
- [77] Antonello Vincenzo and Pietro Luigi Cavallotti. Growth modes of electrodeposited cobalt. *Electrochimica Acta*, 49(24):4079–4089, 2004.
- [78] Andri Demetriou and Ioannis Pashalidis. Adsorption of boron on iron-oxide in aqueous solutions. *Desalination and Water Treatment*, 37(1-3):315–320, 2012.
- [79] Priyank V Kumar, Michael P Short, Sidney Yip, Bilge Yildiz, and Jeffrey C Grossman. First-principles assessment of the reactions of boric acid on nio (001) and zro<sub>2</sub> ( $\bar{1}11$ ) surfaces. *The Journal of Physical Chemistry C*, 116(18):10113–10119, 2012.
- [80] James P Hoare. Boric acid as a catalyst in nickel plating solutions. *Journal of the Electrochemical Society*, 134(12):3102, 1987.

- [81] MA Warne and DC Moore. Titanium-based materials in metal finishing processes. *Transactions of the IMF*, 42(1):93–99, 1964.
- [82] I Epelboin, M Jousselein, and R Wiart. Impedance measurements for nickel deposition in sulfate and chloride electrolytes. *Journal of Electroanalytical Chemistry and Interfacial Electrochemistry*, 119(1):61–71, 1981.
- [83] E Chassaing, M Jousselein, and R Wiart. The kinetics of nickel electrodeposition: Inhibition by adsorbed hydrogen and anions. *Journal of electroanalytical chemistry and interfacial electrochemistry*, 157(1):75–88, 1983.
- [84] J Matulis and R Sližys. On some characteristics of cathodic processes in nickel electrodeposition. *Electrochimica Acta*, 9(9):1177–1188, 1964.
- [85] KE Heusler and L Gaiser. Deposition and dissolution of nickel in perchlorate solutions. *Electrochimica Acta*, 13(1):59–70, 1968.
- [86] Sholeh Hessami and Charles W Tobias. A mathematical model for anomalous codeposition of nickel-iron on a rotating disk electrode. *Journal of the Electrochemical Society*, 136(12):3611, 1989.
- [87] Michael Matlosz. Competitive adsorption effects in the electrodeposition of iron-nickel alloys. *Journal of the Electrochemical Society*, 140(8):2272, 1993.
- [88] Keith Y Sasaki and Jan B Talbot. Electrodeposition of iron-group metals and binary alloys from sulfate baths. ii. modeling. *Journal of the Electrochemical Society*, 147(1):189, 2000.
- [89] Jinxing Ji and W Charles Cooper. Nickel speciation in aqueous chloride solutions. *Electrochimica Acta*, 41(9):1549–1560, 1996.
- [90] John Yeager, JP Cels, Ernest Yeager, and Frank Hovorka. The electrochemistry of nickel: I. codeposition of nickel and hydrogen from simple aqueous solutions. *Journal of the electrochemical society*, 106(4):328, 1959.
- [91] Renáta Oriňáková, Andrea Turoňová, Daniela Kladeková, Miriam Gálová, and Roger M Smith. Recent developments in the electrodeposition of nickel and

- some nickel-based alloys. *Journal of Applied Electrochemistry*, 36(9):957–972, 2006.
- [92] CQ Cui, Jim Y Lee, J Lin, and KL Tana. Effects of oxygen reduction on nickel deposition from unbuffered aqueous solutions: li. characterization of the electrode interface in electrodeposition. *Journal of the Electrochemical Society*, 142(4):1132, 1995.
- [93] Hadi Khani and Joan F Brennecke. Hard chromium composite electroplating on high-strength stainless steel from a cr (iii)-ionic liquid solution. *Electrochemistry Communications*, 107:106537, 2019.
- [94] JO'M Bockris and N Pentland. The mechanism of hydrogen evolution at copper cathodes in aqueous solutions. *Transactions of the Faraday Society*, 48:833–839, 1952.
- [95] Roger Parsons and JO'M Bockris. Calculation of the energy of activation of discharge of hydrogen ions at metal electrodes. *Transactions of the Faraday Society*, 47:914–928, 1951.
- [96] Ki-Deok Song, Kwang-Bum Kim, Seong-Ho Han, and Hongkee Lee. Effect of additives on hydrogen evolution and absorption during zn electrodeposition investigated by eqcm. *Electrochemical and Solid-State Letters*, 7(2):C20, 2003.
- [97] Haixin Chen, Dongqi Ge, Junwei Chen, Ruchun Li, Xiaofeng Zhang, Tongwen Yu, Yi Wang, and Shuqin Song. In situ surface reconstruction synthesis of a nickel oxide/nickel heterostructural film for efficient hydrogen evolution reaction. *Chemical Communications*, 56(72):10529–10532, 2020.
- [98] Yu-Po Lin and J Robert Selman. Electrodeposition of corrosion-resistant ni-zn alloy: I. cyclic voltammetric study. *Journal of the Electrochemical Society*, 140(5):1299, 1993.
- [99] M Šupicová, R Rozik, L Trnkova, R Oriňáková, and M Galova. Influence of boric acid on the electrochemical deposition of ni. *Journal of Solid State Electrochemistry*, 10(2):61–68, 2006.

- [100] J O'M Bockris and EC Potter. The mechanism of hydrogen evolution at nickel cathodes in aqueous solutions. *The Journal of Chemical Physics*, 20(4):614–628, 1952.
- [101] M Fleischmann and A Saraby-Reintjes. The simultaneous deposition of nickel and hydrogen on vitreous carbon. *Electrochimica Acta*, 29(1):69–75, 1984.
- [102] AH DuRose. Boric acid in ni solutions. *Plating and Surface Finishing*, 64(8):52–55, 1977.
- [103] Jean Horkans. On the role of buffers and anions in nife electrodeposition. *Journal of the Electrochemical Society*, 126(11):1861, 1979.
- [104] Rahman MM. Role of n-methylformamide in producing bright and hard nickel deposits. *Materials transactions, JIM*, 30(7):530–536, 1989.
- [105] Yutaka Tsuru, Ryouta Takamatsu, and Kunisuke Hosokawa. Influence of boric acid on nickel deposition from watts bath. *Journal of The Surface Finishing Society of Japan*, 44(1):39–43, 1993.
- [106] US Mohanty, BC Tripathy, P Singh, and SC Das. Effect of  $cd^{2+}$  on the electrodeposition of nickel from sulfate solutions. part ii: Polarisation behaviour. *Journal of Electroanalytical Chemistry*, 566(1):47–52, 2004.
- [107] Z Rao, SJ Hearne, and E Chason. The effects of plating current, grain size, and electrolyte on stress evolution in electrodeposited ni. *Journal of the Electrochemical Society*, 166(1):D3212, 2018.
- [108] CE Davalos, JR Lopez, H Ruiz, Alia Méndez, R Antano-Lopez, and G Trejo. Study of the role of boric acid during the electrochemical deposition of ni in a sulfamate bath. *Int J Electrochem Sci*, 8(7):9785–9800, 2013.
- [109] MY Abyaneh and M Hashemi-Pour. The effect of the concentration of boric acid on the kinetics of electrocrystallization of nickel. *Transactions of the IMF*, 72(1):23–26, 1994.

- [110] Jae Min Lee, Kyung Kuk Jung, and Jong Soo Ko. Formation of nickel microcones by using an electrodeposition solution containing  $\text{H}_3\text{BO}_3$ . *Current Applied Physics*, 16(3):261–266, 2016.
- [111] Wangping Wu, Jiaqi Huang, Johannes Näther, Nurul Amanina Binti Omar, Frank Köster, Thomas Lampke, Yaxuan Liu, Haijun Pan, and Yi Zhang. Texture orientation, morphology and performance of nanocrystalline nickel coatings electrodeposited from a watts-type bath: Effects of  $\text{H}_3\text{BO}_3$  concentration and plating time. *Surface and Coatings Technology*, 424:127648, 2021.
- [112] A Godon, Jordi Creus, X Feaugas, E Conforto, L Pichon, C Armand, and C Savall. Characterization of electrodeposited nickel coatings from sulphamate electrolyte without additive. *Materials characterization*, 62(2):164–173, 2011.
- [113] Anette A Rasmussen, Per Møller, and Marcel AJ Somers. Microstructure and thermal stability of nickel layers electrodeposited from an additive-free sulphamate-based electrolyte. *Surface and Coatings Technology*, 200(20-21):6037–6046, 2006.
- [114] CQ Cui and Jim Y Lee. Effects of oxygen reduction on nickel deposition from unbuffered aqueous solutions: I. deposition process and deposit structure. *Journal of the Electrochemical Society*, 141(8):2030, 1994.
- [115] Roberto CV Piatti, Alejandro Jorge Arvia, and José J Podestá. The electrochemical kinetic behaviour of nickel in acid aqueous solutions containing chloride and perchlorate ions. *Electrochimica Acta*, 14(7):541–560, 1969.
- [116] W Davison and JA Harrison. The deposition of Ni from aqueous sulphate and sulphamate solutions. *Journal of Electroanalytical Chemistry and Interfacial Electrochemistry*, 44(3):431–443, 1973.
- [117] A Lachenwitzer and OM Magnussen. Electrochemical quartz crystal microbalance study on the kinetics of nickel monolayer and multilayer electrodeposition on (111)-oriented gold films. *The Journal of Physical Chemistry B*, 104(31):7424–7430, 2000.

- [118] Atsushi Chiba, Takayuki Gotou, Katsuyoshi Kobayashi, and Wen-Chang Wu. Influence of sonication of nickel plating in a nickel sulfamate bath. *Metal Finishing*, 98(9):66–69, 2000.
- [119] Wolfgang EG Hansal, Barbara Tury, Martina Halmdienst, Magda Lakatos Varsanyi, and Wolfgang Kautek. Pulse reverse plating of ni-co alloys: Deposition kinetics of watts, sulfamate and chloride electrolytes. *Electrochimica Acta*, 52(3):1145–1151, 2006.
- [120] James J Kelly and N.Y.C Yang. Electrodeposition on ni from a sulfamate electrolyte part 1: Effect of a stress relief on annealing behavior and film metallurgy. Technical report, Sandia National Lab.(SNL-NM), Albuquerque, NM (United States); Sandia ..., 2002.
- [121] M Saitou, S Oshiro, and SM Asadul Hossain. Effect of temperature on nickel electrodeposition from a nickel sulfamate electrolyte. *Journal of Applied Electrochemistry*, 38(3):309–313, 2008.
- [122] Eleni Andreou and Sudipta Roy. Modelling the scaling-up of the nickel electroforming process. *Frontiers in Chemical Engineering*, 2022.
- [123] Mordechay Schlesinger and Milan Paunovic. *Modern electroplating*. John Wiley & Sons, 2011.
- [124] AC Hart. High speed electroplating—a review of the subject. *Transactions of the IMF*, 55(1):65–69, 1977.
- [125] OJ Klingenmaier. The effect of anode efficiency on the stability of nickel sulfamate solutions. *Plating*, 52(11):1138, 1965.
- [126] John Keith Dennis and Tony Eugene Such. *Nickel and chromium plating*. Elsevier, 1993.
- [127] AF Greene. Anode. oxidation. products in nickel. sulfamate. solutions, 1968.
- [128] L Jiazhu, Z Haiyan, and Z Liangyu. Investigation of anodic decomposition products in sulfamate solutions. *Plating and surface finishing*, 77(7):54–58, 1990.

- [129] H Zhang and S-M Park. Studies on the anodic decomposition products of sulfamate. *Journal of applied electrochemistry*, 24(11):1182–1187, 1994.
- [130] Hiroaki NAKANO, Satoshi OUE, Shigeo KOBAYASHI, Tetsuya AKIYAMA, and Hisaaki FUKUSHIMA. Anodic oxidation of sulfamate ions in sulfamate baths and its effect on ni deposition. *Hyomen gijutsu*, 54(8):533–538, 2003.
- [131] LU Jing, Qi-hua Yang, and Zhao Zhang. Effects of additives on nickel electrowinning from sulfate system. *Transactions of Nonferrous Metals Society of China*, 20:s97–s101, 2010.
- [132] H Higashino and H Ohkawa. Electroforming method and electroforming apparatus, U.S. Patent 4 696 721, Sep. 1987.
- [133] Man Kim, Joo-Yul Lee, Sik-Chol Kwon, Dongsoo Kim, In-Gon Kim, and Yong Choi. Application of small angle neutron scattering to analyze precision nickel mesh for electro-magnetic interference shielding formed by continuous electroforming technique. *Physica B: Condensed Matter*, 385:914–916, 2006.
- [134] George A DiBari. Faraday's children (and nickel). *Plating and surface finishing*, 86(9):32–43, 1999.
- [135] LG Novikov, GA Kurnoskin, VN Flerov, GP Shul'pin, and IY Ivashkina. Partial anodic processes in a sulfamate electrolyte used for galvanic nickel plating. *Protection of Metals*, 25(5):701–703, 1989.
- [136] Marcel Pourbaix. Atlas of electrochemical equilibria in aqueous solution. *NACE*, 307, 1974.
- [137] G DiBari. Notes on nickel anode materials. *Plating and Surface Finishing*, 66(6):76–80, 1979.
- [138] George A Di Bari, M Schlesinger, and M Paunovic. Modern electroplating. *New York*, M. Schlesinger and M. Paunovic, Eds., John Wiley&Sons, Inc, 2000.
- [139] WA Wesley. Third hothersall memorial lecture of nickel atoms, ions and electrons. *Transactions of the IMF*, 33(1):452–470, 1955.



- [140] George A DiBari and Roger A Covert. A review of different electroplating anode materials. *SAE transactions*, pages 102–115, 1990.
- [141] Nickel plating handbook. 2014.
- [142] Susumu Arai, Takahide Hasegawa, and Norio Kaneko. Effect of s on passivation of ni plating. *Journal of the Electrochemical Society*, 151(1):C15, 2003.
- [143] GL Fisher. Power savings using sulfur-activated nickel anodes. *Plating and Surface Finishing*, 65(9):46–49, 1978.
- [144] CM Whittington, KLK Yeung, and WY Lo. Refined nickel anodes: pointers to industrial best practice. *Transactions of the IMF*, 89(3):122–131, 2011.
- [145] INCO. Nickel electroforming processes and applications. [https://garelectroforming.com/downloads/Inco-ElectroformingGuide\\_Oct-13-2011.pdf](https://garelectroforming.com/downloads/Inco-ElectroformingGuide_Oct-13-2011.pdf).
- [146] Ludwig Mond. The history of my process of nickel extraction, 1990.
- [147] A Morrison, JJ Leitch, G Szymanski, G Moula, B Barlow, IJ Burgess, B Shobeir, H Huang, and J Lipkowski. Mechanism of electrochemical dissolution of nickel grown by carbonyl method. *Electrochimica Acta*, 248:112–122, 2017.
- [148] Andrew Allcock. From the files- electroforming lip skins and beyond (first published in machinery, aerospace supplement october 2018), Sep 2019.
- [149] Norio Sato and Go Okamoto. Kinetics of the anodic dissolution of nickel in sulfuric acid solutions. *Journal of The Electrochemical Society*, 111(8):897, 1964.
- [150] Jorge Roberto Vilche and Alejandro Jorge Arvia. Kinetics and mechanism of the nickel electrode—ii. acid solutions containing a high concentration of sulphate and nickel ions. *Corrosion Science*, 18(5):441–463, 1978.
- [151] SS Abd El Rehim, SM Abd El Wahaab, and EA Abd El Meguid. Potentiodynamic behaviour of the nickel electrode in acid media. *Surface and Coatings Technology*, 29(4):325–333, 1986.

- [152] Masayuki Itagaki, H Nakazawa, K Watanabe, and K Noda. Study of dissolution mechanisms of nickel in sulfuric acid solution by electrochemical quartz crystal microbalance. *Corrosion science*, 39(5):901–911, 1997.
- [153] GT Burstein and GA Wright. The anodic dissolution of nickel—1: Perchlorate and fluoride electrolytes. *Electrochimica Acta*, 20(1):95–99, 1975.
- [154] VS Muralidharan, M Veerashanmugamani, G Paruthimalkalaigan, and I Arulraj. Mechanism of corrosion of pure nickel in sulphuric acid solutions. *Bulletin of Electrochemistry*, 1(3):241–244, 1985.
- [155] Norio Sato and Go Okamoto. Anodic passivation of nickel in sulfuric acid solutions. *Journal of The Electrochemical Society*, 110(6):605, 1963.
- [156] E Kunze and K Schwabe. Beitrag zur passivität des nickels. *Corrosion Science*, 4(1-4):109–136, 1964.
- [157] RR Sayano and Ken Nobe. Continuous and pulse polarization off ni in h<sub>2</sub>so<sub>4</sub>. *Corrosion*, 22(4):81–87, 1966.
- [158] SS Abd El Rehim, SM Abd El Wahaab, and EA Abdel Maguid. Electrochemical behaviour of nickel anode in h<sub>2</sub>so<sub>4</sub> solutions and the effect of halide ions. *Materials and Corrosion*, 37(10):550–555, 1986.
- [159] JO'M Bockris, AKN Reddy, and B Rao. An ellipsometric determination of the mechanism of passivity of nickel. *Journal of the Electrochemical Society*, 113(11):1133, 1966.
- [160] TS De Gromoboy and LL Shreir. The formation of nickel oxides during the passivation of nickel in relation to the potential/ph diagram. *Electrochimica Acta*, 11(7):895–904, 1966.
- [161] AKN Reddy and B Rao. The mechanism of formation of pre-passive films on nickel: a chronoellipsometric study. *Canadian Journal of Chemistry*, 47(14):2687–2692, 1969.

- [162] AKN Reddy and B Rao. The mechanism of passivation of nickel as determined by an automatic recording ellipsometer. *Canadian Journal of Chemistry*, 47(14):2693–2698, 1969.
- [163] H-W Hoppe and H-H Strehblow. Xps and ups examinations of the formation of passive layers on ni in 1 m sodium hydroxide and 0.5 m sulphuric acid. *Surface and interface analysis*, 14(3):121–131, 1989.
- [164] D Zuili, V Maurice, and P Marcus. Surface structure of nickel in acid solution studied by in situ scanning tunneling microscopy. *Journal of the Electrochemical Society*, 147(4):1393, 2000.
- [165] Philippe Marcus, Vincent Maurice, and H-H Strehblow. Localized corrosion (pitting): A model of passivity breakdown including the role of the oxide layer nanostructure. *Corrosion science*, 50(9):2698–2704, 2008.
- [166] H Böhni. Breakdown of passivity and localized corrosion processes. *Langmuir*, 3(6):924–930, 1987.
- [167] GS Frankel. Pitting corrosion of metals: a review of the critical factors. *Journal of the Electrochemical society*, 145(6):2186, 1998.
- [168] SG Real, MR Barbosa, JR Vilche, and AJ Arvia. Influence of chloride concentration on the active dissolution and passivation of nickel electrodes in acid sulfate solutions. *Journal of the Electrochemical Society*, 137(6):1696, 1990.
- [169] EE Abd El Aal, W Zakria, A Diab, and SM Abd El Haleem. Anodic dissolution of nickel in acidic chloride solutions. *Journal of materials engineering and performance*, 12(2):172–178, 2003.
- [170] AB Shein, OS Ivanova, and RN Minkh. The effect of anions on the anodic dissolution of nickel silicide in sulfate electrolytes. *Protection of Metals*, 44(1):32–38, 2008.
- [171] MR Barbosa, JA Bastos, JJ García-Jareño, and F Vicente. Chloride role in the surface of nickel electrode. *Electrochimica acta*, 44(6-7):957–965, 1998.

- [172] Myron B Diggin. Nickel plating from the sulphamate solution. *Transactions of the IMF*, 31(1):243–258, 1954.
- [173] Jack L Marti. The effect of some variables upon internal stress of nickel as deposited from sulfamate electrolytes. *Plating*, 53(1):61–71, 1966.
- [174] Xiang-Kang Chen. Electroforming procedures for shells of moulds and dies for subsequent simultaneous spray peening. *KB thesis scanning project 2015*, 1995.
- [175] Y Tsuru, M Nomura, and FR Foulkes. Effects of chloride, bromide and iodide ions on internal stress in films deposited during high speed nickel electroplating from a nickel sulfamate bath. *Journal of applied electrochemistry*, 30(2):231–238, 2000.
- [176] J Oudar and P Marcus. Role of adsorbed sulphur in the dissolution and passivation of nickel and nickel-sulphur alloys. *Applications of Surface Science*, 3(1):48–67, 1979.
- [177] P Marcus, I Olefjord, and J Oudar. The influence of sulphur on the dissolution and the passivation of a nickel-iron alloy—ii. surface analysis by esca. *Corrosion science*, 24(4):269–278, 1984.
- [178] DR Baer and MJ Danielson. Surface analysis and electrochemical studies of sulfur enhanced corrosion of nickel. *Journal of Vacuum Science & Technology A: Vacuum, Surfaces, and Films*, 5(4):1147–1151, 1987.
- [179] IJ Bear, RC Flann, KJ McDonald, LJ Rogers, and R Woods. Activated basket anodes from nickel powder part iii: Electrochemical behaviour of sulphur activated anodes. *Journal of applied electrochemistry*, 22(1):16–20, 1992.
- [180] Wenhui Yang, Yang Luo, Chongyun Wang, Baoguang Wang, and Wenhui Tian. High plasticity and anodic behavior of electroformed nickel without chloride ion. *Materials & Design*, 93:91–95, 2016.
- [181] S Watson. Modern electroforming. *Transactions of the IMF*, 67(1):89–94, 1989.

- [182] RJ Kendrick and SA Watson. Proceedings of the symposium on sulfamic acid, 1966.
- [183] Milan Paunovic and Mordechai Schlesinger. *Fundamentals of electrochemical deposition*. John Wiley & Sons, 2006.
- [184] John Newman and Karen E Thomas-Alyea. *Electrochemical systems*. John Wiley & Sons, 2012.
- [185] Anthony C Fisher. *Electrode dynamics*, volume 1. Oxford University Press Oxford, 1996.
- [186] Milan Paunovic and Mordechai Schlesinger. *Modern electroplating*. John Wiley, 2000.
- [187] Derek Pletcher, R Greff, R Peat, LM Peter, and J Robinson. *Instrumental methods in electrochemistry*. Elsevier, 2001.
- [188] Klaus J Vetter. *Electrochemical kinetics: theoretical aspects*. Elsevier, 2013.
- [189] Allen J Bard, Larry R Faulkner, et al. Fundamentals and applications. *Electrochemical methods*, 2, 1980.
- [190] J O'M Bockris and Zoltan Nagy. Symmetry factor and transfer coefficient. a source of confusion in electrode kinetics. *Journal of Chemical Education*, 50(12):839, 1973.
- [191] Robert E Meyer. Cathodic processes on passive zirconium. *Journal of The Electrochemical Society*, 107(10):847, 1960.
- [192] H Konno and M Nagayama. Mechanism of electrodeposition of copper from cupric pyrophosphate solutions. *Electrochimica Acta*, 22(4):353–358, 1977.
- [193] Derek Pletcher and Frank C Walsh. *Industrial electrochemistry*. Springer Science & Business Media, 1990.
- [194] Eleni Andreou and Sudipta Roy. Modelling the electroforming process: significance and challenges. *Transactions of the IMF*, 99(6):299–305, 2021.

- [195] Wolfgang Schmickler and Elizabeth Santos. *Interfacial electrochemistry*. Springer Science & Business Media, 2010.
- [196] Pietro Pedferri and Marco Ormellesse. *Corrosion science and engineering*. Springer, 2018.
- [197] D Landolt. Electrodeposition science and technology in the last quarter of the twentieth century. *Journal of the Electrochemical Society*, 149(3):S9, 2002.
- [198] Renáta Oriňáková, Magda Strečková, Libuše Trnková, Roland Rozik, and M Galova. Comparison of chloride and sulphate electrolytes in nickel electrodeposition on a paraffin impregnated graphite electrode. *Journal of Electroanalytical Chemistry*, 594(2):152–159, 2006.
- [199] Carl H Hamann, A Hamnett, and W Vielstich. *Electrochemistry*. 2007.
- [200] J OM. Bockris and akn reddy, modern electrochemistry. *Plenum, New York*, 1970:1238, 1970.
- [201] Fi C Frank. The influence of dislocations on crystal growth. *Discussions of the Faraday Society*, 5:48–54, 1949.
- [202] W-K\_ Burton, N Cabrera, and FC Frank. The growth of crystals and the equilibrium structure of their surfaces. *Philosophical Transactions of the Royal Society of London. Series A, Mathematical and Physical Sciences*, 243(866):299–358, 1951.
- [203] TE Dinan, M Matlosz, and D Landolt. Experimental investigation of the current distribution on a recessed rotating disk electrode. *Journal of the Electrochemical Society*, 138(10):2947, 1991.
- [204] Bradley D Fahlman. *Materials Chemistry [internet resource]*. 3rd ed. 2018.. edition, 2018.
- [205] Naresh Marturi. *Vision and visual servoing for nanomanipulation and nanocharacterization in scanning electron microscope*. PhD thesis, Université de Franche-Comté, 2013.

- [206] PJ Cox. The kirk—othmer encyclopedia of chemical technology:: Volume 4, bearing materials to carbon. ji kroschwitz and m. howe-grant (editors), wiley-interscience, chichester, 1992. pages: xxx+ 1117.£ 150.00. isbn 0-471-52672-x (v. 4)., 1993.
- [207] JJ Kelly, SH Goods, AA Talin, and JT Hachman. Electrodeposition of ni from low-temperature sulfamate electrolytes: I. electrochemistry and film stress. *Journal of The Electrochemical Society*, 153(5):C318, 2006.
- [208] JJ Kelly and NYC Yang. Electrodeposition of ni from a sulfamate electrolyte. *Sand Report, Sandia National Laboratories, Sand2001-8609*, 2001.
- [209] Harvey P Hack, Patrick J Moran, and John R Scully. Influence of electrolyte resistance on electrochemical measurements and procedures to minimize or compensate for resistance errors. In *The Measurement and Correction of Electrolyte Resistance in Electrochemical Tests*. ASTM International, 1990.
- [210] Dennis van der Vliet, Dusan S Strmcnik, Chao Wang, Vojislav R Stamenkovic, Nenad M Markovic, and Marc TM Koper. On the importance of correcting for the uncompensated ohmic resistance in model experiments of the oxygen reduction reaction. *Journal of Electroanalytical Chemistry*, 647(1):29–34, 2010.
- [211] Daniel A Buttry and Michael D Ward. Measurement of interfacial processes at electrode surfaces with the electrochemical quartz crystal microbalance. *Chemical Reviews*, 92(6):1355–1379, 1992.
- [212] Galit Zilberman. *On the Structure of the Metal/solution Interface-an EQCM Study*. University of Tel-Aviv, 2001.
- [213] E Gileadi and V Tsionsky. Studies of electroplating using an eqcm. i. copper and silver on gold. *Journal of the Electrochemical Society*, 147(2):567, 2000.
- [214] K Wang, HW Pickering, and KG Weil. Eqcm studies of the electrodeposition and corrosion of tin–zinc coatings. *Electrochimica acta*, 46(24-25):3835–3840, 2001.
- [215] T Kinoshita, S Akita, Nii Kobayashi, S Nii, F Kawaizumi, and K Takahashi. Metal recovery from non-mounted printed wiring boards via hydrometallurgical processing. *Hydrometallurgy*, 69(1-3):73–79, 2003.

- [216] K Johannsen, D Page, and S Roy. A systematic investigation of current efficiency during brass deposition from a pyrophosphate electrolyte using rde, rce, and qcm. *Electrochimica Acta*, 45(22-23):3691–3702, 2000.
- [217] GJZP Sauerbrey. The use of quartz oscillators for weighing thin layers and for microweighing. *Z. Phys.*, 155:206–222, 1959.
- [218] G Vatankhah, J Lessard, G Jerkiewicz, A Zolfaghari, and BE Conway. Dependence of the reliability of electrochemical quartz-crystal nanobalance mass responses on the calibration constant, cf: analysis of three procedures for its determination. *Electrochimica acta*, 48(11):1613–1622, 2003.
- [219] Martin Leimbach, Christoph Tschaar, Udo Schmidt, and Andreas Bund. Electrochemical characterization of chromium deposition from trivalent solutions for decorative applications by eqcm and near-surface ph measurements. *Electrochimica Acta*, 270:104–109, 2018.
- [220] Naray Pewnim and Sudipta Roy. Effect of fluorosurfactant additive during cu-sn codeposition from methanesulfonic acid. *Journal of the Electrochemical Society*, 162(8):D360, 2015.
- [221] MA Warne and PCS Hayfield. Durability of platinized titanium anodes in electroplating. *Transactions of the IMF*, 45(1):83–92, 1967.
- [222] MG Moula, G Szymanski, B Shobeir, H Huang, IJ Burgess, A Chen, and J Lipkowski. Electrochemical dissolution behavior and the residue formation mechanism of laboratory made carbonyl nickel. *Electrochimica Acta*, 162:108–118, 2015.
- [223] Tony Hart. Personal communication, 2021.
- [224] Daniel C Harris. *Quantitative chemical analysis*. Macmillan, 2010.
- [225] W Oelßner, F Berthold, and U Guth. The ir drop—well-known but often underestimated in electrochemical polarization measurements and corrosion testing. *Materials and Corrosion*, 57(6):455–466, 2006.



- [226] B Metrohm Autolab. Autolab application note ec04. *Ohmic drop Part 2–Measurement*, 2011.
- [227] M Holm and TJ O’keefe. Evaluation of nickel deposition by electrochemical impedance spectroscopy. *Journal of applied electrochemistry*, 30(10):1125–1132, 2000.
- [228] HK Srivastava. Microstructure of nickel electrodeposited from a nickel sulfamate/formamide bath. *Metal Finishing*, 93(5):20–27, 1995.
- [229] S Armyanov and G Sotirova. Diffusion-elastic phenomena in nickel and cobalt electrodeposits plated on to strip cathodes. *Surface and Coatings Technology*, 34(4):441–454, 1988.
- [230] S Armyanov and G Sotirova-Chakarova. Hydrogen desorption and internal stress in nickel coatings obtained by periodic electrodeposition. *Journal of The Electrochemical Society*, 139(12):3454, 1992.
- [231] Virginia Costa Kieling. Parameters influencing the electrodeposition of ni-fe alloys. *Surface and Coatings Technology*, 96(2-3):135–139, 1997.
- [232] E Valles, R Pollina, and E Gomez. Relation between the presence of inhibitors and deposit morphology in nickel deposition. *Journal of applied electrochemistry*, 23(5):508–515, 1993.
- [233] Matthew Fayette, Ugo Bertocci, and Gery R Stafford. In situ stress measurements during cobalt electrodeposition on (111)-textured au. *Journal of The Electrochemical Society*, 163(5):D146, 2016.
- [234] Moo Hong Seo, Dong Jin Kim, and Joung Soo Kim. The effects of ph and temperature on ni–fe–p alloy electrodeposition from a sulfamate bath and the material properties of the deposits. *Thin solid films*, 489(1-2):122–129, 2005.
- [235] JW Dini and HR Johnson. The influence of nickel sulfamate operating parameters on the impurity content and properties of electrodeposits. *Thin Solid Films*, 54(2):183–188, 1978.

- [236] Nobuyoshi Koga, Takaaki Kimizu, Masatora Sakamoto, and Yoshihiro Furukawa. Temperature effect on cobalt (ii)-chloride complex equilibrium in aqueous solution. 2009.
- [237] H Natter and R Hempelmann. Nanocrystalline copper by pulsed electrodeposition: the effects of organic additives, bath temperature, and ph. *The Journal of Physical Chemistry*, 100(50):19525–19532, 1996.
- [238] JS Santos, R Matos, F Trivinho-Strixino, and EC Pereira. Effect of temperature on co electrodeposition in the presence of boric acid. *Electrochimica Acta*, 53(2):644–649, 2007.
- [239] S Bakkali, M Cherkaoui, A Boutouil, MR Laamari, M Ebn Touhami, M Belfakir, and A Zarrouk. Theoretical and experimental studies of tin electrodeposition. *Surfaces and Interfaces*, 19:100480, 2020.
- [240] Mohammad M Fares, AK Maayta, and Mohammad M Al-Qudah. Pectin as promising green corrosion inhibitor of aluminum in hydrochloric acid solution. *Corrosion Science*, 60:112–117, 2012.
- [241] Wendy C Grande and Jan B Talbot. Electrodeposition of thin films of nickel-iron: I. experimental. *Journal of the Electrochemical Society*, 140(3):669, 1993.
- [242] JL Bubendorff, L Cagnon, V Costa-Kieling, JP Bucher, and Philippe Allongue. Anion promoted ni-underpotential deposition on au (111). *Surface science*, 384(1-3):L836–L843, 1997.
- [243] D Golodnitsky, NV Gudin, and GA Volyanuk. Cathode process in nickel-cobalt alloy deposition from sulfamate electrolytes—application to electroforming. *Plating and surface finishing*, 85:65–73, 1998.
- [244] Ashutosh Sharma, Sumit Bhattacharya, Siddhartha Das, and Karabi Das. A study on the effect of pulse electrodeposition parameters on the morphology of pure tin coatings. *Metallurgical and Materials Transactions A*, 45(10):4610–4622, 2014.

- [245] Steven D Leith, Shirley Ramli, and Daniel T Schwartz. Characterization of  $\text{Ni}_{1-x}\text{Fe}_x$  ( $0.10 < x < 0.95$ ) electrodeposition from a family of sulfamate-chloride electrolytes. *Journal of the electrochemical society*, 146(4):1431, 1999.
- [246] Masahiko Morinaga. 11 - local lattice strains around alloying elements in metals. In Masahiko Morinaga, editor, *A Quantum Approach to Alloy Design*, Materials Today, pages 221–260. Elsevier, 2019.
- [247] WH Zachariasen. The precise structure of orthoboric acid. *Acta Crystallographica*, 7(4):305–310, 1954.
- [248] RJ Gillespie and EA Robinson. The sulphur–oxygen bond in sulphuryl and thionyl compounds: Correlation of stretching frequencies and force constants with bond lengths, bond angles, and bond orders. *Canadian journal of chemistry*, 41(8):2074–2085, 1963.
- [249] P Radhakrishnamurthy, S Sathyanarayana, and AKN Reddy. Kinetics of hydrogen evolution reaction on a stainless steel electrode. *Journal of Applied Electrochemistry*, 7(1):51–55, 1977.
- [250] M Drogowska, H Menard, and L Brossard. Electrooxidation of stainless steel aisi 304 in carbonate aqueous solution at ph 8. *Journal of applied electrochemistry*, 26(2):217–225, 1996.
- [251] M Grdeń and K Klimek. Eqcm studies on oxidation of metallic nickel electrode in basic solutions. *Journal of Electroanalytical Chemistry*, 581(1):122–131, 2005.
- [252] Zheng Zhou, Li Wei, Yanqing Wang, H Enis Karahan, Zibin Chen, Yaojie Lei, Xunca Chen, Shengli Zhai, Xiaozhou Liao, and Yuan Chen. Hydrogen evolution reaction activity of nickel phosphide is highly sensitive to electrolyte ph. *Journal of Materials Chemistry A*, 5(38):20390–20397, 2017.
- [253] Digby D Macdonald and Mirna Urquidi-Macdonald. Theory of steady-state passive films. *Journal of the Electrochemical Society*, 137(8):2395, 1990.
- [254] Stephen Fletcher. Tafel slopes from first principles. *Journal of Solid State Electrochemistry*, 13(4):537–549, 2009.

- [255] Zheng Zhou, Zengxia Pei, Li Wei, Shenlong Zhao, Xian Jian, and Yuan Chen. Electrocatalytic hydrogen evolution under neutral pH conditions: current understandings, recent advances, and future prospects. *Energy & Environmental Science*, 13(10):3185–3206, 2020.
- [256] Rongyue Wang, Ugo Bertocci, Haiyan Tan, Leonid A Bendersky, and Thomas P Moffat. Self-terminated electrodeposition of Ni, Co, and Fe ultrathin films. *The Journal of Physical Chemistry C*, 120(29):16228–16237, 2016.
- [257] Nicole L Ritzert and Thomas P Moffat. Ultramicroelectrode studies of self-terminated nickel electrodeposition and nickel hydroxide formation upon water reduction. *The Journal of Physical Chemistry C*, 120(48):27478–27489, 2016.
- [258] N Danilovic, Ram Subbaraman, D Strmcnik, Kee-Chul Chang, AP Paulikas, VR Stamenkovic, and Nenad M Markovic. Enhancing the alkaline hydrogen evolution reaction activity through the bifunctionality of Ni(OH)<sub>2</sub>/metal catalysts. *Angewandte Chemie*, 124(50):12663–12666, 2012.
- [259] Ram Subbaraman, Dusan Tripkovic, Kee-Chul Chang, Dusan Strmcnik, Arvydas P Paulikas, Pussana Hirunsit, Maria Chan, Jeff Greeley, Vojislav Stamenkovic, and Nenad M Markovic. Trends in activity for the water electrolyser reactions on 3d transition metal (Ni, Co, Fe, Mn) hydroxide catalysts. *Nature materials*, 11(6):550–557, 2012.
- [260] RAF Hammond. Electrodeposition from nickel sulphamate solution, 1971.
- [261] Eugene Shalyt, Jingjing Wang, Vishal Parekh, and Michael MacEwan. Advanced process control of nickel electrodeposition for packaging in semiconductor industry. In *ECS Meeting Abstracts*, number 33, page 1714. IOP Publishing, 2014.
- [262] A Morrison, JJ Leitch, G Szymanski, G Moula, B Barlow, Ian J Burgess, B Shobeir, H Huang, and J Lipkowski. Electrochemical dissolution of nickel produced by the Mond method under alternating temperatures and nickel carbonyl gas pressures. *Electrochimica Acta*, 260:684–694, 2018.
- [263] Madhav Datta. *Electrodissolution Processes: Fundamentals and Applications*. CRC Press, 2020.

- [264] Burke C Barlow, Grzegorz Szymanski, Jacek Lipkowski, Babak Shobeir, Bruce Love, and Ian J Burgess. Pulsed potential dissolution reduces anode residue formation during nickel electroplating. *Journal of The Electrochemical Society*, 163(5):C164, 2016.
- [265] Burke C Barlow. *Reducing Residue In Nickel Electroplating Operations*. PhD thesis, University of Saskatchewan, 2016.
- [266] TA Green, P Valverde, and S Roy. Anodic reactions and the corrosion of copper in deep eutectic solvents. *Journal of the Electrochemical Society*, 165(9):D313, 2018.
- [267] J Wang, DR Gabe, AC Hart, and PC Crouch. The chemistry of nickel electroplating solutions. *Transactions of the IMF*, 91(1):4–10, 2013.
- [268] Brian N Figgis and Michael A Hitchman. *Ligand field theory and its applications*. 1999.
- [269] David S Hall, David J Lockwood, Christina Bock, and Barry R MacDougall. Nickel hydroxides and related materials: a review of their structures, synthesis and properties. *Proceedings of the Royal Society A: Mathematical, Physical and Engineering Sciences*, 471(2174):20140792, 2015.
- [270] Weihua Liu, Artas Migdisov, and Anthony Williams-Jones. The stability of aqueous nickel (ii) chloride complexes in hydrothermal solutions: Results of uv–visible spectroscopic experiments. *Geochimica et Cosmochimica Acta*, 94:276–290, 2012.
- [271] JS Sallo, J Kivel, and FC Albers. Radiochemical studies of thiourea in the electroless deposition process. *Journal of the Electrochemical Society*, 110(8):890, 1963.
- [272] NV Sotskaya, EI Ryabinina, TA Kravchenko, and Kh S Shikhaliev. The role of organic additives in the electroless nickel plating bath. *Protection of metals*, 39(3):245–249, 2003.

- [273] Karla C de F Araújo, Jéssica P de P Barreto, Jussara C Cardozo, Elisama Vieira dos Santos, Danyelle M de Araújo, and Carlos A Martínez-Huitle. Sulfate pollution: evidence for electrochemical production of persulfate by oxidizing sulfate released by the surfactant sodium dodecyl sulfate. *Environmental Chemistry Letters*, 16(2):647–652, 2018.
- [274] S-K Kim, John E Bonevich, Daniel Josell, and Thomas P Moffat. Electrodeposition of ni in submicrometer trenches. *Journal of The Electrochemical Society*, 154(9):D443, 2007.

# Chapter 9

## Appendices

### 9.1 Appendix A: Derivation of the ion-transfer kinetic equation

The main purpose of this section is to develop the quantitative relationship between the rate of reaction and the overpotential for a kinetically controlled process involving the ion transfer reaction given in Equation 9.1:



where  $k_c$  and  $k_a$  are heterogeneous rate constants which are functions of the electrode potential. The subscripts "c" and "a" represent quantities for the forward (cathodic) and backward (anodic) reactions, respectively. The current densities,  $j$  for the cathodic and anodic components of reaction 9.1 can be related to the reaction rates,  $\nu$  as follows [48, 183]:

$$j_c = nF\nu_c = -nFk_c c_{M^{n+}} \quad (9.2)$$

$$j_a = nF\nu_a = nFk_a c_M \quad (9.3)$$

It is worth mentioning that electrodes come in different sizes. In order to characterize different systems, the total current is normalised by the surface area ( $A$ ) of the working electrode to give current density ( $j$ ). The net current density flowing for the reaction is:

$$j = j_a + j_c \quad (9.4)$$

therefore

$$j = nFk_a c_M - nFk_c c_{M^{n+}} \quad (9.5)$$

The crucial step is to find the relationship between the net current density and the electrode potential, which is derived from the effect of the potential difference ( $\Delta\phi$ )

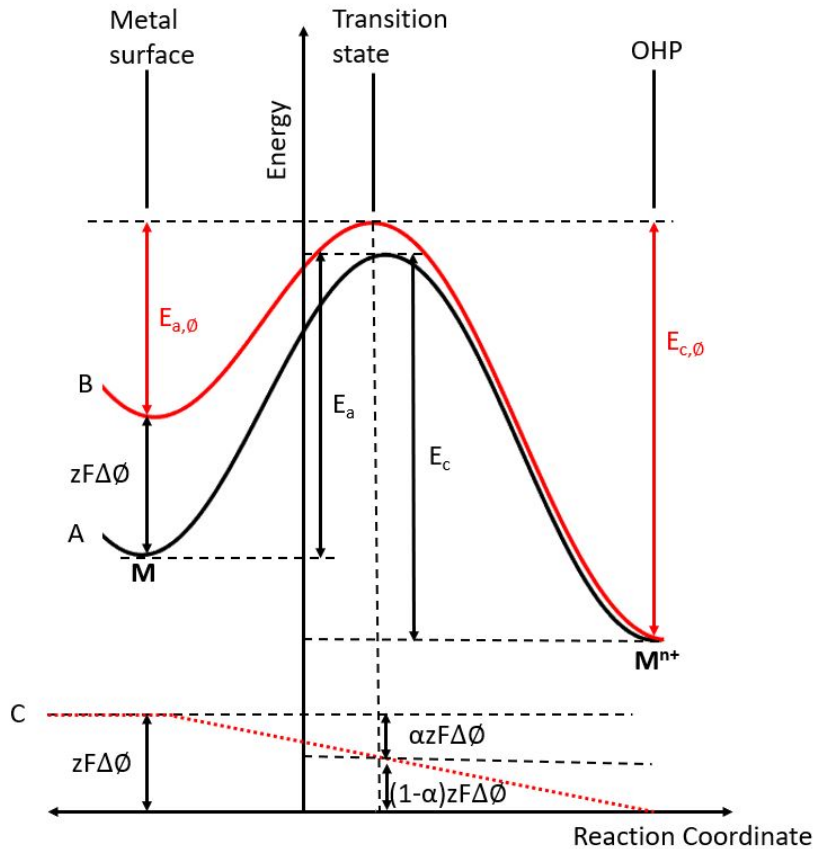


Figure 9.1: The Gibbs energy profile for the transfer of an ion from across the metal-solution interface in the presence and absence of a Galvani potential difference ( $\Delta\phi$ ). Adapted from [48]

across the electrode-solution interface on the activation energies of the forward and backward reactions. This follows the derivation outlined by Hansal et al. [48]. For this derivation, it was assumed that the ion transfer reaction behaves in an analogous manner to chemical rate processes, and might be described using the transition state theory as shown in Figure 9.1. Curve A represents the pure "chemical" energy changes during the ion-transfer reaction at  $\Delta\phi = 0$ . The metal ion sheds its hydration sphere as it approaches the electrode, displacing water molecules from the electrode surface. The Gibbs free energy rises as it gets closer to the electrode surface until it reaches a peak associated with a transition state, at which point the energy starts to fall as the ion approaches the surface and chemically interacts with it [48]. The free energy difference between the transition state and the metal ion located at the OHP is the activation energy,  $E_c$  that the metal ion at the OHP must overcome before it is deposited in the forward process. Similarly, for an ad-atom to become an ion in solution, it must



overcome the free energy of activation for the reverse process,  $E_a$  (Curve B, Figure 9.1) [48]. These activation energies are dependent on the potential difference at the metal-solution interface,  $\Delta\phi$ .

If a Galvani potential difference ( $\Delta\phi > 0$ ) is applied across the metal-solution interface (Curve C, Figure 9.1), then it contributes an additional free energy ( $zF\Delta\phi$ ) which yields an electrochemical energy profile shown in Curve B, Figure 9.1 [48]. In respect to an effect on  $E_a$  and  $E_c$ , it is only necessary to think of the work done to get the reacting species to the transition state which is given by  $\beta zF\Delta\phi$ , where  $\beta$  represents the symmetry factor, which describes the fraction of the potential induced free energy change that is used to modify the activation energy of the anodic reaction while  $(1-\beta)$  is the fraction that impacts the cathodic activation energy [48].

In the present case, a positive potential difference ( $\phi > 0$ ) has been applied which reduces  $E_a$  by  $\beta zF\Delta\phi$  while  $E_c$  is increased by  $(1-\beta)zF\Delta\phi$  to give new values,  $E_{a,\phi}$  and  $E_{c,\phi}$ , respectively, as shown in Equations 9.6 and 9.7. The respective equations have also been expressed in terms of the electrode potential,  $U$ , which is taken relative to a reference electrode. It is noted that the magnitude of the factor  $\beta$  depends on how far along the reaction coordinate the transition state is found. If this state is found close to the electrode surface, then  $\beta$  will tend to be zero; if it is nearer to the OHP then  $\beta$  will be 1 [48].

$$E_{a,\phi} = E_a - \beta zF\Delta\phi = E_a - \beta zFU \quad (9.6)$$

$$E_{c,\phi} = E_c + (1-\beta)zF\Delta\phi = E_c + (1-\beta)zFU \quad (9.7)$$

Based upon the Arrhenius equation 9.8 for the rate constant,  $k$ :

$$k = k_0 \exp\left(-\frac{E}{RT}\right) \quad (9.8)$$

where  $E$  is the free energy of activation and  $k_0$  is a constant, the rate constants,  $k_a$  and  $k_c$ , can be expressed as follows:

$$k_a = k_{0,a} \exp\left(-\frac{E_{a,\phi}}{RT}\right) = k'_a \exp\left(\frac{\beta zFU}{RT}\right) \quad (9.9)$$

$$k_c = k_{0,c} \exp\left(-\frac{E_{c,\phi}}{RT}\right) = k'_c \exp\left(\frac{-(1-\beta)zFU}{RT}\right) \quad (9.10)$$

where  $k_a' = k_{0,a} \exp\left(-\frac{E_a}{RT}\right)$  and  $k_c' = k_{0,c} \exp\left(-\frac{E_c}{RT}\right)$ .

By substituting Equations 9.9 and 9.10 in Equations 9.12 and 9.11, respectively, the current densities for the cathodic process and anodic currents are given by:

$$j_c = -nFc_{M^{n+}}k_c' \exp\left(\frac{-(1-\beta)zFU}{RT}\right) \quad (9.11)$$

$$j_a = nFc_Mk_a' \exp\left(\frac{\beta zFU}{RT}\right) \quad (9.12)$$

It is noted from Equations 9.11 and 9.12 that an applied potential changes the relative rates of the cathodic and anodic reactions happening at the electrode surface. For example, an increase in the magnitude of a positively applied potential will increase the rate of the anodic process while decreasing the rate of the cathodic process. The sum of the cathodic and anodic current densities give rise to a measurable current as expressed in Equation 9.13 [48].

$$j = nFc_Mk_a' \exp\left(\frac{\beta zFU}{RT}\right) - nFc_{M^{n+}}k_c' \exp\left(\frac{-(1-\beta)zFU}{RT}\right) \quad (9.13)$$

This equation describes the current-potential dependence of an ion transfer reaction which can also be expressed in terms of the overpotential,  $\eta$  which is defined as  $\eta = U - U_{eq}$ . The substitution results in the following equation:

$$j = nFc_Mk_a' \exp\left(\frac{\beta zFU_{eq}}{RT}\right) \exp\left(\frac{\beta zF\eta}{RT}\right) - nFc_{M^{n+}}k_c' \exp\left(\frac{-(1-\beta)zFU_{eq}}{RT}\right) \exp\left(\frac{-(1-\beta)zF\eta}{RT}\right) \quad (9.14)$$

At the equilibrium potential,  $U_{eq}$ , the net current density is zero and the magnitude of the cathodic current is equivalent to that of the anodic current. The value of this current density is defined as the exchange current density,  $j_0$  given as:

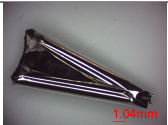

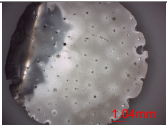
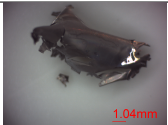
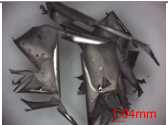
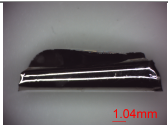
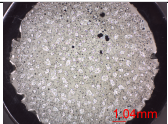
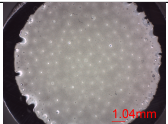
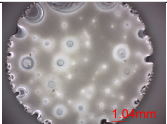
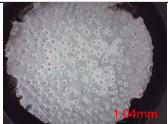
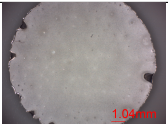
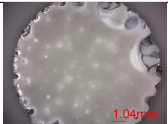
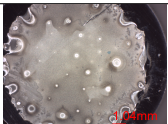
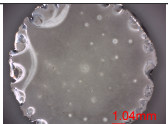
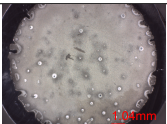
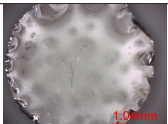
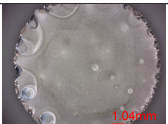
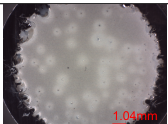


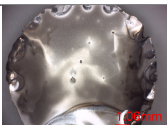

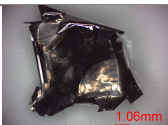

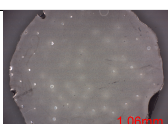
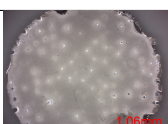
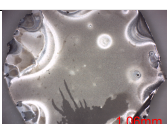
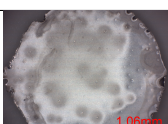
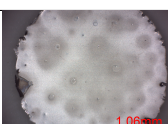
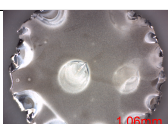
$$j_0 = nFc_Mk_a' \exp\left(\frac{\beta zFU_{eq}}{RT}\right) = nFc_{M^{n+}}k_c' \exp\left(\frac{-(1-\beta)zFU_{eq}}{RT}\right) \quad (9.15)$$

Substituting equation 9.15 in Eq. 9.14 results in equation 9.16.

$$\text{ion-transfer equation : } j = j_0 \left( \exp\left(\frac{\beta nF\eta}{RT}\right) - \exp\left(\frac{-(1-\beta)nF\eta}{RT}\right) \right) \quad (9.16)$$

## 9.2 Appendix B: Optical micrographs of nickel deposited from sulfamate baths

Table 9.1: Optical micrographs of nickel deposited at 20 and 40 mA/cm<sup>2</sup> from sulfamate Baths A-E at 40, 45, and 55 °C, magnification x 1. The table shows that adding boric acid to the bath (Baths B, C, and E) improves deposit appearance.

Baths	20 mA/cm <sup>2</sup>			40 mA/cm <sup>2</sup>		
	40 °C	45 °C	55 °C	40 °C	45 °C	55 °C
A						
B						
C						
D						
E						

### 9.3 Appendix C: Tafel plot for Ni(II) reduction in pure nickel sulfate solution

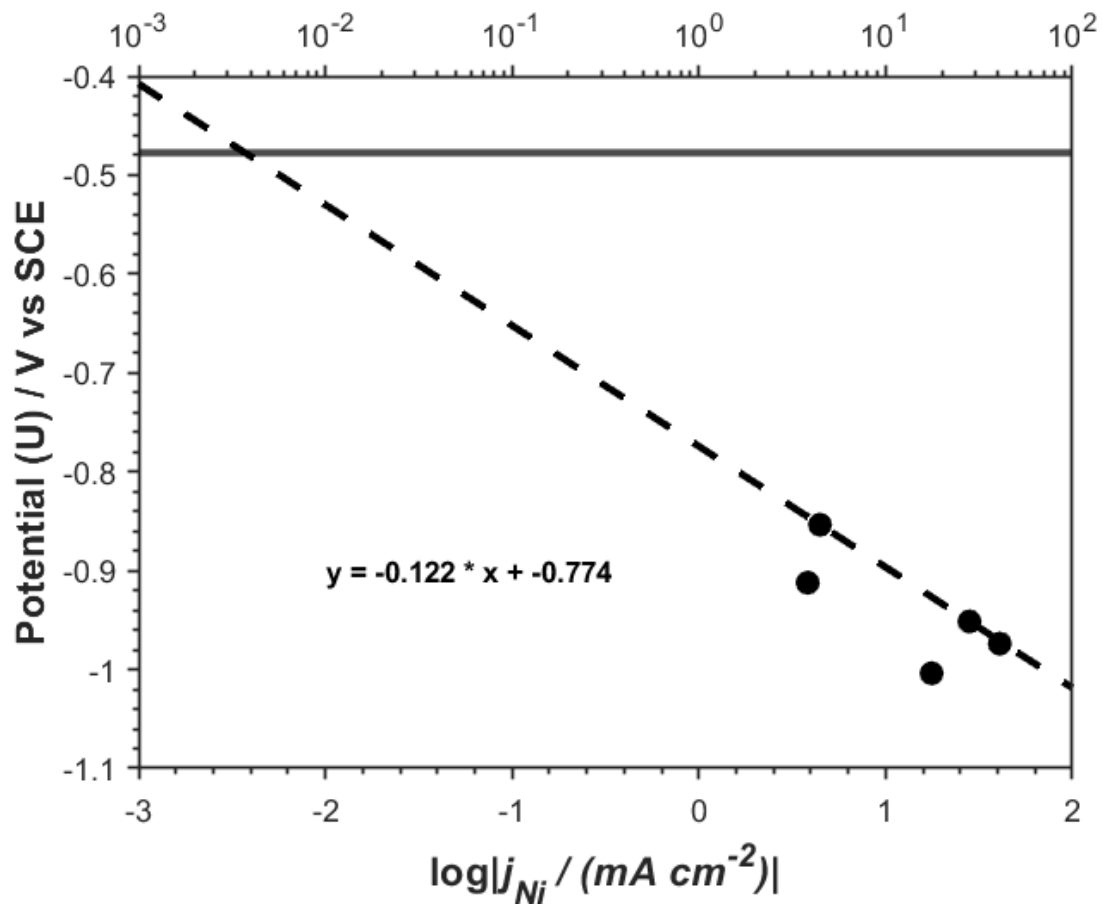


Figure 9.2: Tafel plot in quiescent Bath A at 40 °C.

#### 9.4 Appendix D: EQCM gravimetry curves for Ni(II) reduction on 304 SS in dilute nickel sulfamate electrolytes with and without boric acid

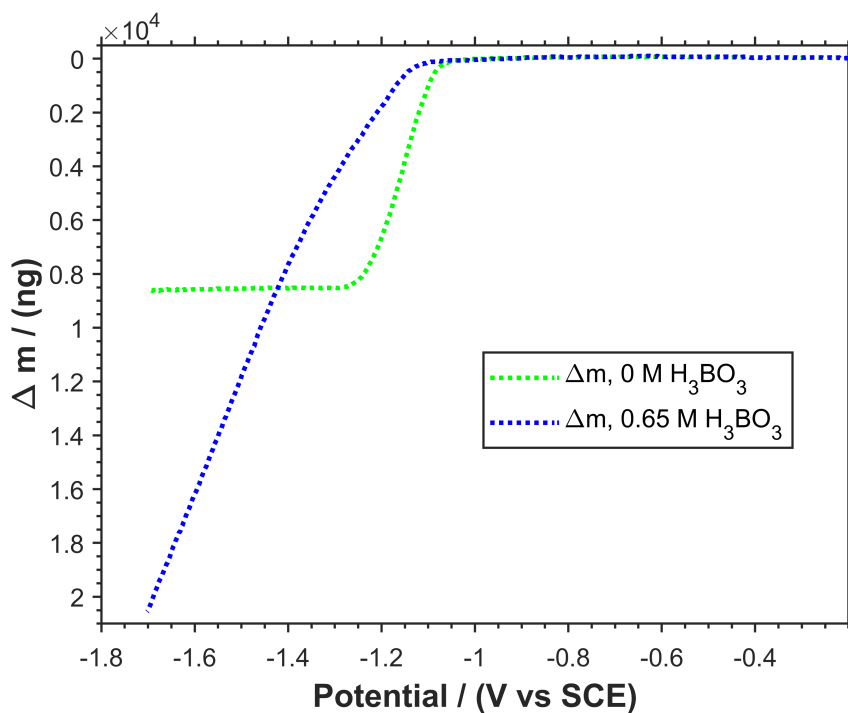


Figure 9.3: Massogram obtained in 17.9 mM Ni(II) + 3.57 M potassium sulfamate (pH 4.0) on 304 SS quartz crystal electrode with (blue) and without (green) boric acid; scan rate =  $5 \text{ mV s}^{-1}$ .

## 9.5 Appendix E: List of Publications

1. Green TA, Tambe CE, Roy S. Characteristics of anode materials for nickel electroforming. *Journal of The Electrochemical Society*. 2022 Sep 9;169(9):092510.
2. Tambe CE, Roy S, Green TA. Effect of boric acid on nickel electrodeposition kinetics during electroforming, *in preparation*.